



University  
of Glasgow

Lacaille, Gregoire (2019) *Hydroxide catalysed bonding applied to new materials for photonics applications*. PhD thesis.

<https://theses.gla.ac.uk/73041/>

Copyright and moral rights for this work are retained by the author

A copy can be downloaded for personal non-commercial research or study, without prior permission or charge

This work cannot be reproduced or quoted extensively from without first obtaining permission in writing from the author

The content must not be changed in any way or sold commercially in any format or medium without the formal permission of the author

When referring to this work, full bibliographic details including the author, title, awarding institution and date of the thesis must be given

COLLEGE OF SCIENCE AND ENGINEERING  
SCHOOL OF PHYSICS AND ASTRONOMY  
INSTITUTE FOR GRAVITATIONAL RESEARCH



# Hydroxide Catalysed Bonding Applied to New Materials for Photonics Applications

---

*By*  
Grégoire Lacaille

*Presented as requirement for completion of the degree of*

DOCTOR OF PHILOSOPHY

June 2019



---

## Summary

---

In the recent years, bonded components have seen a rise in popularity in solid state laser gain media as a way to mitigate thermal issues which are detrimental to their performances and limit power scaling. The bonding technique is currently selected based on a trade-off between cost and performance. Hydroxide catalysed bonding is a rather young technique coming from the field of gravitational research which has not really made an impact in photonics applications. Yet it is believed that thanks to its low cost and overall good performance, there is a non-negligible share of applications for which it could prove as the most advantageous process.

In this work phosphate glass and YAG are selected as materials of interest due to their common use as host matrices for solid-state lasers gain media. Both these materials have a different chemistry from the materials of interest in previous studies on hydroxide catalysed bonding and the bonding mechanisms are to a large extent unknown. Therefore the work has to be carried out from first principles. The highlighted properties to study are the reflectivity and the Light Induced Damage Threshold (LIDT) of the bond which are both of interest when the interface has to be crossed by a laser beam. The mechanical strength is added as a way to check the robustness of the component, to obtain an insight into the curing kinetics and to address concerns associated with manufacturability. Results on how the parameters of the solution used affect both the optical and mechanical properties of the bonded component, and which solution is the most suitable for photonics applications, are presented.

The beginning of this work largely draws on a presentation of the science case and a review of the relevant literature, from the description of the heat generation phenomenon in laser operation, to designs and techniques that allows mitigation of this heating.

Initial trials were carried out on phosphate glass. The parameters for the aqueous solution used in hydroxide catalysed bonding are not standardized and therefore various solutions were used to estimate the range of properties that can be obtained with the technique. Successful bonding of phosphate glass with either pure hydroxide (HCB) or silicate-enriched hydroxide (SB) was achieved. The strength of the bond was tested using 4-point flexure technique and strengths of about 13 MPa and 3 MPa were obtained for SB and HCB, respectively, from the first week of curing and with no significant variation with more time. The reflectivity of the bond at 532 nm was measured using an in-house built setup fully described in this work and the values obtained were of the order of magnitude of 0.01 % (HCB) and 0.1 % (SB). Since the lower strength can be a limitation to handle and manufacture components, it was decided to focus on SB samples for the following trials. The parameters of the solutions were changed and as a result the reflectivity was reduced to

## SUMMARY

---

values between 0.01 % and 0.1 % depending on parameters. The reflectivity trials also allowed an estimation of the bond thickness and refractive index in a non-destructive way using an optical model based on thin-layer interference described in this work. The kinetics of the change of these properties with curing time was studied. These gave valuable insight into the bonding mechanisms, and hypotheses were made on the chemistry occurring. The LIDT trials were outsourced and values obtained were about  $1.75 \text{ GW/cm}^2$  in the near infrared long pulses regime with no significant influence from the parameters of the solution used.

The attention was then shifted towards YAG again with a major focus on the reflectivity of the bond and improvement of the existing setup. Mechanical strengths of about 24 MPa (SB) after 2 months of curing were obtained. The reflectance obtained for the interface was about 0.2 % which makes it borderline for photonics applications without further work. However this value is relatively low compared to the ones obtained in similar studies on sapphire, and further investigations on the chemistry were carried out using x-ray analysis to understand why. From the results, bonding mechanisms that differ from the ones presented until then are suggested – mechanisms that form a hybrid layer of bonding chemical and substrate material - and the outlooks of the use of the techniques for new materials are discussed.

Finally various studies are presented on parameters that could affect the transfer of the process from a laboratory to a production environment such as that at Gooch and Housego. Reduction of curing time by applying elevated temperature would allow decreasing the lead time of the process. Control over the settling time of the bond would allow better yield on parts by making the operation easier. Last but not least, a UV/Ozone cleaning process, as an alternative to the current abrasion process used, would open the technique to a new range of samples designs while increasing the yield for larger batches.

---

## Acknowledgements

---

To Peter MacKay who supported me in my needs during my time at Gooch and Housego.

To Marielle and Christian who gave significant amounts of time in listening, advising and working with me throughout the years to make sure this thesis came to completion.

To Professors Sheila Rowan and James Hough who contributed to the supervision, particularly in the early and late stages of the project.

To the GraWIToN board who gave me the opportunity to join a broad scientific network and provided quality training and support all along.

To the planning staff at G&H who managed to push for my samples to be produced in the middle of busy times and the production staff who provided the samples.

To the administrative and technical staff both at G&H and the University of Glasgow who really facilitated my arrival, stays and travels.

To the people who trained me throughout the project and made me able to achieve what I was willing to: Marielle, Christian, Valentina, Karen, Margot, Roger, Brian.

To all the people met along the way

My colleagues at G&H with whom the lunch breaks really brightened the working days.

The people from the University, past and present, who always made me feel welcome when I visited.

The GraWIToN fellows with whom I was always looking forward to spend time in more or less exotic places.

The people met at Atomic in Yeovil which gave me motivation to brave the countryside public transport network in order to go out every week.

My driving instructor who had no other choice but to listen to me ranting about work for a grand total of 100 hours.

And to the long lasting friends that remained so in spite of geographical constraints and shared the highs and lows as if they were by my side.

Finally, to my family: Thank you for keeping trusting me and for supporting me throughout the experience.

---

## Preface

---

In the very recent years, the field of gravitational wave astronomy has met outstanding success. The first detection of a binary black holes merger system by the American pair of LIGO detectors was announced as recently as in February 2016 followed by later detections in 2016 and 2017. In August 2017, the first detection made jointly with the European VIRGO detector constituted another milestone. Again, in August 2017 the detection of gravitational waves from a binary neutron star merger allowed a first successful overlap between gravitational wave and electromagnetic signals, paving the way to multi-messenger astronomy.

All these achievements come with renewed interest and momentum for subsequent investments in the field. The cryogenic Japanese detector KAGRA should see commissioning within the next few years while the project INDIGO (LIGO India) received approval in 2016. The design of the third generation of ground-based detectors like the Einstein Telescope is also well on its way. Meanwhile, space-based detection has met its own success, with the LISA pathfinder mission performing above expectations and giving a greenlight for LISA to be the L3 research project of the European Space Agency.

A challenge in large fundamental research projects is to get private actors involved. The long scale of the projects and the fundamental nature of the outcome make the return on investment hard to see. However these missions often cannot be completed without technological feats that can be appealing for any industry able to identify them. In 2014, the European Commission funded the Initial Training Network GraWIToN under FP7-Marie Curie Actions with the purpose of bringing private and public institutions to work together on the technologies that will shape the third generation of gravitational waves detectors. Gooch and Housego (G&H) is one of the two companies that committed to the project. G&H is a precision optics manufacturing company based in Ilminster (Somerset, UK) and with additional sites in the UK and the US. The Ilminster site specialises in precision optics and acousto-optics sub-assemblies.

Although gravitational wave research widely relies on optical components, the purpose of the collaboration between the Institute for Gravitational Research at the University of Glasgow and G&H is elsewhere: developing an adhesive-free bonding technique suitable for photonics applications. Gravitational wave research has been using such a process, hydroxide catalysed bonding, in the prototypes and eventually the actual suspensions in place at the time of the various detections. However the designs of the assemblies in the photonics industry and the ones in gravitational wave detectors are radically different and do not result in the same requirements for the bonds. Therefore the purpose of this project

has been to study the suitability of this already well-investigated technique for photonics applications. This involved exploring both new materials and new properties of the bonds as these differ from the ones relevant for the suspensions assemblies.

This thesis presents the results gathered in the frame of the project. About 2/3 of the time was spent in an industrial environment at Gooch and Housego under the supervision of Dr. P. MacKay (Principal Technologist at G&H). The rest of the time was spent at the Institute for Gravitational Research where the supervision was undertaken by Prof. S. Rowan (director of the IGR), Prof. Sir. J. Hough (Associate director of the IGR), Dr. M. van Veggel (Research fellow at the IGR) and Dr. C. Killow (Research fellow at the IGR) at various stages of the project. All the experiments were carried out by the author except when specified otherwise.

In Chapter 1, information from the literature was collected to provide the reader with a comprehensive overview of the project. Starting from the basics, the lasing phenomenon is explained and the focus is rapidly brought onto solid state lasers. The generation of heat and its adverse effects on laser performances are discussed. Then design steps, from the choice of materials to the use of bonded components to mitigate these effects are presented. The bonding techniques available to make such bonded components are described with an emphasis of their pros and cons in the frame of photonics applications. Hydroxide catalysed bonding is selected as the preferred technique and the possibility of its application to new materials, phosphate glass and YAG, are presented. Finally, analytical models for the properties of interest of bonded components are discussed. The optical model for reflectivity is the one that was developed by Dr. V. Mangano during her Ph.D.

In Chapter 2, the properties of Hydroxide Catalysed Bonded (HCB) and Silicate Bonded (SB) phosphate glass are compared. All the samples were prepared in the production line of Gooch and Housego. The author made all the bonds after being trained in the technique by Dr. C. Killow. Sawing and polishing of the bonded components was done by the author. The strength tests were done at Gooch and Housego. The SEM pictures were taken by Dr. J. Scott in the presence of the author and Dr. M. Van Veggel who mounted the samples. The setup for the reflectivity measurement was entirely built by Dr. V. Mangano and the reflectivity measurements were taken by her in the presence of the author. The analysis was made by the author using the script provided by Dr. V. Mangano. The LIDT tests were done by Belford Research Ltd.

In Chapter 3, an attempt is made to tune the properties of the Silicate Bonds (SB) by diluting the solution to various concentrations. The reflectance was monitored in the course of the curing of the bonds leading to an estimation of the refractive index and thickness of the bonds. All the work presented in this chapter was carried out by the author with advice from

## PREFACE

---

Dr. V. Mangano and Dr. M. van Veggel. Only the LIDT tests were once again made by Belford Research Ltd.

In Chapter 4, properties of Silicate Bonded (SB) YAG are studied. The mechanical strength was tested. The setup for reflectance measurements was entirely re-assembled following insights from Dr. V. Mangano, Dr. M. Van Veggel, Prof. S. Rowan and Prof. Sir. J. Hough. Reflectance variations as well as the estimated refractive index and thickness changes with curing time were studied. Chemical analysis was carried out using EDXRF after training by Dr. M. Phelps. All the work presented in this chapter was performed by the author.

In Chapter 5, a set of experiments made to study the implementation of the bonding process in a production environment is presented. Curing time reduction was studied by strength testing silicate bonded quartz samples cured at elevated temperature. Settling time measurements were carried out by the author using a setup designed by Mr. G. Stewart with guidance from Dr. M. Van Veggel. Cleaning trials were carried out with assistance from Dr. K. Haughian, Dr. M. Van Veggel and Dr. C. Killow.

Appendix A presents additional measurements carried out by the author to better characterise some of the material used. The chemical composition was studied using EDXRF and refractive index measurements were made following advice from Dr. C. Killow.

Appendix B presents the 7-stage ultrasonic cleaning process used at Gooch and Housego.

Appendix C discusses Bayesian analysis which was used to estimate the refractive index and thickness of the bond from the reflectance measurements throughout this work.

The research leading to these results has received funding from the People Programme (Marie Curie Actions) of the European Union's Seventh Framework Programme FP7/2007-2013/ (PEOPLE-2013-ITN) under REA grant agreement n° [606176]. It reflects only the authors' view and the Union is not liable for any use that may be made of the information contained therein

## TABLE OF CONTENTS

---

### Table of contents

---

<b>SUMMARY.....</b>	<b>3</b>
<b>ACKNOWLEDGEMENTS .....</b>	<b>5</b>
<b>PREFACE .....</b>	<b>6</b>
<b>TABLE OF CONTENTS .....</b>	<b>9</b>
<b>LIST OF FIGURES.....</b>	<b>13</b>
<b>LIST OF TABLES.....</b>	<b>17</b>
<b>1 MOTIVATIONS FOR BONDED COMPONENTS IN THE PHOTONICS INDUSTRY AND SELECTION OF RELEVANT MATERIALS .....</b>	<b>18</b>
1.1 Generation of heat in solid-state lasers (SSL): A limitation to power scaling .....	18
1.1.1 Laser phenomenon.....	18
1.1.2 Generation of heat in the laser process.....	21
1.1.3 Adverse effects of the heating of the medium.....	23
1.2 Designing laser components to mitigate thermal effects .....	26
1.2.1 Choice of the matrix type: Crystalline or amorphous .....	26
1.2.2 Glass of choice for solid-state lasers: Phosphate glass .....	28
1.2.3 Crystals of choice for SSL: Yttrium Aluminium Garnet (YAG–Y <sub>3</sub> Al <sub>5</sub> O <sub>12</sub> ) and Yttrium othovanadate (YVO <sub>4</sub> ).....	30
1.2.4 Component designs.....	30
1.2.4.1 Thin discs lasers .....	31
1.2.4.2 Zig-zag slab .....	32
1.2.4.3 Composite laser rods .....	32
1.3 Bonding techniques for optical components .....	34
1.3.1 Optical contacting .....	34
1.3.2 Direct Bonding.....	35
1.3.3 Adhesive bonding .....	36
1.3.4 Glass-frit bonding.....	39
1.3.5 Hydroxide Catalysed Bonding (HCB) and Silicate Bonding (SB) .....	39
1.3.6 Synthesis on available techniques.....	43
1.3.7 State of the art and prospects for the materials of interest .....	43
1.3.7.1 Phosphate Glass .....	45
1.3.7.2 YAG .....	45
1.4 Limitations of bonded components .....	46
1.4.1 Reflectivity .....	46
1.4.2 Laser Induced Damage Threshold.....	51

## TABLE OF CONTENTS

---

1.4.3	Thermal induced stresses .....	52
1.5	Conclusion .....	53
<b>2</b>	<b>BONDING OF PHOSPHATE GLASS, AN AMORPHOUS NON-SILICA BASED OXIDE ....</b>	<b>55</b>
2.1	First bonding trial .....	55
2.1.1	Manufacturability .....	56
2.1.2	Scanning Electron Microscopy Observation .....	57
2.2	Strength tests .....	61
2.2.1	Method.....	61
2.2.1.1	Samples.....	61
2.2.1.2	Bonding.....	61
2.2.1.3	Strength testing setup .....	62
2.2.2	Results and discussion.....	63
2.2.3	Comparison with similar studies .....	66
2.3	Optical reflectivity.....	68
2.3.1	Method.....	68
2.3.1.1	Experimental setup .....	68
2.3.1.2	Data acquisition .....	72
2.3.1.3	Modus operandi .....	72
2.3.1.4	Measurement errors .....	74
2.3.2	Measurement and analysis of reflectance data.....	76
2.3.3	Analysis to extract n and t.....	80
2.3.4	Discussion and comparison with similar studies .....	82
2.4	Laser Induced Damage Threshold (LIDT) .....	84
2.4.1	Trials.....	84
2.4.2	Comparison with similar studies .....	86
2.5	Summary .....	86
<b>3</b>	<b>IMPROVEMENT OF THE EXPERIMENTAL SETUP AND MODIFICATION OF SILICATE BOND PROPERTIES BY TUNING THE SOLUTION PARAMETERS .....</b>	<b>89</b>
3.1	Samples.....	89
3.2	Optical reflectivity.....	90
3.2.1	Laser beam radius reduction .....	90
3.2.1.1	Beam profile measurement .....	91
3.2.1.2	Theoretical study.....	95
3.2.1.3	Empirical study .....	98
3.2.1.4	Validation of the layout .....	100
3.2.1.5	Detector characterisation.....	103
3.2.1.6	Modification of errors values.....	106

## TABLE OF CONTENTS

---

3.2.2 Trials.....	106
3.2.2.1 Improvement from the new layout and sample geometry .....	107
3.2.2.2 New sources of errors and how to get around them.....	107
3.2.2.3 Experimental Results .....	111
3.2.2.4 Data analysis.....	115
3.3 Light induced Damage Threshold .....	118
3.4 Summary and discussion .....	120
<b>4 BONDING OF A CRYSTALLINE, NON-SILICA-BASED MATERIAL: YTTRIUM ALUMINIUM GARNET (YAG) .....</b>	<b>123</b>
4.1 Strength tests .....	123
4.1.1 Initial bonding observation .....	123
4.1.2 Strength tests.....	123
4.1.3 Shape factor .....	125
4.2 Optical reflectivity.....	128
4.2.1 Samples.....	128
4.2.2 Setup modifications .....	128
4.2.2.1 Change of layout .....	128
4.2.2.2 New errors .....	131
4.2.2.3 Control measurement .....	134
4.2.3 Trial .....	136
4.2.3.1 Reflectance measurements.....	136
4.2.3.2 Bond parameters.....	139
4.2.4 Discussion.....	142
4.3 Etching .....	143
4.3.1 Method.....	144
4.3.2 Results.....	144
4.3.3 Discussion.....	145
4.4 Summary and conclusion.....	147
<b>5 IMPLEMENTATION OF THE BONDING PROCESS IN PRODUCTION.....</b>	<b>150</b>
5.1 Curing time reduction .....	150
5.1.1 Trials.....	151
5.1.2 Results.....	152
5.2 Settling time.....	154
5.2.1 Setup and modus operandi.....	154
5.2.2 Preliminary Study.....	156
5.2.3 Trial.....	156
5.2.4 Results and discussion.....	157

## TABLE OF CONTENTS

---

5.3	Cleaning .....	159
5.3.1	Cleaning assessment method .....	159
5.3.2	Cleaning processes .....	161
5.3.3	Trials.....	165
5.3.3.1	Materials for silicate bonding.....	165
5.3.3.2	Case Study: Lithium Niobate transducers .....	168
5.4	Conclusion .....	172
<b>6</b>	<b>GENERAL CONCLUSION AND OUTLOOKS .....</b>	<b>174</b>
	<b>APPENDIX A: MATERIAL CHARACTERISATION .....</b>	<b>176</b>
A.1	Material composition.....	176
A.1.1	Method.....	176
A.1.2	Phosphate Glass.....	176
A.1.3	YAG .....	178
A.1.4	Silica glass.....	178
A.2	Refractive index measurement.....	178
	<b>APPENDIX B: G&amp;H 7-STAGE CLEANING PROCESS .....</b>	<b>181</b>
	<b>APPENDIX C: ANALYSIS OF REFLECTANCE DATA: BAYESIAN ANALYSIS.....</b>	<b>182</b>
	<b>BIBLIOGRAPHY .....</b>	<b>191</b>

---

## List of figures

---

Figure 1-1: Schematic of 3-level laser system.....	19
Figure 1-2: Schematics of various ions-ions interactions in solid state lasers.....	23
Figure 1-3: Parabolic temperature profile in a laterally cooled solid-state laser gain medium.....	24
Figure 1-4: Schematic of a thin disc laser system.....	31
Figure 1-5: Schematic of zig zag pumping of the gain medium.....	32
Figure 1-6: Schematic of principle of a composite laser rode.....	33
Figure 1-7: Mechanism of hydroxide catalysed bonding .....	42
Figure 1-8: Figure of merit of the various bonding techniques available.....	44
Figure 1-9: Schematic of the beam reflection on a bonded component .....	47
Figure 1-10: Principle of a LIDT test. ....	51
Figure 1-11: Expected pattern from a LIDT test and determination of LIDT by linear regression.....	52
Figure 2-1: Bonded phosphate glass samples.....	56
Figure 2-2: Bonded phosphate glass samples cut and polished through the bond.....	57
Figure 2-3: Samples mounted for the SEM observation.....	58
Figure 2-4: SEM sample images from the bond observations.....	59
Figure 2-5: Bond thickness measured along the diameter for the SB sample.....	60
Figure 2-6: Layout of the 4-point flexural test.....	62
Figure 2-7: Photograph of samples breaking along and across the bond line.....	64
Figure 2-8: Results of strength versus curing time for bonded phosphate glass .....	65
Figure 2-9: Schematic of the reflectivity setup.....	71
Figure 2-10: Power fluctuation of the laser in the time frame of a measurement.....	75
Figure 2-11: Proportional relation between measurements taken with the oscilloscope and through the DAQ.....	76
Figure 2-12: Reflectance pattern for both HCB and SB at 30°, S-Polarisation. ....	77

## LIST OF FIGURES

---

Figure 2-13: Separated contributions to the bond reflectivity from the “monolithic ” sample (HCB) and the bond for SB, 30°, S-polarisation. ....	78
Figure 2-14: Reflectance pattern for HCB at 55°, P-polarisation. ....	79
Figure 2-15: Reflectance from the bond for both samples, both polarisations depending on the angle of incidence.....	79
Figure 2-16: Raw output from the Matlab script for determination of the thickness and refractive index of the bond. ....	81
Figure 2-17: Results of the LIDT tests of phosphate glass samples .....	85
Figure 3-1: Schematic of a beam radius measurement using the knife-edge technique.....	91
Figure 3-2: Example of a beam width measurement taken with the knife-edge technique....	92
Figure 3-3: Example of output of the beam profile measurement.....	93
Figure 3-4: Measured beam propagation along the setup.....	94
Figure 3-5: Layout for the mode-matching of a Gaussian beam .....	95
Figure 3-6: Beam radius at the photodiode depending on the focusing lens position. ....	98
Figure 3-7: Updated layout of the reflectivity setup and estimation of the beam profile along the optical bench.....	100
Figure 3-8: Reflectance of a reference sample obtained with the original and upgraded setup .....	101
Figure 3-9: Pattern of intensity obtained when translating the photodiode with the original and upgraded setup .....	102
Figure 3-10: Reflectance curves for both setup with the background correction added. ....	102
Figure 3-11: Sample curves from testing the linearity of the detectors.....	104
Figure 3-12: Determination of the error coming from the positioning of the detector. ....	105
Figure 3-13: Highlight of the improvement brought by the modification of the setup and sample geometry.....	107
Figure 3-14: Highlight of issues met in the first measurements.....	108
Figure 3-15: Results of the correction applied to mitigate the issue .....	109
Figure 3-16: Whole reflectance profile obtained with a bonded phosphate glass sample....	110

## LIST OF FIGURES

---

Figure 3-17: Highlight of the variation of the surface peak with time .....	110
Figure 3-18: Reflectance result for SB3 .....	112
Figure 3-19: Reflectance results for SB6 .....	113
Figure 3-20: Reflectance results for SB10 .....	114
Figure 3-21: Summary on the influence of the concentration of the solution on the reflectance of the interface. ....	115
Figure 3-22: Variations of bond parameters with time for the three samples.....	116
Figure 3-23: Experimental LIDT curves for the three samples.....	119
Figure 3-24: Summary of LIDT results for all phosphate glass samples.....	120
Figure 4-1: Results on strength tests of bonded YAG .....	124
Figure 4-2: Results on influence of the sample geometry on the measured strength.....	126
Figure 4-3: Beam profile and stress profile curves.....	127
Figure 4-4: Qualitative risk of failure in strength testing .....	127
Figure 4-5: Upgraded reflectivity measurement setup.....	129
Figure 4-6: Illustration of the degradation of the beam profile. ....	130
Figure 4-7: Beam profile at different positions along the optical bench.....	131
Figure 4-8: Error on $V_{output}$ with the new layout .....	132
Figure 4-9: Intensity profile with new layout using two different slits.....	135
Figure 4-10: Consistency of the measurement within a single day and across several ones for either slit.....	135
Figure 4-11: Background estimation with new layout using two different slits.....	136
Figure 4-12: Reflectance results YAG1 .....	137
Figure 4-13: Reflectance results YAG2 .....	138
Figure 4-14: Example of bad and good fits from the Matlab script .....	139
Figure 4-15: Bond parameters results (YAG) .....	140
Figure 4-16: Bond parameters across four different positions on the two samples .....	142
Figure 4-17: Chemical analysis of the solution after immersing bulky samples.....	146

## LIST OF FIGURES

---

Figure 4-18: Photograph of the test tubes used for chemical analysis .....	146
Figure 5-1: Sketch of the bonded sample featuring the crossed optical axes .....	151
Figure 5-2: Results of strength tests at elevated temperature.....	153
Figure 5-3: Captioned photograph of the setup for settling time measurements.....	155
Figure 5-4: Typical pattern of a settling time measurement.....	155
Figure 5-5: Results on settling time measurements.....	158
Figure 5-6: Sketch of contact angle on different surface states.....	160
Figure 5-7: Photograph of the Droepe Shape Analysis setup and screenshot of the user interface .....	161
Figure 5-8: Step by step illustration of UV/Ozone treatment, .....	163
Figure 5-9: Photograph of the custom UV/Ozone box available at the University of Glasgow.....	166
Figure 5-10: Averaged contact angle of the water drop on surfaces of various materials at various stages of cleaning. ....	166
Figure 5-11: Relative change in contact angle depending on the material and the cleaning process.....	167
Figure 5-12: Cleaning trials on Lithium Niobate.....	170
Figure 5-13: Iterative improvement of hydrophilicity with successive treatments .....	171
Figure A.1: Principle of refractive index measurement for bulky materials. ....	179
Figure A.2: Samples output of refractive index measurement.....	180

## List of tables

---

Table 2.1: Parameters of the LIDT test led at Belford Research, Ltd .....	85
Table 3.1: Output parameters for the system solved with various commercially available focal lengths.....	97
Table 3.2: Updated method and error values for the new campaign of measurements .....	106
Table 4.1: Error values for either slits measured as described in the text.....	133
Table 5.1: Final experimental parameters for each set. The number in brackets is the number of imperfectly bonded samples within the set. RT stands for room temperature.....	152
Table A.1: Phosphate glass composition 1 (PGC1).....	177
Table A.2: Phosphate glass composition 2 (PGC2).....	177
Table A.3: Equivalent molar composition of PGC1 and PGC2 .....	177
Table A.4: Composition of YAG samples provided by Roditi.....	178
Table A.5: Results from the refractive index measurements. ....	180

---

# 1 Motivations for bonded components in the photonics industry and selection of relevant materials

---

In order to understand the motivations of the work of this thesis, it is necessary to go back to some basics in photonics science. The aim of this chapter is to unfold the reasoning that led to this study, from the problem to be solved to the available solutions while mentioning the expected difficulties. In the first part a reminder of the principle of lasers with a focus on solid-state lasers gain media and how the generation of heat is currently limiting the scaling of performances is given. This leads to the introduction of some common materials and designs suggested to tackle the issue in a second part. In a third part, the existing options available to make the so-designed components are presented and the applicability to the selected materials discussed. Finally, some of the expected challenges are listed together with discussions on the theories or experimental methods used to assess their relevance.

## 1.1 Generation of heat in solid-state lasers (SSL): A limitation to power scaling.

### 1.1.1 Laser phenomenon

In this section the basics of the functioning of a laser are discussed and the terms that will be used throughout the chapter are defined. It does not aim at being a comprehensive description and the reader is invited to look at the references for additional details [1],[2],[3],[4].

The LASER effect, for Light Amplification by Stimulated Emission of Radiation, is the phenomenon of generating a coherent, low diverging light beam out of a gain medium provided with energy. The gain medium can be found in any three states of matter and contains species able to emit and absorb light which can be molecules (see e.g. [5]), atoms (see e.g. [6]), free electrons (see e.g. [7]), etc. The amplification phenomenon is achieved thanks to a resonator which in its simplest and most common configuration consists of two mirrors surrounding the host medium, one being only partially reflective at the laser wavelength. For description purposes, we will narrow down to the case where the setup is a solid medium, the active species are atoms and the energy is provided as light.

The core mechanism allowing the laser effect is the fact that the atoms possess a spectrum of various energy levels. At thermal equilibrium, the population of each level follows a Boltzmann distribution i.e.

$$\frac{N_2}{N_1} = e^{\frac{-\Delta E}{k_B T}} \quad (1.1)$$

Where  $N_i$  is the density of population at the level of energy  $i$ ,  $\Delta E$  is the energy gap between the levels 1 and 2,  $k_B$  is the Boltzmann constant and  $T$  the temperature. Therefore, at thermal equilibrium, the lower energy levels are significantly more populated than the upper ones. Active species go from a lower level to an upper level by absorbing energy equal to the gap between the two levels. Upon going through the medium, radiation is absorbed following the relation.

$$\frac{dI}{dx} = \gamma I \quad (1.2)$$

Where  $I$  is the intensity of the radiation,  $x$  is the distance travelled in the gain medium and  $\gamma$  is the gain of the medium. The gain has a negative contribution (absorption by the medium) and a positive contribution (emission by the medium) and amplification will occur if its value is overall positive. It can be shown that this requires an inversion of population, i.e. that an equilibrium must be reached where the upper level is more populated than the lower level and that this cannot be achieved with only two levels of energy involved [1].

Let us consider a system with three levels of energy as pictured in Figure 1-1. The radiation to amplify is the one issued from the transition from the level 2 to the level 1. The objective is to deplete the population of the level 1  $N_1$  and increase the one of the level 2  $N_2$ .

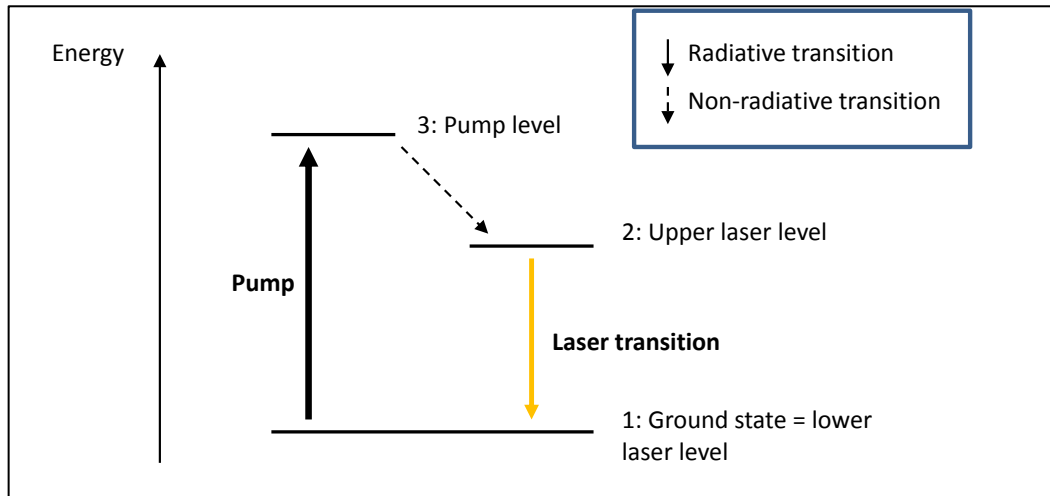


Figure 1-1: Schematic of 3-level laser system. Pumping brings atoms from level 1 to level 3 where they rapidly relax to level 2 in a non-radiative transition and then back to the ground state with emission of laser radiation.

A pump beam with a suitable wavelength is able to excite the atoms from level 1 to 3 according to equation 1.3. The absorption of the medium is proportional to the number of absorbing species  $N_1$  as well as to the beam intensity  $I_{pump}$ . The coefficient of proportionality is called the absorption cross-section  $\sigma_{13}$ .

$$\left(\frac{dN_3}{dt}\right)_{absorption} = \sigma_{13} N_1 I_{pump} \quad (1.3)$$

The relaxation from the level 3 to the level 2 and 1 is a spontaneous process as the atom strives to decrease its energy either by photon or phonon emission. This phenomenon is characterized by lifetimes  $\tau_{32}$  and  $\tau_{31}$  of the upper levels population according to equation 1.4.

$$\left(\frac{dN_3}{dt}\right)_{spontaneous\ emission} = -\frac{N_3}{\tau_{32}} - \frac{N_3}{\tau_{31}} \quad (1.4)$$

If  $\tau_{32}$  is negligible with regards to the rate of the other phenomena involved, including  $\tau_{31}$ , one can consider that every atom of the level 3 relaxes instantaneously to level 2 and therefore

$$\left(\frac{dN_2}{dt}\right)_{pumping} = \sigma_{13} N_1 I_{pump} \quad (1.5)$$

The level 2 is also subject to spontaneous emission towards the level 1. The photons emitted are incoherent and do not contribute to amplifying the laser emission. A long lifetime  $\tau_{21}$  is desired in order for the level 2 to keep an elevated population. The reason is that in addition to this spontaneous mechanism, it is also possible for the relaxation to be stimulated by a photon with energy corresponding to the gap between the energy levels. This stimulated emission results in both photons having the same phase and direction of propagation, amplifying the laser radiation. This is the reverse of the absorption phenomenon and as such can be described in the same way with a gain proportional to the density of population of the excited level and the intensity of the radiation as displayed in equation 1.6.

$$\left(\frac{dN_2}{dt}\right)_{stimulated\ emission} = -\sigma_{21} N_2 I_{laser} \quad (1.6)$$

Where  $\sigma_{21}$  is the emission cross-section.

Finally, once the laser radiation starts building up, it gets partially reabsorbed by the population  $N_1$  for the atoms to reach the energy level 2 following equation 1.7.

$$\left(\frac{dN_2}{dt}\right)_{absorption} = \sigma_{12} N_1 I_{laser} \quad (1.7)$$

With  $\sigma_{12}$  the absorption cross section of the transition.

In the end, the change of population  $N_2$  can be described by equation 1.8.

$$\left( \frac{dN_2}{dt} \right) = \sigma_{21}N_2I_{laser} - \sigma_{12}N_1I_{laser} - \frac{N_2}{\tau_{21}} + \sigma_{13}N_1I_{pump} \quad (1.8)$$

At equilibrium  $\left( \frac{dN_2}{dt} \right) = 0$ , the population inversion  $N_2 > N_1$  requirement results in equation 1.9.

$$I_{pump} > (\sigma_{21} - \sigma_{12})I_{laser} + \frac{1}{\sigma_{13}\tau_{32}} \quad (1.9)$$

Therefore a laser threshold power exists from which the pump power allows the generation and amplification of laser radiation constituted of coherent photons. This threshold depends on the parameters of the energy spectrum of the atoms which depends both on their nature and the host matrix they are in. Lower thresholds can also be reached by making use of 4-energy level configurations, where the lower laser state is not the ground state but an intermediate one [8]. With such a configuration, the lower laser state is constantly depleted making the population inversion happen with lower pump thresholds. 4-level lasers are therefore usually preferred.

It can be seen from equation 1.9 that the power of the laser radiation is capped and depends on the intensity of the pump. Therefore to obtain higher laser intensity, the incentive is to increase the pump power. However doing so also increases heating of the medium, which rapidly limits the performances of the laser [9]. The following section explains the nature of the phenomena that induce heat rather than light emission.

### 1.1.2 Generation of heat in the laser process

Heat generation has been the main obstacle in the power scaling of solid-state lasers in the past years [10]. This section focuses on the origin of heat generation. The effect of heat on the performances of the laser will be discussed in a later section.

The first factor contributing to heat generation is inherent to the laser mechanism and is called the quantum defect. It has been explained in the previous section that to obtain an operational laser, the atoms should be pumped to a level of energy higher than the upper laser level and, in the case of a 4-level laser will relax to a level higher than the ground state. This means that from the amount of energy initially provided, only a fraction will be released as laser light with the rest being lost in the so-called non-radiative transitions (see Figure 1-1 for the 3-level case).

This fraction depends on the difference between the pump wavelength and the laser wavelength and the quantum defect is expressed as [11]:

$$\eta = 1 - \frac{\lambda_{pump}}{\lambda_{laser}} \quad (1.10)$$

With  $\lambda_{laser}$  and  $\lambda_{pump}$  the wavelengths of the laser and the pump, respectively. In the case of Nd:YAG (Neodymium ions in a YAG matrix), one of the most common solid-state lasers, it amounts to 24% due to the absorption and emission peaks being at 805 nm and 1064 nm, respectively [12]. This means that 24 % of the energy is lost during the optical-optical conversion to laser radiation. Non-radiative transitions comprise all the transitions aside from the laser one. There are two ways an excited ion in a host matrix can release its energy: releasing a photon through spontaneous emission which will rarely be amplified due to the parameters of the cavity, or releasing its energy through the phonons (vibrations) of the host matrix [13]. The second case is the one which generates heat. Decreasing the quantum defect is done by selecting appropriate dopant and matrixes to allow pumping at a wavelength close to the lasing one and minimising the ion-phonon coupling [14].

A second source of non-radiative transitions is the interaction between the individual doping species. The phenomenon known as “quenching” is the main reason why, from a certain threshold, increasing the doping concentration does not increase the extracted power but on the contrary decreases the laser performance [15]. In the above, laser configurations were described using three or four energy levels. However, having an energy spectrum with three levels isolated from any other possible transition with the energies involved is not common. More energy levels will result in additional non-radiative transitions and contribute to heat production in the medium. The main known mechanisms are described below and illustrated in Figure 1-2.

Cross relaxations occur when the photon emitted by an upper-level ion is absorbed by an ion in an intermediate level and then relaxes in a non-radiative transition to the ground state. This is particularly likely to happen when the levels of energy multiply in sublevels due to the interaction between the ion and the matrix. It is damaging for the yield as an initially laser photon is converted to heat.

Up-conversion occurs when the photon released by a radiative transition from the upper level is reabsorbed by an ion already excited to the same level. Both the ions then relax via non-radiative transitions. This is likely to happen when there is an energy level above the upper-level of the laser transition with the same energy gap as the laser transition.

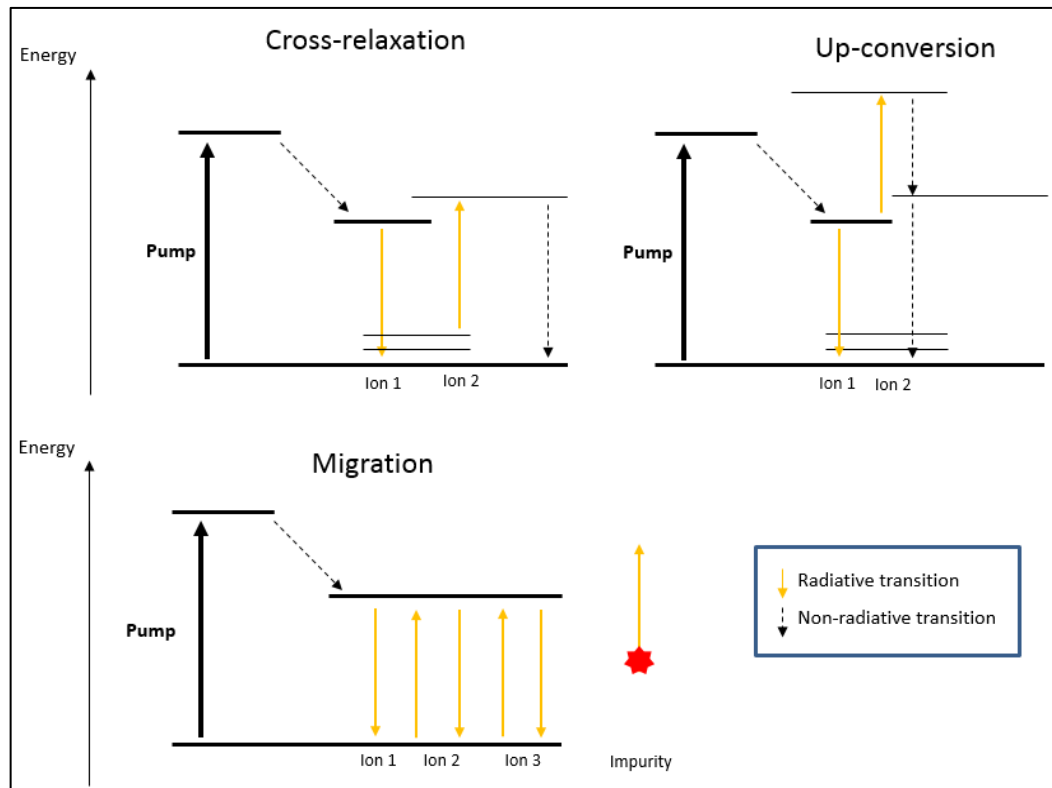


Figure 1-2: Schematics of various ions-ions interactions in solid state lasers.

The last mechanism is a simple migration of the excited state from site to site. In theory this should still eventually result in a radiative transition but multiplying the transitions increases the risk of the photon being absorbed by an impurity instead of an active ion and dissipating in the form of heat.

### 1.1.3 Adverse effects of the heating of the medium

The heat deposited in the medium must be dissipated in order to avoid damaging the performance of the component and ultimately the component itself. Therefore the gain medium is usually surrounded by a coolant or in contact with a heat sink [16][17]. Although it mitigates the risk of thermal runaway, this surface cooling brings undesired effects on its own which are described below.

The first and most dramatic effect of the heating of the medium is thermal fracture rendering the crystal unusable. When a component is surface-cooled, there is a boundary layer experiencing significant thermal gradients and ensuing thermal-induced stresses. These are all the more susceptible to lead to a fracture since micro-cracks are also present in this layer as a result of a polishing step in the surface preparation. Therefore laser gain media failure generally initiates at the surface, and surface treatment (acid etch, pre-stressing, etc.) are recommended to avoid it [18].

The surface tensile stress,  $\sigma$ , that develops in a slab of material of thickness  $t$  is given by equation 1.11 [19].

$$\sigma = \frac{Pt^2\alpha E}{12k(1-\nu)} = \frac{Pt^2K_{IC}}{12R_s} \quad (1.11)$$

Where  $R_s$  is a factor representing the resistance to thermal fracture of a material and is written as

$$R_s = \frac{k(1-\nu)K_{IC}}{E\alpha} \quad (1.12)$$

And  $P$  is the thermal power deposited in the medium,  $k$  the thermal conductivity of the material,  $\nu$  its Poisson's ratio,  $K_{IC}$  its fracture toughness,  $E$  its Young modulus and  $\alpha$  its coefficient of thermal expansion. All the parameters in equation 1.12 are intrinsic properties of the material and therefore  $R_s$  can be seen as a figure of merit of the material with regards to its resistance to thermal-induced stress that has to be maximised to allow high thermal loading. Different modifications of this equation exist where the fracture toughness is replaced by factors more component-related than material-related [20]. In the general case, components are designed to work at power well below the critical power and thermal fracture can be avoided by design. However, before thermal fracture is reached, there are several more insidious thermal-induced effects that take place. Due to surface cooling, thermal gradients develop in the medium and with them gradients of various properties that affect the laser performances.

If the component is pumped homogeneously, the temperature profile ends up being parabolic as displayed in Figure 1-3.

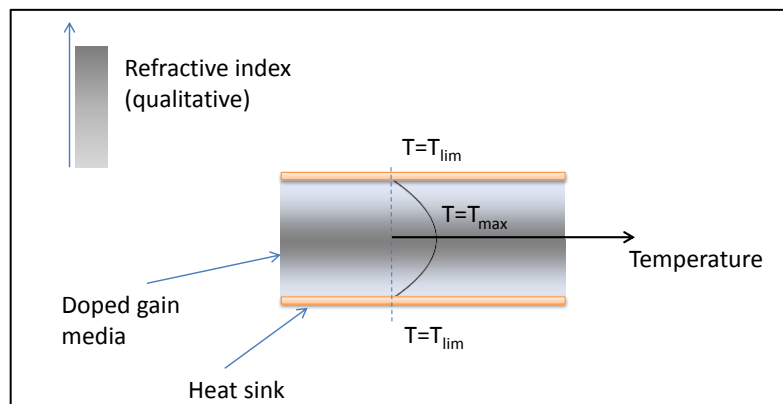


Figure 1-3: Parabolic temperature profile in a laterally cooled solid-state laser gain medium. The boundary temperature is kept at  $T_{lim}$  through cooling and a gradient develop in the medium following a parabolic profile (from the resolution of 2D-Fourier equation in steady state [21]).

The non-uniform temperature profile in the medium, with the cooled surface being cooler than the inner part, has various consequences [22][23][24].

- A parabolic profile for the refractive index which makes the medium act as a lens as the wave front is delayed in the inner part compared to the outer part. This is due to the thermal dependence of the refractive index and is known as the thermal lensing effect. Having a lens that is not accounted for in the design of the resonator can compromise the stability of the cavity and the input power is therefore limited. Depending on the focal length of the lens, high energy density may also be reached in the medium or on the resonator mirrors leading to permanent damage of the setup. In addition, this thermal lens displays spherical aberration due to the higher order terms in the thermo-optic dependency. This makes its compensation all the more difficult although some solutions have been described in the literature and will be presented in later sections.
- Bulging of the medium surfaces due to different thermal-induced strains between the outer and inner parts (see e.g. [25]). As a result the medium as a whole acts as a focusing lens as the outer portion of the beam experiences a shorter optical path than the inner portion. This adds up to the thermal lensing issue aforementioned although depending on the material one contribution can be negligible with regards to the other.
- Thermal induced radial stresses which in turn induce birefringence in the medium. The tangentially and radially polarised components of the beam see different refractive indices when propagating in the medium as the stresses have a radial profile. This may alter the polarisation state of the beam but also cause its splitting in an ordinary and extraordinary ray (bifocus effect) resulting in energy losses and beam quality degradation. Here again, several solutions have been put forward to mitigate the issue [26][27].

The effects described above show the importance of a good management and mitigation of the heat in the medium, even at power levels far from the one leading to thermal fracture of the medium. A lot of approaches exist, from the selection of the material to the geometry of the medium or the insertion of compensation elements in the cavity [28]. The next section focuses on the issues that motivated the present work.

## 1.2 Designing laser components to mitigate thermal effects

The above sections have highlighted how important the energy spectrum of the system is for the performances of the laser. This goes from the availability of the source to pump at the right level, to the lifetimes and cross-sections of the different transitions in order to obtain amplification, with consideration of the multiplicity of energy levels to avoid non-radiative transitions. Although the energy spectra of the common doping species are nowadays well known, it has been understood that they can be significantly modified by the host matrix they are put in. Ion-phonon coupling, which dictate level's lifetimes, depends strongly on the environment of the ion in the matrix. The properties of the material also define how much the heat generated impacts the performances of the components through their thermal conductivity, thermal dependence of refractive index or coefficient of thermal expansion. In the following part, the peculiarities of glass or crystal matrices are detailed to understand why one or the other is preferred depending on the application.

### 1.2.1 Choice of the matrix type: Crystalline or amorphous

The parameters of a laser strongly depend on the interaction between the host matrix and the doping ion. In solid-state lasers, the latter is often a cation from either the transition metals (see e.g. [29]) or from the rare-earth elements (see e.g. [31]). Transition metal cations have their outer shell incomplete which make them very likely to interact with the host matrix electrons [30]. On the contrary, the electrons of the incomplete layer of rare-earth ions are shielded by a full outer shell which reduces the interactions. As a result, the energy levels for the rare-earth ions are discrete values whereas they show as bands for the transition metals [31][32]. In the following, only rare-earth ions will be considered for illustration purpose.

In a similar way, the host matrix affects the repartition of the energy levels. Crystals have well-ordered atomic structures which means that the rare-earth ions can only fit in specific sites and steric configurations. Therefore the interaction between the ion and the network has few degrees of freedom resulting in the energy levels remaining discrete. In glass however, where neither the nature nor the arrangement of the atoms surrounding the rare-earth ion is fixed, the energy levels multiply in sublevels due to the various possibilities of interactions.

Both energy distributions have their advantages and find their own range of applications. A broader spectrum of absorption (glasses) allows pumping with a flash lamp due to the better overlap of the spectra whereas a narrow one (crystals) requires monochromatic light of the suitable wavelength (and will only be efficient if lasers of such wavelength can be used to pump the medium) [33]. From the point of view of the emission spectrum, having broad

bands allows wavelength tunability and short pulses (see e.g. [34]) while narrow bands allow accurate wavelengths. Therefore the choice of one or the other type of matrix can initially be done by considering the application and the pumping layout. However, the energy spectra are not the only parameters that differ from glass to crystals.

In addition to energy spectrum considerations, the volume of gain medium required must be taken into account. The volume requirement often comes from the amount of energy to extract. Ignoring quenching effects one can consider, to first approximation, that the extractable energy is proportional to the amount of doping of the medium. Due to their loose network, glasses can accommodate higher doping rates than crystals for which the amount of sites is limited. Therefore, it requires a lower volume of glass than crystal to reach a given quantity of doping species in the medium.

Glasses also have the advantage to be cast in large volumes. Progress in glass melting and manufacturing during the end of the 20<sup>th</sup> century now allows better control and tunability of the properties. Their homogeneity across batches but also within single blocks has improved too. This not only makes better gain media but additionally reduces waste, decreasing the overall cost of production. In comparison, growth of single crystal comes as an expensive process while also being limited in the size of medium that can be achieved. These considerations give a large economic advantage to glasses, while also making the use of crystals impracticable for certain applications. The large High Energy High Power laser facilities around the world for example require a large volume of gain medium to extract the most energy possible. Multiple large slabs of gain medium must be used in series which is not practicable at reasonable cost with crystals [36]. Research on ceramic crystals made by powder sintering could however solve this issue if the components made are performing as well as their single-crystal counterparts [35][37].

The main advantage of crystals over glasses is their better performances with regards to the heating of the medium [38]. This is not negligible as thermal effects are to date the principal limit to power scaling of solid-state lasers. As discussed in the previous section, heat is generated in the medium through non radiative transitions. These non-radiative transitions originate from the inclination of the excited ion to relax by transferring its energy to the network through phonons rather than emitting a photon. Since crystals have less resonating phonon energies than glass, it is easier to select a matrix that allows desired ion-phonon coupling and avoids the undesired ones. Additionally, crystals display a higher thermal conductivity than glasses which helps managing the heat level in the medium [39]. Last but not least, their mechanical properties (hardness, Young modulus, etc.) make them more resistant to thermally-induced fracture [38].

To summarise, both glasses and crystals are of interest as solid-state laser gain media, the final choice depending on the application. Glasses are more economic and allow flexibility of the matrix properties by modifying the composition of the melt. Their disordered structure results in broader absorption and emission peaks which make the pumping parameters less tight and allow tunability of the output radiation and the generation of short pulses. However the multiplicity of energy levels easily leads to undesired non radiative transitions which generate heat in the medium. In addition, their relatively low thermal conductivity does not help mitigating these effects. Crystals on the other hand have less variable properties as neither their chemical composition nor atomic structure can significantly vary. This results in narrow absorption bands, which require specific monochromatic sources for efficient pumping. However, they also provide monochromatic output and therefore it is often the case that this radiation is used to pump a subsequent solid-state laser [40]. Although the first laser was demonstrated using a crystal gain medium (ruby laser) in 1960 [41], the rise of use of crystalline matrices only happened from 1980 [42]. Before that, laser diodes were not at a stage of development allowing high enough power to efficiently pump crystals. Pumping diodes changed this, reducing by a lot the required size and therefore the cost of the gain medium and popularising crystal solid-state lasers. Their thermo-mechanical properties are better than glasses which increases the pumping power possible and can make up for lower doping ceiling.

In the following sections, the most commonly used glasses and crystals for solid-state lasers are introduced. These are the materials that will be the focus of the present work.

### 1.2.2 Glass of choice for solid-state lasers: Phosphate glass

The name phosphate glass comprises glasses with  $P_2O_5$  as main constituent. Usually these glasses contain about 60 % of  $P_2O_5$  in mass and 40 % of other oxides to tune their properties. At the time the laser effect was discovered, silicate glass ( $SiO_2$ ) was the only glass for which the manufacturing process was mature enough to yield laser glass quality [43]. Phosphate glass was seen as unusable due to its poor chemical durability and mechanical properties. However with the progress in glass manufacturing, phosphate glass reliability has increased and is nowadays the most common laser glass used. Its advantages over silicate glass are numerous and some of them are described below.

From an optical point of view first, phosphate glass has a higher refractive index, lower dispersion and is highly transparent in the ultraviolet range. When it comes to lasing, doping ions have higher cross sections and narrower bandwidth when put in a matrix of phosphate glass compared to silicate glass [36][44][45]. It means that the pump threshold to reach population inversion is lower and the luminescence at a given wavelength of emission is higher with phosphate glass, which are both advantageous features. The lifetime of the

metastable (upper-laser) level is also longer which means that the medium can store a larger amount of energy for pulsed operation. Besides, a common ion used in solid-state is erbium for its infrared eye-safe radiation. Erbium cannot be pumped easily and the common configuration is to co-dope the network with ytterbium. The pump radiation is absorbed by the ytterbium ions which upon relaxation emit a radiation able to pump the erbium ones. The energy transfer between ytterbium and erbium is twice as efficient in phosphate glass as in silicate glass and the lifetime of the excited erbium is also shorter which makes the reverse transition less likely [33].

Last but not least, the feature that makes phosphate glass stand out from its competitors is the possibility of tuning the composition to obtain a negative thermo-optic coefficient [46]. In section 1.1.3, it was discussed how the parabolic temperature profile led to a thermal lens due to the combination of thermal expansion and thermally-induced change of refractive index. The change in optical path experienced by a beam in a heated medium is given by equation 1.13 (ignoring the terms higher than second order).

$$\Delta_{OL} = d * \Delta T * \left( \alpha + \frac{\partial n}{\partial T} \right) \quad (1.13)$$

With  $\Delta_{OL}$  the change in optical length upon a change of temperature  $\Delta T$ ,  $d$  the initial length of the medium,  $\alpha$  the coefficient of thermal expansion (CTE) and  $\frac{\partial n}{\partial T}$  the thermo-optic coefficient (TOC) of the material.

From equation 1.13 one can see that if the term in parentheses can be cancelled, the change in optical length is null and a so-called athermal medium can be obtained. Materials with CTE and TOC of opposite signs such as phosphate glass are therefore of prime interest to mitigate the effect of thermal lensing.

The main drawbacks of phosphate glass compared to silicate lie in its inferior mechanical properties, chemical durability as well as it being more expensive [47]. Improving the thermo-mechanical properties through composition modification usually comes at the cost of laser performances. In common systems, the laser performances are prioritised but it becomes an issue in High Power High Energy (HPHE) systems as the risk of thermal fracture cannot be disregarded anymore. Surface treatments are then applied to mitigate this risk, increasing the costs further.

### 1.2.3 Crystals of choice for SSL: Yttrium Aluminium Garnet (YAG–Y<sub>3</sub>Al<sub>5</sub>O<sub>12</sub>) and Yttrium othovanadate (YVO<sub>4</sub>)

The most common crystal matrices used nowadays are YAG and YVO<sub>4</sub>. The reason is that neodymium or ytterbium, which are rare-earth ions commonly used for lasing, have a similar atomic radius as yttrium and therefore they take the place of the atom in the network, only slightly disturbing the crystalline mesh and maintaining the good thermo-mechanical properties crystals are sought for [48]. The energy spectrum of neodymium put in YAG is not ideal however as despite forming a 4-level system, the quantum defect is high and it displays multiple additional levels which favour the phenomena described in section 1.1.2 and therefore the generation of heat [43]. The reasons YAG is used in spite of that are its superior thermal conductivity, mechanical properties and the high transition cross sections (as defined in section 1.1.1) and lifetime that make lasing efficient despite thermal effects. Consistent research and use of Nd:YAG has led to a good understanding of its energy structure and mastery of the crystal growth. Therefore it is common for studies to default back to Nd:YAG for its reliability despite knowing that some more exotic crystals might yield better performance [22].

YVO<sub>4</sub> matrices display similar performances to YAG ones in particular emission wavelengths of Nd:YVO<sub>4</sub> match the main ones of Nd:YAG. YVO<sub>4</sub> matrices present a few advantages [49]. They display a strong natural birefringence which makes the effects of thermally induced birefringence (see section 1.1.3) negligible. Pumping is more efficient thanks to higher absorption gain and broader absorption bands. They have a lower thermal conductivity than YAG but the thermo-optic coefficient is also lower which means that the overall thermal lens is not worse. The choice of one matrix over the other often comes down to the application. Since the lifetime of the metastable level in YVO<sub>4</sub> is shorter, the crystal can store less energy and therefore is less suitable for high energy pulses in Q-switch operations. The crystals are also harder to grow with good optical properties compared to YAG [50].

### 1.2.4 Component designs

Although heating effects can be partially tackled by selecting an adequate material, requirements for the system quickly limit the freedom one can take. Therefore in addition to material selection, the design of the component plays an important role in mitigating heat effects. In this section, a few examples of designs are described with particular interest for ones involving bonded components to address heat management issues.

1.2.4.1 *Thin discs lasers*

Thin disc lasers made their appearance in 1994 following an idea from Adolf Giesen to significantly improve the cooling of the gain medium and mitigate its heating [51][52]. It relies on a thin disc ( $100\text{-}200\ \mu\text{m}$ ) being bonded on one face to a thermostat that acts as a heat sink as depicted on Figure 1-4 .

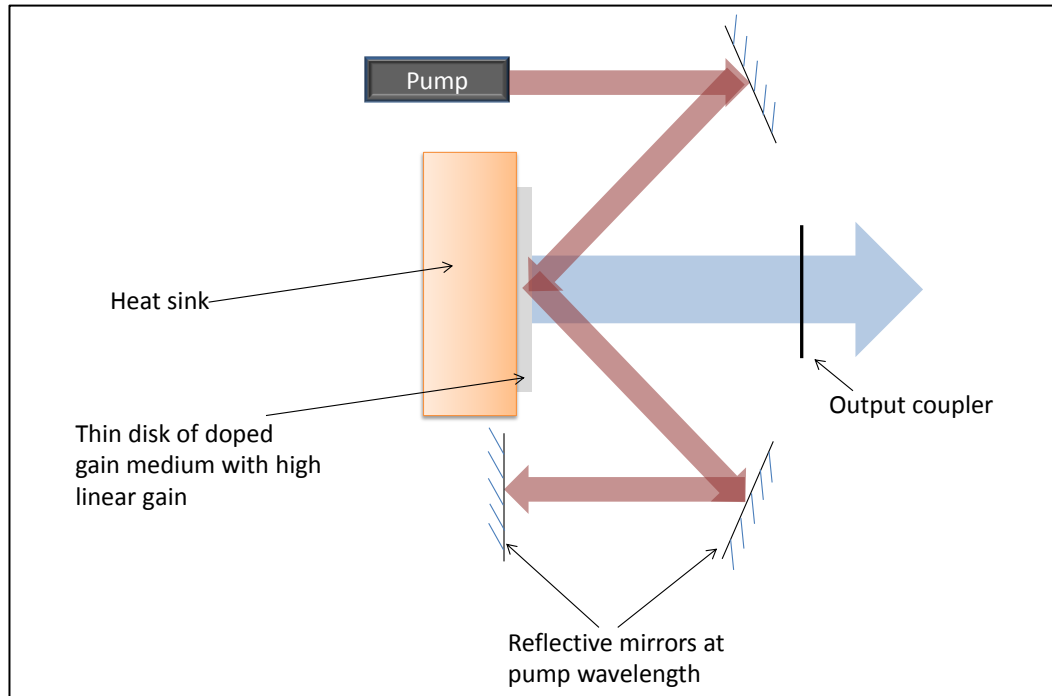


*Figure 1-4: Schematic of a thin disc laser system. The Laser radiation is represented by the blue arrow. The mirrors can be arranged to increase the number of pass of the pump beam in the gain medium, leading to an increase in obtained power.*

Due to the large surface to volume ratio and the cooling configuration, thermal gradients are damped to a large extent and the thermal lens effect is essentially non-existent. However there are some requirements for the design to be successful. The medium requires a high linear gain because of the short interaction length and therefore needs to be doped to high concentration. Good thermomechanical properties are required for the medium to bear the cooling. This combination of requirements limits the range of materials that can be considered. In addition, in order to make up for the short interaction length, the pump beam has to make several passages in the medium using multiple mirrors, thus complicating the design.

Generally speaking, laser glasses are not suitable for thin disk design due to their weak pump absorption. The most common crystals used are Yb:YAG although research on sesquioxides discs are of interest [53]. The quality of the interface between the disc and the heat sink is

paramount in such a system as it is where the risk of failure is the highest. Improving the bond has been the focus of some studies in the past years [54].

#### 1.2.4.2 Zig-zag slab

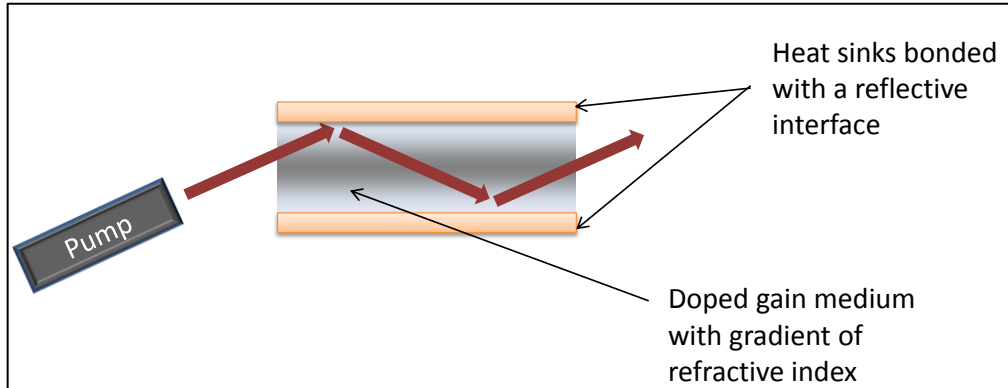


*Figure 1-5: Zig zag pumping of the gain medium. The beam is guided in the medium to "see" the same variations of refractive index across its width.*

Another design used to mitigate the thermal lens effects is pumping the medium in zig-zag as displayed in Figure 1-5 [55][56]. The configuration of the resonator is such that the laser beam bounces on the surfaces of the medium instead of travelling longitudinally. As a result, every part of the beam sees the same refractive index variation and the overall thermal lens due to index gradient is mitigated [22]. Total internal reflection can be achieved if the slab is bonded to a medium with a lower refractive index. An advantageous design is to bond a heat sink with lower refractive index that helps both in waveguiding and heat mitigation. Heat sinks are commonly metals for their high thermal conductivity [57]. However maintaining the beam quality upon reflection requires a surface finish of optical quality. Therefore, an intermediate layer of sapphire or diamond has been used between the gain medium and the metallic part [58]. These materials have high thermal conductivity, can be polished to an optical quality and avoid putting metal in contact to the gain medium. Sapphire is particularly interesting as it has a lower refractive index than doped YAG ( $\sim 1.76$  versus  $\sim 1.83$ ) and therefore total internal reflection can theoretically occur at a YAG/Sapphire interface. Besides, YAG and sapphire have similar chemistry which eases chemical-based bonding processes [59][60].

#### 1.2.4.3 Composite laser rods

The last design that will be discussed in this section is the composite laser rod. Composite rods have several applications in solid-state lasers from simply mitigating thermal effects to enabling compact passive Q-Switch operations [61][62][63].

Heat mitigation can be achieved by bonding successive slices with different concentrations (including none) of doping species. In fact, in an end pumped laser, the absorption in an evenly doped medium is not homogeneous. The pump intensity decreases as it is absorbed and hence the absorption and heating is larger at the entrance of the rod. Consequences are for example concentration of the thermal load and risk of thermal fracture, or the pump beam being too weak to pump the further medium. This can be mitigated by increasing the concentration of active species progressively from the entrance face so that the product (pump intensity \* absorption) remains constant with the travelled distance.

A simpler design that has showed significant improvement of the lasing performances of the medium is to bond undoped caps at both ends of a laser rod as displayed on Figure 1-6. Several studies have reported reduced pump thresholds, better slope efficiency and reduced thermal lens which happen mainly thanks to the better heat distribution in the rod [61][62].

A common point between all the designs discussed in this section is the involvement of a bonded interface. The requirements on the interface change depending on the materials that are bonded, and the function of the interface (reflective or transmissive). In the following section an inventory of the existing bonding techniques is presented.

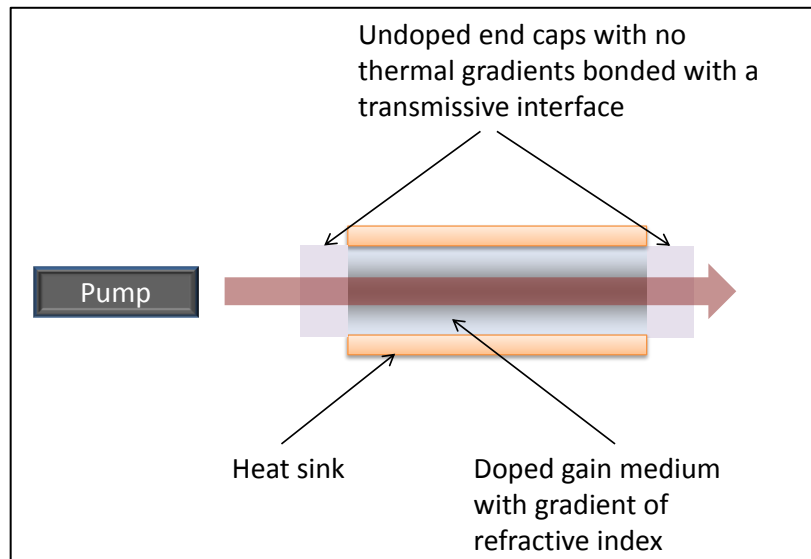


Figure 1-6: Schematic of principle of a composite laser rode. The end caps do not heat and prevent bulging, smoothing the transition between the gain medium and air.

### 1.3 Bonding techniques for optical components

#### 1.3.1 Optical contacting

Optical contacting is the purest bonding process possible as it does not involve the inclusion of a third body between the surfaces to be bonded. Although highlighted in the 17<sup>th</sup> century for the first time by Newton as a way to form reflection-free interfaces, it was only at the beginning of the 20<sup>th</sup> century that the process was seen as a reliable way to produce mechanically strong and precisely aligned assemblies [64]. This is mainly due to the progress in surface preparation made during the 19<sup>th</sup> century which allowed meeting the stringent requirements for effective bonding as they are described below. After World War 2, the rise of chemico-mechanical polishing improved even more the surface preparation and allowed direct bonding to become the prime bonding technique in the semi-conductor industry still to date even if it has evolved since its first applications.

The process relies on Van Der Waals forces rather than chemical bonds between the surfaces. A system constituted of two atoms separated by a distance  $r$  has an attractive Van Der Waals potential  $w(r)$  that can be written in the form of (the minus sign denotes the attractive nature of the potential) [65]:

$$w(r) = -\frac{C}{r^6} \quad (1.14)$$

With  $C$  an interaction constant ( $J.m^6$ ) depending on the chemical nature of the atoms. Integrating the potential on all the atoms from each surface to be bonded, one can derive the expression of the bonding force per unit area as

$$P(D) = \frac{A}{6\pi D^3} \quad (1.15)$$

Where  $A$  is the Hamaker constant which includes the density of atoms on the surfaces and the interaction constant  $C$  previously introduced, and  $D$  is the effective distance between the surfaces and therefore the “thickness” of the resulting bond.

As can be seen, the force decreases quickly with the distance and consequently, the surfaces need to be very close to each other to bond with sufficient strength. This only happens when on the one hand the surfaces shapes perfectly match each other (or can deform to do so) and on the other hand both surfaces are smooth and clear of any particles.

Some teams have carried out research to characterise the bonds so formed. The accepted strength test process consists in indenting a calibrated blade at the interface and measuring

the distance to which the debonding propagates [66]. Strengths of the order of magnitude of a few MPa are reported for the bonding of crystalline silicon [67]. Therefore the characteristic strength of optical contact at room temperature is taken of the order of magnitude of 1MPa.

By collecting strength data from the literature and using the theory above, Greco and al derived a bond thickness of about 2 nm which is only a few atomic lengths [68]. Consequently samples that are optically bonded show the same optical properties as the bulk material and especially no reflection at the interface [69][70]. An adverse consequence is that the interface is not able to deform elastically to absorb stress and therefore is very sensitive to deformation. Such deformations can be caused by indentation from the edge or by thermal-induced stresses when the two materials have different coefficients of thermal expansion. It also means that any foreign body that gets into the bond from the edge and locally increases the distance between the surfaces significantly weakens the bond and can lead to its failure. Therefore, optical contacted plates often must be sealed to assure resistance to contamination<sup>1</sup>. Finally one of the main drawbacks that prevents reliably using optical contacts is that the bonding occurs as soon as the pieces are in contact leaving no room for alignment. This can be avoided by using a drop of solvent to prevent unwanted bonding [71] but generally speaking surfaces to be bonded must be precisely aligned before contact which can only be achieved with high yield through automation or skilful personnel.

Nowadays, optical contacting is less used in its simplest forms and some additional steps are added to the process to solve some of the aforementioned issues (see section 1.3.2). It is still used for provisional assemblies such as bonding components on polishing plates as the thinness of the bond allows reaching accurate angles between the surfaces and the bond can be easily broken after manufacturing. Bonded components that should not be subject to large stresses or contaminating environment in their lifetime are also good beneficiaries of the technique (e.g. beam splitters in a controlled environment laboratory).

### 1.3.2 Direct Bonding

It has been rapidly identified that the performances of the bond, and mainly the strength, could be largely improved by applying a post-treatment (electric or thermal) to the contacted component [67][72]. At the atomic scale, it upgrades the van Der Waals interaction to covalent bonds which means that an actual chemical bond is formed between the surfaces yielding strength about an order of magnitude higher. Optical contacting followed by a post treatment belongs to the more general process of direct bonding which comprises all bonding process where no third body is needed between the surfaces.

---

<sup>1</sup> Internal communication.

One can distinguish two ranges for the heat treatment applied and therefore two processes. Low temperature direct bonding is carried out below 500°C [73][74]. This range of temperature allows the bond strengthening but is low enough to prevent atom diffusion. Therefore doping profiles can be preserved while the bond strengthens which is recommended for applications in the semi-conductor industry. The main drawback of the process is the development of thermal-induced stresses in the components which causes the issues mentioned in section 1.1.3. To maintain these stresses at a low level, the thermal variations must be kept at about 0.1°C/min which significantly increases the time scale of the process.

At higher temperature, around 80 % of the melting point of the material to be joined, one enters in the diffusion bonding regime [75]. As implied in the name, diffusion bonding relies on atoms from both surfaces diffusing across the interface into the opposite network resulting in a monolithic component with a thin interfacial region. Resulting bonds are as strong as the bulk material while the diffusion driven composition profile results in smoother gradients of properties that improve the optical behaviour of the interface. For these reasons, diffusion bonding is currently the preferred method to assemble composite laser media as discussed in a later section. The downsides of the technique are not in the performance of the bond but in the cost of the process and the requirement on the sample preparation. Samples must fit the optical contact requirement as the surfaces need to be within atomic interaction distances to allow diffusion. The thermal treatment must be progressive enough to prevent undesired thermal effects from kicking in which in view of the temperatures involved significantly extends the duration, and hence the costs, of the process. Finally allowing diffusion of atoms can affect doping profiles which can be relevant when sharp profiles are required [76]. Diffusion bonding is not favoured in these cases.

### 1.3.3 Adhesive bonding

Adhesive bonding is an opposing technique in the sense that it is acknowledged that the component is bonded by a macroscopic layer with properties differing from the ones of the bulk material. The challenge is then to select the desired properties in a range that does not prevent the component from performing.

Adhesive bonding remains to date the main process to join components in assemblies. The reasons are the wide range of properties available from the formulation, the relative ease of use and low costs [77][78]. This section deals with the use of adhesive to bond glass components and will be restricted to optical adhesives for the sake of comparison with the other techniques discussed in this work.

Adhesives consist in most cases of a liquid polymer that solidifies when conditions are met and therefore is able to form a solid bond between two surfaces. The actual bonding mechanisms can be of two types. In the first case, the adhesive reacts with the surfaces to form a chemical bond. Optical glass surfaces are often alkaline, with free OH radicals, whereas adhesives are acidic. This sets up the interface for acid-base reactions that lead to strong ionic bonds [79]. Providing heat to the reaction increases its rate and leads to stronger adhesion in shorter time.

In the second case, the bond is formed by mechanical interlocking of the two surfaces, which means that the adhesive has to flow in the pores or cracks of the surface to hang them together [79]. The interface may also be reinforced by chemical bonds but the interlocking remains the main contributor to the bond strength. Mechanical interlocking is generally not suitable to bond optical components as it requires roughness and pores to be effective, which contradicts the common requirements for optical surfaces. However it can be used when it is possible to have the bond outside the clear aperture.

In either case, the bonding effectively occurs when the adhesive changes from a viscous, liquid state to a rigid, solid one. There are different ways to activate this phase change. Two part adhesives store two separate components that will react and solidify when put together in the proper ratio. One part adhesives do not need mixing as the chemical reaction is blocked as long as an additional condition is not met. This condition can be providing activation energy (heat [81], UV light [82], etc.) or having the adhesive squeezed between the parts (oxygen deprivation) or put into contact with prepared surfaces (moisture) for example [80]. The variety of mechanisms allows tuning of the curing step to fit the requirements. For example UV curing enables on-demand, quick curing but requires the substrate to transmit and bear UV light. Curing at elevated temperature accelerates the curing step but thermal stresses will develop in the bond and can ultimately lead to its failure. Curing reactions are generally exothermic which means that the reaction catalyses itself but also that thermal effects may occur.

As adhesives can cover a wide range of properties thanks to the flexibility in their formulation, their pros and cons are not immediately clear [83]. There are however several general considerations that apply to most adhesives that are not specialised. First, adhesives are viscous and provided good wetting of the surface, flow into pores and cracks and therefore allow looser tolerances on the parts to be bonded. The relatively thick layer allows compensation of rougher surfaces that would prevent optical contacting for example. The bond is also able to moderately (depending on the mechanical properties of the layer) deform in order to absorb shocks and stress thanks to its elastic properties and non-negligible thickness, which is not the case for the direct bonding techniques [80].

However, the added thickness and viscosity comes together with a loss in precision in the alignment which remains one of the main drawbacks to the use of adhesives. Usual optical adhesives also have much higher coefficient of thermal expansion (CTE) than the glasses they bond, ranging from 50 to 1000 ppm/ $^{\circ}$ C [84]. Some marketed low CTE-epoxies manage to get close to the CTE of glass at 10-20 ppm/ $^{\circ}$ C but they are already specially designed products [85]. The high CTE will cause the bond layer to expand or shrink when subjected to temperature change. Depending on the relative mechanical properties and thicknesses of the substrate and layer, the optical surfaces may experience deformations or large amount of stress can develop in the component leading to stress-induced birefringence, surface figure distortion or even fractures.

Polymers also feature a glass transition temperature, i.e. a range of temperatures from which the polymer goes from a glassy to a viscous state. Rigid polymers are often in their glassy state while flexible ones are in their viscous state. It is mandatory to keep the adhesive on one single side of this boundary temperature during its life in service or its properties (modulus, coefficient of thermal expansion, etc.) will significantly change putting the component at risk [86]. Therefore, adhesives usually come with a limited range of temperature they can be used at, which depend on the formulation.

Another recurring issue with the use of adhesives is their propensity to outgas. Adhesive formulations contain volatile species in addition to the structural polymer, be it the solvent or filler or properties modifiers. When exposed to the atmosphere or in a vacuum, these species diffuse towards the surfaces and desorb. If these volatile compounds are not extracted, they may condense on optical surfaces and degrade their properties [87]. Low outgassing adhesives have been designed to comply with the standards of NASA for use in space missions. It is also possible to apply a post treatment to bonds in order to significantly decrease their volatile content and therefore their outgassing during their life in service.

For optical adhesives, the optical thickness of the bond is also a parameter to take into account. The bond layer is several orders of magnitude larger and therefore beam deviation or absorption can become relevant if the adhesive is not selected properly. Fortunately, the use of fillers to tune the optical index of adhesive has become common and makes the available optical indexes various enough to tackle this issue [88].

From a performance point of view, bonds made with adhesive are able to cover a wide range of strength, outgassing, resistance to environment and optical properties. There does not seem to exist a comprehensive comparison of what is available on the market and providing this is not the purpose of this work. Instead, a few representative values provided by different suppliers are used to make a relevant comparison to the other techniques discussed in this section. The constraints in bonding optical assemblies exclude the use of several types

of adhesives. UV-cured acrylic adhesives are the most common optical cements used for that purpose, with Norland or Dymax as examples of suppliers. From their technical datasheets, the best performing adhesives can reach tensile strengths up to 40 MPa depending on the formulation while maintaining low shrinkage and outgassing level. However these properties seem to be accompanied by high coefficients of thermal expansion (about 10 times that of glass, 100 times that of fused silica) and low glass transition temperature which will limit the range of temperature the component can be used over [78][89]. Typical thickness of optical adhesive bonds is between 25 µm and 150 µm [90][91]. Using adhesive in excess leads to increased outgassing, heat release and shrinkage upon curing and also amplifies temperature-induced effects due to CTE mismatches.

#### 1.3.4 Glass-frit bonding

Glass-frit bonding is a process close to adhesive bonding but tailored to the needs of the semiconductor industry. Instead of polymer, the bond paste is constituted of small particles (less than 15 µm) of low-melting point glass put in an organic binder that will be evaporated during the curing process, leaving a dense glass layer to bond the surfaces [92]. Due to similarities, the pros and cons of the two techniques are close: the surfaces do not need stringent roughness requirements as the paste can make up for the topography, the final bond shows high strength - about 20 MPa - and the properties can be widely tuned by changing the composition. However, glass-frit bond curing is based on a set process involving elevated temperature which makes matching the CTE of the bond and the substrate a priority, limiting the flexibility in other properties [93]. This is because the glass-frit bond is rigid and cannot deform to release energy leading to a high risk of fracture if stresses are present. The rigidity of the bond and its resistance to moisture and environment, allowing good sealing, remain the reason why glass-frit bonding is preferred in the semiconductor industry compared to adhesives [94]. If not as popular in the photonics industry, it is because the viscosity of the paste and the relatively high thickness – several micrometres- of the final bond make the alignment of the parts complicated. The absence of flexibility in the curing process also comes problematic if the material cannot stand high temperature or if the CTE mismatch is too large.

#### 1.3.5 Hydroxide Catalysed Bonding (HCB) and Silicate Bonding (SB)

Narrowing down to a more niche technique, the last bonding process that will be discussed and which will be the focus of this project is Hydroxide Catalysed/Silicate Bonding.

Silicate bonding consists in bonding two surfaces together by catalysing the development of a silica network between them. The principle is close to the one of adhesive but the special nature of the binding agent makes it a technique of its own with new range of constraints but

also performances. The process was initially developed and patented by Gwo in 1998 for application in the Gravity Probe B project [95] and has since been instrumental in numerous breakthroughs in the field of ground and space-based Gravitational Wave research [96][97][98].

In the initial development, the materials to be bonded were silica and its derivatives (fused silica, BK7, Zerodur®, ULE®, etc.) and the chemical solutions used to perform the bonding could be as elementary as a simple hydroxide solution (sodium hydroxide NaOH or potassium hydroxide KOH for example). The chemistry of silica has been the focus of numerous studies particularly during the 20<sup>th</sup> century as referenced in the book from Iler [99]. The following description of the mechanism and in particular the threshold values are derived from his study. Figure 1-7 displays a schematic of the various steps. The numbers in brackets in the description and equations link to the associated picture in Figure 1-7.

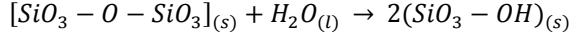
A surface of silica glass made free of contamination and activated<sup>2</sup> will have some dangling bonds of silicon atoms. These readily attract hydroxyl radicals and become highly hydrophilic once turned into silanol  $Si - O - H$  terminations. If a hydroxide solution is confined between such activated surfaces, the hydroxide ions  $OH^-$  present into the solution weaken the linkage between the atoms from the surface layer (1) and the bulk and these are released in the solution in the form of  $Si(OH)_5^-$  complexes (2). The concentration of  $OH^-$  in the solution decreases as they are being consumed and the pH falls as well until it reaches  $\approx 10.8$ . At this point  $Si(OH)_5^-$  is not stable anymore and dissociates into silicates  $Si(OH)_4$  and hydroxide ions, which in turn contribute to etching the surface (3). This cycle results in an increase in loose  $Si(OH)_4$  in the solution. This dynamic goes on until the molecular concentration of silicate in solution reaches  $\approx 1\%$  at which point the polymerisation process starts. During this step, the silicates  $Si(OH)_4$  in solution and the silanol bonds from the surfaces combine to form siloxane chains while releasing water (4 and 5) that then proceeds to diffuse out of the bond through the bulk. As dehydration continues, a rigid, dense silica network anchored to both surfaces builds up and ends up bonding the parts (6).

The chemical equations describing the process are as follow. It can be noted that even if silica is written as  $SiO_4$  to illustrate the four bonds silicon can form, silica networks are formed by complex cross-linked 3D arrangements of siloxane  $Si - O - Si$  chains and as such the correct nomenclature to describe the glass is  $SiO_2$ .

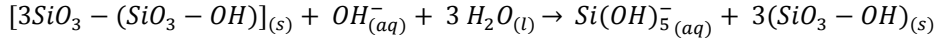
---

<sup>2</sup> Activation processes will be detailed in section 5.3.2.

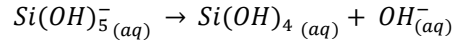
1. Hydration (2)



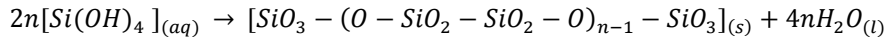
2. Etching and hydration (2)



3. Dissociation at pH < 11 (3)



4. Polymerisation once the concentration in  $Si(OH)_4^-_{(aq)}$  in solution reaches 1 % (4&5)



As explained the contribution of silicate is instrumental in forming the bond since polymerisation relies on reaching a critical concentration of the species in the solution. When it is not possible to reach the threshold, which can happen either if the bulk material cannot provide silicate or if the surface mismatch between the parts is too large, it is possible to use a hydroxide solution readily enriched in silicate ions such as a sodium silicate solution. With this knowledge, the bonding technique can be extended to a wide range of materials provided that the siloxane chains can hang on the surface before polymerising into a bond. Therefore in addition to the silica based materials, Gwo's patent states applicability to metals, oxides and oxygen-containing ceramics whose surface can be activated by forming  $O - H$  terminations. In the rest of this work, hydroxide catalysed bonding (HCB) will refer to bonding with pure hydroxide solution while silicate bonding (SB) will refer to bonding with a silicate-enriched solution.

Requirements wise, the process offers a few advantages compared to the techniques described above. First and foremost it is a room temperature process which reduces its cost and makes it potentially applicable to materials that will not bear heating such as coated substrates. The bonding operation is easy to perform with a window of a few tens of seconds to align the parts properly and a few hours to undo the bond without damaging the parts [100][101]. Requirements on the surface preparation are stringent but less than for direct bonding as the silicate-enriched solution will make up for small surface mismatch. However since the quality of the bond relies on a chemical process, chemical activation is at least as important as surface topography. The process indeed requires very hydrophilic surfaces in order for the solution to spread homogeneously and the silicate network to hang on the parts.

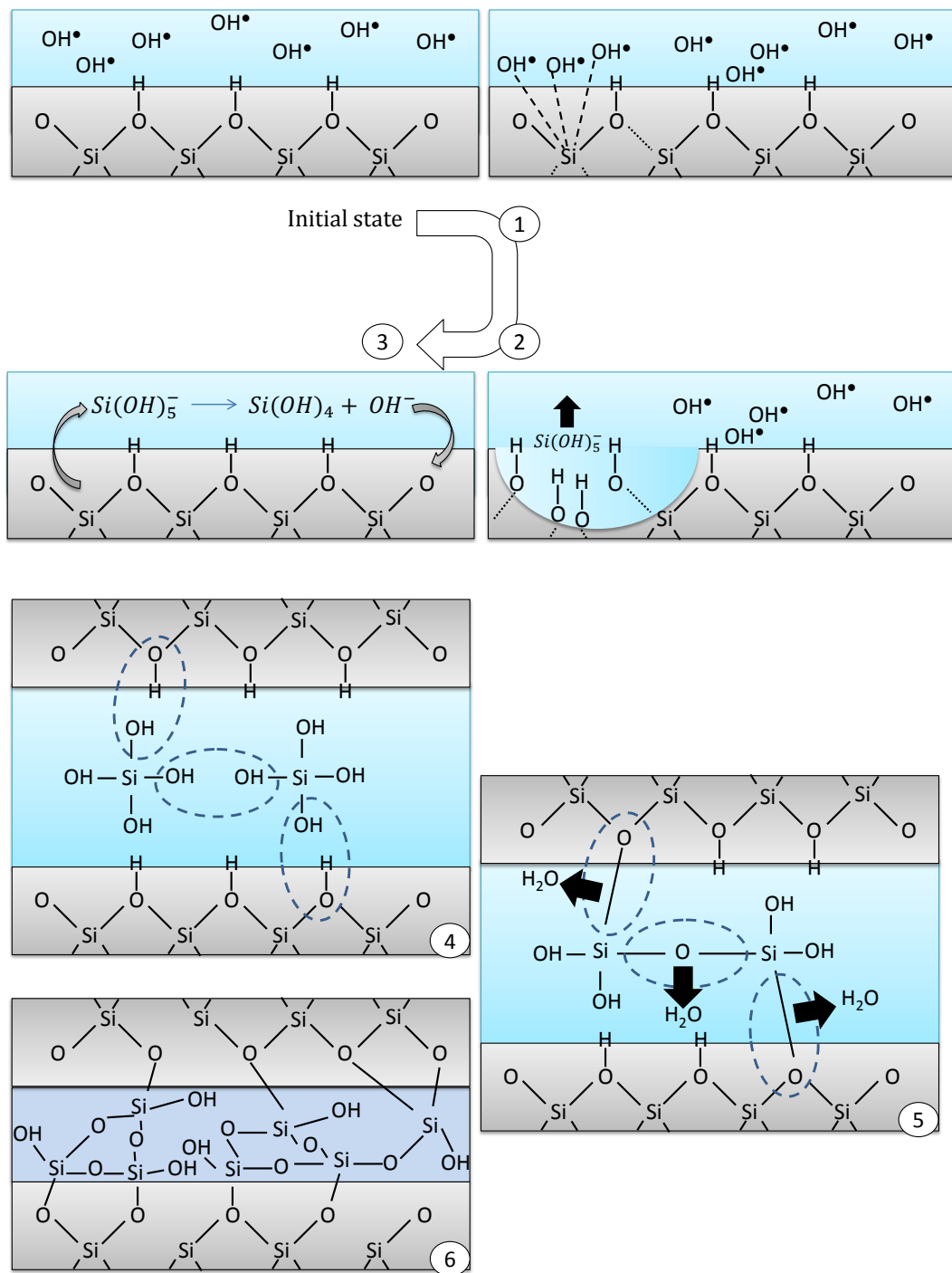


Figure 1-7: Mechanism of hydroxide catalysed bonding. Refer to text for description.

From a performance point of view, a strong asset of silicate bonds and what prompted them for space-based missions is their lightness and their ability not to outgas, discarding the risk of optics contamination. In fact the resulting silicate bonds display a thickness of the order of magnitude of the surface mismatch between the surfaces. This means that the interface will

generally be thicker than for direct bonding but thinner than for adhesive or glass-frit bonding, reducing the weight added to the assembly in the process.

As the bond is made of a silica network, its mechanical and thermal properties are similar to the ones of glass and it displays a high Young modulus and a low ability to deform plastically to absorb stresses [102]. This limits the temperature shift the bond can bear (when thermal-induced stresses develop) especially when bonding dissimilar materials with different coefficients of thermal expansion. However research has been made to bring bonds down to cryogenics levels or moderately high temperature with success [103][104]. The data on the bond strength are quite numerous and it has been accepted that the representative strength of silicate bonds is of the order of a few tens of MPa [103][104]. This will be discussed with more details in later sections.

A noticeable drawback of the technique which can limit its applications in photonics is the insertion of a silica layer in the component which can act as a reflective surface depending on the refractive index of the bulk material. Although Gwo suggests that the bond composition and therefore refractive index can be tuned to the material (by adding aluminate to bond alumina-based materials for example), only few works exist on the performances of bonds made this way. For example Douglas reports that the strength is significantly reduced when using an aluminate solution compared to a silicate one [104] and therefore the hypothesis of tunability might be wrong. Regarding reflectivity, both Sinha and Mangano report good performances when bonding silicate-based materials but if the process is applied to sapphire ( $Al_2O_3$ ) instead the transmissivity of the bond significantly degrades [105][106].

### 1.3.6 Synthesis on available techniques

In Figure 1-8, the relevant characteristics of the bonding techniques described above are summarized. The colour code indicate a qualitative ranking between the techniques from bad/inconvenient (orange) to intermediate (grey) and good/convenient (Blue).

### 1.3.7 State of the art and prospects for the materials of interest

With the knowledge of the various techniques available and their pros and cons, this section discusses the current status of bonding technique for the two materials of interest: phosphate glass and YAG.

	<b>Simplicity (cost, time)</b>	<b>Precision (human)</b>	<b>Strength</b>	<b>Outgassing</b>	<b>Surf. prep. requirements</b>	<b>Thermal stress issues</b>
<b>Optical Contact</b>	No equipment, No curing	Accurate alignment but risk of unwanted bonding	Good strength but very sensitive to inclusions or certain types of stress	None	Need perfect surface matching and smoothness	Can not deform and will break if CTE are not matching
<b>Adhesive bonding</b>	Process-dependent but usually easy and rather cheap	Thick bond, hardly reversible	High strength achievable	Specific low outgassing adhesives exist but generally a limiting factor	Thick bond and viscosity can make up for the surface mismatch. Depending on the curing mechanism, preparation of the surface may be required	Can deform but due to the high CTE mismatch the level of stress rises quickly with temperature even for tailored formulations
<b>Frit Bonding</b>	Equipment and thermal cycling required	Relies on flow and produces thick bonds. Clamps are required	High	Organic binder	Thick bond and viscosity can make up for the surface mismatch	CTE in the OoM of the substrates but the bond has a high modulus and can not deform. Asymmetric bonding very limited
<b>Diffusion Bonding</b>	Requires facilities to heat to high temperatures	Accurate alignment but risk of unwanted bonding	Very high strength	None	Need very good surface matching (within a few atomic length) but can also use pressure to deform plastically the surfaces during the heating process	Monolithic sample not too sensitive to CTE mismatch but the process at high temperature induces thermal stresses upon cooling
<b>HCB/Silicate Bonding</b>	Room temperature process with little equipment required	No instantaneous bonding and reversible for a few hours	High strength	None	Need good surface matching but the solution can partly make up for mismatches. Requires chemical activation of the surfaces	Near-monolithic samples but the bond can not deform. Studies show better results than expected

Figure 1-8: Figure of merit of the various bonding techniques available. CTE: Coefficient of Thermal Expansion; OoM: Order Of Magnitude.

### 1.3.7.1 *Phosphate Glass*

Reports on assemblies including bonded phosphate glass are scarce and it is not clear what the current preferred method is. Dane and Campbell both report use of adhesive to assemble composite phosphate glass media in High Energy High Power or High Average Power laser facilities[107][108]. More recently, Schott AG developed and patented a Low Temperature Bonding (LTB) technique that would be applicable to phosphate glass with good properties with regards to strength, reflectivity and chemical durability of the interface [109][110]. The technique is very similar to what is described by Gwo although the bonding solution is a phosphoric acid instead of a silicate-enriched hydroxide and therefore the chemistry matches the one of phosphate glass better.

Although using the phosphoric/phosphate solution is sensible, there is interest in having a single generic solution which works for multiple materials and therefore in trying HCB/SB on phosphate glass. Bunker extensively studied the etching of phosphate glass by various aqueous solutions including hydroxides [111]. It looks like etching of the surface readily occurs which is encouraging for the prospect of hydroxide catalysed bonding. Besides with its large oxygen content the hypothesis is that phosphate glass surfaces can be activated to develop  $P - O - H$  terminations that will act as roots for the siloxane chains and thus, that silicate bonding can also be successful. In this case, it is likely that the optical transmissivity of the interface will suffer from the injection of silica. However, silica glass is stronger and more chemically durable than phosphate glass and therefore, this inconvenience could be traded for other improvements [47][111].

### 1.3.7.2 *YAG*

There are several works available that relate to the use of bonded YAG components. Fujioka discusses a composite assembly bonded through diffusion bonding [76] while Sundeen investigates the properties of optical contacted and diffusion bonded YAG [112]. De Vido describes the characterisation of Adhesive-Free Bonded (AFB®) YAG components [113] while in a white paper from Precision Photonics, Lyngnes describes a thin laser disc bonded to the heat sink through Chemically Activated Direct Bonding (CADB®)[114]. Both the latter look to be derivative of direct bonding techniques developed by private companies. It seems therefore that direct bonding at either low or high temperature is the current method of choice to design composite YAG assemblies. Being able to perform HCB or SB on YAG would give an alternative process at room temperature, decreasing the costs and the thermal-induced issues.

YAG is supposedly inert to hydroxide, assuming that it reacts the same way as other alumina ceramics [115]. This means that HCB is not expected to produce strong bonds from etching of the bulk material. However, silicate bonding is likely to find success thanks to oxide-based

composition of the network that would allow siloxane chains to hang on the surface. Silicate bonding of YAG has actually been performed in the past in a work from Rutherford but the resulting bond was only characterised to a limited extent [116]. Once again however the injection of a layer of silica could end up being detrimental to the performance of the component.

## 1.4 Limitations of bonded components

In the previous sections, the interests in bonded components were highlighted. However these also come with their drawbacks, most of which were partly discussed in the pros and cons of the various techniques. In this section, theoretical models underlying the physics of thin layers and characterisation techniques are presented in order to assess how experimental observations can be interpreted.

### 1.4.1 Reflectivity

Let us consider the schematic in Figure 1-9. The component is made of two slabs of the same isotropic, non-absorbing material with a refractive index  $n_1$  and a thickness  $d_1$ . These two slabs are joined by a thin layer (thickness  $d_2$  of few hundreds of nanometres) of isotropic material with a refractive index  $n_2 < n_1$ . An incident beam propagates in the air with a refractive index  $n_0 = 1$  and reaches the first slab with an angle of incidence  $\alpha$ . The beam partially reflects at the surface and is partially transmitted to propagate in the slab at an angle  $\beta$  given by Snell's law:

$$n_0 \sin(\alpha) = n_1 \sin(\beta) \quad (1.16)$$

The beam then reaches the bond where it is again partially reflected and partially transmitted. It propagates in the bond layer at an angle  $\gamma$  given by

$$n_2 \sin(\gamma) = n_1 \sin(\beta) \quad (1.17)$$

In the bond layer, the beam bounces several times on the interfaces with both slabs, transmitting part of its energy each time. Since the bond thickness is of the order of magnitude of the wavelength of the light, the reflected beam from the interface actually results from interferences between the initial reflected beam (marked by  $E_A$ ) and the ones from higher orders reflections (marked by  $E_B$ ). The transmitted beam then reaches the back surface, is partially reflected and follows a similar path back to the front surface where it emerges at an angle  $\alpha$  and a distance  $\Delta = 4 d_1 \tan(\beta)$  from the initial entrance point. The coefficient of reflection and transmission in amplitude when the beam goes from medium i to

medium  $j$  are noted  $r_{ij}$  and  $t_{ij}$ , respectively. The relation between the electric fields of the incident beam  $E_{incident}$  and of the one of the beam reflected by the bond back in air  $E_{bond}$  gives the coefficient of reflection of the bond and can be derived from the known parameters.

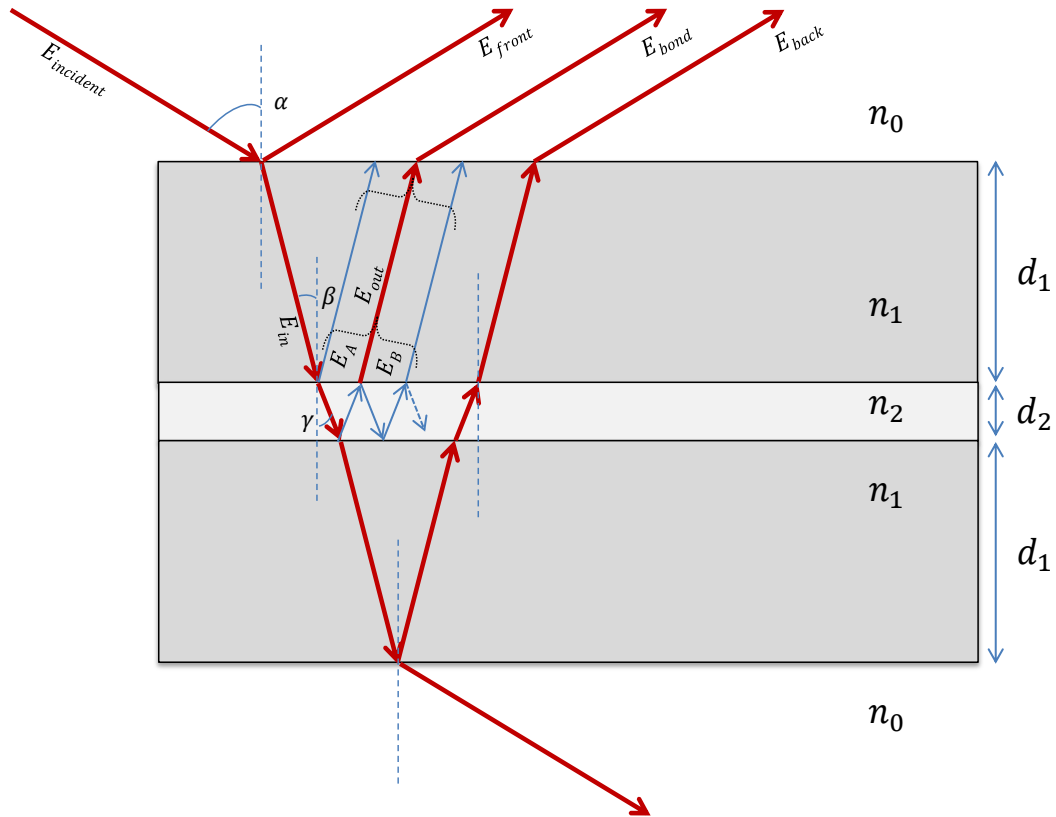


Figure 1-9: Schematic of the beam reflection on a bonded component (not to scale). The beam partially transmits and reflects on each interface. Due to the thickness of the bond layer being of the order of magnitude of the wavelength, all beams crossing the bond result from the sum of interfering beams. The light arrows illustrate how the beam from the bond contains several contributions. This is only depicted for the beam of interest  $E_{bond}$  for clarity purpose.  $n_i$  is the refractive index of the medium.

The electric field reaching the bond interface is linked to the initial one by equation 1.18.

$$E_{in} = E_{incident} * t_{01} * e^{-i\delta_1} \quad (1.18)$$

With  $\delta_1 = \left(\frac{2\pi}{\lambda}\right) n_1 d_1 \cos(\beta)$  the phase shift experienced by the beam while propagating in the first slab of material and  $\lambda$  the wavelength of the radiation. The reflection at the bond interface comes from two contributions:

$$E_{out} = E_A + E_B \quad (1.19)$$

$E_A$  is the initial reflection when the beam first reaches the interface:

$$E_A = E_{in} * r_{12} \quad (1.20)$$

$E_B$  gathers the subsequent reflections coming from the beam bouncing off the two boundary interfaces of the thin layer. From one order to the next, the beam experiences two more reflections from medium 2 to medium 1. The beam also experiences a phase shift from the additional distance travelled in the bond. This can be written as the following geometrical series:

$$\begin{aligned} E_n &= t_{12}r_{21}t_{21} * E_{in} * e^{-2i\delta_2} && \text{for } n = 0 \\ E_n &= (r_{21})^2 * E_{n-1} * e^{-2i\delta_2} && \text{for } n \geq 1 \end{aligned} \quad (1.21)$$

With  $\delta_2 = \left(\frac{4\pi}{\lambda}\right)n_2d_2 \cos(\gamma)$  the phase shift experienced by the beam while propagating in the bond from one order to the next.

In fact, only the first few orders contribute to the bond reflection but since the amplitude is quickly decreasing,  $E_B$  can be approximated by the limit of the sum of the terms of the geometrical series from equation 1.21.

$$\begin{aligned} E_B &= \lim_{n \rightarrow \infty} \sum_{k=0}^n E_k \\ &\Leftrightarrow E_B = E_{in} * t_{12}r_{21}t_{21} * e^{-2i\delta_2} * \sum_{k=0}^{\infty} [(r_{21})^2 e^{-2i\delta_2}]^k \end{aligned} \quad (1.22)$$

The beam then propagates back to the surface and finally  $E_{bond}$  can be written

$$E_{bond} = E_{out} * t_{10} * e^{-i\delta_1} \quad (1.23)$$

Combining equations 1.18-1.23, one obtains

$$E_{bond} = \left( t_{12}r_{21}t_{21} * e^{-2i\delta_2} * \sum_{k=0}^{\infty} [(r_{21})^2 e^{-2i\delta_2}]^k + r_{12} \right) t_{10} * e^{-2i\delta_1} * t_{01} * E_{incident}$$

The following relations can be used to rewrite the coefficient of reflection of the bond

$r_{ij} = -r_{ji}$  and  $t_{ij}t_{ji} = 1 - r_{ij}^2$  as the materials is a lossless dielectric [117].

$$\lim_{n \rightarrow \infty} \sum_{k=0}^n x^k = \frac{1}{1-x}, \forall x \text{ with } |x| < 1$$

And thus

$$\begin{aligned}
 r_{bond} &= \frac{E_{bond}}{E_{incident}} \\
 &= \left( r_{12} + t_{12}r_{21}t_{21} * e^{-2i\delta_2} * \sum_{k=0}^{\infty} [(r_{21})^2 e^{-2i\delta_2}]^k \right) t_{10} * e^{-2i\delta_1} * t_{01} \\
 &= r_{12}t_{10}t_{01}e^{-2i\delta_1} + \frac{t_{12}r_{21}t_{21}t_{10}t_{01}e^{-2i\delta_1}e^{-2i\delta_2}}{1 - r_{21}^2 e^{-2i\delta_2}} \\
 &= (1 - r_{01}^2)r_{12}e^{-2i\delta_1} - \frac{(1 - r_{12}^2)(1 - r_{01}^2)r_{12}e^{-2i\delta_1}e^{-2i\delta_2}}{1 - r_{12}^2 e^{-2i\delta_2}} \\
 &= \frac{(1 - r_{01}^2)r_{12}e^{-2i\delta_1}(1 - r_{12}^2 e^{-2i\delta_2}) - (1 - r_{12}^2)(1 - r_{01}^2)r_{12}e^{-2i\delta_1}e^{-2i\delta_2}}{1 - r_{12}^2 e^{-2i\delta_2}} \\
 &= \frac{(1 - r_{01}^2)r_{12}e^{-2i\delta_1}(1 - e^{-2i\delta_2})}{1 - r_{12}^2 e^{-2i\delta_2}}
 \end{aligned} \tag{1.24}$$

Experimentally one has access to powers and not electric fields and therefore it is useful to define the reflectance of the bond as

$$R_{bond} = \frac{|P_{bond}|}{|P_{incident}|} = \frac{|E_{bond}|^2}{|E_{incident}|^2} = |r_{bond}|^2 \tag{1.25}$$

With  $|x|^2 = x\bar{x}$  and  $\bar{x}$  denotes the conjugate of  $x$ .

From equations 1.24 and 1.25, the relationship between the measured reflectance and the parameters of the system can be written:

$$\begin{aligned}
 R_{bond} &= \frac{(1 - r_{01}^2)r_{12}e^{-2i\delta_1}(1 - e^{-2i\delta_2})}{1 - r_{12}^2 e^{-2i\delta_2}} * \frac{(1 - r_{01}^2)r_{12}e^{2i\delta_1}(1 - e^{2i\delta_2})}{1 - r_{12}^2 e^{2i\delta_2}} \\
 &= \frac{(1 - r_{01}^2)^2 r_{12}^2 (2 - e^{-2i\delta_2} - e^{2i\delta_2})}{1 + r_{12}^4 - r_{12}^2 e^{-2i\delta_2} - r_{12}^2 e^{2i\delta_2}} \\
 &= \frac{2(1 - r_{01}^2)^2 r_{12}^2 (1 - \cos(2\delta_2))}{1 + r_{12}^4 - 2r_{12}^2 \cos(2\delta_2)}
 \end{aligned} \tag{1.26}$$

Equation 1.26 translates how some of the intrinsic bond parameters affect the reflectivity of the interface. The parameters in question are the bond thickness  $d_2$  and the refractive index  $n_2$  which are contained in the terms  $r_{12}$  and/or  $\delta_2$ .

The coefficient  $r_{ij}$  is given by the Fresnel relations and changes with the polarisation of the incident beam as displayed in equations 1.27-1.30 [117]. The index S on the left term stands for perpendicularly polarised light (from the German “senkrecht”) and P for parallel polarised light. These refer to the direction of oscillation of the electric field with respect to the plane of incidence. The refractive index  $n_0$  is replaced by its value 1 and all the angles are expressed in function of the angle of incidence  $\alpha$  by the mean of equation 1.17.

$$r_{01, S} = \frac{\cos(\alpha) - \sqrt{n_1^2 - \sin^2(\alpha)}}{\cos(\alpha) + \sqrt{n_1^2 - \sin^2(\alpha)}} \quad (1.27)$$

$$r_{01, P} = \frac{n_1^2 \cos(\alpha) - \sqrt{n_1^2 - \sin^2(\alpha)}}{n_1^2 \cos(\alpha) + \sqrt{n_1^2 - \sin^2(\alpha)}} \quad (1.28)$$

$$r_{12, S} = \frac{\sqrt{1 - \frac{\sin^2(\alpha)}{n_1^2}} - \sqrt{\left(\frac{n_2}{n_1}\right)^2 - \frac{\sin^2(\alpha)}{n_1^2}}}{\sqrt{1 - \frac{\sin^2(\alpha)}{n_1^2}} + \sqrt{\left(\frac{n_2}{n_1}\right)^2 - \frac{\sin^2(\alpha)}{n_1^2}}} \quad (1.29)$$

$$r_{12, P} = \frac{\left(\frac{n_2}{n_1}\right)^2 \sqrt{1 - \frac{\sin^2(\alpha)}{n_1^2}} - \sqrt{\left(\frac{n_2}{n_1}\right)^2 - \frac{\sin^2(\alpha)}{n_1^2}}}{\left(\frac{n_2}{n_1}\right)^2 \sqrt{1 - \frac{\sin^2(\alpha)}{n_1^2}} + \sqrt{\left(\frac{n_2}{n_1}\right)^2 - \frac{\sin^2(\alpha)}{n_1^2}}} \quad (1.30)$$

The quantity  $\delta_2$  can also be written explicitly from the same set of parameters with the addition of the wavelength  $\lambda$  as shown by equation 1.31.

$$\delta_2 = \left(\frac{4\pi}{\lambda}\right) n_2 d_2 \sqrt{1 - \frac{\sin^2(\alpha)}{n_2^2}} \quad (1.31)$$

Therefore the measurement of the reflectance of the bond can conversely allow the derivation of those parameters. By varying the angle of incidence, the wavelength and/or the polarisation of the incident beam, the data points can be multiplied and the estimation of  $n_2$  and  $d_2$  is made possible as shown in the works of Taylor [118] or Mangano [105].

### 1.4.2 Laser Induced Damage Threshold

Surfaces and interfaces represent weak points in materials as they are favourable sites for inclusions or defects in the network which are prone to interact with light radiation in different ways from the bulk. The Laser Induced Damage Threshold (LIDT) is the lowest power that leads to a permanent damage on the component and therefore represents a boundary for the parameters of the system in which it will be used (with a safety factor). As such it is a compulsory test to carry out when designing interfaces. This is particularly true since, due to the complexity of the mechanisms involved, the parameters which affect the LIDT depend as much on the process as on the intrinsic properties of the material and therefore analytical models are not easily derived. A recent work from Manenkov provides a good overview of some of the mechanisms and related equations [119]. Since the LIDT is not commonly estimated analytically, the focus of this section is on the standard experimental procedure to derive the threshold [120].

The test is made as follows. A laser is focused on the surface/interface to test. The parameters of the laser (wavelength, continuous or pulsed regime, etc.) can have a strong effect on the results and therefore the test should be made with parameters close to the ones of the system for which the component is designed. The clear aperture of the component (“useful” surface) is virtually divided in a grid of 10 columns and any number of rows its size allows. On each row the ten spots are tested at constant power for a pass or fail test, where a fail is given for a noticeable damage of the component caused by the laser radiation. The assessment for damage is usually done through microscopy. A schematic of the principle of the test is presented in Figure 1-10.

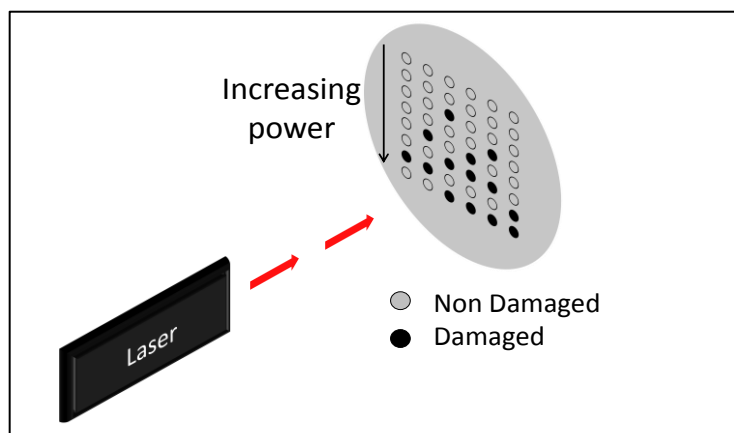


*Figure 1-10: Schematic of principle of a LIDT test. Each circle represents a tested spot. The power is kept constant on each row and incrementally increased from one row to the next.*

To increase the chance of an exploitable curve, the difference between powers is coarse in the lower powers and refined around the level at which the threshold is expected. Each row

gives a number of damaged sites out of ten which starts at zero at low powers and should reach ten consistently once well above the threshold. An example of curve pattern that can be expected is displayed in Figure 1-11.

The threshold is estimated by doing a linear fit between the last point at zero damaged sites and the first point at ten damaged sites (or all the subsequent points if it does not reach ten in the frame of the test). The LIDT is taken equal to the intersection of this regression and the zero damage axis. The value obtained can be rather approximate if there are not enough rows but since it is recommended to work far away from the threshold as a precaution this is not detrimental to the test.

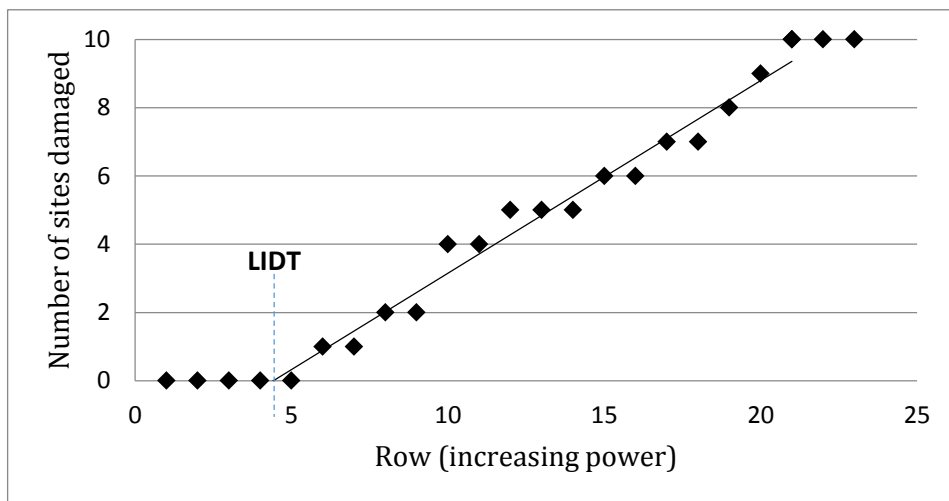


Figure 1-11: Expected pattern from a LIDT test and determination of LIDT by linear regression. The power/row number relation can be linear but generally the step is large between the first few rows and gets finer closer to the threshold. See Figure 3-23 for such an example.

#### 1.4.3 Thermal induced stresses

In section 1.3, the question of thermal induced stresses was frequently evoked as a limit for different methods of bonding. These stresses develop when the temperature at which the bond is made is not the same as the temperature at which the component operates. This can be due to the process being carried out at high temperature (Glass frit bonding, diffusion bonding) or if the component is bonded at room temperature (optical contacting, adhesive bonding, silicate bonding) but experiences significant cooling (cryogenics systems) or heating (laser rods) afterwards. Since they can be damaging to the component, several research teams have tried to analytically link the level of stresses reached to the parameters of the components. In this section a review of the studies on multilayer bonded components is presented. The equations are not detailed as they can get very complex and will be of little use in the present work and the reader is invited to consult the papers for additional information.

Chen [121] first solved the equilibrium equations for a bonded bilayer in the case where the Young modulus of the joint is much lower than the one of the substrate. He derived that the shear thermal stress ended up being maximal at the edges and null at the centre. Both Hsueh [122] and Suhir [123] solved the equations in a new way, considering first that the layers slid on the top of one another before applying corrections to maintain the component integrity. This method proved to be quite effective at showing some of the expected behaviours such as the continuity of the displacement and strains across the interfaces. Finally, Wang [124] made an additional hypothesis that the peeling stress was not constant across the bond and solved the constitutive equations of the system. His work seems to bring an improvement to Suhir's method as the calculated stress profiles fit the numerical models better. In particular the condition of null shear stress at the edge is respected which is essential for the component integrity and was not met in the other works discussed.

Wang's work seems to be the most accurate model to date to estimate the thermal stress from the parameters of the system. However it was carried out in the frame of adhesive bonds with relatively low modulus and high thickness. It appears that the equations cannot be easily solved for thinner bonds of higher modulus such as silicate bonds and therefore there is currently no suitable analytical model that was developed to anticipate the thermally induced stress from the known parameters. Finite Elements Analysis (FEA) seems to be the best way to tackle the issue but there currently has not been dedicated study for this type of bond. However, other properties such as the mechanical loss [125] or thermal conductivity [126] of the bond have already been studied using FEA and results on the thermal induced stresses could likely follow in the near future.

## 1.5 Conclusion

In this chapter, the motivations that led to the present work were described. The laser phenomenon by its very nature generates losses in the form of heat, which is the main obstacle to power scaling in new laser systems. Bonded components have proved to be able to partially mitigate the adverse effects of heat and a wide range of bonding techniques are available to the photonics industry to realise such assemblies. Each of these methods comes with its sets of assets and drawbacks. Hydroxide catalysed bonding, one of the youngest processes, has been used with remarkable success for structural assemblies but research for photonics application is still quite scarce. However its simplicity and affordability, together with its good properties with regards to strength, precision and outgassing make it a prime candidate for some of the proposed designs. In this work, HCB is going to be performed on two of the most common materials used for solid-state laser gain media: Phosphate glass as a sample of an amorphous material and Yttrium Aluminium Garnet (YAG) as a sample of a crystalline material. There are some question marks left over the performance of the

technique applied to these new materials. In particular the optical properties of the component used not to be a concern for structural assemblies and have not been extensively investigated. Theoretical models and experimental methods have been described to tackle these new issues.

---

## 2 Bonding of phosphate glass, an amorphous non-silica based oxide

---

The interest in bonding phosphate glass was explained in section 1.2. This section reports on the trials made to produce bonded phosphate glass samples using Hydroxide Catalysed Bonding (HCB). The trials were based on the knowledge gathered from the experience of bonding amorphous silica glasses such as fused silica or BK7. In order to verify that phosphate glass could bond, initial tests were performed as this glass had not been previously bonded with HCB. Once bonding was successfully demonstrated a programme of tests was conducted. This involved tests for manufacturability, strength, reflectivity (and subsequent bond thickness and refractive index determination) and Light Induced Damage Threshold.

### 2.1 First bonding trial

The samples used for the first tests were Ø 30 mm x 3 mm discs (Ø denotes the diameter) of composition PGC1 (see Appendix A). The bonding surface was polished to approximately 60 nm peak-to-valley flatness and endured a chemico-mechanical polishing finish with a Syton®<sup>3</sup> suspension. Samples were cleaned using a seven-stage ultrasonic bath prior to delivery (see Appendix B). Before the solution deposition, the bonding surfaces were given a final wipe with a clean cloth wetted with high purity (> 99.98 %) methanol to remove adsorbed water.

The solutions used were on the one hand a commercial sodium silicate solution (Sigma Aldrich<sup>4</sup>, which is about 11 % sodium hydroxide, 27 % silicate and 62 % water in volume per specifications) diluted at 1:6 in volume in deionised water and on the other hand a 1 M sodium hydroxide solution<sup>5</sup> diluted 100 times in deionised water. The ratio of 1:6 has been used consistently in similar studies [96][127] and the hydroxide solution parameters were chosen to have similar pH (12) and chemistry (sodium) in order to make comparisons more relevant. After dilution, the solution was centrifuged in order to segregate the largest particles and then pressed through a 0.2 µm filter<sup>6</sup> to get rid of the smaller particles. 7.06 µl (volume per surface unit equal to 1 µl/cm<sup>2</sup>) were taken with a micropipette and deposited on one surface and the parts were brought into contact for bonding.

---

<sup>3</sup> <https://www.sigmaaldrich.com/catalog/product/aldrich/421553?lang=en&region=GB>

<sup>4</sup> <https://www.sigmaaldrich.com/catalog/product/sigald/338443?lang=en&region=GB>

<sup>5</sup> <https://www.sigmaaldrich.com/catalog/product/sial/s2567?lang=en&region=GB>

<sup>6</sup>

<https://www.sigmaaldrich.com/catalog/product/aldrich/whaav125eorg?lang=en&region=GB>

Four samples were bonded with each solution. The samples bonded with sodium silicate will be referred to as SB (for Silicate Bond/Bonded) while the samples bonded with sodium hydroxide will be referred to as HCB (for Hydroxide Catalysed Bond/Bonded). They were left to cure at ambient conditions in a cleanroom for 75 days before use for testing (based on schedule constraints). After curing, all samples looked well-bonded and mostly clear of defects at the interface. There was no visual difference between the HCB and SB samples. Figure 2-1 shows sample photographs of the resulting bonded pieces.

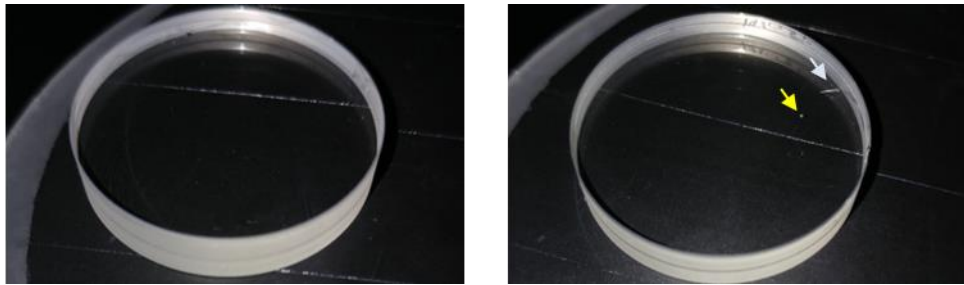


*Figure 2-1: Bonded samples. Left: HCB sample. Right: SB sample with a small spot (yellow arrow) in the bond. The scratch (white arrow) is on an outer surface.*

### 2.1.1 Manufacturability

A first qualitative assessment of the strength of bonded components can be made by subjecting them to manufacturing steps. Sawing and polishing apply various stresses from loads and vibrations to the component, most likely to a higher level than what they will experience in their application. It is hard to quantify the forces applied during sawing and polishing as several mechanisms are involved as well as the distribution and size of particles [128], but here only a pass/fail result was needed. Being able to cut and polish bonded samples is time-saving from a production point of view as it allows a single large component to be bonded before being diced into smaller sized components.

One sample from each of the sets was cut in half and, as they survived, hand-polished using the regular manufacturing compounds at Gooch and Housego. Pictures of the obtained samples are presented in Figure 2-2.

After cutting and polishing, the bond interface was not visible on the polished surface of the HCB sample. However, there was a hint on the SB sample by looking carefully which suggested that further tests would highlight some differences in properties between the two types of samples.

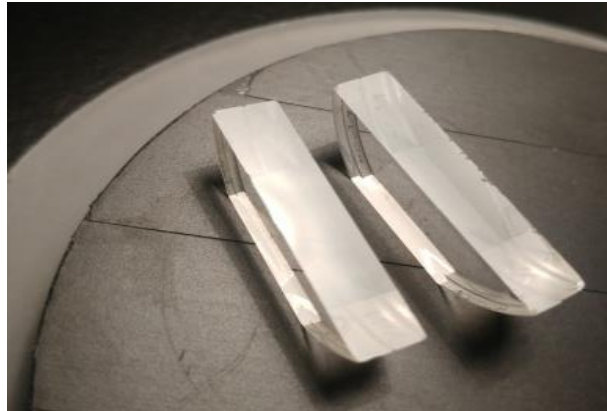


Figure 2-2: Photograph of the samples cut and polished through the bond HCB (left) and SB (right) samples. Polishing compound used was aluminium oxide from 20 to 3  $\mu\text{m}$  particle sizes and a finishing Syton® solution.

### 2.1.2 Scanning Electron Microscopy Observation

By polishing the surface, the bond interface became suitable for Scanning Electron Microscopy (SEM), which was done after 270 days of curing. The SEM used was a FEI Nova 200 Dual Beam system<sup>7</sup> and the measurement was made with secondary electron detection which gave images with the best contrast. The two surfaces were coated with a thin layer (no more than 10 nm) of gold in order to yield a conductive surface. Coating was evaporated with an Emitech K950X thermal evaporator<sup>8</sup> by melting pure 99.9 % gold<sup>9</sup> in a tungsten resistance boat. The samples were mounted as displayed in Figure 2-3. The bluish tint due to the gold coating can be seen.

Ten scratches were cut in the coating perpendicular to the bond with a spacing of about 3 mm between them to have a visual marking on the surface for reference and potentially take measurements in the scratches. Images were taken close to each scratch in order to determine the thickness profile along the diameter. For both HCB and SB samples it appeared that too much charging occurred in the scratches to obtain good images. However, on the rest of the sample the gold film was thin enough to take measurements. More accurate data were likely to be obtainable by better control of the coating thickness but the ones available were good enough to achieve an estimate of the bond line width. Figure 2-4 shows a sample of images.

---

<sup>7</sup> <http://nanolabs.narod.ru/equipment/01/pdf/Nova200NanoLab.pdf>

<sup>8</sup> [https://www.quorumtech.com/\\_assets\\_/pdf/Manuals/K950X-Iss9.pdf](https://www.quorumtech.com/_assets_/pdf/Manuals/K950X-Iss9.pdf)

<sup>9</sup> <https://www.sigmaldrich.com/catalog/product/aldrich/310980?lang=en&region=GB>

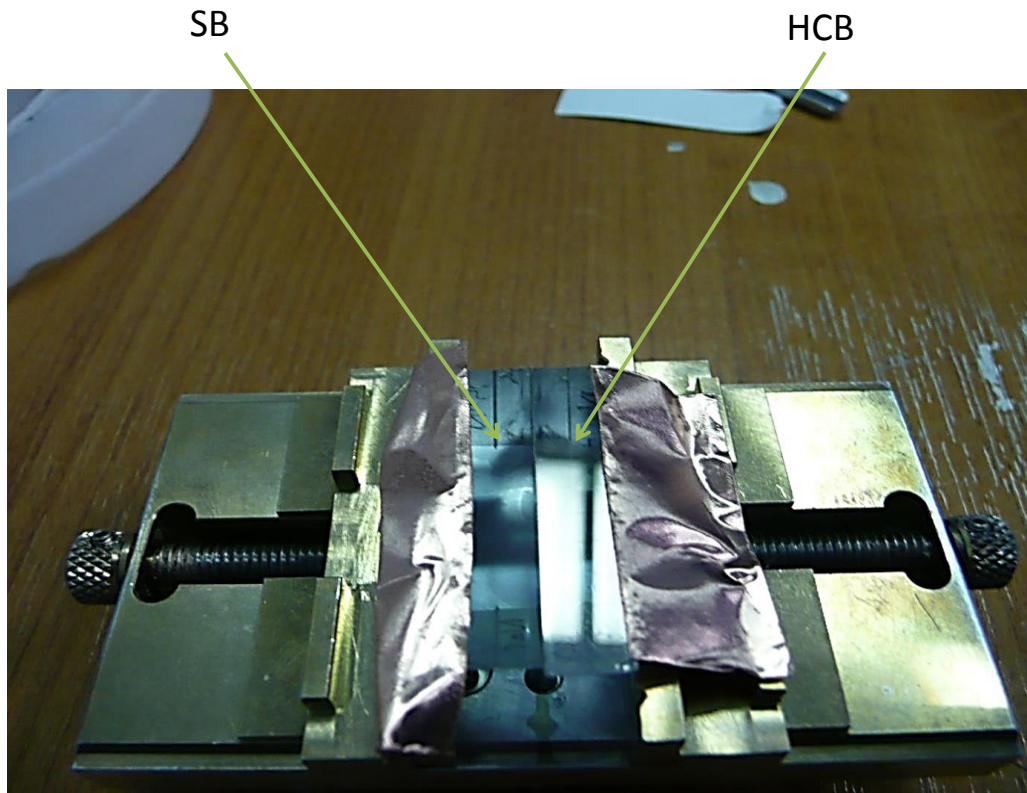


*Figure 2-3: SB and HCB samples mounted side by side for the SEM observation. Samples were gold coated (bluish tint). The surfaces under analysis are indicated by green arrows.*

In the case of the HCB sample (images 1-3 in Figure 2-4), it appears that despite the increasing magnification the bond shows up as a thin line which makes estimation of its thickness difficult. A gross estimation of about  $40 \pm 15$  nm can be given from image 3 where the magnification factor is 25000. It was not possible to increase it further as drifting and charge effects prevented this. Thus this estimation is the most accurate value that could be obtained.

The images from the SB sample (images 4-6 in Figure 2-4) are more conclusive. The zoomed out (x63) image displays a neat vertical line for the bond. By zooming to x 1200 (image 5), the bond line displays as a dark area with a width of about 5  $\mu\text{m}$ . Increasing the magnification up to x 25000 (image 6) it appears that this dark region actually results from shadowing effects and contains a thinner bond line. The width of the core of this area can be estimated as 120 nm and is taken as the measured bond thickness for this sample.

Additional pictures of the bond were taken between each scratch along the diameter and at the edges and the value of thickness was taken down. The resulting profile is displayed in Figure 2-5.

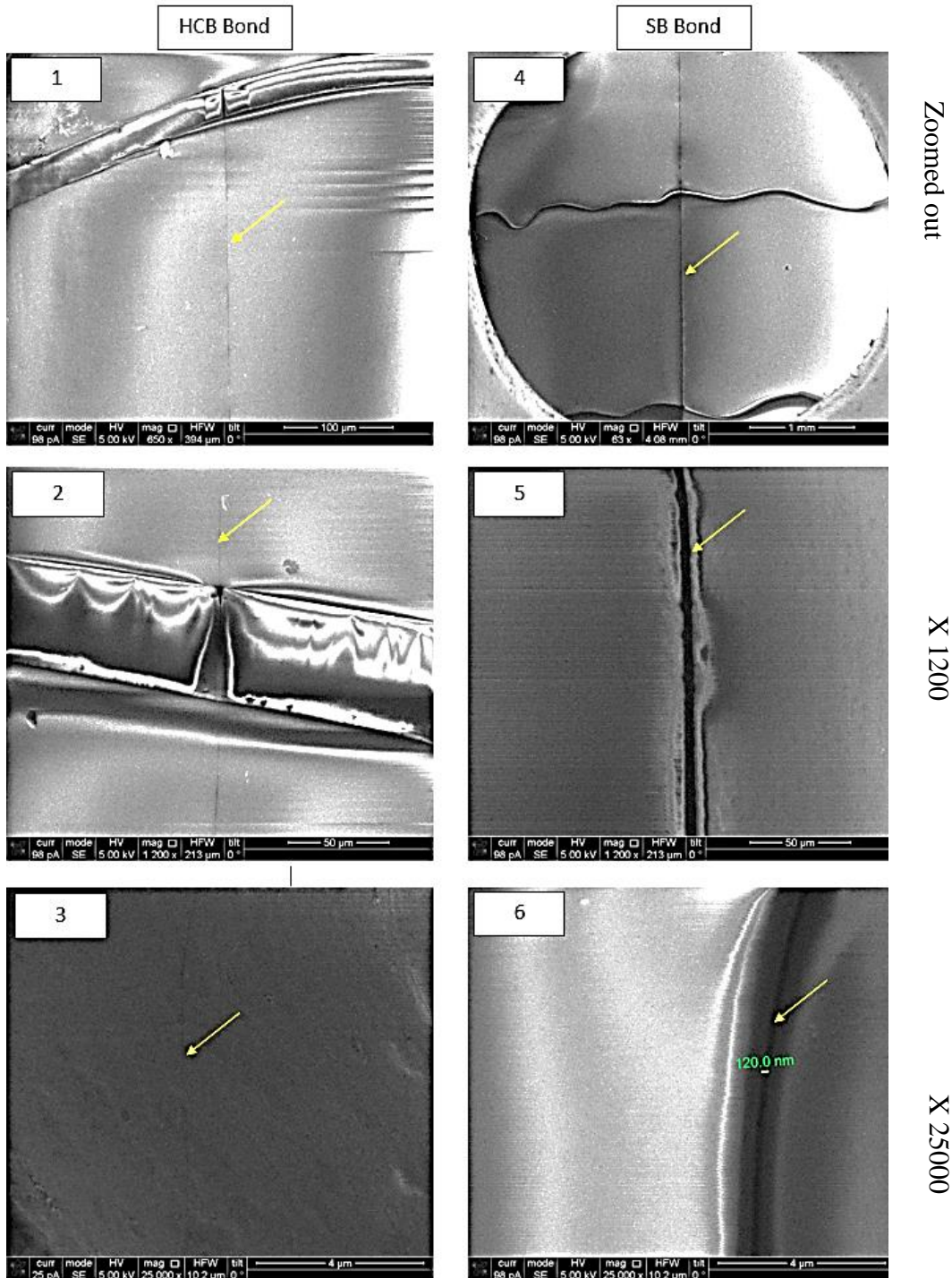


Figure 2-4: SEM sample images from the bond observations. On left HCB at increasing magnification and on right SB. Magnification is highlighted on the right. The large horizontal features are cuts made as spatial references. The bond line is indicated by a yellow arrow (The contrast is clearer in the electronic version).

It can be seen that the thickness is approximately constant at  $120 \pm 10$  nm along the diameter. One of the edges shows a wider gap between the two parts, up to about 175 nm. A flatness map of the bonded surfaces could not be obtained prior to bonding with the available equipment due to striations in the bulk material. Therefore, any shape mismatch between the bonded surfaces that would explain this feature could not be foreseen. As it does not appear at the other edge, it likely does not come from the curing of the bond. The variation in bond thickness could be either due to a local defect or to the way the part was polished in preparation for the SEM. The part was handheld on the polishing plate and it is possible that one edge faced the flow longer than the other and that the parts got slightly pulled apart at this edge.

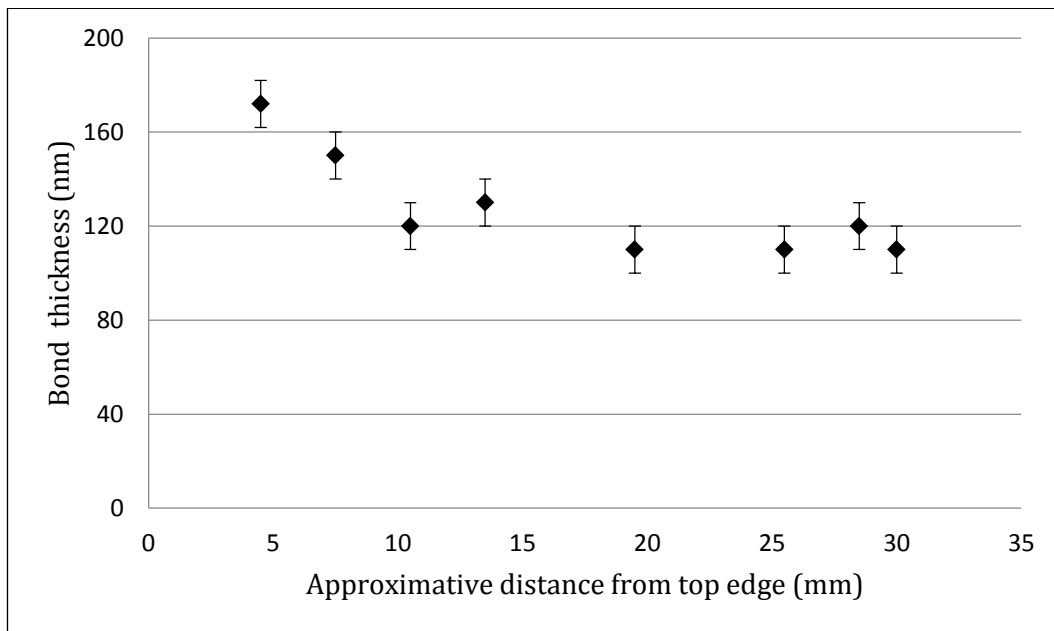


Figure 2-5: Bond thickness measured along the diameter for the SB sample. The reference position is the top edge. Position is identified by the marks made on the sample. The error is based on the uncertainty from the readout.

There is a clear difference between the results obtained with HCB and SB. For HCB, the thickness can only approximately be obtained using SEM and the most accurate estimate is about  $40 \pm 15$  nm. For SB, the bond line appears clearly and the estimated thickness is about  $120 \pm 15$  nm along the diameter. This difference in thickness is likely to propagate to the other properties of interest. From a structural point of view, with all other parameters being equal, a thicker bond can absorb more of the deformation energy when put under stress and therefore increases the strength of the component, but also increases the risk of cohesive failure in the bond (which initiate from a defect in the bond volume). From an optical point of view, a thicker bond increases the optical path and, if the bond thickness gets to the order of

magnitude of the wavelength of the light, may lead to interference effects modifying the optical properties with regard to the monolithic component.

## 2.2 Strength tests

The objectives of the strength trials on phosphate glass were two-fold. The first one was to monitor the change of strength with curing time at room temperature and the second was to compare the performance and behaviour of Hydroxide Catalysed Bonds (HCB) and Silicate Bonds (SB).

### 2.2.1 Method

#### 2.2.1.1 *Samples*

45 bonded samples were prepared, 36 of which were bonded with sodium hydroxide solution (HCB samples) diluted to 0.01 M and 9 bonded with sodium silicate solution diluted to 1 : 6 parts in volume in deionized water (SB samples) as in the manufacturing trial. The HCB samples were used to monitor the strength at regularly separated times within the first two months of curing while the SB samples were broken after 7 weeks to compare the strength at what is expected to be a steady state based on previous work [127][129]. The bonded parts were 20 mm x 5 mm x 5 mm with the 5 mm x 5 mm surface bonded, giving a 40 mm x 5 mm x 5 mm sample. Samples were numbered to allow their identification after bonding.

#### 2.2.1.2 *Bonding*

HCB samples were cleaned with full “cerox” cleaning process<sup>10</sup>, left overnight and bonded on the following day after a cleaning with spectroscopic grade methanol. The volume of solution per unit area used was 0.8 µl/cm<sup>2</sup>. Most bonds took well and looked clear but seven immediately debonded. They were cleaned with the same method and rebonded. All samples were left for two days to cure in a vertical orientation before being moved for further inspection. However, most of them failed while moved. It appeared that the samples did not bond and the liquid had evaporated. This was attributed to the cleaning being done over two days which left time for the bonding surface to re-adsorb species that prevented good bonding. The twelve samples that did bond were marked and laid to cure on a clean cloth in ambient conditions. The other samples were re-cleaned with the full process and bonded immediately afterwards. The SB samples were prepared at the same time.

---

<sup>10</sup> Cerox is a cerium oxide-based cleaning process. Cleaning processes will be discussed in details in section 5.3.2.

After this second step, the distribution of samples was as follow:

- 12 HCB samples were “first time bonded” with cleaning the day before bonding.
- 24 HCB samples were rebonded with cleaning immediately prior to bonding.
- 8 SB samples were first time bonded with cleaning immediately before bonding.

After two days of curing, inspection of the interfaces showed that only 11 of the rebonded HCB samples were bonded over more than 75 % of the full area. Well-bonded area displayed as a fully invisible interface. In the set of samples, the edges particularly were “cloudy” which suggests that the bond had not taken well. The SB samples bonded well over the whole area although two of them showed some contamination or bubbles. The difference could be accounted for by the presence of the silicate ions in the solution which helped forming the siloxane network.

#### 2.2.1.3 Strength testing setup

To maximise the applicability of the tests, strength testing trials using a 4-point flexure setup were conducted [130]. It allowed fundamental and quantitative assessment of the strength of the bond and how various parameters affected it. It also made possible direct comparison with similar experiments carried out in other studies [104][131].

The testing layout is presented in Figure 2-6. The load cell used was a Novatech Loadcell<sup>11</sup>. The system was not automated and the force was applied manually using a crank. The force was slowly increased at an approximately constant rate ( $\sim 2 \pm 1$  N/sec) until the sample failed. The load cell recorded and displayed the peak force applied in the course of the trial and this was the value taken to derive the stress at failure.

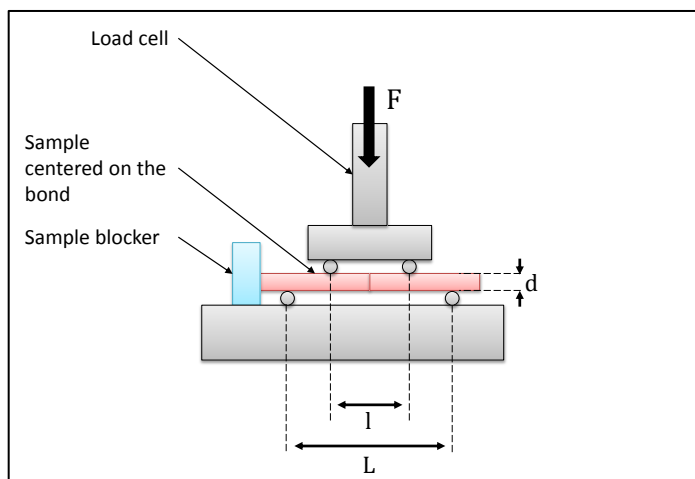


Figure 2-6: Layout of the 4-point flexural test. For this setup,  $l = 18$  mm,  $L = 36$  mm.

<sup>11</sup> <https://www.novatechloadcells.co.uk/ds/f313.html>

The flexural strength for square base beams is derived from the parameters of the setup according to the equation [131]:

$$\sigma_{max} = \frac{3(L - l)F}{2d^3} \quad (2.1)$$

Where F is the peak force recorded at failure, L is the width between the bottom supports (36 mm in this case), l is the distance between the top supports (18 mm in this case) and d the thickness, equal to the width for the following trials (5 mm).

### **2.2.2 Results and discussion**

- Trial 1: Fresh samples

Although all the interfaces were not free of defects, no sample was discarded for the trial. The bond quality was tracked throughout to allow this to be taken into account during analysis. The HCB samples were split into four sets of different bonds quality (approximatively 25, 50, 75, 100% bonded) and these were used to make the set balanced with regards to quality. The sets were broken at 9, 21, and 49 days of curing at room temperature. The SB set was broken at 49 days.

- Trial 2: Repolished samples

After the samples were broken once, the trial was repeated with the same parts polished, cleaned and bonded again in order to increase the set size. It was assumed that as the surfaces were not damaged in the first trial and thanks to the polishing and cleaning steps, the results from the two trials would not be correlated. Therefore there was no attempt to track the history of each part. For this trial, the samples were also left in vertical position for the whole duration of the curing instead of laid on a cloth, with hope that gravity would help obtaining more homogeneous bonds.

- Trial 3: Re-used but not repolished samples

Finally after this second trial, the parts were bonded one more time, this time with sodium silicate only. However, due to schedule constraints they could not go through the factory for repolishing of the surface. A more thorough cleaning with multiplication of the scrubbing steps was done in order to try and lower the influence of the previous trials. Once again the samples cured in a vertical position. The 33 samples were split in four sets and broken at 7, 14, 21, 35 days to get information on the rate of the curing. As the surfaces started getting damaged after this trial the samples were not used again.

In the course of the trial, it was witnessed that samples could fail in two different ways. In the first case, the fracture propagated along the bond line which meant that the bond represented a path of least resistance for the propagation. The initiation of the fracture could occur at the bond or away from it but it was clear that the propagation was not crossing the line. In the second case, the fracture would cross the bond line and chips of the opposite part would be left on the surface on both surfaces after the test. Figure 2-7 shows an example of samples breaking following one or the other mode. When displaying the results in Figure 2-8, different markers are used for the two modes.

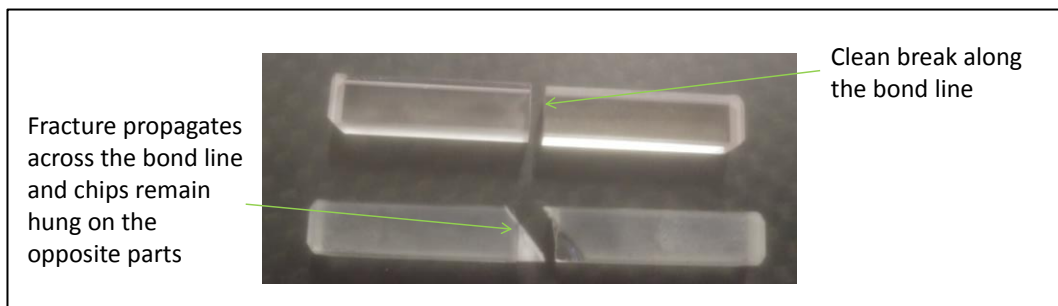


Figure 2-7: Photograph of samples breaking along (top) and across (bottom) the bond line.

It can be seen in Figure 2-8 that the strength of all the HCB samples lies between 0.5 and 5 MPa and show no significant variation of strength with curing time. Due to the layout of the setup, it is estimated that a load of 10 N (or a 2 MPa stress) is required to have the proper 4-point contact. Therefore samples that display a strength around 2 MPa are too weak to bear the test. Samples that have a strength between 2 MPa and 5 MPa (Most of the HCB samples in trial 1 and 2) cannot be ranked with accuracy and it is assumed that no strong chemical bond was formed for those samples. This means that although sodium hydroxide probably still etched the surfaces, the conditions were not met for a solid phosphate network to form between them leaving only a weak bond. As said before, the edges in particular seemed to fail to bond (hazy aspect). This particular test method is very sensitive to the quality of the edges as it is the location of the high tensile stress. This also could explain why the amount of bonded area did not seem to affect significantly the strength as no correlation could be made between the weakest and least bonded samples. In the trial, the edge with the fewest defects was always placed at the bottom to get an insight on the strength of a supposedly good bond and avoid variance from random features. A lap shear test<sup>12</sup> would likely have yielded higher strength while being closer to the type of stress experienced during a component lifetime but a reliable setup was far more challenging to assemble.

<sup>12</sup> <https://www.admet.com/how-to-perform-an-adhesive-lap-joint-shear-strength-test-astm-d1002/>

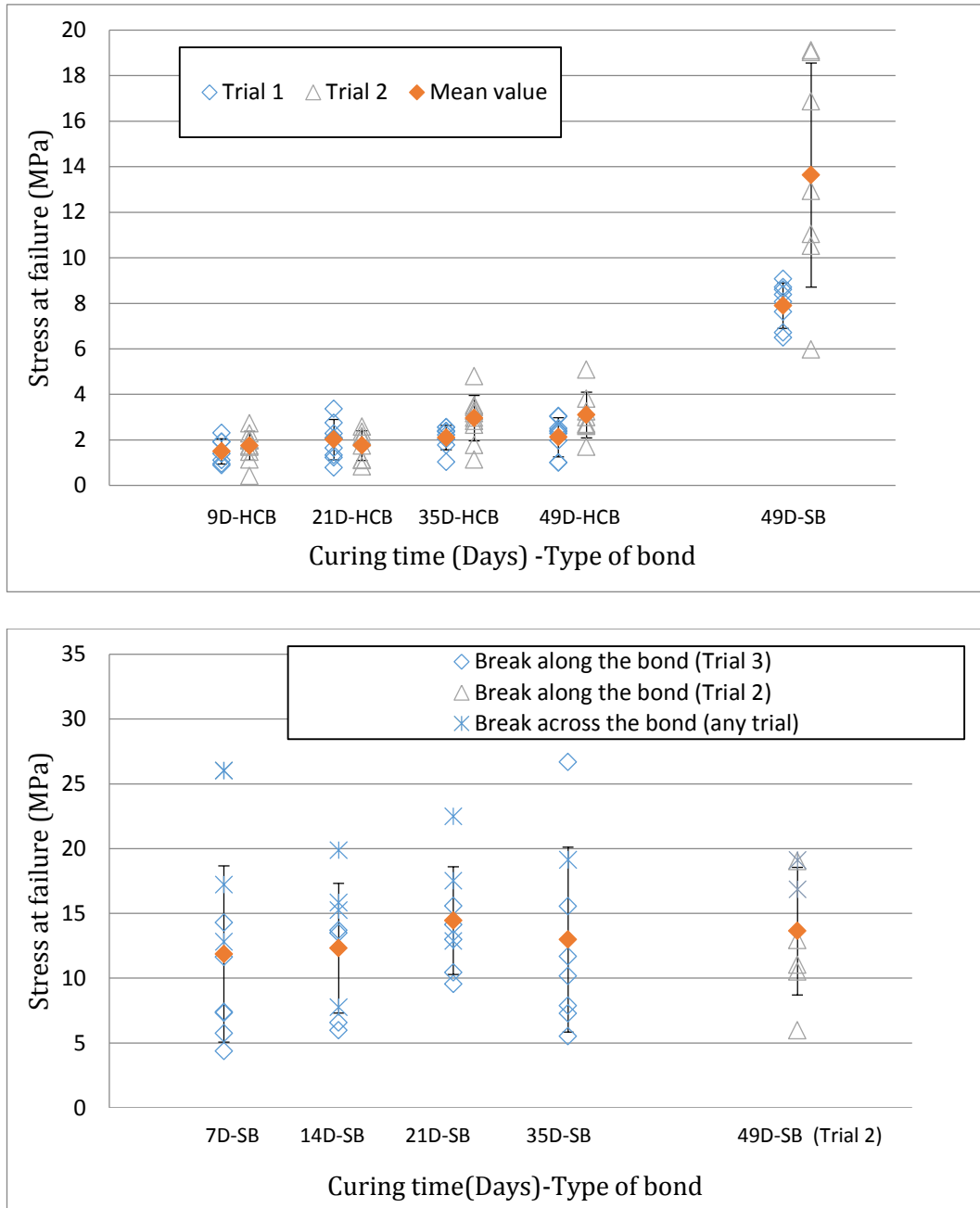


Figure 2-8: Top: Strength variation with curing time for hydroxide catalysed bonds (Bonded with sodium hydroxide) and comparative strength of silicate bonds (bonded with sodium silicate) at 49 days. Bottom: Strength variation with curing time for silicate bonds where samples were used for a third time but could not be repolished beforehand. Errors bars are given by the standard deviation of the set.

The strengths of the SB samples at 49 days are higher than the ones of HCB samples with an average value of  $7.9 \pm 1.0$  MPa for the first trial and  $13.6 \pm 4.9$  MPa for the second trial. The difference between these values is possibly accounted for by the standing curing position in the case of the second trial which helped pulling the two parts together through gravity. From the results displayed in Figure 2-8 (bottom), it appears that the values from Trial 2 are

more in line with the strength achievable when bonding phosphate glass with sodium silicate (Trial 3) than the ones from Trial 1. The average over all the samples of the third trial is  $12.9 \pm 5.7$  MPa which is similar to the results obtained in the second trial for the sodium silicate set. It is not obvious whether the observations on the thickness made previously are directly linked to the gap in strength between the two types of samples witnessed here. Although it can be a contributing factor, the main hypothesis remains the different chemistry between the two solutions. Another observation from Trial 3 is that apart from a few exceptions, the samples that break across the bond show an overall higher strength than the ones that break along the bond.

It can be seen that for either the HCB or SB trials, there is no clear change in the range of strength measured with the curing time. This would mean that the bond reaches a steady state after only seven days and the strength does not change afterwards.

### 2.2.3 Comparison with similar studies

The strength of HCB/SB has been of interest for a long time as this jointing technique has been used for structural applications in gravitational wave research [132][133][134]. Therefore several teams carried out trials similar to the ones presented in this chapter, although not on phosphate glass.

From the trials presented in the previous section, a representative value of the strength of phosphate glass bonded with sodium silicate is  $12.9 \pm 5.7$  MPa. The order of magnitude matches rather well the ones obtained in previous studies carried out in similar conditions, although the values seem overall lower (with a few exceptions). Haughian [135] reports a strength of  $17.6 \pm 2.8$  MPa for fused silica bonds bonded and tested in the same conditions after four weeks curing at room temperature while Beveridge [136] reports a strength of  $22.0 \pm 1.0$  MPa for BK7 bonds (low set size) after the same curing time. The structure of those materials is also amorphous and therefore it is expected to witness similarities in the bonding mechanisms and bond characteristics. The fact that the strength is still noticeably lower in the case of phosphate glass could be due to the phosphorus-based bulk material. It is possible that instead of a pure siloxane network between the surfaces, leaching of phosphorus into the bond occurs and would yield a hybrid bond made of phosphate and siloxane chains which might be weaker. In any case, the strength obtained with the sodium silicate solution is still high enough for many desired photonics application.

In the case of HCB samples, the representative value obtained here is about  $2.5 \pm 0.9$  MPa. This is noticeably below the literature values obtained for these types of bonds and can rather be compared to the strength reported for optical contacting of silica glass (see

Beveridge [136]). It suggests an actual failure in chemically bonding the two surfaces for phosphate glass. Douglas [104] observed a similar behaviour with sapphire samples where samples bonded with potassium hydroxide reached a strength of 16 MPa whereas samples bonded with sodium silicate displayed a strength of about 65 MPa. Although the discrepancy with the values from this work is significant, the fact that HCB samples are weaker leaves little doubt.

In either sodium silicate or sodium hydroxide bonding, there is no obvious improvement in strength with increasing curing time. A number of previous studies reported that the strength of sodium silicate bonds slowly ramped up to reach a maximum around three or four weeks. However, combining the increasing amount of data available, the most recent studies seem to suggest instead that the peak of strength is reached around the first week and slowly decreases with increasing curing time. In her work on bonded sapphire, Phelps observes such a trend and makes the hypothesis that the water initially contained in the bond increases its cohesion until it diffuses out leaving a less bound network [137]. It means that the trend that has been seemingly observed until then would result from the statistical nature of the trial which has been lowered by the increasing number of studies. The results presented in this section align with this new hypothesis better as the strength of the bond does not seem to change passed the first week. The values measured ( $12.9 \pm 5.7$  MPa) are lower but within error than the values reported for sapphire ( $15 \pm 4$  MPa) and fused silica ( $15.5 \pm 6$  MPa) in the hypothesis of an asymptotic behaviour of the strength.

Since the most recent hypotheses link the trend of the strength to water diffusion through the bulk material, it is relevant to look there for an explanation in the difference of rate in the curing time. Bunker reports that at room temperature, water cannot diffuse in its molecular form in glass due to the network being too dense [138]. Therefore diffusion of water goes through local hydrolysis followed by relaxation of network chains resulting in a displacement of the OH groups until equilibrium is found. The energy of activation for this reaction is reported to be 70 kJ/mol for fused silica [139] and 26 kJ/mol for a commercial phosphate glass LG-770 [140]. The glass used in this study would be closer to another commercial glass LHG-8, the properties of which with regards to aqueous corrosion have been investigated in a few studies [141][142]. However the parameters in these studies are too different or not detailed enough to derive an actual value for LHG-8 and the value of LG-770 will be taken for the glass used in the current work. These values mean that the diffusion of water is much faster in the phosphate glass network than it is in the fused silica, which could explain why the phosphate glass bonds are in a seemingly steady state after only one week whereas the fused silica strength keeps decreasing over time.

In the case of sapphire, as a monocrystalline material, water only diffuses through the dislocations. The activation energy reported in single crystals is 220 kJ/mol [143] which is much larger than the ones reported for glasses. Therefore the diffusion of water in sapphire is slower and the curing time of the bonds longer which is in line with the results presented by Phelps.

In addition to diffusion phenomena, water goes out of the bond through evaporation by the side of the interface. The activation energy for that reaction is reported to be about 45 kJ/mol but it is acknowledged that it depends on the network hosting the water molecules [144]. Given that the activation energy is of the same order of magnitude as the diffusion ones while the ratio of surface for that phenomenon compared to the one for diffusion is of the order of magnitude of  $10^{-5}$  (thickness of the bond – 100 nm – out of sample radius – 1 cm –), the hypothesis is that the mechanism is negligible compared to diffusion.

## 2.3 Optical reflectivity

The previous sections highlighted differences between bonds made with sodium hydroxide and sodium silicate both from the structural and strength points of view. Photonics applications, in addition to mechanical properties, require knowledge on the optical properties of the bond. However, these are not independent from its structure. In particular, as the thickness can be of the order of magnitude of the wavelength of light, interference effects are expected.

In the first instance of potential photonics applications, the bond is required to produce a highly transmissive interface. Therefore it is easier to work with the reflected beam than the transmitted one to study the optical behaviour of the interface depending on the bonding parameters. The experiment used was designed to study the angle-dependant reflectance of the bond, which will allow calculation of its thickness and refractive index using the model described in section 1.4.1.

### 2.3.1 Method

#### 2.3.1.1 *Experimental setup*

The setup was designed to measure the reflectivity of the bond at various angles of incidence in order to derive its thickness and refractive index. The principle of the experiment is to send a laser beam through a bonded sample and measure which fraction of the input power is reflected at the bonded interface. To derive the intrinsic properties of the bond from such

a measurement, the light source must be linearly polarised in either S or P mode (as defined in section 1.4.1) and the angle of incidence on the sample must be varied over the largest range possible.

A schematic of the setup layout is displayed in Figure 2-9. This section describes the function and specifications of the various components and, when relevant, the reason behind their arrangement.

In the optical model proposed in section 1.4.1, there is no requirement on the wavelength to use but it has to be known to derive the parameters of interest. A visible green laser was therefore selected as it allowed an easier alignment in a lit environment than infrared or other visible lights.

The light source is a collimated green laser of wavelength 532 nm (Thorlabs CPS532-C2). From the specification sheet provided, the power output is between 0.8 mW and 1 mW and the beam has a diameter of 3.5 mm measured at 50.8 mm from the housing and a low divergence (0.5 mrad max).

A spatial filter is placed at the output of the laser in order to clean the high order modes from the beam and thus to reduce its radius. A detailed study of the exit beam propagation profile will be presented in section 3.2.1.1.

The next set of components in the beam path allows the selection of the desired polarisation of the beam. It is composed of two half-wave plates *HWP1* and *HWP2* (Thorlabs WPH10M-532) and a Polarising Beam Splitter *PBS* (Thorlabs PBS101). *PBS* is used to split randomly polarised light into two linearly polarised components. The perpendicular component is reflected towards a beam dump while the parallel component is transmitted. *HWP1* is placed before *PBS*. The combination of these two components allows the maximum output of parallel-polarised light possible by rotating *HWP1*. *HWP2* is placed after *PBS*. By rotating it by 45°, it allows switching from parallel to perpendicular polarisation.

A non-polarising beam splitter *NPBS* (Thorlabs BS025) is then used to extract a fraction of the beam before it reaches the sample in order to be able to monitor the incident power. Its ratio transmission to reflection is 90:10 according to specifications; however the actual measured ratio proved to be different at 86:14 for S polarised light and 99:1 for P-Polarised light. This was not an issue per se as this variation was made up for in the calibration measurements.

The reflected beam is sent towards a photodiode *PD1* (Vishay TEMD5510FX01). A pinhole with a diameter of 3 mm (Thorlabs ID12/M) is placed between the beam splitter and the photodiode and a thin slit (1 mm width) made out of two razorblades is stuck on its frame, both with the purpose of shielding parasitic light. The *PD1* position is then fixed and used as

a reference so that the beam intensity is kept at a maximum value when aligning the various components.

The transmitted beam hits the sample which is placed on a rotational stage (Thorlabs PR01/M) to control the angle of incidence by allowing rotation around its central vertical axis. The beam is reflected to a photodiode *PD2* (Centronic OSD5-5T) for acquisition of the bond reflection signal. Both the photodiodes display a maximal sensitivity around the wavelength of green light. *PD2* is placed on a translation stage (Thorlabs LNR50K1/M), which is in turn placed on a rotating breadboard (Thorlabs RBB450A/M). The two rotation stages have the same axis of rotation. This allows the reflected beam to be tracked when the sample is rotated and normal incidence to be maintained, resulting in a constant distance between the sample and the photodiode. A pinhole (Thorlabs ID12/M) is placed between the sample and the photodiode in order to isolate the bond spot from the spots from the front and back of the sample (see Figure 2-9).

The various components are positioned in such a way that the following requirements are met:

- The beam has to have a minimal radius when reaching the sample which means the sample has to be placed at the focus of the beam. This is to reduce the effects of scattering in the material (due to roughness or optical features in the bulk) and maintain the beam profile.
- The beam also has to be of minimal radius when reaching *PD2* to avoid the overlap of the three reflected beams, which means that *PD2* has to be as close as possible to the sample to prevent significant expansion of the reflected beams. Due to footprint considerations, the minimum distance between *PD2* and the sample is 17 cm.

The overall large footprint of all the optical components prevents placing of the sample at the focus of the beam exiting the spatial filter (estimated at 32.4 cm after the output). Therefore an additional lens  $f_3$  is needed to refocus the beam at a further position. To use all the space available, *PD2* is placed at the end of the bench, i.e. 128 cm away from the output of the spatial filter. The sample is placed as close as possible to *PD2*, i.e. at 111 cm from the spatial filter output and the focal length and position of  $f_3$  are determined by solving the mode-matching equations with these distances<sup>13</sup>. This results in a commercial plano-convex lens of focal length  $f_3 = 200\text{ mm}$  (Thorlabs LA1253) being placed at 71.5 cm from the output of the spatial filter.

---

<sup>13</sup> This will be dealt with in further details in section 3.2.1.

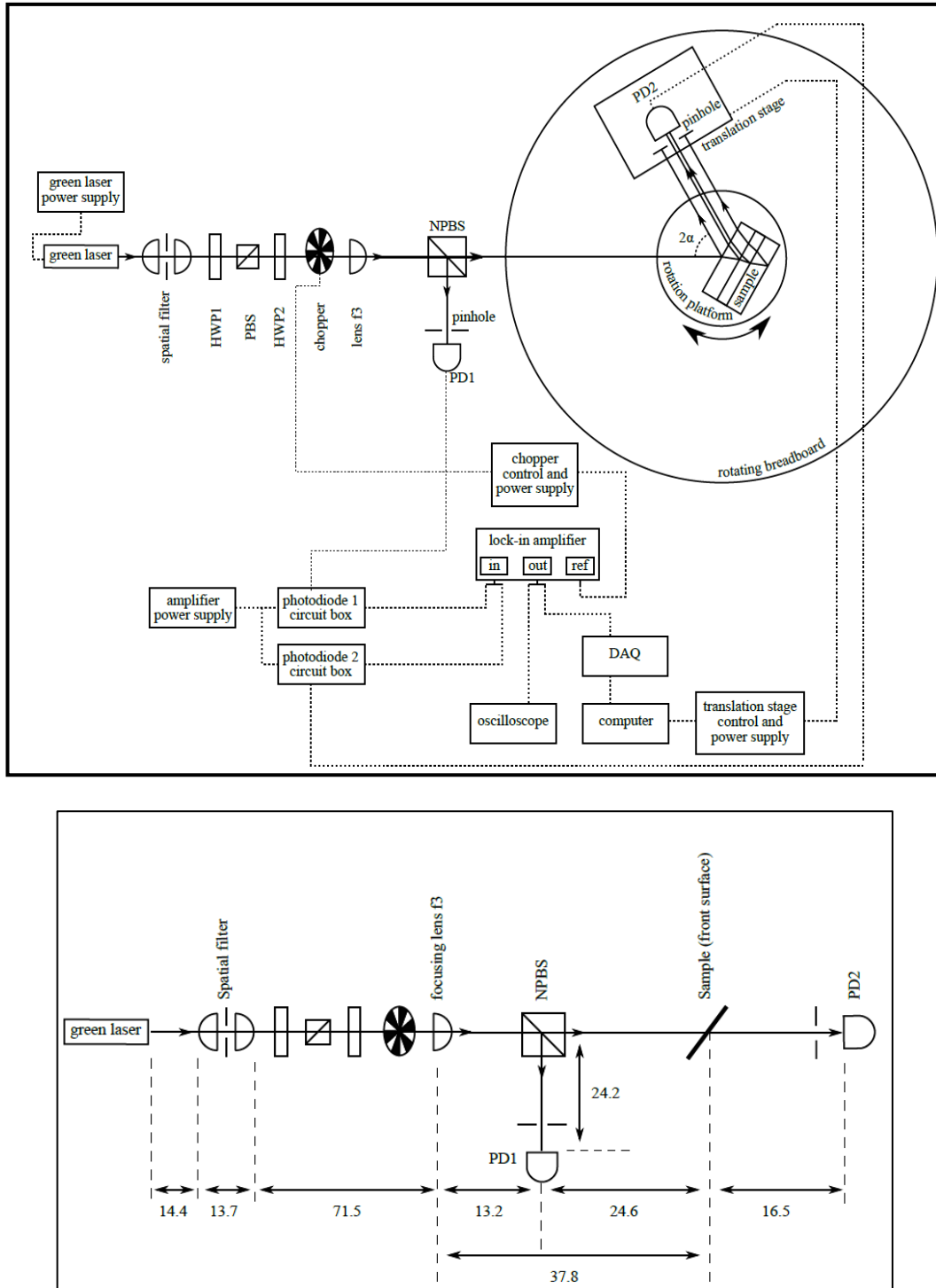


Figure 2-9: Top: Schematic of the experimental setup (courtesy of Mangano [105]). The beam goes through a spatial filter, a polarising assembly, an optical chopper before being focused on the sample and reflected to a photodiode. A beam splitter is added to extract a part of the signal and send it to another photodiode for input power monitoring. The acquisition part is made using a lock-in amplifier and either a computer (using a Labview program) or an oscilloscope. Bottom: Relevant distances between the components (in centimetres).

- The distance between *NPBS* and the sample and between *NPBS* and *PD1* should be the same to make sure that the recorded input beam is similar in profile to the one reaching the sample. *NPBS* cannot be closer than 23 cm to the sample because of the breadboard. Therefore *NPBS* is placed 24.6 cm before the front surface of the sample and *PD1* 24.2 cm away from the beam splitter to match this value within possible accuracy.

The sample is placed in such a way that the axis of rotation of the stage is aligned with the front surface. Due to refraction, the beam does not reflect at the same location on the bond interface depending on the angle of incidence. The maximum shift  $\Delta x$  in the probed position for a slab with parallel faces can be estimated through equation 2.2 which is derived using geometrical considerations.

$$\Delta x = d * \left[ \tan\left(\arcsin\left(\frac{n_0}{n_1} \sin(\alpha_{\max})\right)\right) - \tan\left(\arcsin\left(\frac{n_0}{n_1} \sin(\alpha_{\min})\right)\right) \right] \quad (2.2)$$

With  $d$  the thickness of the slab,  $n_1$  its refractive index,  $n_0$  the refractive index of air and  $\alpha_{\min}$  and  $\alpha_{\max}$  the boundary angles for the measurement. A numerical estimation of this shift with the values for the samples being used in this trial, i.e.  $d = 3 \text{ mm}$ ,  $n_0 = 1$ ,  $n_1 = 1.564$ ,  $\alpha_{\max} = 60^\circ$ ,  $\alpha_{\min} = 25^\circ$ , yields  $\Delta x = 1.32 \text{ mm}$ . This is deemed acceptable as a position variation given the expected homogeneity of the bond.

### 2.3.1.2 Data acquisition

As the signal measured is weak, a lock-in amplifier (Stanford Research Systems SR830) is used to allow amplification of the signal above noise level. An optical chopper (Thorlabs MC2000) is placed between *HWP2* and *NPBS* for that purpose. The chopping frequency is set to 429 Hz through a controller and sent as a reference signal to the lock-in. It allows filtering all the signals of different frequencies and makes the desired one stand out from the noise. This frequency was chosen following a spectrum analysis of the noise picked-up from the room and selecting an interval clear of parasitic signals.

The other input on the lock-in receives the signal from *PD1* or *PD2* depending on the step in the acquisition process. The signal from the lock-in can be sent either to an oscilloscope (Tektronix TDS2002) for single measurements or to the computer for automated measurement. The DAQ device used for that purpose is a National Instrument USB-6218.

### 2.3.1.3 Modus operandi

The measurements are taken in the dark to minimize the noise from the room lighting although it is expected that the combination of the thin slits and the lock-in allows an already effective reduction of the ambient light reaching the detector.

The sample is placed on a tailored crib and positioned using templates and shims to align the incident and reflected beam at 0° incidence. *HWP2* is rotated to have a P-polarised beam as it yields a less bright spot and helps with alignment. A calibration of the factor between the detectors (called k factor in the following) is made at the beginning and end of each day of measurement as described below.

*PD2* is placed in the space between the beam splitter and the sample. In this layout, both *PD1* and *PD2* measure the incident beam power. The value is taken in succession for the two detectors by inputting the signal in the lock-in and reading it on the oscilloscope. The process is then repeated for the S-polarisation by rotating *HWP2* by 45°. As the detectors receive the direct beam, the sensitivity of the photodiode circuitry box has to be set to a sensitivity of 10 V/mA. Once these values are taken, *PD2* can be placed back in the configuration for the measurement.

The range of angles of incidence used for the measurements depends on the thickness and the width of the sample and is set by rotating the sample and observing the reflection pattern on a screen. The lower boundary is set when the reflection spots from the surfaces overlap with the one from the bond, preventing a reliable measurement. The upper boundary is set when the beams reflected at the bond interface or the back surface hit the edges of the sample, leading to altered patterns. In the trials, the typical range of angles that could be covered was 25°-60° for a sample of thickness of 3 mm. An angular step of 5° was taken, leading to eight angles tested per sample.

The positioning of *PD2* and its pinhole is done at a high angle of incidence (usually 60°) where the three spots are well apart from each other. The pinhole is placed so that the reflected beam from the front surface goes through. The photodiode is vertically and laterally adjusted behind the pinhole to maximise the received power. Once this is done, the travel range necessary for *PD2* to scan the whole profile between the two surface spots is assessed by moving the stage using the controller on the computer. The maximum lock-in sensitivity that will not lead to saturation when passing on the bond peak is also determined. As the bond spot can be of low intensity, *PD2* must be used at 100 V/mA to record an exploitable signal. This means that an additional corrective factor is needed for the data analysis as will be discussed in section 2.3.1.4.

Once the scan distance has been determined, a file is created to dictate the translation stage motion and allow automation. The incremental displacement taken for usual samples is 0.1 mm. It can be 0.05 mm for thin samples to increase the resolution. The lock-in takes about 20 s to stabilize upon a change of signal. Therefore the acquisition cannot be made at a frequency higher than 0.05 Hz. The frequency taken was actually a bit lower to account for the time for the stage displacement.

The stage is then placed at the initial position and the automated measurement is started. When the stage reaches the end of the set interval, the acquisition is manually interrupted. Once the measurement is completed, the incident power is taken again by inputting *PD1* in the lock-in and reading the value on the oscilloscope. This allows checking for a potential drift of the laser power during the measurement. Afterwards the polarisation is switched (from S to P or vice versa) and the measurement is repeated.

This is then reiterated for each angle by increment of five degrees up to the low boundary angle determined beforehand. If the sample is placed correctly, it is not necessary to reposition *PD2* (apart from translating the stage back to the initial position) when changing angles or polarisation.

#### 2.3.1.4 Measurement errors

The reflectance of the bond is defined as the ratio between the power reflected at the bonded interface and the incident power. The reflectance of the bond is derived from the measured signal following equation 2.3.

$$R = \frac{k * V_{output}}{10 * V_{input}} \quad (2.3)$$

The *k* factor is a calibration factor between the two measured quantities and accounts for the fact that the incident and reflected beams are sent to two different detectors after splitting the beam. It contains a contribution from the different responses of the detectors and one from the ratio reflection/transmission of *NPBS*. Its measurement is made as described in section 2.3.1.3. The additional factor 10 comes from the difference in the sensitivity used for *PD2* between the calibration and measurement steps.

In equation 2.3, *V<sub>output</sub>* is obtained from the signal recorded by the Labview program through *PD2* (*V<sub>meas</sub>* in V) and the sensitivity of the lock-in amplifier used for the measurement *s* (s in V) according to equation

$$V_{output} = \frac{s * V_{meas}}{10} \quad (2.4)$$

*V<sub>input</sub>* is derived from the average between the incident powers measured before and after the measurement by *PD1* on the oscilloscope (*V<sub>osc</sub>* in V). The transition between *V<sub>osc</sub>* and *V<sub>input</sub>* is the same as in equation 1.26 except that the sensitivity is always equal to 1 V and therefore

$$V_{input} = \frac{V_{osc}}{10}$$

With the reflectance resulting from the measurement of various parameters and variables, the relative error propagates as described in equation 2.5.

$$\frac{\delta R}{R} = \sqrt{\left(\frac{\delta(V_{output})}{V_{output}}\right)^2 + \left(\frac{\delta V_{input}}{V_{input}}\right)^2 + \left(\frac{\delta k}{k}\right)^2} \quad (2.5)$$

With  $\delta X$  denoting the absolute error made in determining the value  $X$  and the other quantities being the ones previously described. The errors of order higher than one are neglected.

$\delta(V_{output})$  is estimated to be the error made by the experimenter when taking a measurement. In a first approximation, it was taken equal to 5% in relative value but will be more accurately estimated in chapter 3.

$\delta V_{input}$  comes from the power fluctuations of the laser and from the fact that  $V_{input}$  is read on the oscilloscope whereas  $V_{output}$  is obtained through the DAQ. The incident power is not registered in real time compared to the reflected power but taken as the average of the value before and after the measurement. The fluctuations in power between these two values are thus accounted for by the error. An example of measurement of power fluctuations is displayed in Figure 2-10.

In this example, the standard deviation of the set is 0.07 V. This yields a relative uncertainty of 1.5 % on the average value taken for  $V_{input}$ . By repeating a similar measurement several times, the error due to power fluctuations has been estimated to  $\frac{\delta V_{input}}{V_{input}} = 2\%$ .

The error made by reading  $V_{input}$  on the oscilloscope instead of through the DAQ is estimated by comparing the values obtained for the same signal through the two methods. The result is displayed in Figure 2-11. The value obtained is 1.2 % which increases  $\frac{\delta V_{input}}{V_{input}}$  to 2.3 %.

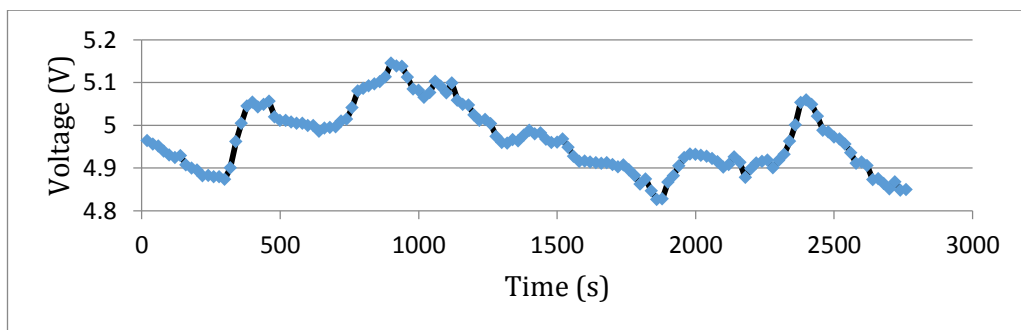


Figure 2-10: Power fluctuation of the laser in the time frame of a measurement.

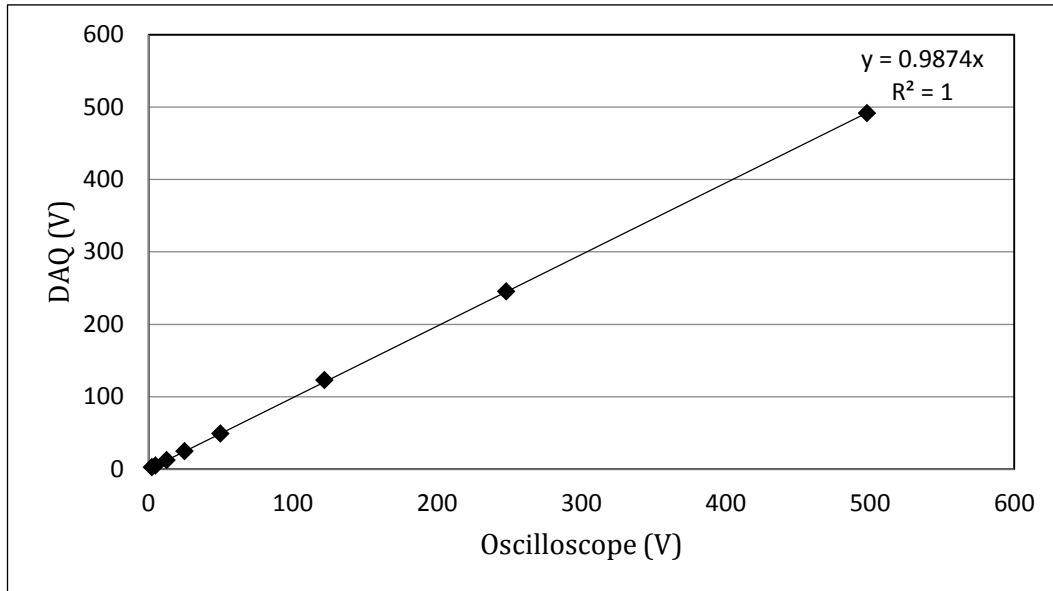


Figure 2-11: Proportional relation between measurements taken with the oscilloscope and through the DAQ. The error can be averaged to 1.2 %.

Finally,  $\delta k$  is obtained by taking the standard deviation of the set of all  $k$  values measured in the course of a trial campaign relevant to the measurement of a sample. For the measurement described in section 2.3.2,  $\left(\frac{\delta k}{k}\right)$  amounts 6.1 % and 4.0 % for S and P polarisation, respectively.

By summing the different contributions, the relative error on the reflectance can finally be estimated by equation 2.5.

$$\frac{\delta R_s}{R_s} = \sqrt{0.05^2 + 0.023^2 + 0.061^2} = 8.1 \%$$

$$\frac{\delta R_p}{R_p} = \sqrt{0.05^2 + 0.023^2 + 0.04^2} = 6.7 \%$$

Where  $R_s$  and  $R_p$  denote the reflectance measured with S-polarised and P-polarised light, respectively.

### 2.3.2 Measurement and analysis of reflectance data

The purpose of the first trial was to highlight any difference between the reflectivity of Hydroxide Catalysed Bonded (HCB) and Silicate Bonded (SB) phosphate glass. A sample from each set described in section 2.1 (HCB and SB Ø 30 mm x 3 mm discs) was used. The measurement was carried for SB and HCB samples both after 150 days of curing at room temperature. The process used was the one described in section 2.3.1.3. The measurement on the HCB sample was taken with higher lock-in sensitivity than for the SB sample because

of the lower reflectivity of the HCB sample. This means that the lock-in saturated with a lower signal and the scanned interval has to be reduced.

Figure 2-12 displays a sample of the curves obtained for both samples after they have been scaled with the appropriate factors described in the previous section. In this case the angle of incidence is  $30^\circ$  and the beam is S-polarised.

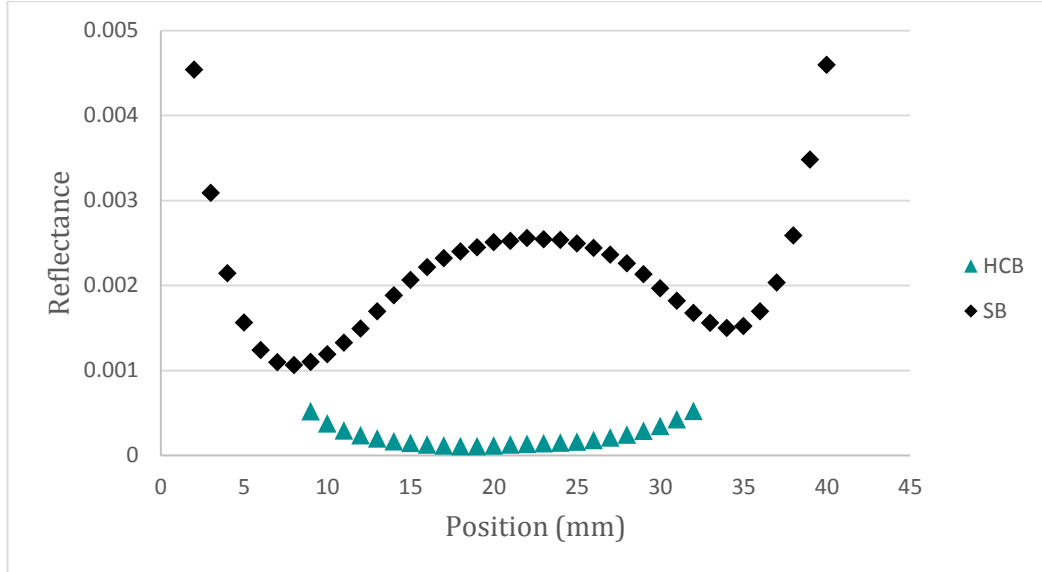


Figure 2-12: Reflectance pattern for both HCB and SB at  $30^\circ$ , S-Polarisation. The reflectance pattern for SB features a clear bond peak whereas the profile is flat for HCB.

The difference between the two profiles appears clearly. In the case of the SB sample, the bond produces a reflected beam which can be detected between the two reflected beams from the surfaces. It appears as a peak on the reflectance profile between the two high slopes from the surface peaks. The maximum reflectance of the interface, defined as the ratio between the maximum intensity of this peak and the intensity of the incident beam amounts to 0.256 % in the present case.

In the case of the HCB sample, there is no peak that can be detected from the interface. This means that its intensity is low enough that it is hindered by the brighter peaks from the surfaces. It happens for the low incidence angle when the two surface peaks are close to each other. In this case, the background coming from the peaks tails is about 0.012 %. Having this background value is useful as it allows the quantification of the contribution from the background to the intensity of the bond peak for the SB sample. This would usually be done using a monolithic sample of the same geometry but such a sample was not available for this trial. In Figure 2-13 the curves from Figure 2-12 are plotted again and the colour changed to highlight the silicate bond contribution. The tails from the surface peaks are also extrapolated towards the interface position to assess their contribution (note the logarithmic

scale on the vertical axis). Owing to the signal (black curve) to background (blue curve) ratio at the peak, which is about 20, a correction to account for this contribution was not deemed necessary as it is negligible with regards to the other sources of error (see section 2.3.1.4).

From the extrapolated curves, it can be seen that the contribution of the tails in the case of the monolithic sample would amount to 0.006 % (0.003 % each) which is only half of the value of 0.012 % in the valley. The difference could be accounted for by the signal from the interface or by other sources of noise.

For higher angles, the separation between the front, bond and back peaks is larger and it may be possible to have the bond peak stand out from the background. This is the case at 55° for the P-polarisation where the surface peaks get low due to the extinction around the Brewster angle. Figure 2-14 displays the pattern detected in that configuration. The maximum reflectance of the peak is 3.9 ppm in this case while the background noise from the tails is seemingly between 1.0 and 2.0 ppm. This point is the only one for which a peak could be obtained from the bond thanks to the particular situation around the Brewster angle. At this angle of incidence, the direction of the reflected and refracted rays are perpendicular resulting in a an extinction of the surface-reflected beam at P polarisation, For the other angles, only the value of the background signal, from which the contribution from the tails was subtracted, could be taken as an upper limit for the reflectivity of the interface.

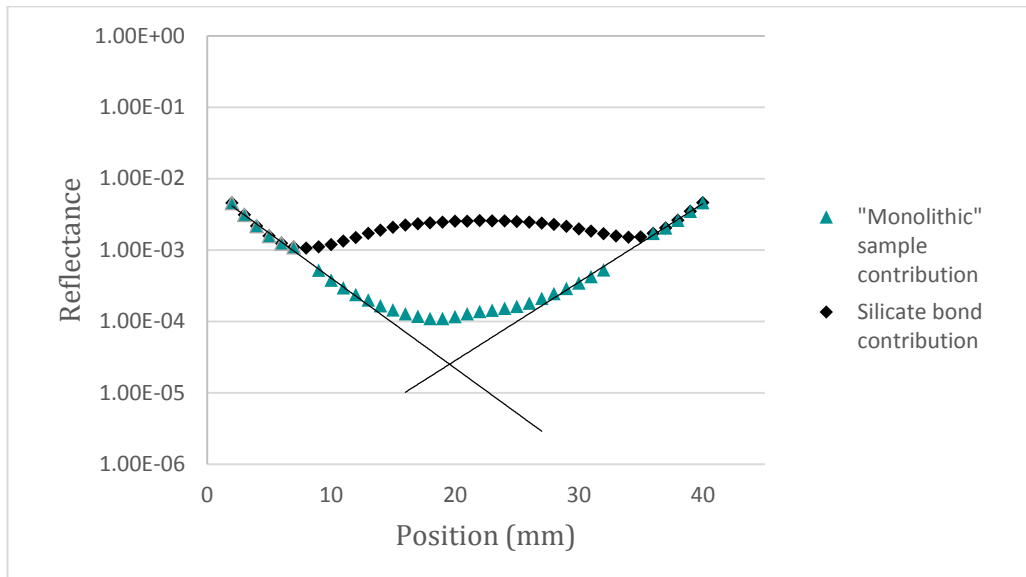


Figure 2-13: Separated contributions to the bond reflectivity from the “monolithic” sample (HCB) and the bond for SB, 30°, S-polarisation.

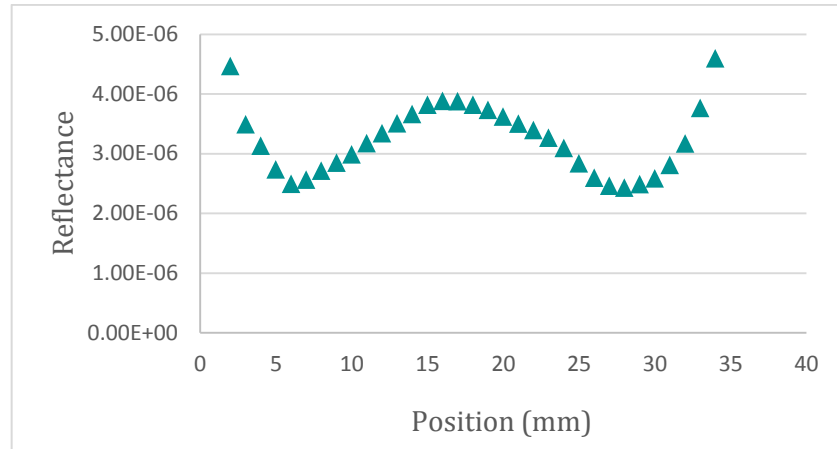


Figure 2-14: Reflectance pattern for HCB at  $55^\circ$ , P-polarisation. A peak appears clearly with an approximate maximal value at 3.9 ppm.

The values of reflectance obtained for both samples for each angle and both polarisations are summarised in Figure 2-15. Hollow points are points for which an actual peak was not obtained and therefore correspond to background values.

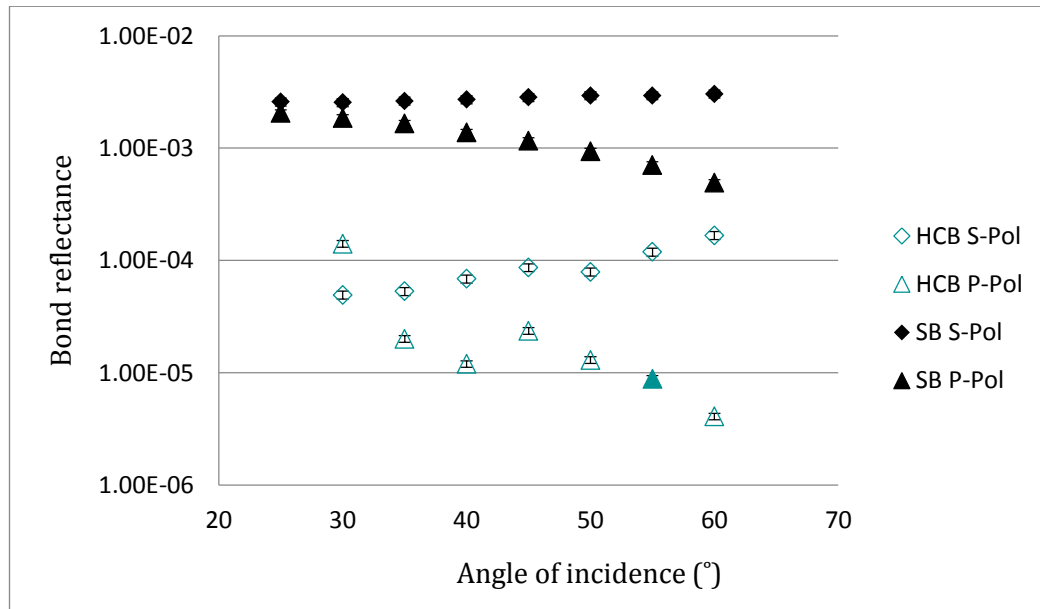


Figure 2-15: Reflectance from the bond for both samples, both polarisations depending on the angle of incidence. The hollow points correspond to measurements where the signal from the bond was hindered by the surface peaks and therefore the background value was taken as a ceiling value.

Although it was not possible to obtain exact values for most cases with the HCB sample, the measurements display a noticeable gap between the reflectivity of the two types of bond. The silicate bond is at least ten times more reflective than the hydroxide catalysed bond with an upper limit value of about 0.20 % for the former and 0.015 % (either polarisation in both cases) for the latter.

### 2.3.3 Analysis to extract n and t

From these reflectivity curves, it is possible to derive an estimation of the thickness  $t$  and refractive index  $n$  of the bond using a Matlab script written by Dr. Mangano. The script realises a maximum likelihood analysis to find which pair of values ( $n; t$ ) yields the best match between the associated theoretical curves (see section 1.4.1) and experimental ones. The script requires as input a file containing the list of angles and the associated measured reflectance values with errors. The outputs are the most likely pairs of values that fit the system and a confidence map around these values. The theoretical curves with the parameters set to these values are also plotted over the experimental curves so that the match can be assessed. More details about the method and the script can be found in Appendix C.

For this measurement, the refractive index values considered were between 1.300 and 1.600 with an increment of 0.001. The estimated refractive index of the phosphate glass used was 1.564 (see Appendix A). Therefore these values corresponded to the refractive index of water and an upper limit of the refractive index of the bulk material, respectively. This also encompassed the refractive index of dry sodium silicate estimated at 1.52<sup>14</sup>. It was believed that the bond would be constituted of species from the bulk and the solution and, with this hypothesis, its refractive index should have been within these boundaries. The thickness range considered was between 1 and 1000 nanometres with an increment of 1 nanometre. This was based on results from Mangano's work [105] and allows scanning a wide range of values with acceptable resolution.

The output for the SB sample is given in Figure 2-16. The upper part features the experimental curves input (discrete curves) fitted with the theoretical curves derived by the analysis (continuous curves). The value of refractive index and thickness associated with those theoretical curves appears at the top of the graph. The lower graph features a map of probability for the various pairs of values, centred on the most likely ones. Areas with less than 5 % probability are not considered.

The analysis gives a value of  $n = 1.47_{-0.5}^{+0.2}$  and  $d = 55_{-20}^{+30} \text{ nm}$ . The uncertainty is obtained from the boundaries of coloured domain (containing 99.7 % of the probability density as explained in Appendix C). It was not possible to put the measurements from the HCB sample through the script as the values taken were not exact ones and therefore there were no theoretical curves that would correspond to the actual bond.

---

<sup>14</sup> [https://www.chemicalbook.com/ChemicalProductProperty\\_EN\\_CB2199386.html](https://www.chemicalbook.com/ChemicalProductProperty_EN_CB2199386.html)

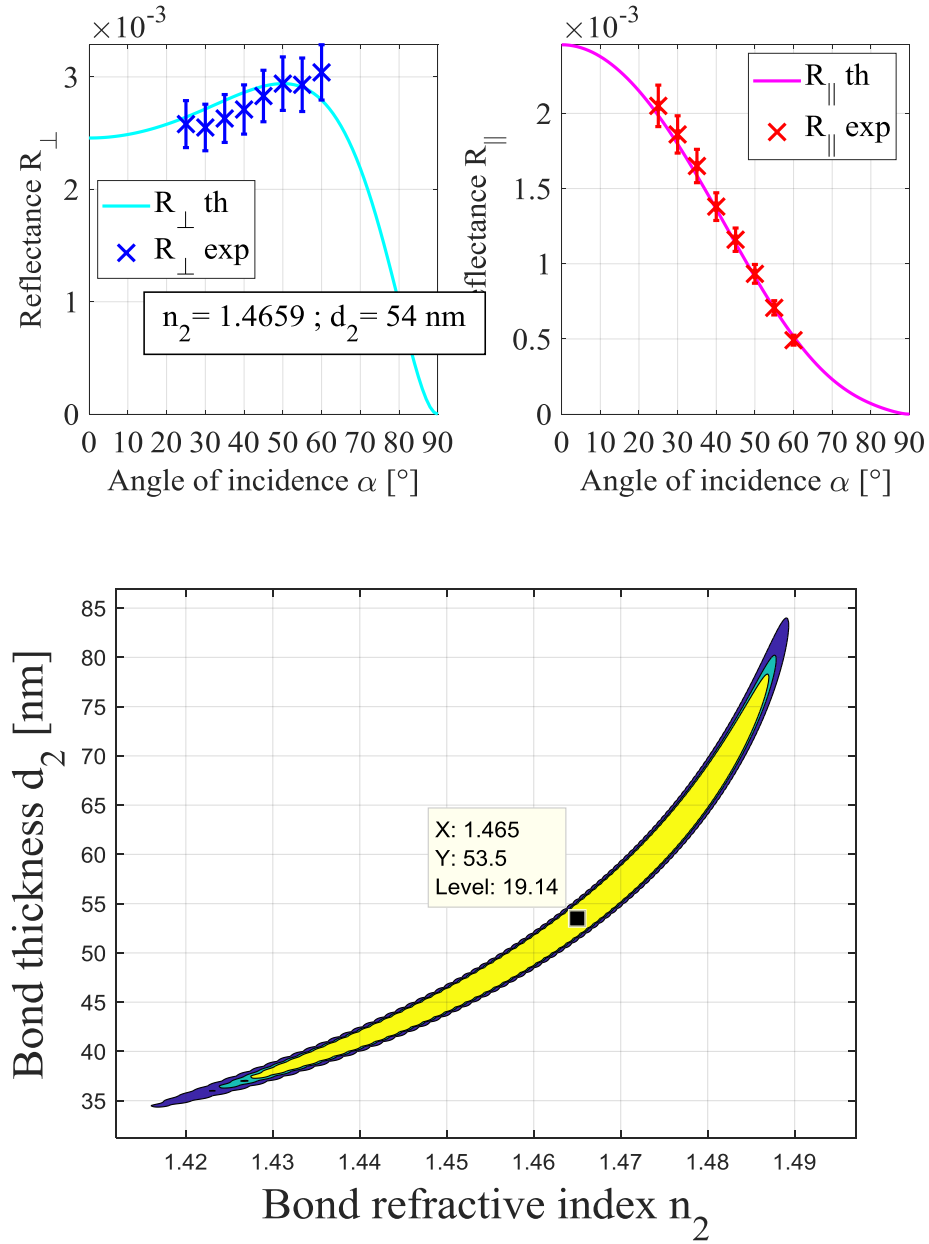


Figure 2-16: Raw output from the Matlab script using the SB reflectivity measurement as input. Top: Experimental curves (discrete) versus theoretical curves from the derived values (continuous). Bottom: Map of confidence on the identified couple of values (zoomed on the most likely area). The whole coloured area represents the domain that contains the pair of parameters with a 99.7% probability. The yellow area contains 68.3% of the probability density function. The marked point is the data point with the highest probability.

### 2.3.4 Discussion and comparison with similar studies

Putting the present results together with the ones presented in Figure 2-5, there is a noticeable gap in thickness between the value obtained by direct observation through SEM ( $120 \pm 10$  nm) and the value derived indirectly by this analysis ( $55^{+30}_{-20}$  nm). They are both sensible as they are of the order of magnitude of the flatness of the sample but too far apart to simply be within error of the measurement. The observation under the microscope has already showed that shadowing effects could lead to overestimating the thickness of the actual bond when looking through gold and it could still be the case with the current pictures. However the robustness of the optical model and setup that allowed the derivation of parameters from the reflectivity measurements also needs to be assessed and it is not possible to put it above the other methods in term of reliance at the moment. Both the values will be kept until further trials are made or improvement brought to settle on the most likely one.

The refractive index value extracted from the analysis however is the only measurement available, as no other direct or indirect observation have been made before on such bonds. The value of  $n = 1.47^{+0.2}_{-0.5}$  conforms to expectations which strengthen the confidence in the model. In fact, the bond is constituted of sodium silicate solution which, upon dehydration should form a network of silica glass. Fused silica has a refractive index of 1.4570 at 532 nm<sup>15</sup> and therefore it is expected to be the refractive index of the fully cured bond. However, literature has showed that phosphate glass could get etched by sodium hydroxide solution leading to phosphate chains dissolving in the bond [111]. As the refractive index of the bulk material used in this trial is about 1.57, the refractive index of the resulting bond should be comprised between 1.45 and 1.57 which is the case here.

This trial was a first of its kind made on HCB and SB phosphate glass. The first highlight is the significant difference between the reflectivity of the interfaces, with it being about 0.2 % for the SB sample and one order of magnitude lower for the HCB sample. Although the measurements on the HCB sample could not be completed as intended, the fact that the setup was able to measure such a difference make its use relevant for further trials. The estimated intrinsic properties of the bond that are derived from the analysis also match the expectations although the SEM observations are not fully in agreement with the reflectivity results, demonstrating the need for further investigations.

Looking at the literature, there are a few research teams that presented results on the issue, albeit mostly focused on fused silica and none on phosphate glass. Sinha [106] led pioneering work on reflectivity measurement for bonded silica although he used a different

---

<sup>15</sup> <https://refractiveindex.info/?shelf=main&book=SiO2&page=Malitson>

wavelength (1064 nm) and setup layout. A notable difference is that he measured the feedback at normal incidence, using temporal separation rather than spatial separation of the signals from the different interfaces. However the optical model described in section 1.4.1 suggests that the reflectivity at normal incidence would be close in value to the ones in the range presented in this section. Sinha measured a reflectance from the bond of 0.07 % for samples prepared in the closest conditions to the SB ones of this work. This means that the reflectivity of the bond is lower than the one obtained with SB but larger than the one obtained with HCB in this work. This can be easily explained by the fact that in the case of SB the silicate solution matches better the index of fused silica than the one of phosphate glass (at the respective wavelengths at which the measurements are made), reducing the Fresnel reflection at the interface. In the case of HCB however there is no input of silicate in the network and the bond composition should be closer to the one from the bulk, hence reducing even further the reflectivity which is witnessed here.

Another work of interest is from Mangano who designed and worked on the experiment presented here. The relevant results for comparison are her tests on fused silica for both SB and HCB samples. Using the same setup and model, she reports a reflectivity of the order of magnitude of 0.1 % (S-pol) or 0.01 % (P-Pol) for a SB sample at 98 days and 10 ppm (S-Pol) or 1 ppm (P-Pol) for a HCB sample (Bonded with potassium hydroxide 0.1 N) at 56 days [145]. The reflectivity she obtains for the SB sample is similar to the one presented in this work whereas the one obtained for HCB is at least one order of magnitude lower. This is surprising as, in theory, the composition mismatch between the bond and bulk should translate into a higher reflectivity in the case of SB phosphate glass. It seems that etching of elements from the bulk into the bond occurs and is sufficient to swamp the silicate layer and reduce the Fresnel reflection to the same level as for silicate bonded silica. The hint is given by the measurement of the refractive index of the layer ( $n = 1.47^{+0.2}_{-0.5}$ ) which is higher than the one of fused silica and suggests that other elements are present in the bond.

It is hard to comment on the HCB samples results as the ones presented in this work are only an upper limit of the reflectance whereas Mangano used a more suitable sample geometry (in particular thicker samples that allowed better separation of the beams) to be able to take measurements of lower values. Although her values could be transferrable to the HCB phosphate glass sample studied here, the different hydroxide solution and bulk material make this assumption debatable.

Finally, Taylor [118] also carried similar experiment on bonded fused silica and used a heterodyne interferometer to measure the amplitude of the signal reflected from the bond at 532, 633 and 1064 nm. It is not clear whether the bonded solution was a simple hydroxide solution (HCB) or a silicate-enriched one (SB). Due to a different method of measurement and the use of two wavelengths, there is no need to vary the polarisation or the angle of

incidence to obtain the bond parameters from the reflectivity measurement. The angle is set at 45° and the polarisation to S-polarised. He measured a reflectance of 4 ppm in rough agreement with Mangano's results on HCB and the deduced parameters for the bond are a thickness of  $120 \pm 20$  nm and refractive index of  $1.433 \pm 0.02$  for a fully cured bond made of fused silica. The thickness value matches well the one observed with SEM in this work and the refractive index is consistent with the expectations of having an index close to the one of fused silica (1.45) but lowered by the water still present in the bond. It strengthens the confidence in the optical model based on thin layer interferences even though the parameters and variables set are different.

## 2.4 Laser Induced Damage Threshold (LIDT)

As introduced in chapter 1, the LIDT is the second main optical property of interest for interfaces in photonics components. The method used was described in section 1.4.2.

### 2.4.1 Trials

LIDT measurements were carried out by Belford Research Ltd (Edinburgh) in agreement with ISO standards (see Table 2.1). One sample of each set prepared as described in section 2.1 was sent for testing. They were tested after 115 days curing. The light source used was a linearly polarized laser with a wavelength of 1535 nm. This wavelength was selected as it is the wavelength of emission of erbium which is a usual doping element in phosphate glass lasers [146][147]. For each power, ten spots were tested with twenty pulses per spot. All the parameters of the test are presented in Table 2.1. The results of the tests for both the HCB and the SB samples are displayed in Figure 2-17. The way to analyse such curves were detailed in section 1.4.2.

It can be seen on the graphics that the first damage appears at much lower power in the case of the SB sample than in the case of the HCB sample, i.e. at  $0.71 \text{ GW/cm}^2$  and  $1.77 \text{ GW/cm}^2$ , respectively. In the case of the HCB sample, the trend of the graph then follows a regular pattern with increasing number of damaged spots when the power rises which allows an easy derivation of the LIDT from the standard method. The value obtained for this sample is  $1.62 \text{ GW/cm}^2$ . Due to the discrete measurement and the statistical nature of the damage, the uncertainty is estimated at  $\pm 0.05 \text{ GW/cm}^2$ .

Table 2.1: Parameters of the LIDT test led at Belford Research, Ltd.

TEST SPECIFICATIONS	
Test	Laser Induced Damage Threshold
LIDT Type	S-on-1
Sample Size	25.4mm x 6.6.5mm
Optic or Witness	Optic
Side to Test	Interface
Polarization	Linear
Wavelength (nm)	1535
Angle of Incidence (deg)	0°
Spot Diameter ( $1/e^2$ ) ( $\mu\text{m}$ )	Smallest Spot 200
Pulse Duration (FWHM) (ns)	10
Repetition Rate (Hz)	10
Threshold Determination	Least Fluence
Test Beam Profile	$\text{TEM}_{\infty}$
Axial Modes	Multiple
Number of Sites per Row	10
Number of Shots per Site	20
Number of Rows tested	20
Total Number of Shots	4000
Sample Handling	Cleanroom Glove
Test Compliance	ISO Standards 21254-1; 21254-2; 21254-3 and ISO-TR-21254-4 2011

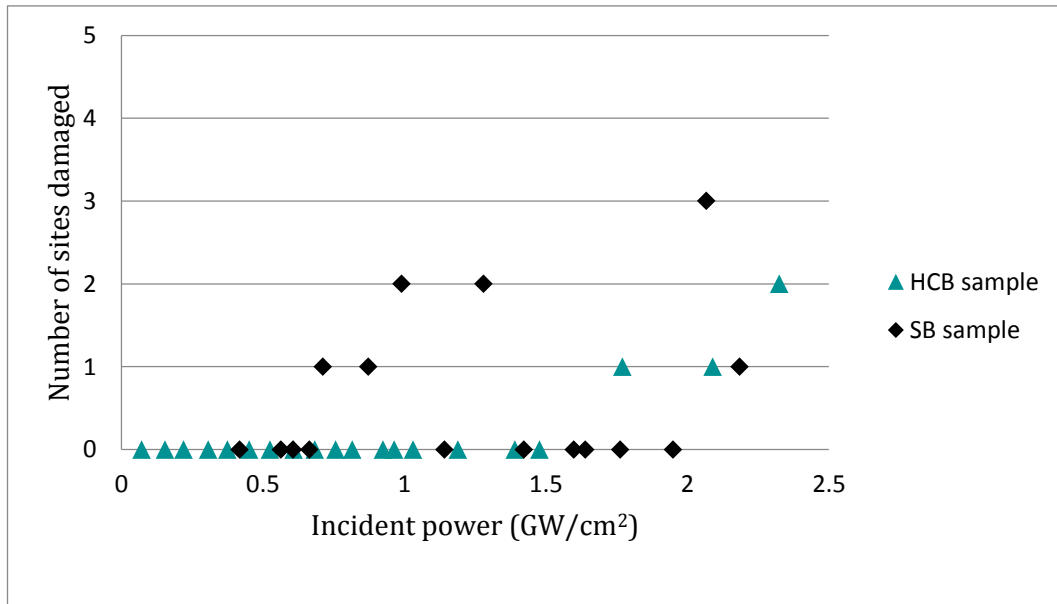


Figure 2-17: Number of sites damaged out of ten with increasing power for both HCB (triangle) and SB (diamonds) samples.

The analysis is less straightforward for the SB sample. The curve initially follows the usual trend of a LIDT test up to  $1.28 \text{ GW/cm}^2$  and from these first points a LIDT of  $0.71 \text{ GW/cm}^2$  can be derived. However, going further in power, there are several rows that show no damage up to  $2.07 \text{ GW/cm}^2$  from where the sample seems to be consistently damaged again. As the test is statistical, it is possible to obtain rows that are clear of damage even at powers

higher than the LIDT. However, as it happens on four consecutive rows, it is also possible that the earlier damage results from local inclusions in the bond and does not represent the average threshold of the bond. The lower power damage cannot be ignored as it could lead to a failure of the component. Further trials will be needed to settle on a hypothesis but at the moment, HCB seems more reliable than SB from the LIDT point of view.

#### 2.4.2 Comparison with similar studies

There are only a few studies on the LIDT of SB and once again they are focused on bonded fused silica. Beveridge [136] reports LIDT in a range from 0.3 to 0.86 GW/cm<sup>2</sup> for fused silica SB bonds at 1064 nm while Sinha [106] recorded values as high as 2.2 GW/cm<sup>2</sup> for similar samples and parameters. There are noticeable differences between the reported values as well as the one measured in the present work (0.7 GW/cm<sup>2</sup> for SB and 1.6 GW/cm<sup>2</sup> for HCB) which can be accounted for the statistical nature of the test. Without a large sample size, the deviation can be significant with varying parameters between the studies. However, despite the different wavelength and materials, all the thresholds reported in these studies alongside the ones of this work suggest that the LIDT of the bond is above what is required for common applications in photonics and high power lasers. A threshold of 1 GW/cm<sup>2</sup> would be of interest for particular commercial applications<sup>16</sup> and it seems that several combinations of bond types and materials could be capable of reaching this.

## 2.5 Summary

This section has focused on highlighting the feasibility of bonding phosphate glass with either a sodium hydroxide solution or a sodium silicate solution. The samples of the two types have then undergone a series of tests to identify whether their properties were different and which would be performing the best. The conclusions of these trials are summarized in this section.

The first result of this study is the successful bonding of phosphate glass with a sodium silicate solution. From theory, it is expected that it would be possible to bond most oxides using such a solution and the present work reinforces this hypothesis. However, a more significant advance is the possibility to make bonds with a simple hydroxide solution. Although the chemistry was not thoroughly investigated, both the large HCB and SB samples appeared free of defects and the sample could be handled and manufactured proving useful strength. However edge effects seemed to occur in the case of HCB when bonding samples of smaller area with potential consequences on their performances.

---

<sup>16</sup> Internal communication

Both the samples could be cut and polished which allowed observations under Scanning Electron Microscope. Estimations of silicate bonds thickness from direct observation usually lie between 40 nm and 100 nm for bonds between materials such as fused silica or oxidised silicon, with various bonding parameters [127][148]. The values observed in this work are in the same range which is reassuring given the similarities in surface preparation. In fact, SEM observations show HCB and SB samples with bond thickness below 50 nm and around  $120 \pm 10$  nm, respectively.

Trying to confirm those observations through the indirect method of reflectivity measurement brings a new set of challenges. First, the thickness of the HCB bond could not be derived due to a combination of sample geometry and low reflectivity not allowing a proper measurement. Then, the value of  $55^{+30}_{-20}$  nm derived for the silicate bond does not align well with the SEM observations, although they are both in a sensible range. The limited resolution on the SEM pictures introduces uncertainty in this value. However, as a direct measurement, there is less room for error than with the reflectivity setup. Therefore until the trials are multiplied and validated, both values remain in consideration.

Nevertheless the reflectivity of the bond, which is directly measured, is valuable information by itself for any photonics application. Results show that the HCB sample is at least ten times less reflective than the SB sample, which gives it a large edge when transmissive interfaces are desired. It is relevant as with a reflectivity of an order of magnitude of 0.01 % at worst, an HCB interface is suitable for applications in photonics whereas the reflectivity of 0.1 % of SB makes it borderline. This difference can be accounted for the fact that the sodium silicate solution yields a bond layer of different refractive index than the bulk material by bringing silica to the interface. On the contrary, sodium hydroxide only etches the surface to form the bond so that the bond chemistry is closer to the one of the bulk.

The data analysis from the reflectivity measurements reinforces the hypothesis that the silicate bond layer has a different refractive index from the bulk material, with a derived value of  $1.47^{+0.2}_{-0.5}$  for the bond versus the 1.564 of phosphate glass. This value is logical as the bond layer is expected to be constituted of both silicate (refractive index 1.45) and phosphate (refractive index 1.564) glass and therefore the refractive index of the compound layer should be between the ones from each material. However, this value cannot be considered without the associated thickness derived from the model which, as discussed above, might be inaccurate. Therefore, although it matches the theory it has to be taken with care as long as the reliability of the setup and the model has not been guaranteed.

Finally, the LIDT measurements support the fact that the HCB sample has better optical properties than the SB one for photonics applications. The LIDT derived from the tests is 1.6 GW/cm<sup>2</sup> for the former and 0.71 GW/cm<sup>2</sup> for the latter. Moreover, the trend of the curves

obtained suggests that the interface is more homogeneous in the case of HCB than SB samples. This could come from the silica particles in the sodium silicate solution favouring the formation of clusters or voids in the interface or from the bond being thicker increasing the absorption. It might be possible to work on the sodium silicate solution to avoid such issue but until it is done, sodium hydroxide seems to be a more reliable solution.

These trials both suggest that HCB performs better than SB to obtain transmissive interfaces as desired by the photonics industry. However, previous studies have showed that the main advantage of SB over HCB comes from its superior mechanical strength [104][136]. The strength tests presented in this section support these observations as the average strength of HCB is about 2.5 MPa whereas it is about 12.9 MPa for SB. Although the considered photonics components are not designed to bear a lot of stress during their service, they still should be strong enough to survive basic handling and occasional vibration and shock occurring during shipping for example. Therefore, the mechanical strength cannot be ignored and the choice between HCB and SB must result of a trade-off between optical and mechanical properties.

A number of previous studies have showed that the optical properties of a silicate bond could be tuned by modifying the parameters of the sodium silicate solution used for bonding [105][106]. However these studies have focused on fused silica and it is not certain whether or not those observations transfer to phosphate glass. SB phosphate glass has shown suitable mechanical properties but only borderline optical properties (mostly reflectivity) whereas HCB has suitable optical properties but significantly worse mechanical properties. If such a tuning of the properties is possible with phosphate glass too, it is worth trying to find a solution that yields intermediate bond properties which would both fit from a mechanical and optical point of view. In chapter 3, we investigate how modifying the concentration of sodium silicate in the solution affects the optical properties of the bond in order to find such a compromise.

---

### 3 Improvement of the experimental setup and modification of silicate bond properties by tuning the solution parameters

---

The previous chapter focused on applying a wide range of tests to phosphate glass samples bonded for the first time using a sodium silicate solution or a sodium hydroxide solution. The purpose was two-fold: proving the relevance and suitability of the test setups and highlighting differences between the properties of the two types of bond. In this chapter, the focus is put on silicate bonds. The concentration of the solution is changed to see whether it is possible to tailor the properties of the bond, potentially increasing its range of applications. The characterisation techniques used are the same as in chapter 2. The reflectivity setup is upgraded to improve the quality of the measurements and an extended trial is carried out to highlight the change of bond properties with time. Afterwards, the bond interfaces are tested for Laser Induced Damage Threshold.

#### 3.1 Samples

The samples used for this trial were phosphate glass samples of composition PGC2 (see Appendix A). The composition was different from that of the samples used in chapter 2 as the formulation used by the supplier changed in between the two sets of trials. This was not expected to have a significant impact on the results as the trials described in this chapter were self-contained.

The geometry of the samples was also modified to better fit the requirements of the reflectivity setup. The thickness was increased from 3 mm to 5 mm to better separate the three reflected beams. The samples were cuboids of dimensions 10 mm x 35 mm x 5 mm bonded on the 10 mm x 35 mm face. The faces to be bonded were polished to about 60 nm peak-to-valley flatness and endured a chemico-mechanical finishing with Syton® polishing compound at Gooch and Housego.

The bonding solution used was a sodium silicate solution diluted at 1: 3, 1: 6 and 1: 10 volumetric parts in deionised water. In the following the bonded samples will be referred to as SB3, SB6 and SB10, respectively. The silicate bonded samples used in the previous chapters are thus equivalent to SB6. The solution went through the same steps as the ones described in section 2.1(filtration and centrifugation) and a volume per unit area equal to 0.8  $\mu\text{l}/\text{cm}^2$  was used for bonding. This volume differed slightly from the one used in the trials presented in chapter 2 but matched up with other works in the field (e.g. [101][104][105]).

Given the number of parts available, a single sample was bonded with each solution. Bonding worked well with each of the three solutions and the samples could be handled after no more

than a few minutes. The interfaces were clear of defects for each sample and no noticeable difference could be witnessed between the samples.

The samples were used for reflectivity and LIDT measurements and cut and polished to assess their strength. The low number of samples made this an initial study without being able to guarantee statistical accuracy.

### 3.2 Optical reflectivity

Reflectivity trials were carried out in the same way as presented in chapter 2. The objective was to highlight any difference in reflectivity when using three different solutions of sodium silicate. Moreover, given the longer time available for these trials, it was decided that the change of reflectivity and of the derived bond properties (refractive index, thickness) during the curing of the bond would be monitored. Therefore the bonds were measured four times each from day 2 to day 28 after bonding. An additional measurement was taken at 75 days but since the samples had been sawed in the meantime this will be discussed separately.

Given the limitations of the setup met in the course of the first trial, some modifications were made. The purpose was to reduce the beam radius in order to better separate the three reflected beams and therefore reduce the background noise at the position of the bond peak.

#### 3.2.1 Laser beam radius reduction

As seen in the trials made in chapter 2, it was not possible to measure the bond spot of the low reflective HCB sample. The high intensity from the surface peaks, and those being too close to each other due to the geometry of the sample swamped the signal from the bond. A few ways to improve the setup for low reflectivity measurements were identified:

- Increase the sample thickness to better separate the three reflected beams.

This was a practicable and fairly easy solution to implement. Increasing the thickness also required increasing the width of the sample or face edge effects as discussed in section 1.4.1. This change was implemented.

- Apply an anti-reflective coating to either or both the surfaces.

This would have allowed reducing the parasitic light from the front and back surfaces reflection and might have allowed the bond spot to stand out from the tails of the peaks. However, anti-reflective coatings are wavelength and more importantly angle dependent. Given the layout of the setup and the necessity to vary the angle it would not have been efficient and would likely have required a lot of post treatment of the data to estimate the transmitted light.

- Reduce the parasitic light by improving the setup.

If acting on the sample is not possible, the logical approach is to tackle the problem by modifying the setup. As the bond spot was already noticeable by eye, it was assumed that there was more potential for progress by working on the detection, i.e. reducing the parasitic light at the photodiode location. For that purpose, a slit of 0.6 mm instead of 1.0 mm width was placed in front of the photodiode. However, care had to be taken that the beam did not clip at the edges of the slit. It was assumed that as long as the slit was larger than the beam, this effect would be avoided. To this end the beam propagation was investigated.

### 3.2.1.1 Beam profile measurement

The reflectivity measurement setup was shown in Figure 2-9. In order to optimise the beam diameter the beam was optically profiled, initially using a knife edge technique as shown in Figure 3-1 and described below.

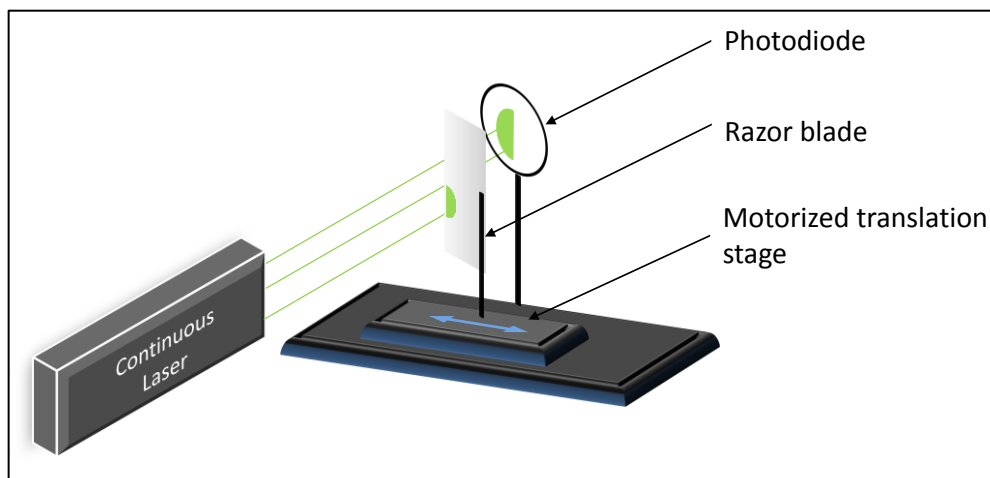


*Figure 3-1: Schematic of a beam radius measurement using the knife-edge technique. Only the main components are represented for clarity. The photodiode remains still while the razor blade is translated to progressively mask the beam.*

The continuous beam is sent to the photodiode  $PD_2$ . The signal from  $PD_2$  is sent to the lock-in amplifier and read on the oscilloscope. A razorblade is mounted on a translation stage, perpendicular to the beam propagation direction without intercepting the beam. The distance between the photodiode and the central axis of the translation stage (and therefore the blade) is fixed to approximately 75 mm. At that point the photodiode records the full power from the beam. The blade is then translated until a change in power is recorded while the photodiode remains still. From that position, the incremental displacement step of the translation stage is set to 25  $\mu\text{m}$  and the power recorded is noted down manually at each position until it reaches zero.

Assuming a Gaussian beam, the power distribution follows the parametric equation 3.1 [149].

$$P = \frac{A}{2} \left(1 - \operatorname{erf} \frac{\sqrt{2}(x - B)}{C}\right) \quad (3.1)$$

With A the power from the full beam, B the reference position of the razorblade and C the  $1/e^2$  radius of the beam, which is the desired parameter. An example of a measurement taken with a fit to the data using equation 3.13.1 is displayed in Figure 3-2. The fit was done using the curve fitting tool of Matlab.

This measurement was taken by positioning the razorblade at 32.4 cm after the spatial filter, in the space between *PBS* and the focusing lens  $f_3$  after removal of *HWP2* (see Figure 2-9).

The values obtained are  $A = 66.9 \pm 0.3$  mV,  $B = 0.464 \pm 0.002$  mm,  $C = 0.259 \pm 0.004$  mm with an R-square value of 0.9998.

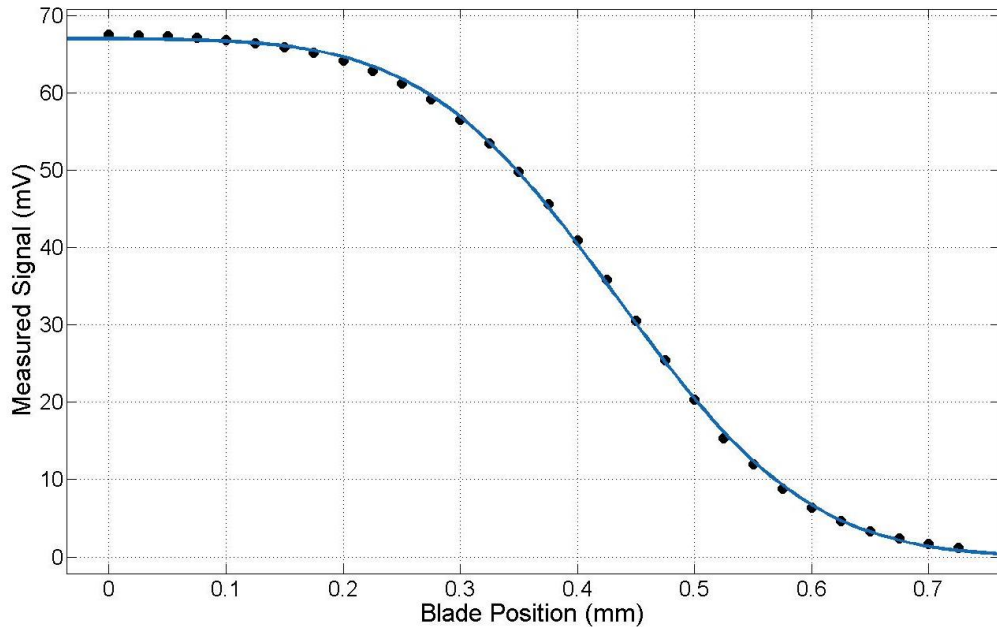


Figure 3-2: Example of a beam width measurement taken with the knife-edge technique (dotted line) and curve fit realised using MATLAB curve fitting tool (continuous line).

The obtained value of 260  $\mu\text{m}$  was believable for the radius of the beam; however the setup had been built with a target of reaching 100  $\mu\text{m}$ <sup>17</sup> which had not been verified experimentally. This means that the real beam profile might have been far off the intended

<sup>17</sup> According to Mangano's thesis.

one and therefore a more complete characterisation was needed to understand exactly how it evolved through the setup.

A beam profiler<sup>18</sup> was acquired, which allowed multiple measurements at different positions as they were faster. In the following the reference zero position is the output of the spatial filter. Some non-focusing components (Half wave plates and beam splitters) had to be moved in order to place the chopper and profiler. These elements have a refractive index close to 1.5 and a total thickness around 1.5 cm. Therefore the error made on the optical length by not taking these into account is less than a centimetre which is acceptable considering the uncertainty of position reference with the profiler. Since these are non-focusing, their effect on the beam is limited to scattering. Due to the low thickness and the good quality of the material this effect is deemed negligible on the measured beam profile. The measurements were taken without the additional lens  $f_3$  that enabled the refocus of the beam in the earlier trial as the objective was to study the propagation of the beam in free space. An example of the output from the beam profiler is displayed in Figure 3-3. It can be seen that the projection of the beam (right on Figure 3-3) was not circular and the maximum power was off-centre. This could have been due to a misalignment of the pinhole in the spatial filter but the beam was considered suitably Gaussian for the purpose of the measurement. For the following trial the radius value was taken equal to the minor radius while checking that the 2D profile was close enough to circular. These data were given by the software.

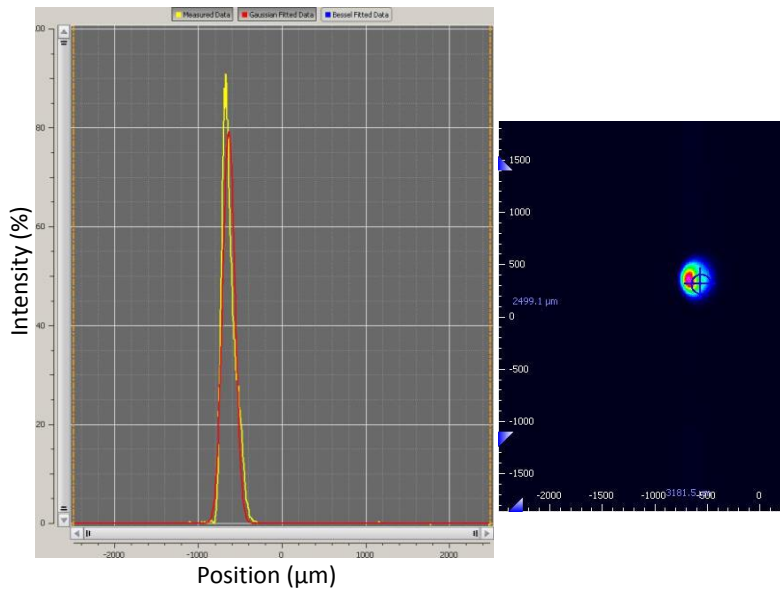


*Figure 3-3: Example of output of the beam profile measurement. Left: Intensity profile along the horizontal axis. The software fits a Gaussian profile (Red) to the measured intensity profile (Yellow). Right: The 2D intensity profile of the beam is displayed to assess its ellipticity.*

<sup>18</sup> <https://www.thorlabs.com/thorproduct.cfm?partnumber=BC106N-VIS/M>

The classical propagation equation of a Gaussian beam is given by equation 3.2 [150].

$$w(x) = w_0 * \sqrt{1 + \left( \frac{\lambda * (x - x_0)}{\pi w_0^2} \right)^2} \quad (3.2)$$

With  $w(x)$  the beam radius along the direction of propagation,  $w_0$  the beam waist and  $x_0$  the position of focus. The data obtained were fitted using the fitting tool of Matlab and are displayed in Figure 3-4.

The first observation is the good agreement between the two methods for the measurement of the beam radius at around 35 cm with the razor edge method yielding 259  $\mu\text{m}$  at 32.4 cm and the beam profiler 244  $\mu\text{m}$  at 37 cm and increasing towards lower distances.

The parameters obtained were a beam waist of  $253 \pm 37 \mu\text{m}$  and its position at  $58 \pm 8 \text{ cm}$  after the output of the spatial filter. It can be noted that the uncertainty is rather large (almost 15 %) and for this fit the R-square value is only equal to 0.900. This might have been due to the discrepancy between a proper Gaussian TEM00 and the beam profile displayed in Figure 3-3.

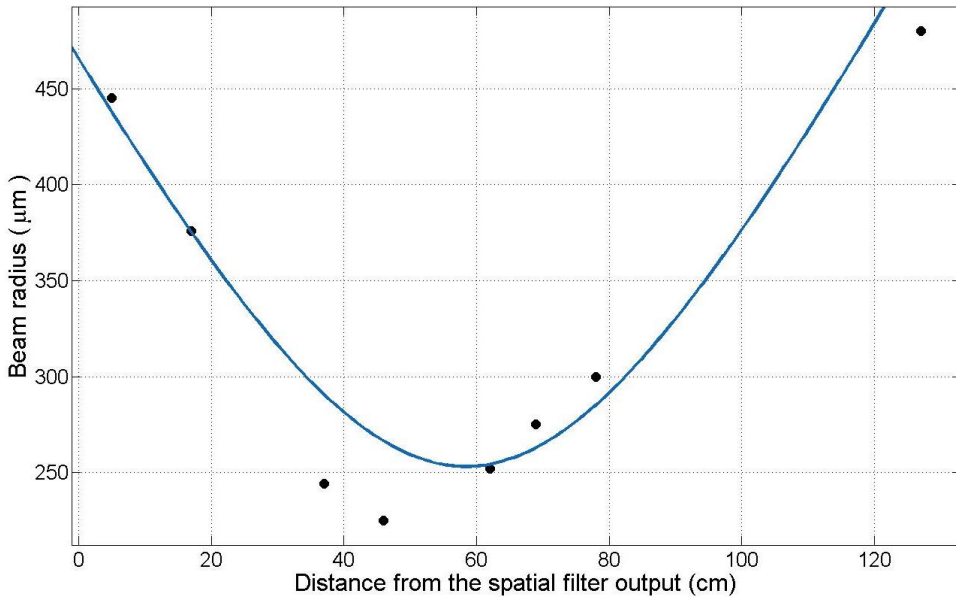


Figure 3-4: Curve fit (continuous line) of the beam profile along the optical bench obtained from experimental measurements (dotted line) according to equation 3.2. The  $R^2$  value is only 90 % which means a relative high uncertainty on the derived parameters. The reference (zero) position is the output of the spatial filter.

### 3.2.1.2 Theoretical study

In this section, a theoretical study of the beam profile is carried out. A range of parameters are fixed as it was not practicable to change them with the amount of time or space available, and ways to optimise the beam profile are studied. The targeted layout for the mode-matched Gaussian beam featuring the relevant distances and parameters is displayed in Figure 3-5.

Let us consider that the beam waist after the spatial filter  $w_2$  was 253 µm at a distance of 58 cm. The objective was to reach a waist after the refocusing lens  $w_3$  of 100 µm while keeping the total length of the setup equal to 128 cm as there was no room to extend the bench.

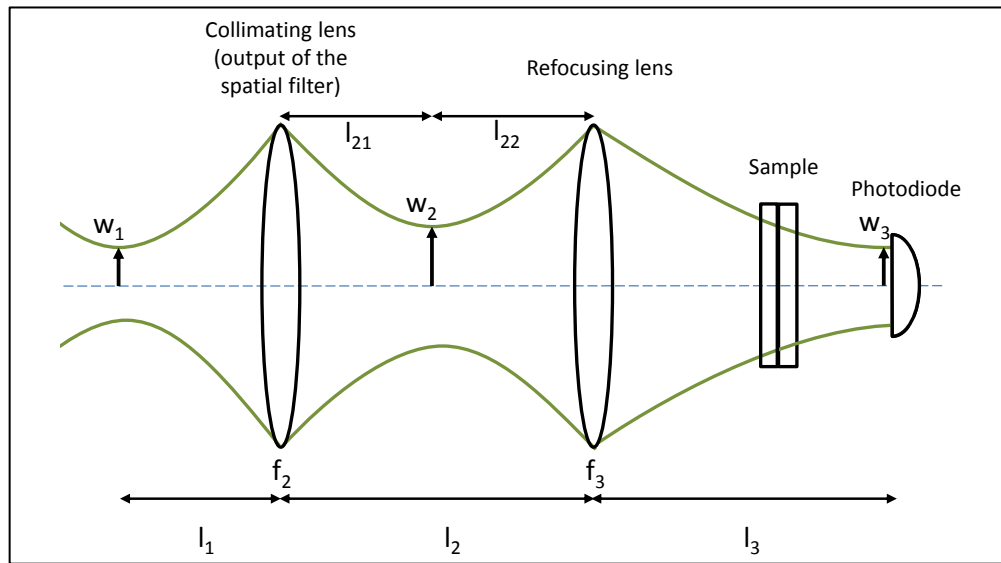


Figure 3-5: Layout for the mode-matching of a Gaussian beam (not to scale). Due to the footprint of the components, it was not practicable to have the photodiode at the position of  $w_2$ . Therefore the target was to place a lens  $f_3$  to refocus the beam on the photodiode.

The mode-matching equations for a Gaussian beam link the different parameters as follows [151].

$$l_{22} = f_3 + \frac{w_2}{w_3} \sqrt{f_3^2 - f^{*2}} \quad (3.3)$$

$$l_3 = f_3 + \frac{w_3}{w_2} \sqrt{f_3^2 - f^{*2}} \quad (3.4)$$

$$f^* = \frac{\pi * w_2 * w_3}{\lambda}$$

Where  $f_3$  and  $l_{22}$  are the parameters we wish to solve for (refer to Figure 3-5) and  $f^*$  is a characteristic length of the system.

Summing equations 3.3 and 3.4 yields equation 3.5.

$$B = 2f_3 + C\sqrt{f_3^2 - f^{*2}} \quad (3.5)$$

With

$$B = l_{22} + l_3$$

$$C = \frac{w_2}{w_3} + \frac{w_3}{w_2}$$

Reorganising and squaring equation 3.5, one obtains the quadratic equation:

$$Df_3^2 - 4Bf_3 + E = 0 \quad (3.6)$$

With

$$D = 4 - C^2$$

$$E = B^2 + C^2f^{*2}$$

Inputting the values  $w_2 = 253 \text{ } \mu\text{m}$ ,  $w_3 = 100 \text{ } \mu\text{m}$ ,  $\lambda = 532 \text{ nm}$ ,  $B = 70 \text{ cm}$ , equation 3.6 has two solutions:

$$f_3 = 0.19 \text{ m}$$

$$f'_3 = -0.80 \text{ m}$$

The second solution is not feasible given the layout of the system and therefore a focal lens of 19 cm is needed to achieve the desired waist. The closest commercial lens available had a focal lens of 20 cm.

To assess the effect of the difference of focal length between the theoretical solution and the practical availability, the reverse problem can be considered. Taking the reverse problem where  $f_3$  is given and  $w_3$  is the unknown, one obtains the following cubic equation from equations 3.3 and 3.4:

$$A_3W^3 + A_2W^2 + A_1W + A_0 = 0 \quad (3.7)$$

Where

$$\begin{aligned} A_3 &= \left(\frac{\pi w_2}{\lambda}\right)^2 \\ A_2 &= -f_3^2 + 2\left(\frac{\pi}{\lambda}\right)^2 w_2^4 \\ A_1 &= (B - 2f_3)^2 w_2^2 + \left(\frac{\pi}{\lambda}\right)^2 w_2^6 - 2f_3^2 w_2^2 \\ A_0 &= -f_3^2 w_2^4 \\ W &= w_3^2 \end{aligned}$$

Equation 3.7 is solved with  $f_3 = 20$  cm as input using the online Wolfram equation solver<sup>19</sup>. This yields three real solutions for  $w_3$ , one being negative and therefore not physical while another is not compatible with the requirements on the characteristic length  $f^*$  and therefore with the system. The solution left yields a beam waist equal to 111 μm which is in an acceptable range of the 100 μm initially desired. However, inputting this value in equation 3.4 yields a value of 25 cm for  $l_3$ . This was not practicable with the current setup as it would have placed the lens on the rotating breadboard which has a diameter of 20 cm preventing components to be placed less than roughly 40 cm away from the photodiode. Other options for commercial lenses available were theoretically studied to see if there was a suitable alternative. Results are summarised in Table 3.1.

Table 3.1: Output parameters for the system solved with various commercially available focal lengths.

$f_3$ (m)	$l_{22}$ (cm)	$l_3$ (cm)	$w_3$ (μm)	Total length (cm)
0.15	52	18	72	128
0.175	49	22	90	129
0.2	45	25	111	128
0.25	39	30	156	127

As can be seen, none of these lenses would have fitted as  $l_3 < 40$  cm for each case. It was then decided to keep using the  $f_3 = 20$  cm lens but to study how its positioning along the beam affected the radius at the photodiode.

<sup>19</sup> <https://www.wolframalpha.com/>

### 3.2.1.3 Empirical study

In this part, the additional lens of focal length  $f_3 = 20$  cm was moved along the beam. The beam profiler was placed at the photodiode location (128 cm) and recorded the beam profile with regards to the position of the lens. The possible range of positions for the lens was after the beam waist and before the non-polarising beam splitter. The non-polarising beam splitter needed to remain at its location as it defined the reference for the beam alignment together with the second photodiode. Changing this reference would have required the rebuilding and realignment of the whole set up which was not possible at the time.

The lens was then moved from 64 cm to 85 cm after the spatial filter with an increment of about 2.5 cm. The beam radius was written down at each position of the refocussing lens. The results are displayed in Figure 3-6.

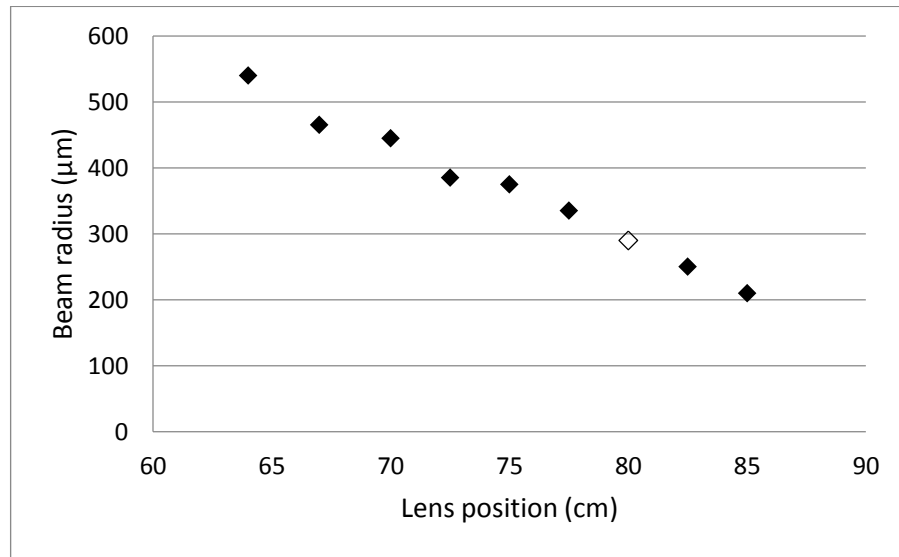


Figure 3-6: Beam radius at the photodiode (128 cm) depending on the focusing lens position. The reference (zero) position is the output of the spatial filter. The hollow point is the furthest position practically possible to place the lens during actual measurements as afterwards it would require the beam splitter to be moved.

As predicted by the theory, the beam radius decreased when the lens was placed further away from the spatial filter. The beam splitter was temporarily removed to allow measurements up to 85 cm. The previous trials had been carried out with the lens at 71.5 cm from the spatial filter, which according to the trend yielded a beam radius of 415  $\mu\text{m}$ . It appeared that it was possible to reduce the beam radius at the detector to about 290  $\mu\text{m}$  only by moving the lens 9 cm forward. Further reduction of the beam radius was likely to be achievable but would have required more time and larger modifications of the setup. It was therefore decided to work with this new arrangement.

It can be noted that the setup layout was arranged to focus the beam on *PD2* instead of the front surface of the sample as was the case in the trials in chapter 2. The objective was once again to reduce the beam size at the photodetector. The trade-off was that the beam was larger when going through the sample, reducing the accuracy on the beam position at the interface and potentially increasing scattering effects. It is possible to assess the effect of this loss of accuracy by considering the Rayleigh range of the beam, which is the distance at which the beam radius is equal to  $\sqrt{2}$  times the beam waist and from which the beam starts expanding at a linear rate.

The Rayleigh range is given by [152]:

$$z_R = \frac{\pi w_3^2}{\lambda} \quad (3.8)$$

Using  $w_3 = 290 \mu\text{m}$  as the value for the beam waist, the obtained value is  $z_R = 50 \text{ cm}$ . As the distance between *PD2* and the sample was shorter than the Rayleigh range, the beam radius at the sample would be smaller than  $w_R = \sqrt{2}w_3 = 410 \mu\text{m}$ . Therefore, the loss of spatial resolution by changing the focus was at worst  $2 * (w_R - w_3) = 240 \mu\text{m}$ . In chapter 2, the shift in positioning due to the refraction at the interface was discussed. Inputting the parameters of the samples described in section 3.1 in equation 2.2, a value of  $\Delta x = 1.9 \text{ mm}$  for the shift in position on the bond is obtained. One can then see that the loss in accuracy due to the change of focus was negligible with regards to the effect of refraction.

Figure 3-7 displays the new layout of the system as well as the estimated beam radius at the relevant positions. As it was not possible to carry out the proper mode matching the beam waist  $w_3$  was located behind *PD2*. It can be noted that due to the beam waist  $w_2$  being located close to the focus of the lens  $f_3$ , the output beam was almost collimated and the beam radii at  $f_3$  and *PD2* were close to each other. This is not optimal as a beam radius reduction but was the best that could be done with only minor changes to the setup. Having the beam size being low both at the sample and at the photodiodes was also an advantage for the reasons mentioned in section 2.3.1.1.

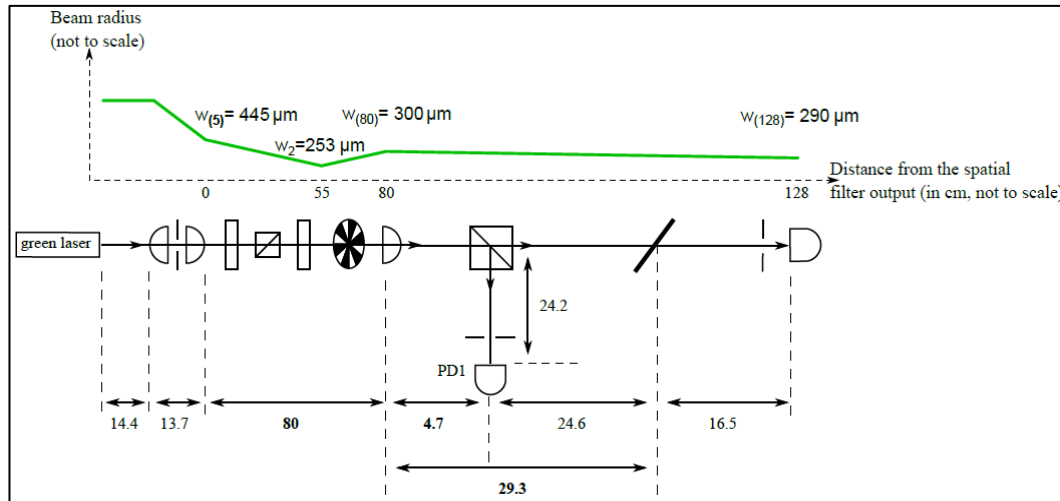


*Figure 3-7: Updated layout of the reflectivity setup and estimation of the beam profile along the optical bench. The distances that have been changed are in bold. Matching the modes was not possible due to spatial constraints and therefore  $w_3$  is located behind the photodiode.*

### 3.2.1.4 Validation of the layout

As explained in the beginning of the section, the purpose of reducing the beam radius was to avoid experiencing edges effects with the 0.6 mm slit placed at the photodiode to reduce parasitic light. With a diameter of 0.58 mm, the beam was only slightly narrower than the slit. To assess whether it was suitable for measurements, reflectivity trials were made with a reference sample for which the values of reflectivity had been verified several times. The reference sample was a Ø 50 mm x 10 mm fused silica sample bonded with sodium silicate solution at 1: 6 parts in water. It had been bonded for 434 days when these trials were made. The process followed was the one described in section 2.3.1.3.

The results are presented in Figure 3-8. The square curves represent the data taken with the 1 mm slit while the triangle curve are obtained with the 0.6 mm slit for S (filled) and P (hollow) polarisations. It appears that for the S-polarisation the curve follows the same trend with the two slits with an offset of about 2 ppm. For the P-Polarisation however the gap between the curves increases with increasing angle of incidence.

Reducing the slit size decreased the amount of light collected by the detector. Therefore, when the signal was low as in the case for the P-Polarisation around the Brewster angle, a very high sensitivity on the lock-in had to be used. It is not clear whether the setup is suitable for such low signals and therefore the point taken at 60° for the P-polarisation with the 0.6 mm slit will be discarded.

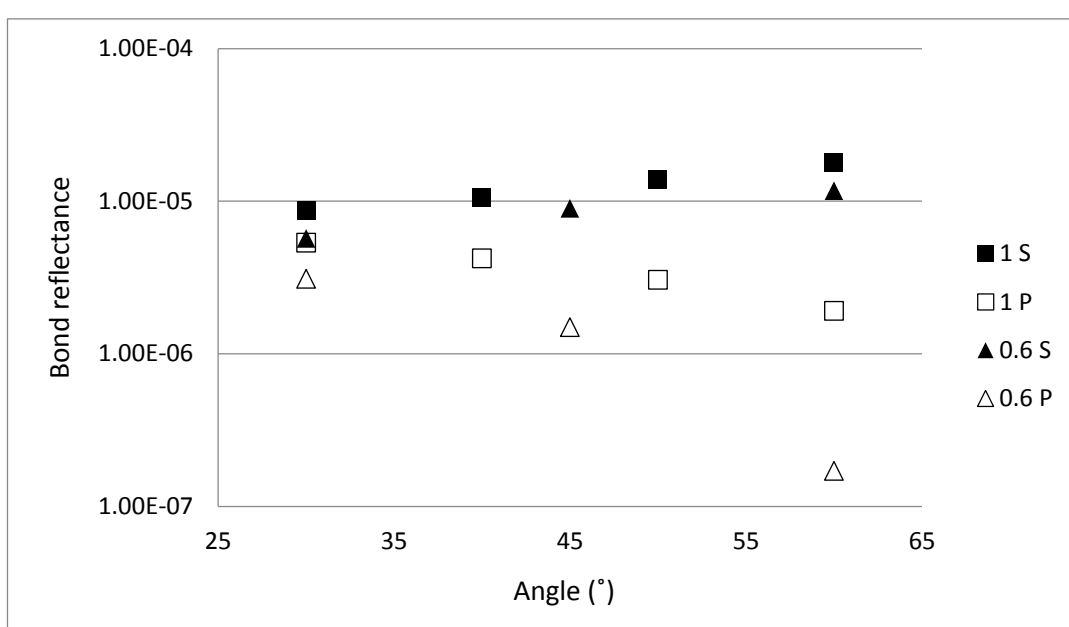


Figure 3-8: Reflectivity of a reference sample obtained with the original (square) and upgraded (triangle) setup for both polarisations and several angles. The errors on the measurement are smaller than the marker size.

The offset between the curves obtained with the different slits was accounted for by the difference in background signal. When reducing the slit size, there should be less ambient light collected as a larger part of the detector is shielded, therefore decreasing the overall signal. In order to verify this hypothesis, the background noise level was studied for each measurement.

Figure 3-9 displays measurements taken at the same angle ( $60^\circ$ ) and same polarisation (S-polarisation) with both slits. The outcomes of the beam radius reduction trials are noticeable from the reduced peak width and the increased gaps between the central peak (bond) and the boundary high slopes (which come from the beams reflected from the surfaces).

From these curves, it is clear that the offset is on the overall signal and not a loss resulting from edge effects. Therefore, subtracting the background difference from the whole signal should compensate the offset. The background amount is taken equal to the average between the minimum on each side of the central peak. The value is noted for each measurement (angle, polarisation, slit size). In Figure 3-10, the curves from Figure 3-8 are plotted again with an offset applied to the 0.6 mm curves so that the reference for the peak height is the same.

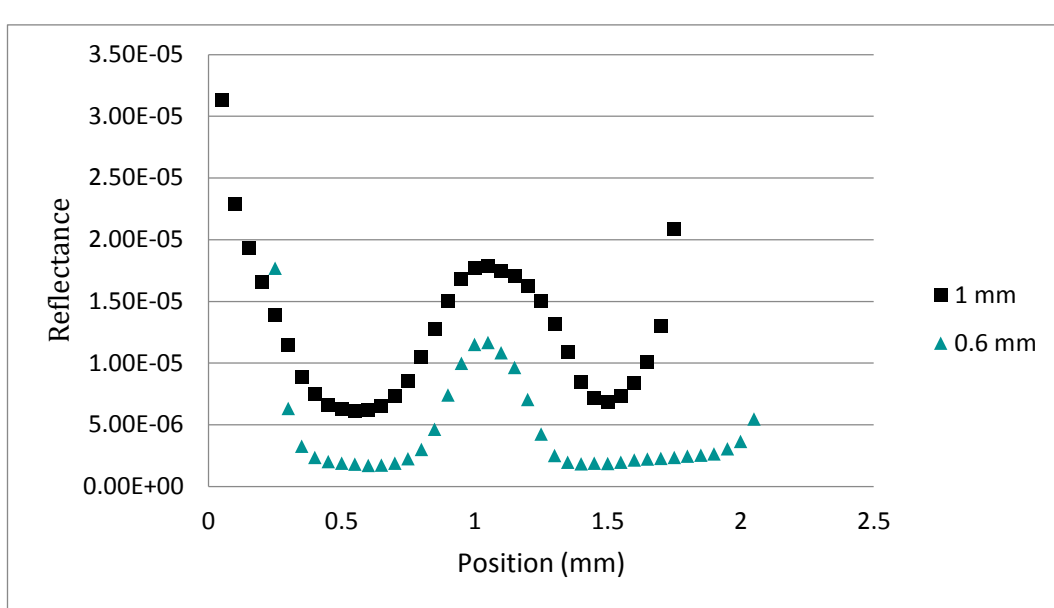


Figure 3-9: Pattern of intensity (expressed as reflectance) obtained when translating the photodiode. The two curves are obtained from the same sample at same angle ( $60^\circ$ ) and polarisation (S) but with one or the other layout and slit. The offset in the background is noticeable while the relative height of the peaks looks the same.

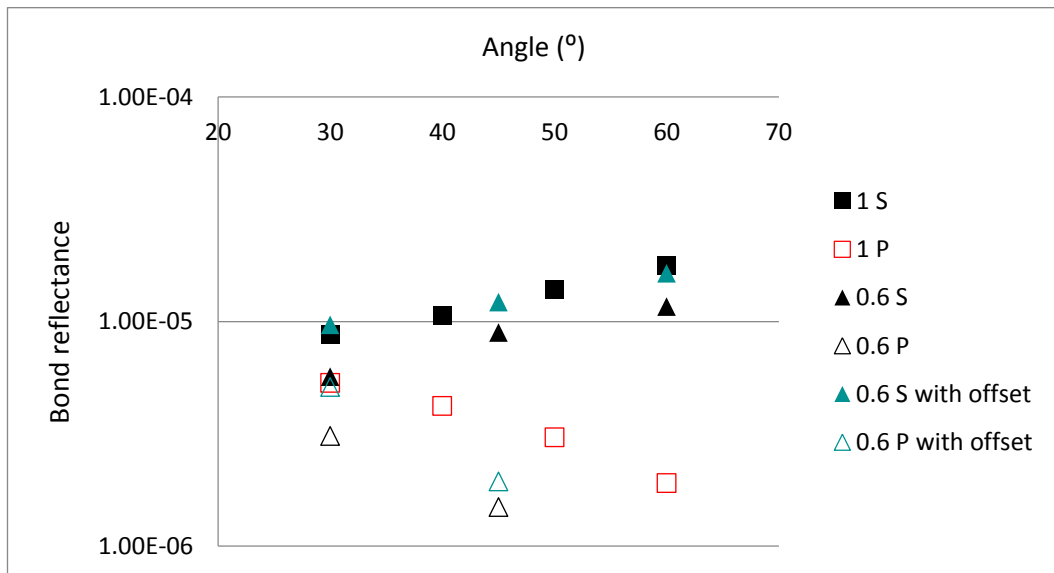


Figure 3-10: Reflectivity curves for both setup with the background correction added. The light triangle points match well the dark square ones apart from the 45P measurement which could result from effects at low intensity.

It can be seen that the correction technique works well for all the measurements taken with S-polarisation and for the 30P point as well as the light triangle curves fit much better the square ones than the dark triangle. However, it does not improve the match from the 45P point. The hypothesis is that the correction only works when the peaks are close to each

other (low angle of incidence) or when the surface reflection is strong (S-polarisation). This could be due to the fact that in these cases the tails of the side peaks significantly increase the parasitic light around the central peak and therefore the correction is efficient. However, as the peaks split from each other and the intensity decreases, the tails do not affect the measurement anymore and the only background noise remaining is collected from the room. In that case the correction does not bring a significant improvement in matching the two sets of data. As the method worked for all the other points, it was decided that the setup with the new slit was suitable to obtain reliable measurements. The odd one could be accounted for effects that appear below threshold signal intensity.

It must be noted that the samples that will be tested with this new slit are expected to have significantly larger signal from the bond than the one studied here. Therefore, the effects due to low intensity should not be relevant. Due to high surface reflection, the parasitic light from the tails should be accounted for and it was showed in this trial how efficient the reduction of the slit width was for that purpose.

### 3.2.1.5 *Detector characterisation*

As the detector layout was changed (new slit), a series of calibration measurements was taken to guarantee the right interpretation of the raw data. The linearity of the detector was checked for every configuration of polarisation and photodiode response (10 V/mA or 100 V/mA). The reference detector was also checked again at the same time. Three optical density filters were available with values of 0.3, 0.5 and 1. By combining them in different ways, eight values of power can be reached (including no density). The attenuation is linked to the optical density by the relation

$$\frac{P}{P_0} = 10^{-OD} \quad (3.9)$$

Where  $P_0$  is the incident power,  $OD$  the value of the optical density added and  $P$  the power after attenuation. The detector response is linear if the resulting curve of power measured versus attenuation is a linear function. The acquisition was made using the lock-in at a sensitivity of 1V. The lock-in amplifier saturates at 10 V and some measured powers were over or under the limits that can be measured and therefore had to be discarded. A sample of the resulting curves is displayed in Figure 3-11. The attenuation factor is the quantity defined as  $10^{-OD}$ .

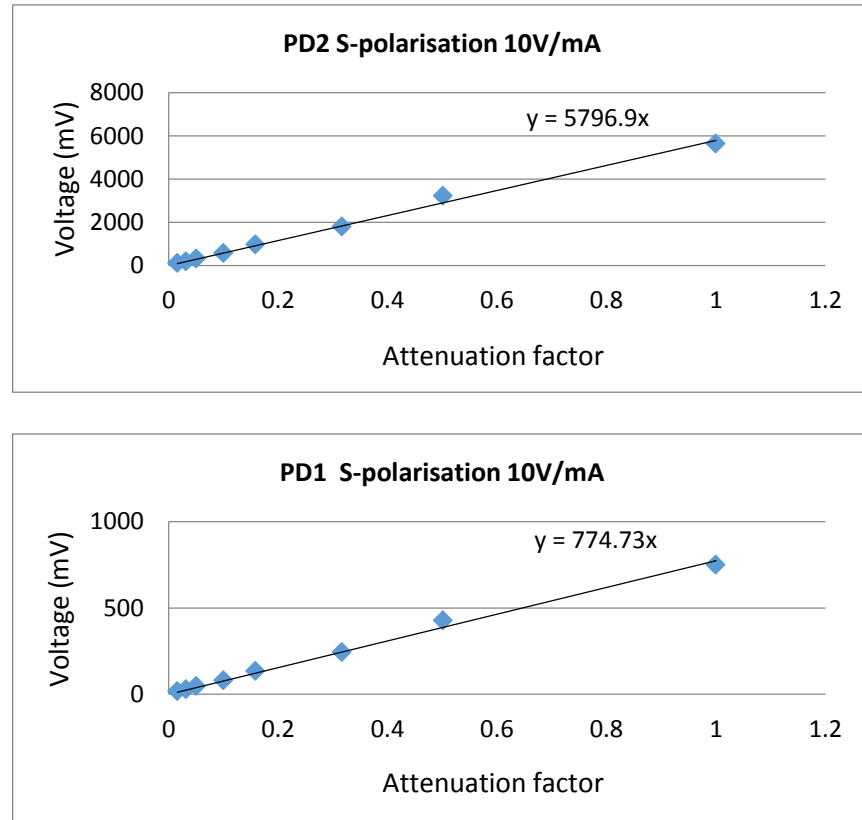
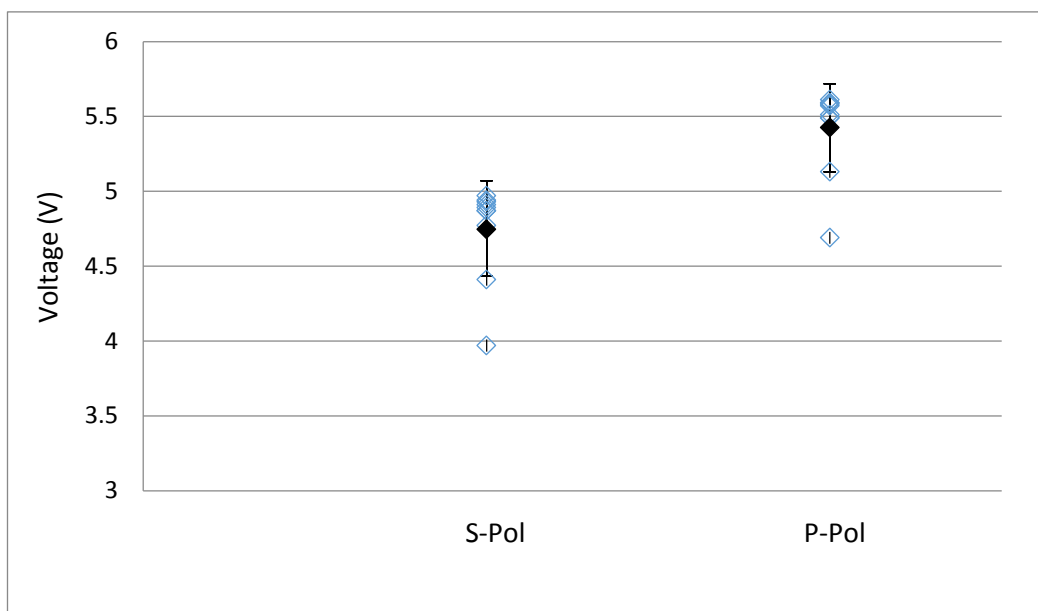


Figure 3-11: Sample curves from the trials of the linearity of the detectors PD2 (top) and PD1 (bottom). There is no significant non-linear behaviour for the sensitivities displayed and neither for any of the other ones.

It can be seen that there are no significant non-linearities that occur from the detector modification. This is expected as the photodiode remains the same and only the aperture was changed.

The last test carried out was made to estimate repeatability while carrying out a measurement with the new detector. When taking a measurement, the detector must be placed so that the beam hits its centre with normal incidence to avoid clipping on the edge of the slit. When this is done properly the intensity recorded is maximal but if the height or tilt is not accurate the recorded intensity will be lower than the actual value which contributes to the overall error of the measurement.

To estimate that error, the same measurement was taken ten times for each polarisation. For each time the detector was placed at normal incidence in a way that would maximise the intensity according to the experimenter. The intensity recorded was written down afterwards. The results are displayed in Figure 3-12.



*Figure 3-12: Determination of the error coming from the positioning of the detector (normal incidence). The same measurement was taken 10 times for each polarisation and the error is taken equal to the standard deviation of the set. The full point represents the average value and the standard deviations are showed as error bars.*

The results presented in Figure 3-12 show that if the experimenter tries to place the detector in the correct position ten times in a row, two out of these may lie out of the rest of the set. This will be accounted for by an “experimenter error” and will be considered in the error calculation as discussed in section 3.2.1.6.

The trial gave an average value of the recorded voltage of

$$V_S = 4.75 \pm 0.23 \text{ V} \text{ for the S polarisation}$$

$$V_P = 5.43 \pm 0.29 \text{ V} \text{ for the P polarisation}$$

As it is expected that the variation depends on the maximal input available, it is more relevant to express it as a percentage of the measurement. Therefore, the positioning of the detector induced an error of

$$\varepsilon_S = \frac{0.23}{4.75} = 4.9 \% \text{ for any measurement taken with a S polarisation}$$

$$\varepsilon_P = \frac{0.29}{5.43} = 5.4 \% \text{ for any measurement taken with a P polarisation}$$

It can be noted that these errors are close to 5 %, which was the value taken as first approximation in chapter 2.

### 3.2.1.6 *Modification of errors values*

Due to a few parameters having been changed since the first trial, the errors on the measurement were re-estimated. Table 3.2 shows the new values as well as a reminder of how they were measured. It must be noted that the error for the k factor is taken as standard error of the set instead of standard deviation. This is because the value for k was taken as the average of all the values measured across the trial instead of the individual values. Therefore the relevant error is the error made on estimating the mean which is given by the standard error.

*Table 3.2: Updated method and error values for the new campaign of measurements*

Error	Method	Relative value
Experimenter error $\delta(V_{\text{output}} * s)$	Take 10 times a measurement and take the standard deviation	4.9 % for S-polarisation 5.4 % for P-polarisation
Power fluctuation $\delta(V_{\text{input}})$	Maximal power drift recorded in the course of a 40 min measurement	2.8 % for S-polarisation 5.4 % for P-polarisation
Calibration factor between detectors ( $\delta k$ )	Take the standard error of the set of measured values for k across all measurements	3.8 % for S-polarisation 1.4 % for P-polarisation
Total error ( $\delta R$ )	Sum of contributions	6.9 % for S-polarisation 6.0 % for P-polarisation

### 3.2.2 Trials

With the setup validated and all the calibrating factors that allow the data analysis estimated, measurements on the samples bonded in section 3.1 could be carried out. As explained before, the objective was to get an insight into the influence of the bonding solution on the reflectivity of the bond but also to monitor the change of reflectivity with time with a focus on the early stage. The samples were tested at 3, 10, 16, 28 and 75 days. Due to the tight schedule and the importance of following it to make relevant comparison, each measurement could only be taken once. Some of them were erroneous or incomplete due to experimental issues but could not be made up for. This will be dealt with in a further section.

The modus operandi was described in section 2.3.1.3. When measurements were made on successive days, the laser was left on overnight ensuring it was at operating temperature.

The input power was still regularly measured but this allowed more stable beam power over the measurement.

### 3.2.2.1 Improvement from the new layout and sample geometry

The purpose of changing the layout and sample thickness was to better separate the three beams and reduce the background noise on the bond peak. An example of a measurement taken in the course of this trial is displayed in Figure 3-13 alongside a measurement taken with the layout and sample of chapter 2 at the same angle and polarisation. Due to the different curing time, it is not relevant to compare the calculated reflectance. Therefore, only the raw intensity profile is displayed in order to highlight the differences in the pattern. Both measurements are taken at 60° incidence and with the S-polarised beam.

Figure 3-13 highlights how much the modifications of sample and geometry improved the quality of the measurement. Increasing the sample thickness allowed a neat separation of the three peaks and reduced overlapping of the signals. The reduction in width of the central peak width due to the reduction of the beam size can also be noticed even if the signals from the surfaces partially hide it. Although this reduction contributed to the separation of the peaks, it was probably not the main factor here.

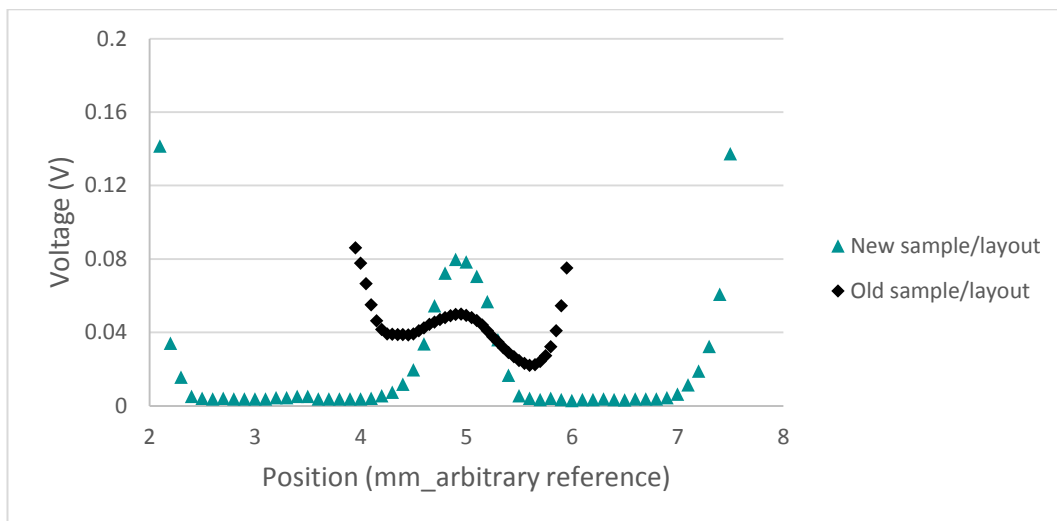


Figure 3-13: Demonstration of the improvement brought about by the modification of the setup and sample geometry between the original and upgraded setup. The two measurements are taken at same angle of incidence and the better separation of the three peaks appears clearly.

### 3.2.2.2 New sources of errors and how to get around them

In the course of the trials, it became apparent that the change in the sample geometry came with new sources of experimental error. As the trials were time-dependent and therefore had to be made at a precise time for them to be usable, it was not possible to interrupt the test campaign to fix these errors but instead a solution to work around them was found. This

allowed for using most of the data instead of fixing the error and starting a new set of tests which would have led to the loss of all the earlier measurements.

The first issue identified was that in the course of a single measurement, the height of the reflected beam changed significantly when rotating the sample. This was noticed during the measurement as an unexpected loss of signal was recorded for some of the samples and was confirmed outside of the measurement by measuring an actual height shift of about 4 mm between the low boundary ( $25^\circ$ ) and high boundary ( $60^\circ$ ) angles. As the photodiode diameter was only 2.5 mm it meant that the beam was not aligned with the PD as the sample was rotated. This led to noticeable loss of signal and erroneous measurements. Figure 3-14 displays the first measurement taken on SB10 (3 Days curing) which shows this feature well.

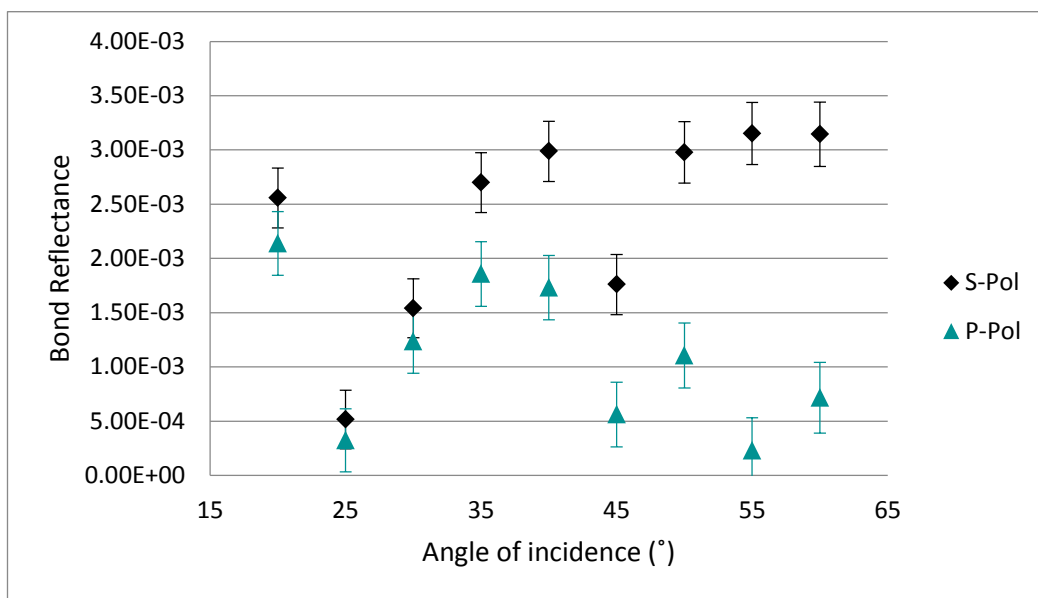


Figure 3-14: Angle dependent reflectance measured for SB10 at 3 days of curing. The scattered pattern shows issues with the setup that were not foreseen during the test phase.

In this measurement, the loss of signal was noticed after the first few measurements. In fact, the signal falls from  $3.0 \times 10^{-3}$  to  $1.8 \times 10^{-3}$  between 50S and 45S (the measurements are taken from high angles to low angles) in a range of angles where it is expected to remain more or less constant. In order to “hotfix” this issue, the photodiode was repositioned for the following measurements at  $40^\circ$  and  $35^\circ$  and a loss of signal was witnessed again between  $35^\circ$  and  $30^\circ$  and then between  $30^\circ$  and  $25^\circ$ . The photodiode was then repositioned again for the final measurement at  $20^\circ$ .

It was later found out that this effect came from a problem with the fixation of the crib on the rotation stage that led to the tilt changing with the angle of rotation. It meant that the height of the beam changed with its path in the sample which is angle dependent. This was not corrected throughout the trial but as repositioning the photodiode seemed to make up for

the issue, it was decided that an additional step of realigning it for each angle would be added. The second measurement (at 10 days curing) on the same sample was made in this way and is displayed on Figure 3-15.

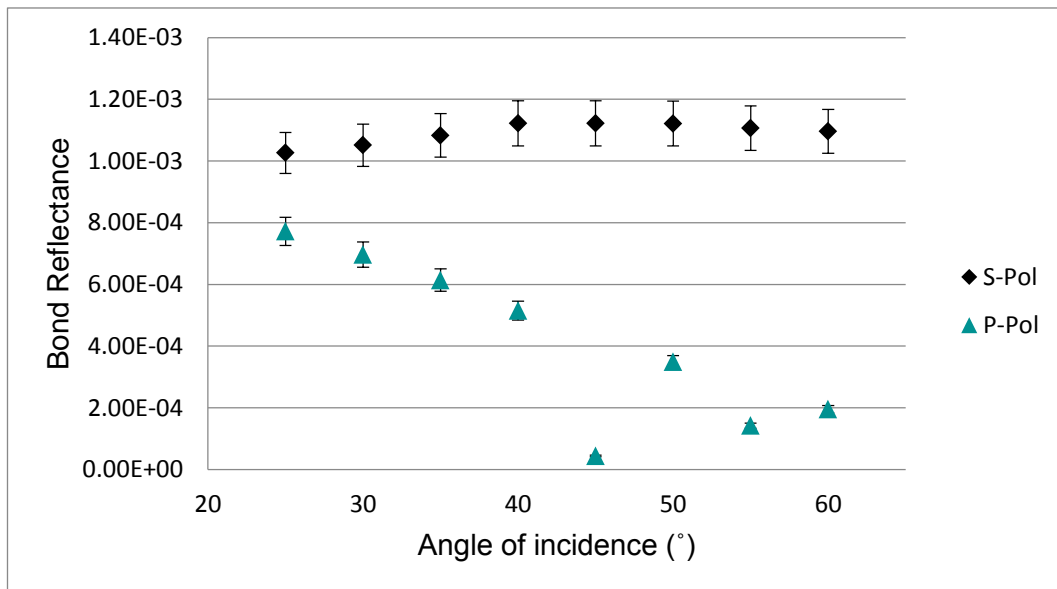
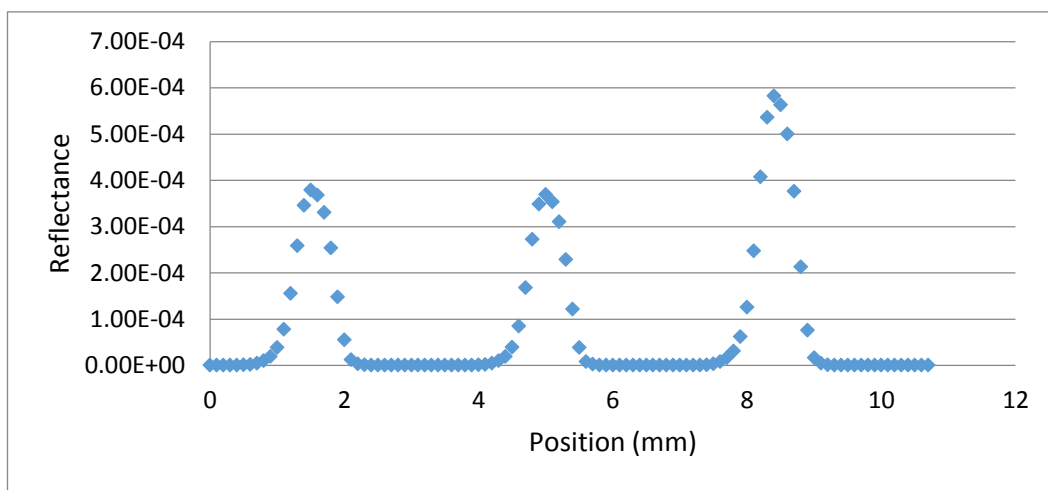


Figure 3-15: Angle dependent reflectance measured for SB10 at 10 days curing. The improved smoothness of the curves compared to the ones on Figure 3-14 shows that the correction technique is effective.

It can be seen that the curves obtained are much smoother which suggested that repositioning the photodiode worked well to cancel the aforementioned effect. The erroneous point for 45P was accounted for an error during the measuring process. This additional step made the measurement more cumbersome but was necessary to obtain exploitable data from the samples available. It also increased the risk of error due to the operator positioning the photodiode which was estimated in section 2.2.1.5. However, thanks to the large number of measurements, erroneous points could often be pinpointed and taken out to allow a correct analysis going forward.

A second source of error was found during the analysis of the data. Contrary to the samples presented in chapter 2 which were at an advanced stage of curing, in the case of the samples used in this trial the bond peak was non-negligible with regards to the surface peaks. This meant that it was possible to take the full profile of the intensity pattern without saturating the amplifier and still have a visible peak. This was done for the 60P measurement of each sample where the three peaks are of similar size. An example of measurement taken this way is displayed in Figure 3-16.



*Figure 3-16: Whole reflectance profile obtained when translating the photodiode for SB10 at 60P, 3 days of curing. The two peaks from the surfaces together with the one from the bond appear clearly. The measurement is taken from the back spot to the front spot, hence the relative intensity of the first and third peaks.*

When putting together these measurements for the same sample at different curing time, it appeared that the intensity of the peak from the front surface (peak on the right) was changing in an unexplained manner as can be seen on Figure 3-17.

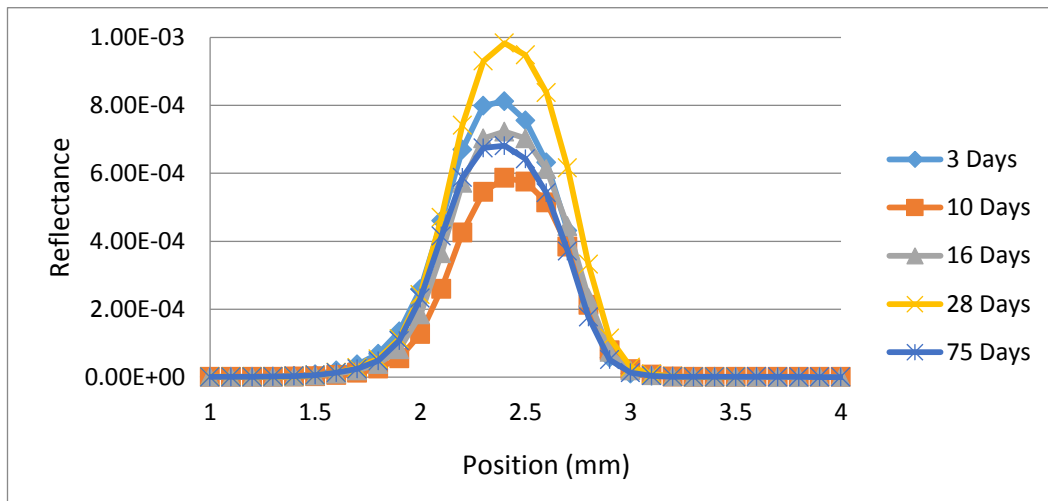


*Figure 3-17: Variation of the front surface peak for SB3 60P depending on the trial. The change in intensity is accounted for an experimental factor rather than actual physical change.*

It can be seen that the intensity of the peak changes with time without following a trend as it decreases between the 3-Day and 10-Day measurements before increasing for the 16-Day and again for the 28-Day measurement. The hypothesis that the surface condition of the sample changed with time which would have affected its reflectivity is discarded given that the sample was cleaned prior to each trial. Any alteration that would have survived cleaning

could theoretically have affected the reflectivity but a more defined pattern would likely be noticeable. Therefore, the hypothesis is made that the front surface reflectivity should not have changed with time and the change witnessed here resulted from an experimental factor. To account for this error, it was decided to apply a multiplying factor to the curves obtained in order to scale them so that the front peak reflectance was the same for each curing time. It was believed that it would make the comparison of the bond peak signals more relevant. This factor was determined from the 60P measurement for each sample and was applied to both S and P measurements as it was not possible to obtain it for an S measurement. This was due to the surface peaks being much brighter with an S-polarisation as there is no extinction and therefore the dynamic range required to get both the surface and bond peaks was too large. The hypothesis was made that any factor that would lead to a loss of intensity for the P measurement would transfer the same way to the S measurement. The reference measurement for each of the three samples is the one that gave the highest intensity for the front surface peak as the alignment should be optimised to get the most signal possible.

### 3.2.2.3 *Experimental Results*

With these corrections being applied, the results on the reflectivity trials on SB3, SB6 and SB10 are presented in the summarising Figure 3-18, Figure 3-19 and Figure 3-20. A few points are hidden in order for the trends to stand out. They are randomly spread and likely result from an erroneous measurement which could not be taken again due to the time-sensitive data. An example is the 45P point on Figure 3-15 that is not shown in Figure 3-20. In the discussion of the curves, the representative value for a set of measurements will be the maximum of the measured reflectance with regards to the angle (which will be most of the time at 60° for S-polarisation and 25° for P-polarisation).

It can be seen that for SB3 the reflectivity decreases alike for S and P polarisations with increasing curing time as it goes from  $6.0 * 10^{-3}$  to  $1.7 * 10^{-3}$  (S-Pol) and from  $2.8 * 10^{-3}$  to  $0.98 * 10^{-3}$  in the course of the 75 days. It seems that a steady state is reached between 16 and 28 Days as the measurements taken at 28 and 75 days are similar in values.

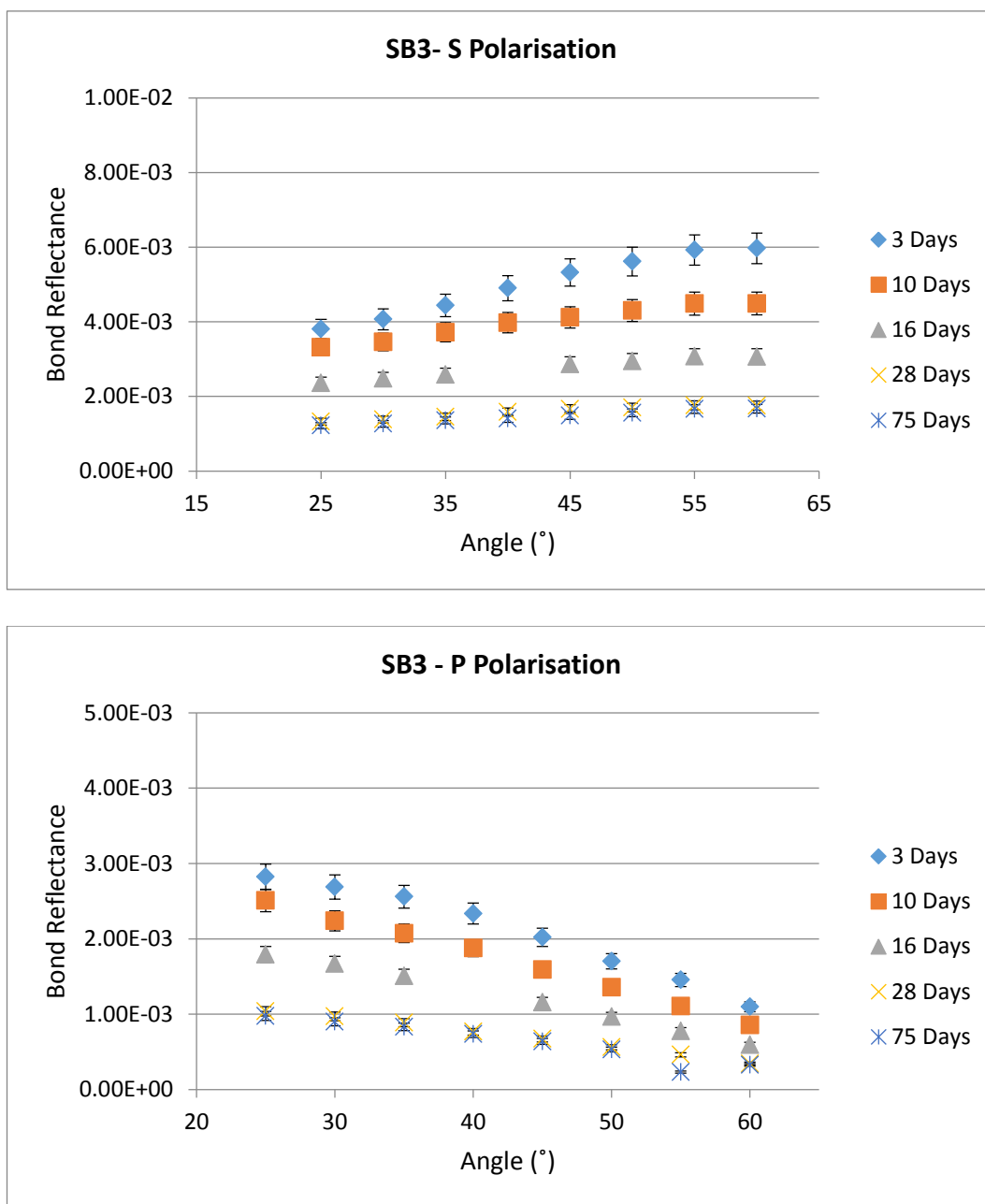


Figure 3-18: Reflectance dependent measurement for SB3 at different curing times with S (top) and P (bottom) polarised beam.

The curves for SB6 follow approximately the same trend with the reflectance decreasing from  $7.8 \times 10^{-3}$  to  $1.1 \times 10^{-3}$  (S-pol) and  $4.0 \times 10^{-3}$  to  $0.42 \times 10^{-3}$  (P-pol). The 10-Day measurement was discarded for this sample as the whole profile had not been taken in this case. It is thought that not being able to apply a proper scaling factor for this measurement prevents it from being usable (see section 3.2.2.2). This time the data at 28 and 75 days still display a significant difference and therefore it is not possible to suggest that the steady state has been reached.

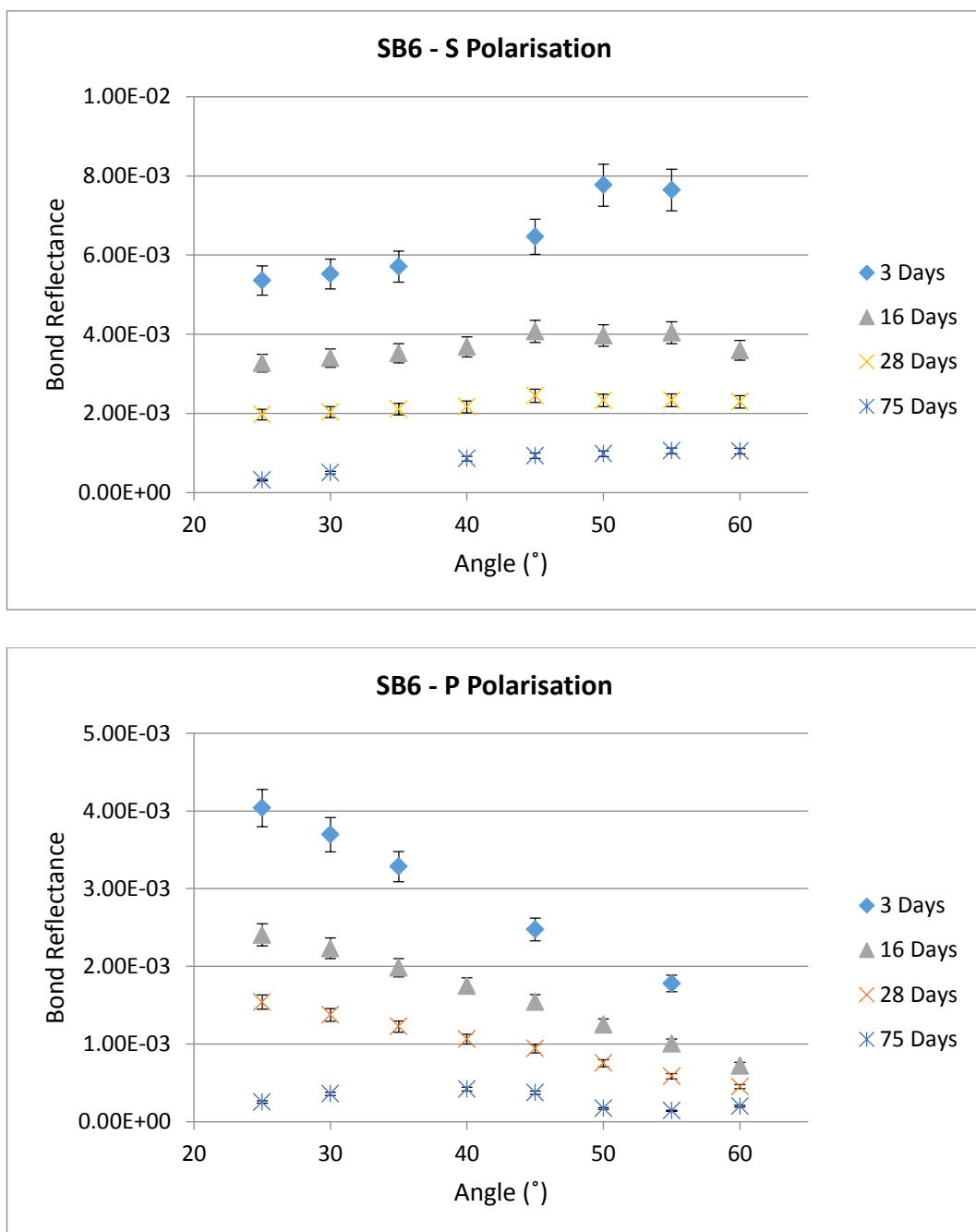


Figure 3-19: Reflectance dependent measurement for SB6 at different curing times with S (top) and P (bottom) polarised beam.

Finally, SB10 shows the same behaviour with the reflectance decreasing from  $3.5 * 10^{-3}$  to  $5.2 * 10^{-4}$  (S-pol) and  $1.7 * 10^{-3}$  to  $1.67 * 10^{-4}$  (P-pol). The 10-Day and 16-Day measurements are oddly similar but the next measurements at 28 and then 75 days show that the trend keeps changing and the steady state cannot be pronounced.

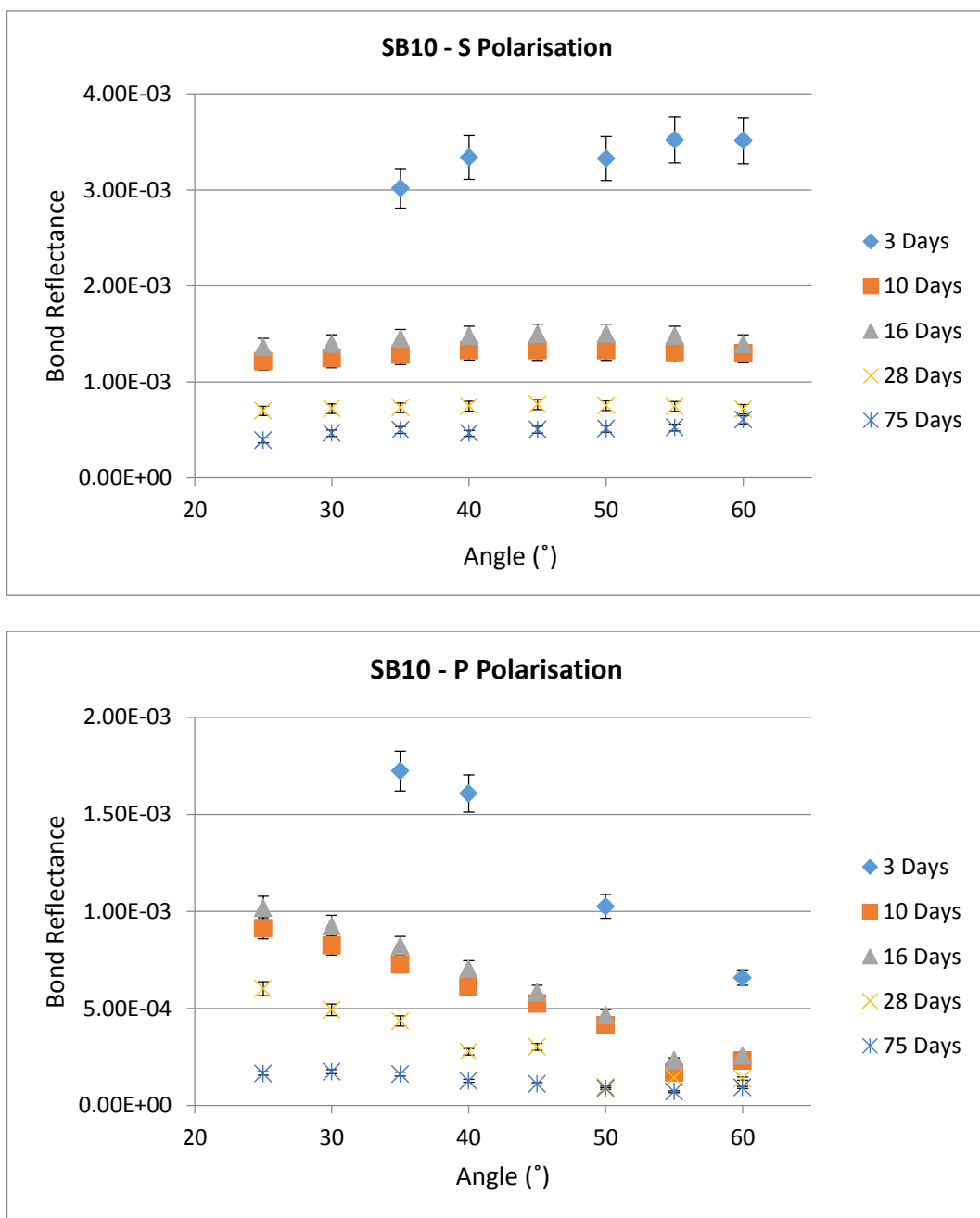
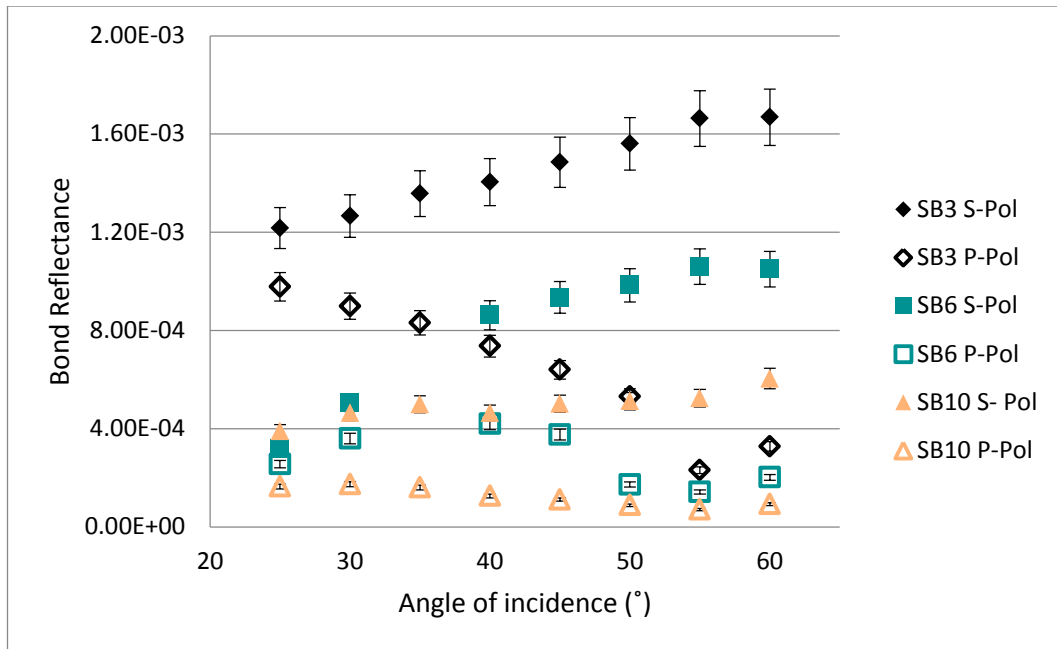


Figure 3-20: Reflectance dependent measurement for SB10 at different curing times with S (top) and P (bottom) polarised beam.

A new presentation of the curves in Figure 3-21 highlights how the concentration of solution affects the reflectivity at an equivalent curing time (75 days).



*Figure 3-21: Influence of the concentration of the solution on the reflectance of the interface at 75 days curing for both polarisations.*

According to the curves displayed, there seem to be an actual effect of the concentration of solution on the reflectivity of the bond at 75 days of curing. The curve obtained for SB6 and SB10 lies at about 60 % and 30 % of the curve obtained for SB3, respectively (the reference point for this estimation is the point at 50S) and the shapes of the curve also change with the concentration. It is expected that these gaps come from the parameters of the bond layer and as for the samples tested in chapter 2, the reflectivity trials could be used to estimate the refractive index and thickness of the bond

#### 3.2.2.4 Data analysis

The change of bond parameters with time could be obtained from the reflectance data through the Matlab script (see section 2.3.3) and the resulting curves are displayed in Figure 3-22.

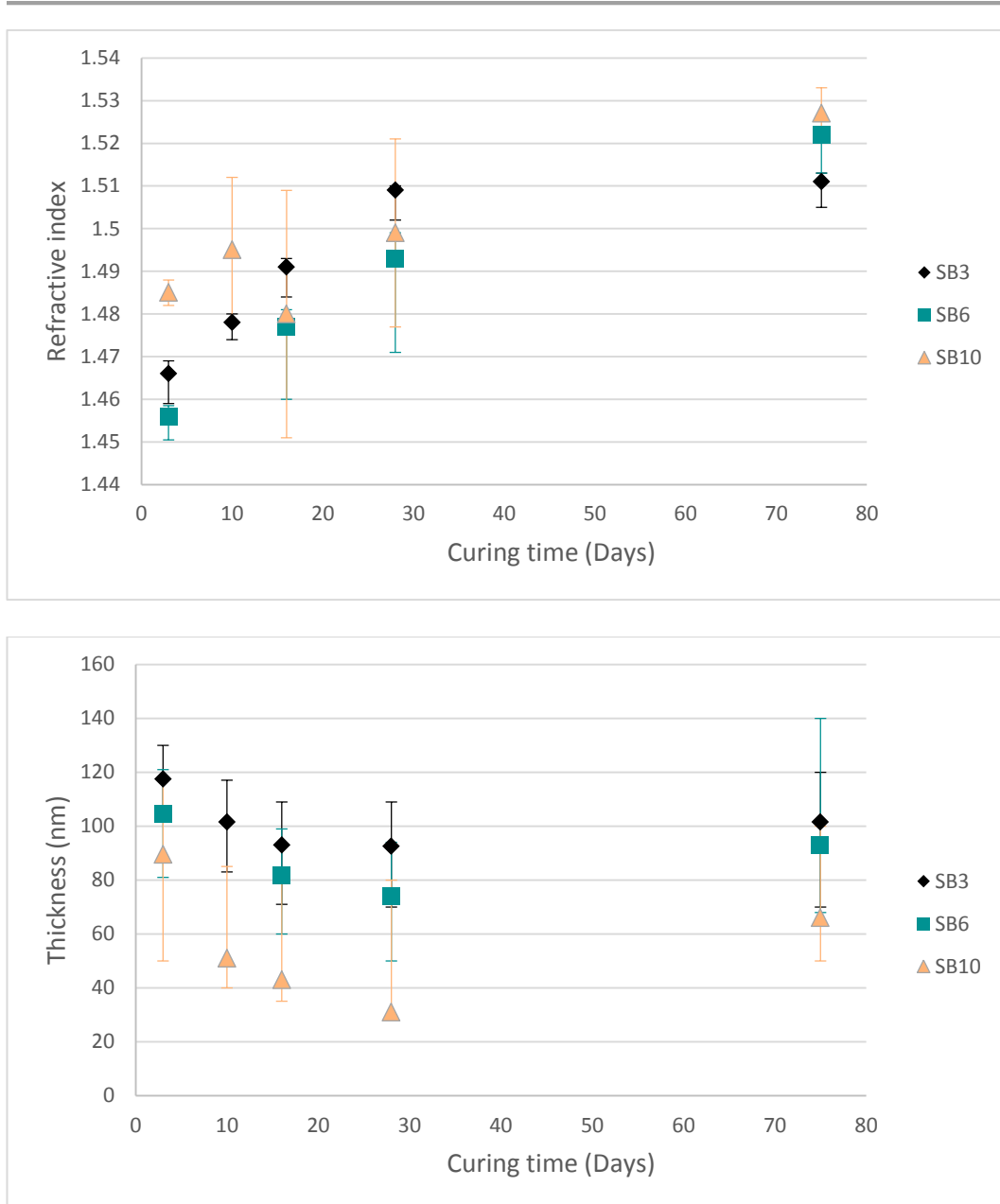


Figure 3-22: Variation of refractive index (top) and thickness (bottom) of the bond for all three samples. The parameters are inferred from the optical model described in section 1.4.1 using Bayesian analysis (see Appendix C)

It can be seen that the three samples display similar trends for the refractive index and thickness change with time. The refractive index clearly increases upon curing at what looks like a linear rate until 28 days for SB3 and SB6. The further point at 75 days shows that SB3 seemingly reached a steady state whereas the refractive index for SB6 kept increasing, although at a slower rate. This difference was already mentioned following the reflectance curves in section 3.2.2.3. SB10 shows a less clear development which could be accounted for by some inhomogeneity in the bond that makes the automated parameters inference less

accurate. In particular the point at 16 days seems clearly out of the trend and as such will not be taken into account in the discussion. For the other points, a similar increase as for the case of the two other samples is noticeable in the course of the first 28 days but the rate seems to already be slowing down at that point. However the point at 75 days invalidates the hypothesis of an earlier steady state as it lies noticeably above the previous one.

With regards to the values taken, the refractive indices for all three bonds are already above the refractive index of the solution at 3 days with them being estimated at  $1.465^{+0.004}_{-0.006}$ ,  $1.455^{+0.003}_{-0.006}$  and  $1.485^{+0.003}_{-0.003}$  for SB3, SB6 and SB10, respectively. It is not obvious that the refractive indices can be ranked as the curves are close to each other and even intersect but it seems that the least concentrated solutions lead to higher refractive index once in an advanced stage of curing. In fact, the last measured values are  $1.511^{+0.003}_{-0.005}$ ,  $1.522^{+0.001}_{-0.009}$  and  $1.527^{+0.006}_{-0.006}$  for SB3, SB6 and SB10, respectively. It is interesting to note that these values all land again between the refractive index of silica (around 1.45) and the one of the bulk material (measured at 1.564). This suggests that the bond layer is formed by a mixed network of silica and elements from the bulk as it was already speculated in section 2.4.2. These values are higher than the one presented in chapter 2 but this could be due to the hypothesis of the refractive indices of the two compositions being the same being wrong.

The results on the thickness are easier to read as they are homogeneous across all three samples. From 3 days to 28 days, the thickness decreases at a slowing rate from  $117^{+13}_{-13}$  nm to  $92^{+19}_{-32}$  nm for SB3,  $104^{+17}_{-24}$  nm to  $74^{+47}_{-25}$  nm for SB6 and  $89^{+28}_{-40}$  nm to  $31^{+34}_{-16}$  nm for SB10. Therefore the relative loss of volume from the bond in this period amounts to 22 %, 29 % and 65 % for SB3, SB6 and SB10, respectively. The higher loss for more diluted solutions is consistent with the higher volume of water initially contained that leaves the bond upon dehydration. It appears clear from the data that the thickness of the bond decreases with the concentration of the solution in sodium silicate and also faster for the more diluted solutions.

The point at 75 days is more surprising as it looks like after a consistent decrease towards a steady state the bond springs back and the thickness ends up at a higher value. The increase amounts to 9 %, 20 % and 53 % for SB3, SB6, SB10, respectively and therefore is lower than the initial loss in volume in the first regime. The ranking between the thicknesses of the three bonds is also maintained. A first hypothesis can be made that the bonded parts got slightly pulled apart in the course of sawing and polishing that happened between the measurements at 28 and 75 days to allow the LIDT tests. Another hypothesis, less bound to experimental factors, would be that the network shrinks to a minimal thickness as the excess water leaves the bond. At that stage the water molecules that remains in the bond bridges and pull together the chains. When these molecules in turn leave the bond, the network become less bound and the chains relax slightly. This hypothesis is consistent with the

relative expansion of the three layers as it makes sense that the denser the layer, the more constrained it remains by solid chains and the less it can spring back.

In the end, the trial allowed a good insight in how the properties of the bond layer can be made flexible by acting on the bond solution and potential outlook on how to bring the reflectivity of silicate bonds down to requirements for photonics applications.

### 3.3 Light induced Damage Threshold

In this section the LIDT of the new samples are measured in order to reinforce the hypotheses made in chapter 2 and see if the concentration of solution could also affect this property of the bond. The LIDT of the three samples at 1535 nm was estimated in the same way as it was done in chapter 2.

The samples used for the reflectivity measurements were cut in two after 40 days of curing, a few millimetres apart from the centre in order to preserve the area of interest for additional reflectivity trials. It yielded samples with a surface of about 10 x 12 mm for the LIDT tests. The tests were done 46 days after bonding. The experimental curve obtained for the three samples are given in Figure 3-23. It can be seen that due to a much smaller area than for the previous tests, the step in power from a row to the next had to be increased and the fidelity of the result is diminished. In fact, only two or three points could be taken above the first noticed damage which prevents an accurate linear regression (see section 1.4.2). The estimated LIDT is therefore taken equal to the average between the last power with no damage and the first power with damage. The values obtained are  $1.87 \pm 0.05 \text{ GW/cm}^2$ ,  $1.68 \pm 0.05 \text{ GW/cm}^2$  and  $1.91 \pm 0.05 \text{ GW/cm}^2$  for SB3, SB6 and SB10, respectively. The uncertainty comes from the incremental step used for the power. These values are summarized in Figure 3-24, together with the ones obtained in chapter 2.

Comparing these values together and with the ones obtained in chapter 2, there seem to be no clear trend that would link the concentration to a lower or higher LIDT and all the values are between 1.6 and 1.9  $\text{GW/cm}^2$ . It also seems to confirm the fact that the low LIDT that was witnessed in the case of SB in chapter 2 (which equates to a SB6 sample owing to the solution preparation) was not representative of the average value for silicate bonds. The value of  $2 \text{ GW/cm}^2$ , which was hinted as the actual LIDT in section 2.4.2, is more in line with the ones observed in this chapter and is added as a hollow point in Figure 3-24. As a result, the value obtained in this study show that the bond will be suitable for many photonics applications.

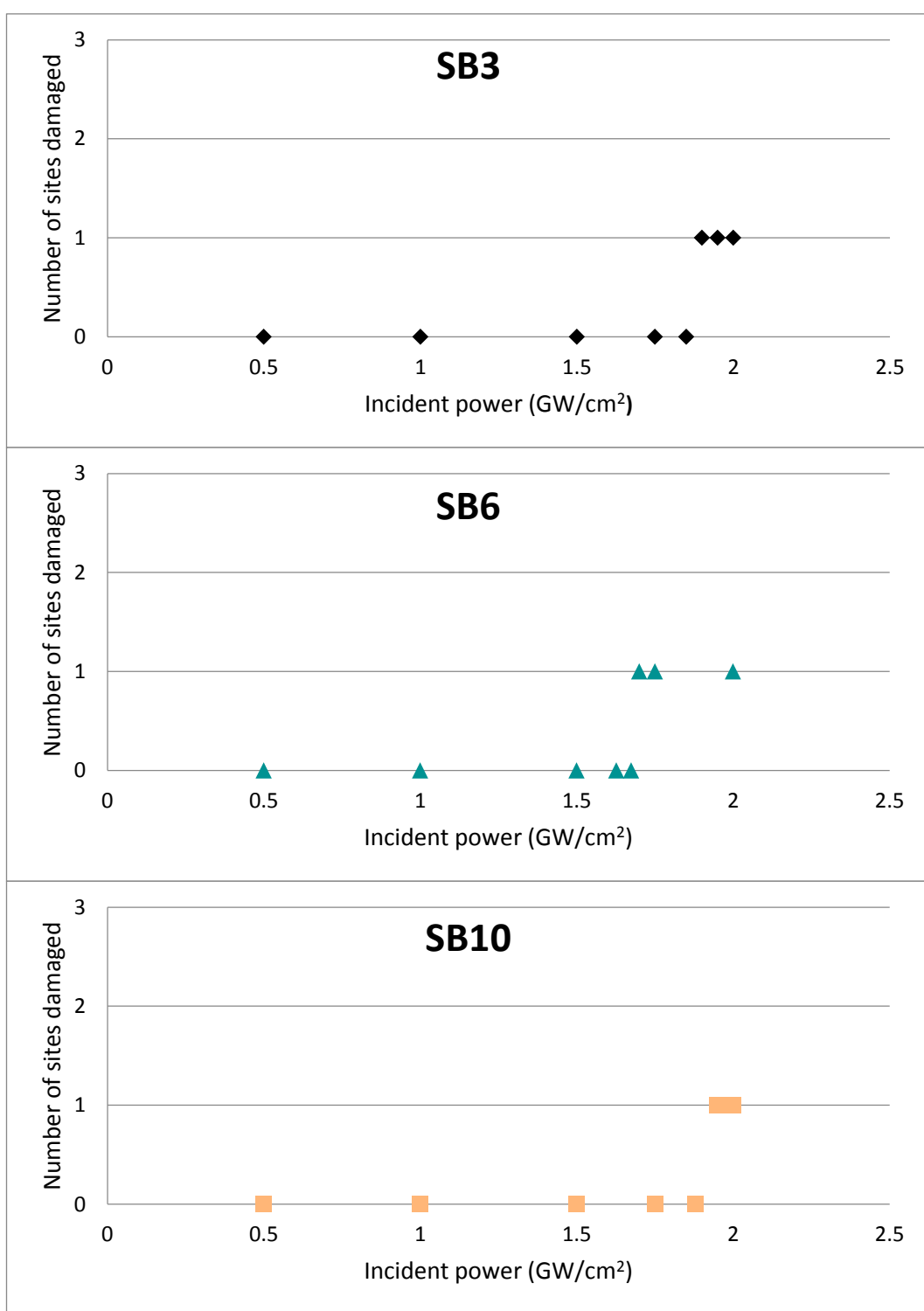
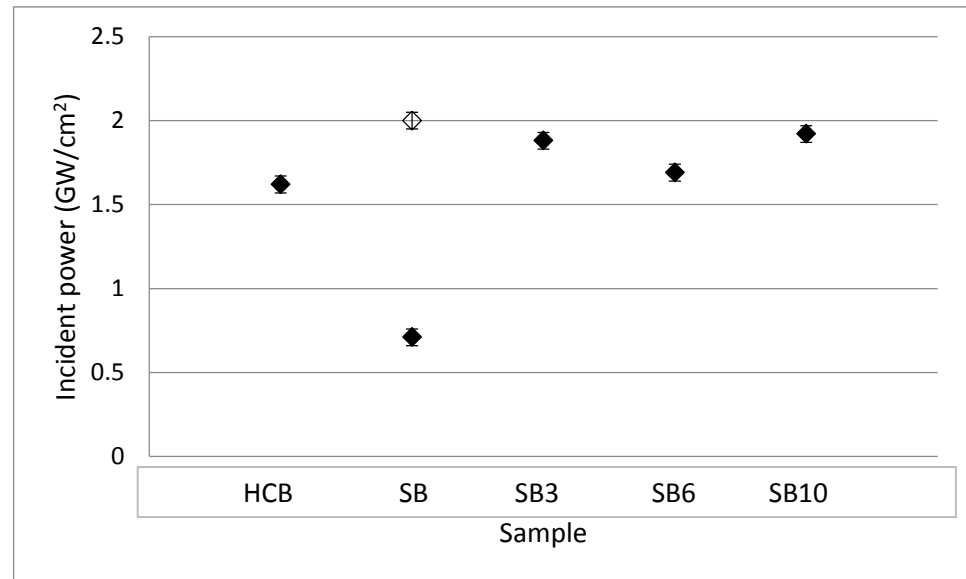


Figure 3-23: Experimental curves from the LIDT tests carried at Belford Research for the samples SB3 (Top), SB6 (middle) and SB10 (Bottom). The tests were done at 20Hz, 20ns, 1535 nm.



*Figure 3-24: Summary of the values obtained for the least incident power leading to damage for all samples tested in chapters 2 and 3. The hollow point comes from the uncertainty in the measurement presented in section 2.4.1.*

### 3.4 Summary and discussion

In this chapter, the preliminary phosphate glass trials presented in chapter 2 were extended to obtain further knowledge on the bonding process, in particular how the concentration of solution affected the optical properties tested. This section summarizes the results obtained and when applicable, compares them with similar studies from the literature.

The first part was about increasing the quality of the reflectivity measurements as limitations of the setup appeared during the trials made in chapter 2. This went through a complete characterisation of the beam profile along the optical bench to highlight that the theoretical parameters from which the layout was built were not achieved and therefore that there was room for improvement. However due to a lack of time and the necessity to keep the changes easily reversible, only minor tweaks could be brought to the layout. A theoretical and empirical study was conducted to optimise the setup with a number of constraints with regards to the components to use and their positioning. The beam radius was reduced by 30 %, to 290 µm, and suggestions for further improvement were described. Combined with a change in the dimension of the sample, it led to improved quality of measurements. Further it was demonstrated that results obtained with previous iterations of the setup could be recovered during the data analysis.

With this improved setup, the dependence of reflectivity of the silicate bond between phosphate glass parts on the solution parameters and curing time was investigated. It was shown that the reflectivity of the bond could be decreased by using a more dilute solution,

with measured reflectances of about  $1.7 * 10^{-3}$ ,  $1.1 * 10^{-3}$  and  $0.52 * 10^{-3}$  for a solution diluted 4, 7 and 11 times, respectively (representative results taken from S-polarisation measurements at an advanced stage of curing). Mangano [105] carried out the same experiment on fused silica discs using solutions prepared with the same ratios. The reflectance values she obtained seemed to converge to about  $0.3 * 10^{-3}$  regardless of the concentration of the solution used (value taken at about 92 Days with S-polarisation). The rate at which this convergence occurs depended on the level of dilution of the solution, with it being faster for less diluted solutions which was also observed here. These results seem sensible when considering the mechanisms of the process described in section 1.3.5.

However, in his work on bonded fused silica, Sinha reported a decrease in reflectivity with less diluted solutions, amounting to 0.28 % for a solution diluted 8 times and 0.07 % for a solution diluted 5 times for example [106]. The gap in the orders of magnitude of the reflectivity has already been discussed in chapter 2. However, it is interesting to address the difference in the trend between the two studies. The explanation seems to again lie in the difference in refractive indices of the bonded materials. In the case of fused silica, increasing the concentration of silicate in the bond leads to a denser bond layer with a refractive index close to the bulk material, which decreases the Fresnel reflection at the interface. In the case of phosphate glass, the hypothesis is that there are two competing effects that come into play when increasing the solution concentration. On the one hand, there is a larger amount of silicate ions that will remain in the bond when it is fully cured, dragging the refractive index of the phosphate-silicate layer down. On the other hand, there are also a larger amount of hydroxide ions that are available to etch phosphorus from the surfaces and increase the amount of phosphate in the bond. The relative strength of these adverse effects is unknown but can be assessed by looking at the estimated refractive index for the layer.

In fact, the estimation of the refractive index of the bond layer from the reflectivity data seems to suggest that decreasing the initial concentration of sodium silicate will lead to higher refractive index at an advanced stage of curing. This means that of the two effects described above, bringing additional silicate to the bond (more concentrated solution) overcomes the additional etching of bulk species and drags the refractive index down. This hypothesis has to be taken with care however as the gap between the values of refractive indexes for the three samples is not large enough to confidently rank them.

The other result coming from these reflectivity trials is that the bond thickness can be decreased by using less concentrated solution. This was already observed by Elliffe [127] on fused silica through direct observation with Atomic Force Microscopy and the results presented here confirm that it is also applicable to phosphate glass. The gap of thickness between the three samples is clear and the cured bond ends up at 101 nm, 93 nm and 66 nm for SB3, SB6 and SB10, respectively. This matches well the values of 100 nm (equivalent SB4)

and 81 nm (equivalent SB6) reported by Elliffe. Although the thickness itself might be of less of interest than its consequences on other properties (strength, optical properties, etc.), it is useful to know that it can be tuned by changing the solution parameters.

Finally, changing the solution concentration seems to have little effect on the LIDT of the interface or at least there is no defined trend as the LIDT for SB6 is lower than the values for either SB3 or SB10 with the values being 1.68 GW/cm<sup>2</sup>, 1.87 GW/cm<sup>2</sup> and 1.91 GW/cm<sup>2</sup>, respectively. This contrasts with the observations from Sinha who reported that a more concentrated solution reduced the amount of micro-voids in the bond therefore increasing the LIDT. As such, he obtained a threshold of 1.25 GW/cm<sup>2</sup> for an equivalent SB7 (one part of sodium silicate in 7 parts of water) and of 1.56 GW/cm<sup>2</sup> for an equivalent SB4. The difference could be from various reasons due to the complexity of the LID mechanisms. Added to this is the low sample size for the tests presented in this work that prevents any statistical analysis. The conclusion to take from both these trials is that the estimated threshold is high enough to remove any concern with regards to the validity of the bonding technique for common photonics applications.

---

## 4 Bonding of a crystalline, non-silica-based material: Yttrium Aluminium Garnet (YAG)

---

For the reasons detailed in section 1.2.1, the solid state laser material market is shared between laser glasses and laser crystals. After the extensive study on bonded phosphate glass, the attention is now shifted towards one of the most used and known crystalline matrix: YAG. The approach is to a large extent the same as in the previous chapters. It is first assessed that the proposed process allows bonding of the parts, yields an invisible interface and that the bonded component can hold itself when handled. A first assessment of the strength is done by attempting to manufacture the sample before a more quantitative study is carried out by the mean of 4-point strength testing. In parallel, the optical properties of the interface are studied using the same techniques as before but upgraded to the new requirements.

### 4.1 Strength tests

#### 4.1.1 Initial bonding observation

In a first instance, samples were discs of Ø18 mm x 2 mm bonded using either a sodium hydroxide (0.01 N) or a sodium silicate solution (one to six parts in DI water). As was the case for phosphate glass the bonds were invisible and there was no difference between one and the other type of interface. A first attempt at sawing the samples was made. When put to the test, the HCB sample immediately debonded and shattered. This could have been due to the size of the blade relative to the sample which made the level of stress too high for it to survive. The SB samples were not tested as the risk of destroying them was too high and they were needed for initial trials. In the end the size of these samples ended up making them unsuitable for most tests and new sets with more tailored geometry were prepared. Due to the limited amount of samples available, it was decided to focus on SB samples (bonded using sodium silicate) and put tests on HCB samples (bonded using sodium hydroxide) on hold.

#### 4.1.2 Strength tests

YAG strength trials were limited to a single set as the material does not usually come in large volume. Additionally, similar works exist on sapphire and it was believed that due to similar chemistry it would be possible to transfer their results to YAG [104][137].

As the raw material came in the form of cylindrical sticks of Ø6.75 mm it was decided to keep this geometry instead of the square sticks used previously in order to minimize the manufacturing steps. The diameter of the bonded surface was taken down to 6 mm after

polishing and chamfering while the length of the parts was 20 mm, the same as in the other trials. 10 samples were bonded using the bonding process described in section 2.1. The samples were then left to cure at room temperature in a vertical position and were broken in a single set after eight weeks. This curing time was selected as it had been the one of the sapphire trials led at the University beforehand [104][137]. Due to the geometry of the samples it was not practicable to polish the outer surface to a level that allowed visual inspection. Observation through the end-faces did not allow the assessment of quality of the bond either due to the depth of the sample. Since the geometry was modified, the relation between the force applied and the stress differs from the one given in section 2.2.1 and is instead given by equation 4.1 (derived from [151]).

$$\sigma_{max} = \frac{8(L - l)F}{\pi d^3} \quad (4.1)$$

With L the width between the bottom supports (36 mm), l is the distance between the top supports (18 mm) and d the diameter (6 mm).

Results of the test are displayed in Figure 4-1.

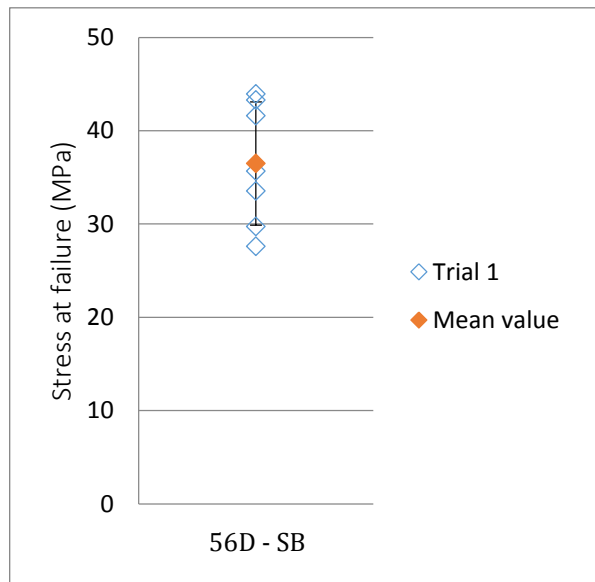


Figure 4-1: Strength test of silicate bonded YAG samples using 4-point bending method after 56 days curing at room temperature.

It can be seen that the samples show a significant strength at  $36.5 \pm 6.6$  MPa. All the samples broke along the bond and left a neat fracture pattern on the surfaces. Some showed a small chunk of material still bonded but not large enough to be characterized as a bulk failure. These occurred at the inner surface, where the material is in compression.

As explained before, YAG is close in chemistry to sapphire and therefore it is relevant to compare the existing results for those two materials. Sapphire has been investigated to a significant extent since it is a material in consideration for the next generation of gravitational waves detectors (and already being used in the Japanese KAGRA detector)[137]. Douglas [104] and Phelps [137] studied the change of strength with curing time. They report a strength of about  $29 \pm 5$  MPa and  $25 \pm 7$  MPa in two different trials held under similar conditions for sapphire bonded with sodium silicate after 8 weeks curing. These results are in a similar range as the ones presented here, although noticeably lower on average. Since the geometry of the samples used in both trials are different, an additional calibration trial was made to investigate the influence of the shape on the strength at failure as described in the next section.

#### 4.1.3 Shape factor

For this trial fused silica samples were manufactured in both square and circular base beams. The dimensions of the base were 5 x 5 mm for the square beams and Ø6 mm for the circular ones, both after chamfering. Although it yielded a ratio of the bonded area of about 1.3, it was deemed more relevant to match the dimensions used in the various trials than to try to match the bonded areas. This allowed direct comparison of the results instead of making assumptions on the effect of rescaling. The drawback was that the results would be less transferable to future trials.

Ten samples of each type were bonded using the common cleaning process and sodium silicate solution. They were left to cure for four weeks in a vertical position at room temperature before being broken.

Results on the measured stress at failure are displayed in Figure 4-2.

There is a noticeable difference in the average strength of the bonds for the different geometries. The square bonds break at a stress of  $28.2 \pm 6.6$  MPa while the circular ones do at around  $43.9 \pm 7.6$  MPa. It should also be noticed that more than half the square ones broke across the bond and left large chips of material bonded. It means that the bond itself is not the main seed of the failure in the case of square beams. This is not the case with the circular sample for which all the failures were along the bond line, with sometimes some tiny chips hung on the surface.

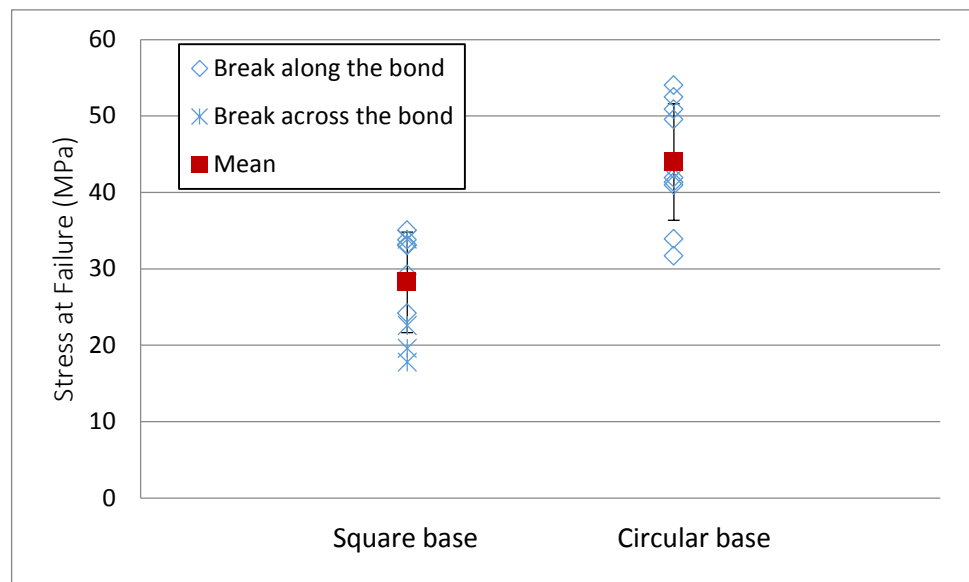


Figure 4-2: Influence of the geometry of the sample on the breaking strength of silicate bonded fused silica tested after 28 days curing. The error bars are the standard deviations of the sets

This result can be understood by considering that the likeliness of failure is proportional to the chance of having a defect in the material which increases with volume. Let us consider the curves plotted in Figure 4-3. The black and blue curves represent the beam profiles for a circular beam of radius 1 (top) and for a square beam of half-height 0.89 (bottom), respectively, when moving from the outer edge towards the neutral axis. The value for the square beam was taken to match the areas of the cross-section of the two beams. The orange curves represent the normalised stress in the beam during the flexural test: The tensile stress is maximum at the outer edge and decreases linearly towards null value at the neutral axis.

From these curves, it is possible to define a qualitative “failure risk”. The risk of failure is in a first approximation proportional to the stress applied and to the probability of presence of a weak point in the layer bearing this stress. The likeliness of having a weak point is itself proportional to the width of the beam at the distance from the outer edge considered. The failure risk can then be written qualitatively ( $\text{failure risk} \propto \text{stress} * \text{width}$ ) at a given distance from the outer edge.

This “failure risk” for both geometries is plotted in Figure 4-4. It appears clearly that the overall risk of failure (area under the curves) is higher for square based beams even for matched cross-section areas. This is due to a larger part of the volume being located where the stress is high.

In addition to this, a hypothesis is made that the presence of sharp edges in the case of square beams can be an additional source of weakness that can initiate the fracture of the part tested.

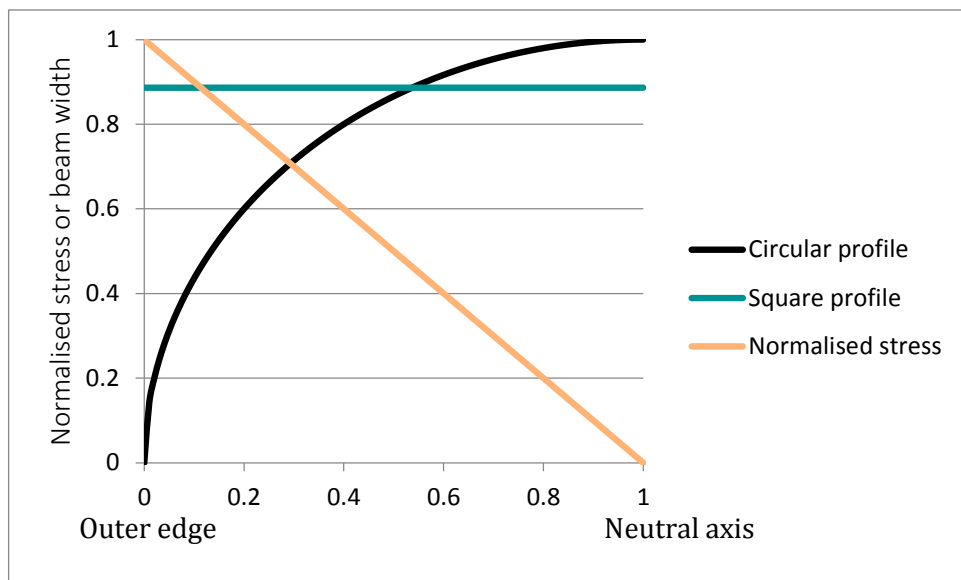


Figure 4-3: Profiles for two different geometries and normalised tensile stress in 4-point flexure test from the outer edge to the neutral axis of the beam.

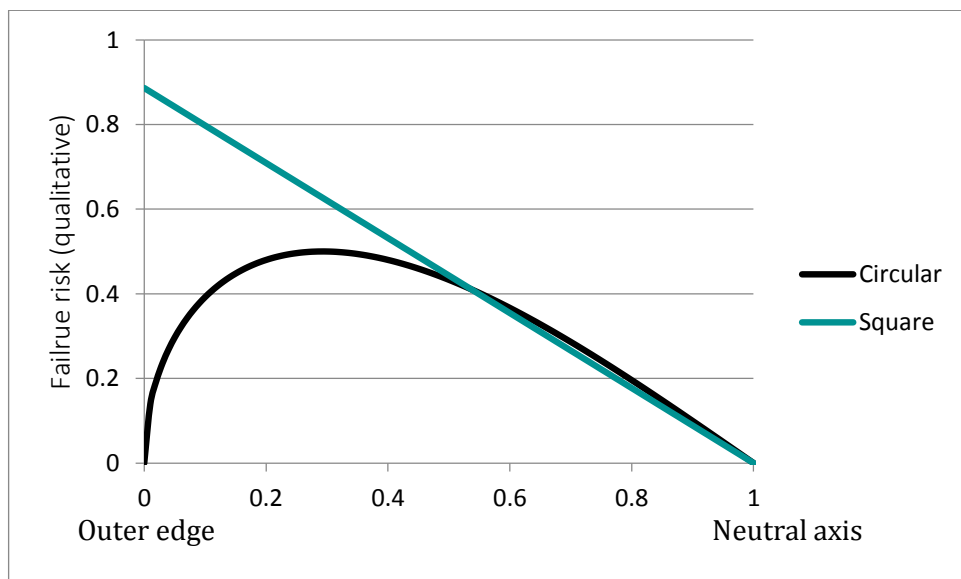


Figure 4-4: Qualitative risk of failure plotted for circular and square beams. It is clear that the risk is higher for square beams due to a larger part of the volume being located in the high tensile stress area.

The results from these trials suggest that when comparing samples of circular and square geometries, for the dimension tested, a factor of  $\frac{43.9}{28.2} = 1.5$  should be applied. Applying this factor to the YAG trials yields a strength of  $24.3 \pm 2.2$  MPa which is closer to the results

---

presented on sapphire. However, this ratio is likely to depend on the defect density in the material and at the surfaces of the sample and therefore should be treated with care. In any case, the strength of the bond is satisfactory for any application in photonics as it is not expected that samples will face such high stresses.

## 4.2 Optical reflectivity

As was the case for phosphate glass, optical reflectivity of the interface of bonded YAG is of prime interest for components that are to be put in optical cavities. Following the work in chapter 3, the setup was this time entirely rebuilt and some components modified. The sample geometry was also adapted to increase the likeliness of good measurements. Due to limited number of samples, only the reflectivity of SB YAG was tested.

### 4.2.1 Samples

Samples for this trial were Ø25.4 mm x 8 mm (Ø25.4 mm x 16 mm once bonded) discs provided by Newlight Photonics Inc. Due to the high refractive index of YAG (measured equal to 1.815 for those samples, see Appendix A), the thickness of the sample had to be increased compared to the samples used previously in order to obtain a good separation of the three beams (see Figure 1-9). The diameter was selected as the largest commercially available as it would allow measurements over a wider range of angles. Two samples were bonded using the regular bonding process with a sodium silicate solution diluted to 1:6 in volume.

### 4.2.2 Setup modifications

#### 4.2.2.1 *Change of layout*

After the issues encountered during the trial on phosphate glass, the setup endured some significant modifications which it was believed would be beneficial to the quality of measurements. The setup was also entirely rebuilt, and the components re-aligned. The new layout is displayed in Figure 4-5.

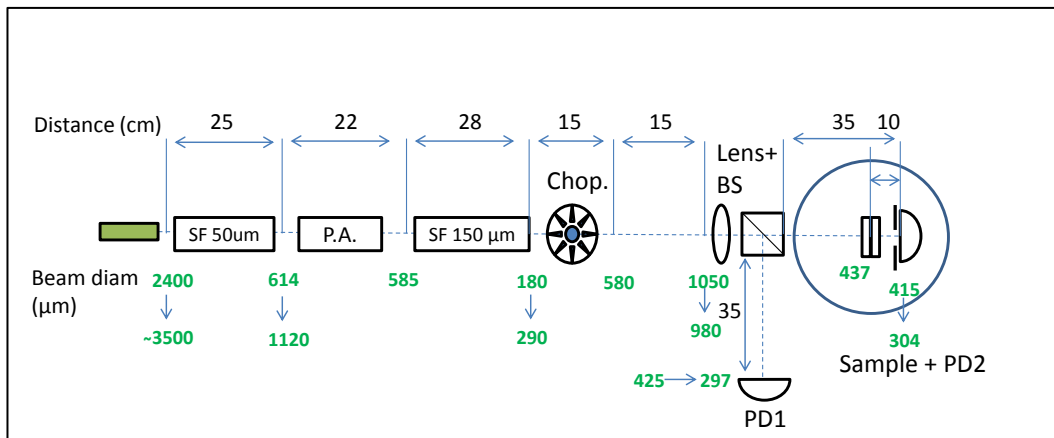


Figure 4-5: New setup layout displaying the relevant distances and the change in beam diameter from the setup used in chapter 2. SF: Spatial filter with pinhole size used, PA: Polarising assembly, Chop: Chopper, BS: Beam Splitter, PD: Photodiode.

The first modification was the acquisition of a new laser module since the beam profiler showed that the previous one had deteriorated in the course of the 3 years (see Figure 4-6). This prevented from a good Gaussian beam being obtained and complicated the study of propagation. The new laser had a much better profile that could be filtered down to a clean Gaussian beam. In Figure 4-5, the numbers in green show the change of beam diameter along the setup for the old (top row) and new (bottom row) laser. A consequence of a new module was the increased size of initial beam diameter to about 3500 μm. The parameters of the spatial filter that was used for the beam radius reduction had to be modified in consequence. The optimal size of pinhole for a spatial filter is given by equation 4.2 [154].

$$d = \frac{8\lambda f}{\pi D} \quad (4.2)$$

With  $d$  the diameter of the pinhole,  $\lambda$  the wavelength of the laser,  $f$  the focal length of the front lens of the spatial filter and  $D$  the beam diameter. The lenses of the spatial filter were the same as the ones that were used in the previous chapters and therefore  $f = 0.1 \text{ m}$ . With  $\lambda = 532 * 10^{-9} \text{ m}$  and  $D = 3500 * 10^{-6} \text{ m}$ , one obtains  $d = 38.7 \mu\text{m}$ . The best pinhole available to match this value had a diameter of 50 μm and therefore it replaced the 75 μm - diameter pinhole that was used previously.

After the spatial filter, the beam radius reduction was about  $\frac{1120}{3500} = 0.32$  which matched well the theoretical value of  $\frac{f_2}{f_1} = \frac{3}{10} = 0.3$  (ratio of the focal lengths of the lenses used in the spatial filter).

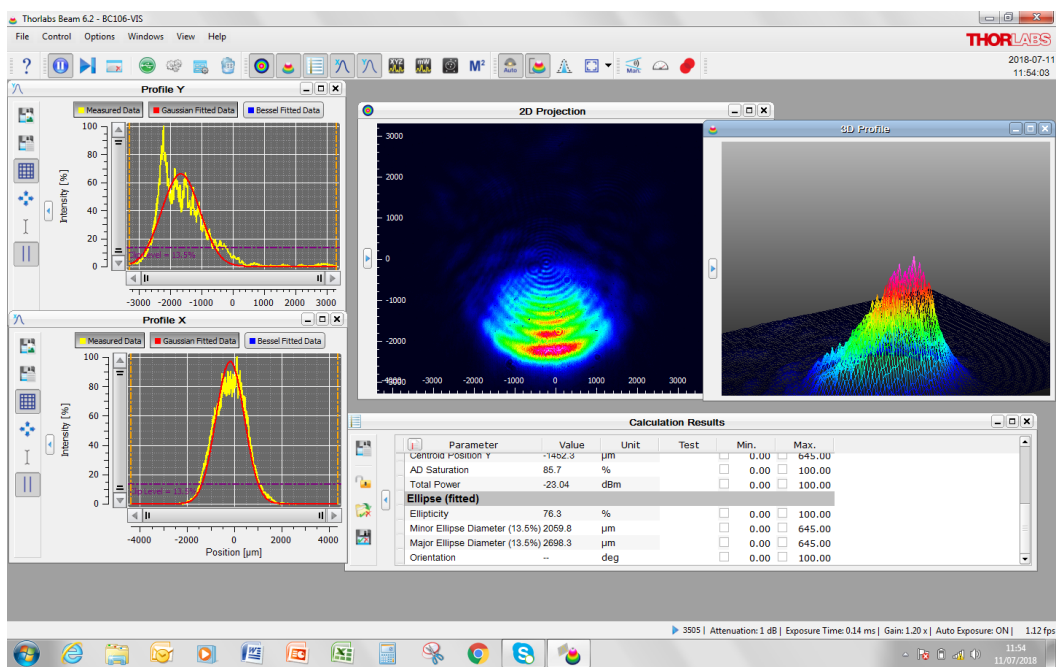


Figure 4-6: Illustration of the degradation of the beam profile. It seems that the internal alignment in the laser is off compared to the optical aperture making a clean Gaussian beam harder to obtain.

At the output of the first spatial filter, the beam was fairly well collimated but its diameter needed to be reduced further. It was decided to use a second 2-lens assembly and an additional spatial filter with the same focal lengths ratio as in the first one was put in the beam path. As the diameter of the input beam was about three times lower than for the first spatial filter, the pinhole selected had to be accordingly larger and a 150  $\mu\text{m}$  - diameter pinhole was used. The ratio of diameters between the input and output beams was about  $\frac{290}{1120} = 0.26$ .

Due to the significant reduction of beam diameter, it was not possible to maintain a low diverging beam and therefore its diameter increased back to 980  $\mu\text{m}$  after only 30 cm of propagation. In order to focus the beam on the detector, a converging lens with a focal length equal to 20 cm was placed as forward as possible on the beam path. There was no attempt to match the mode as it would have required getting new components or increasing the setup length but the profile obtained was already satisfying. The diameter was taken down to about 440  $\mu\text{m}$  at the sample position and 300  $\mu\text{m}$  at the detector position which was significantly better than what could be achieved in the previous trial (580  $\mu\text{m}$  at the detector).

Another improvement was that the two detectors were now placed at the same distance from the beam splitter which meant that the beam profile was similar for the reference and measured signal. This simplified the calibration operation. Figure 4-7 shows the evolution of the beam profile across the various optical components. It can be seen that a TEM00 mode

was produced and maintained along the propagation length. An unbonded YAG sample (8 mm thick) was put on the sample holder to assess the level of beam deformation when propagating through the substrate. When comparing the front and back reflection, it appears that the contour lines become a bit more blurry for the latter. This highlights that some scattering occurred when propagating in the substrate but the beam profile was overall well maintained.

The acquisition method was also changed for this trial with the purpose of reducing the error on the measurement. The acquisition of the reference (PD1) was made through a second lock-in amplifier instead of reading it on the oscilloscope. This allowed real time monitoring of  $V_{input}$  and getting rid of the error due to power fluctuations as the value taken was the instantaneous one rather than an average over the measurement.

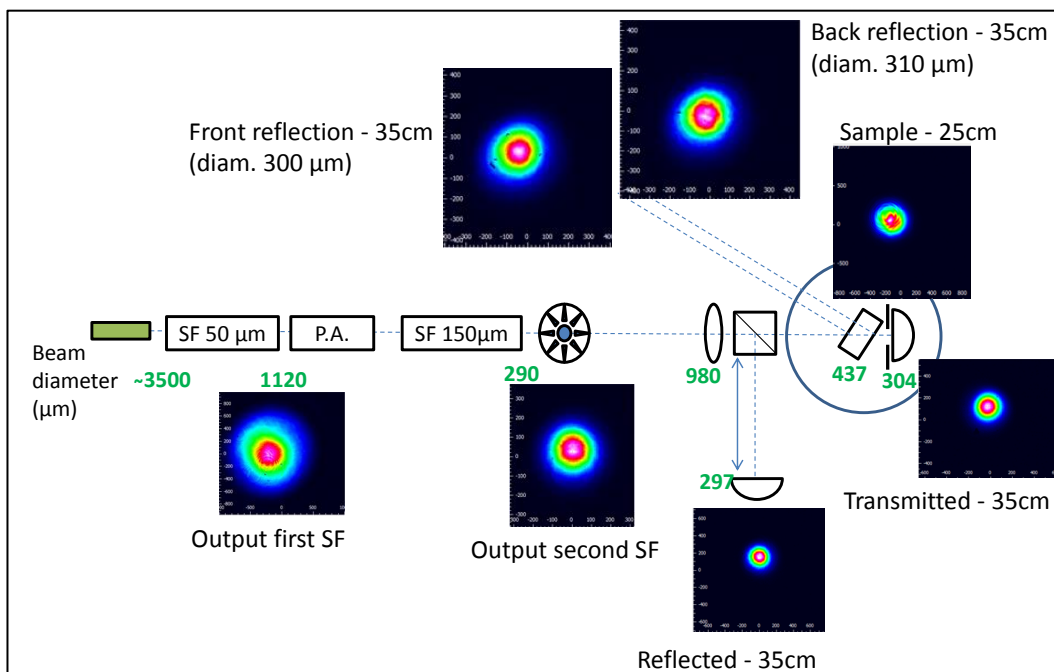


Figure 4-7: Beam profile at different positions along the optical bench. The scales of the inserted pictures vary and only the beam shape should be considered. The beam diameters are given by the green numbers. When highlighted, the positions are taken with the exit face of the beam splitter as reference. The clean TEM<sub>00</sub> mode at the PD position is noticeable.

#### 4.2.2.2 New errors

With the changes in the setup, the transition between raw data and calculated reflectance was slightly modified and the errors were recalculated. The updated equation 4.3 is similar to equation 2.3 but the quantities are calculated differently.

$$R = \frac{k * V_{output}}{V_{input}} \quad (4.3)$$

In equation 4.3,  $V_{output}$  is given by the same relation as in section 2.3.1.4.

$$V_{output} = \frac{s * V_{acq}}{10}$$

With  $s$  the sensitivity (in V) and  $V_{acq}$  the raw data obtained through the DAQ (in V). The error on  $V_{output}$  was estimated as described in section 3.2.1.5 although a new set of measurements was made as the laser parameters changed. The measurement of the error is displayed in Figure 4-8 and the estimated values in Table 4.1. It can be seen that the standard deviation of the sets are much smaller than the ones that were presented in section 3.2.1.6. This is attributed to the smaller beam size which made it easier to reliably collect the full signal.

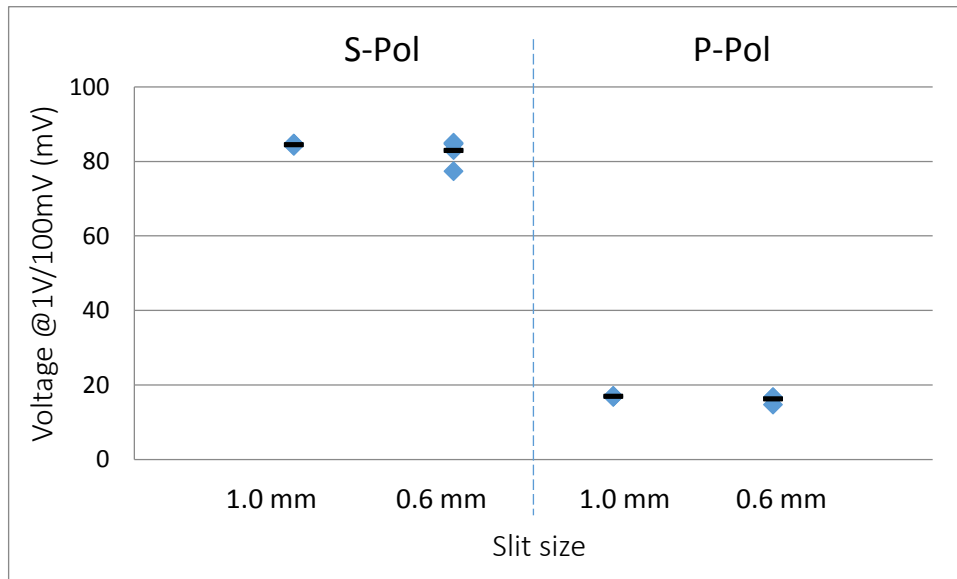


Figure 4-8: Error on  $V_{output}$  obtained by taking the same measurement ten times and estimating the standard deviation of the set. The horizontal axis highlights the width of the slit used.

The factor  $k$  carries the same information as in chapter 2, i.e. the ratio transmission/reflection of the beam splitter and the difference in response between the two detectors. However, its measurement was made differently with the purpose of increasing its accuracy and robustness.

In a first configuration,  $PD1$  was placed 35 cm away from  $NPBS$  in transmission while  $PD2$  was placed 35 cm away in reflection. For each detector and each polarisation (S and P) the measured signal was written down. In the second configuration, the positions of the two detectors were swapped and the values written down again. This set of measurements gave a total of eight values (two polarisations, two detectors and two positions) which were then used to estimate the different contributions to the  $k$  factor as detailed in equation 4.4. In equation 4.4,  $\left(\frac{V_A}{V_B}\right)_{c,i}$  denotes the ratio of the measured signal when changing the parameter

A to B while keeping C the same. The parameters in question are the position (reflection or transmission) or detector ( $PD1$  or  $PD2$ ). The index  $i$  denotes the polarisation (S or P).

$$k_i = \frac{\left(\frac{V_{ref}}{V_{trans}}\right)_{PD1,i} + \left(\frac{V_{ref}}{V_{trans}}\right)_{PD2,i}}{2} * \frac{\left(\frac{V_{PD2}}{V_{PD1}}\right)_{ref,i} + \left(\frac{V_{PD2}}{V_{PD1}}\right)_{trans,i}}{2} \quad (4.4)$$

Due to the large number of manipulations and positioning of detectors to take this measurement, it was understood that the experimenter error could be quite significant. Therefore the measurement was taken nine times over several days. The average of this set was used as a single value of  $k_i$  for all the measurements and the error was taken equal to the standard error of the set. These values were:

$$k_S = 0.165 \pm 0.006$$

$$k_P = 0.0073 \pm 0.0003$$

Finally,  $V_{input}$  was read directly on the lock-in display and used as such. The sensitivity was set to the highest value that did not allow saturation. Since the reading was done in real time, there was no need to account for the power fluctuation and with the detector position being carefully positioned a single time for all measurements, the experimenter error was made minimum. Therefore the term  $V_{input}$  brought no contribution to the error on the measurement.

The total error value for both polarisations is displayed in Table 4.1.

It can be seen that the error made on the measurement is significantly higher when using the 0.6 mm slit. This comes from the experimenter error being increased as it is harder to position the detector properly for the beam to fully go through the slit, which then propagates to the determination of the k factor. These errors were the ones used in the control measurements of the next section in order to settle on a slit size.

*Table 4.1: Error values for either slits measured as described in the text.*

	1 mm slit	0.6 mm slit
Experimenter error $\left(\frac{\delta V_{output}}{V_{output}}\right)$	0.3 % for S-polarisation 0.6 % for P-polarisation	3.9 % for S-polarisation 5.4 % for P-polarisation
Calibration factor $\left(\frac{\delta k}{k}\right)$	3.7 % for S-polarisation 4.4 % for P-polarisation	7.8 % for S-polarisation 5.7 % for P-polarisation
Total error	3.7 % for S-polarisation 4.4 % for P-polarisation	8.7 % for S-polarisation 7.8 % for P-polarisation

#### 4.2.2.3 Control measurement

Since YAG has a high refractive index, it was expected that the intensity of the reflected beams would be higher than they were for phosphate glass in chapter 3. Therefore the risk of having the front and back beams polluting the bond signal was increased. The choice of sample dimensions and the reduction of beam radius were done to prevent this from happening. In order to assess whether these precautions were sufficient, some control measurements were carried out on an unbonded YAG sample (8 mm thick). The distance between the front and back reflection should be the same as the one between the surfaces and bond reflections for a bonded sample and therefore the measurement would allow a good preview of the intensity profile to expect.

The control measurement was taken at an angle of incidence of  $30^\circ$  and with P-polarised light. As in section 3.2.1, a 1 mm-slit and a 0.6 mm-slit were used and the intensity profiles were analysed. The displacement step was 0.1 mm and the amplification was set on 1 V/50 mV<sup>20</sup> as it was the highest amplification that did not lead to saturation. The measurement was taken several times within the same day and over three different days to assess the repeatability of the obtained peak value.

Afterwards, the amplification was set on 1V /1 mV in order to scan the profile between the two peaks with a higher sensitivity. By doing so, it was possible to assess whether there was a risk of light pollution when measuring the bond peak in the course of the trial.

Figure 4-9 displays the intensity profiles for either slit when scanning the front (right peak) and back (left peak) reflections while Figure 4-10 shows an overview of the consistency of the value obtained for the front surface reflectance across several measurements over several days. Finally, Figure 4-11 displays the curve obtained when scanning the interval between the two peaks at higher sensitivity to estimate the background signal.

Looking at Figure 4-9, the difference in profile is noticeable. When using a 0.6 mm-slit, the maximum reflectance is reached at a single position whereas when using a 1 mm-slit, several successive positions of the detector measure the same intensity which displays as a plateau on the profile. This result could be anticipated when noticing that the beam diameter is about 0.3 mm and the displacement step 0.1 mm.

Besides there is a noticeable difference between the maximum reflectance values obtained with the two slits. Looking at Figure 4-10 however, this difference is not systematic across

---

<sup>20</sup> The notation 1 V/X mV indicates that the lock-in returns 1V for each X mV in input. X is the quantity that was called sensitivity throughout the text even though the actual sensitivity decreases when X increases.

the days and is also within the error of the measurement and therefore will not have to be accounted for.

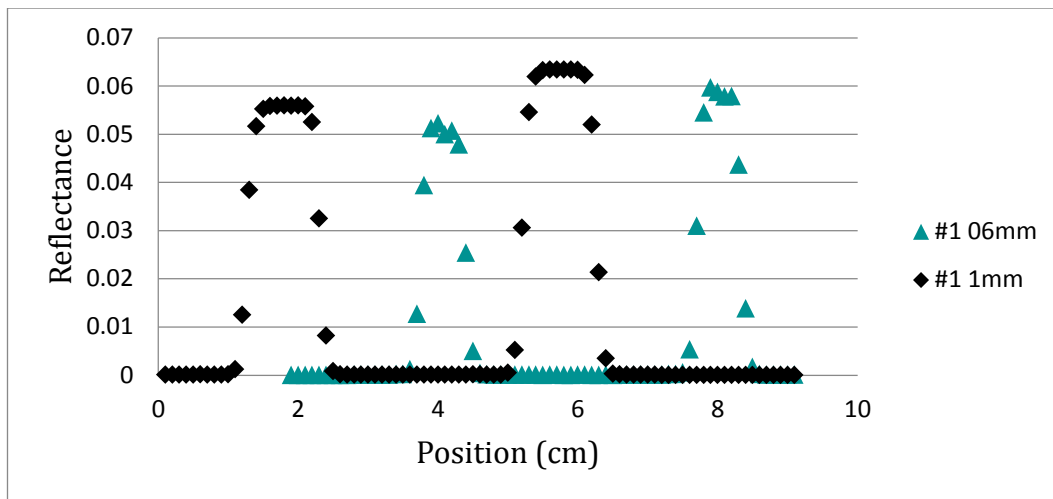


Figure 4-9: Intensity profile (expressed as reflectance) when scanning from the back to the front reflected beam position for both slits. The measurement is taken at  $30^\circ$  in P-Polarised mode. The positions of the curves are shifted for clarity.

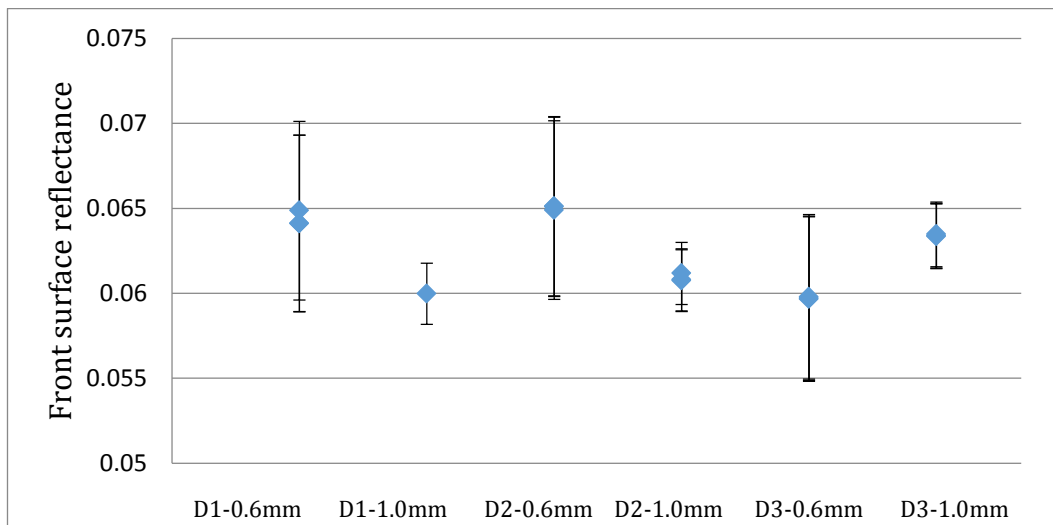


Figure 4-10: Consistency of the measurement within a single day and across several ones for either slit. All measurements are taken at  $30^\circ$  in P-Polarised mode. The error bars correspond to the values estimated in Table 4.1.

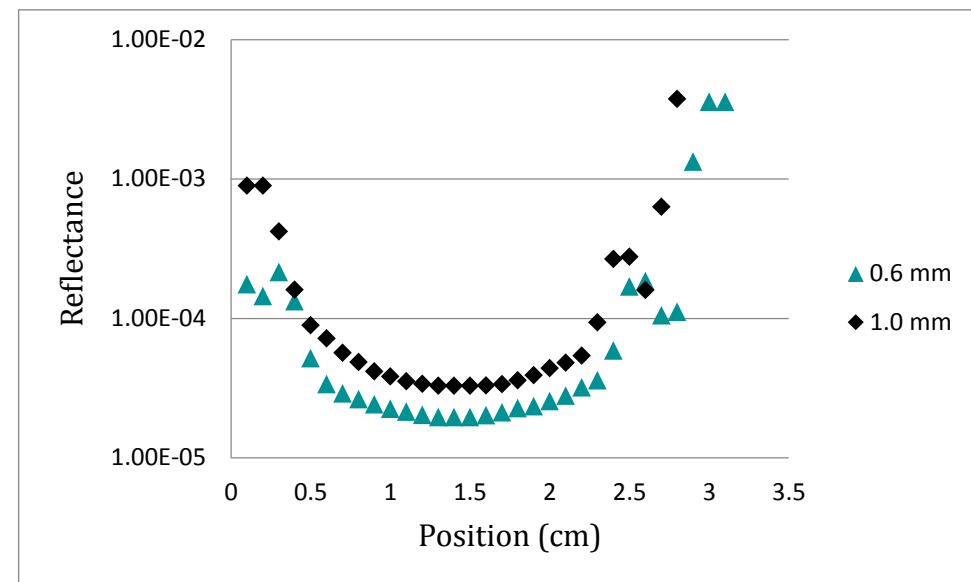


Figure 4-11: Intensity profile (expressed as reflectance) measured at higher sensitivity between the peaks for both slits.

Finally, Figure 4-11 shows that, as was the case in section 3.2.1.4, there is more background pick-up with a 1.0 mm slit than with a 0.6 mm one with the values in the dip being about 32 ppm and 20 ppm, respectively. If one considers that the background noise can be neglected from a signal to noise ratio of 100, this means that the measured value for the bond reflectance will be only negligibly altered down to 0.1 %.

From these series of measurements, it was decided to use a 1.0 mm slit in the course of the trial as it would allow easier positioning of the detector and therefore smaller errors. The measurements showed that the peaks were well enough separated for the background pick-up to be negligible with regards to the measured reflectance as long as the latter is of the order of magnitude of 0.1 %. Having several points available when determining the maximum value is also beneficial as it makes it easier to see if the measurement is consistent and validate it.

#### 4.2.3 Trial

The trial consisted of two sets of measurements on two different samples. The first sample YAG1 was measured regularly from day 2 of curing until day 38 of curing without taking it off the setup for all that time to avoid unnecessary manipulation and risk of miss-positioning. Afterwards, the second sample YAG2 was placed and measured the same way from day 3 of curing to day 25 of curing. YAG1 was then measured again at 64 days of curing.

##### 4.2.3.1 Reflectance measurements

The results are presented in Figure 4-12 and Figure 4-13.

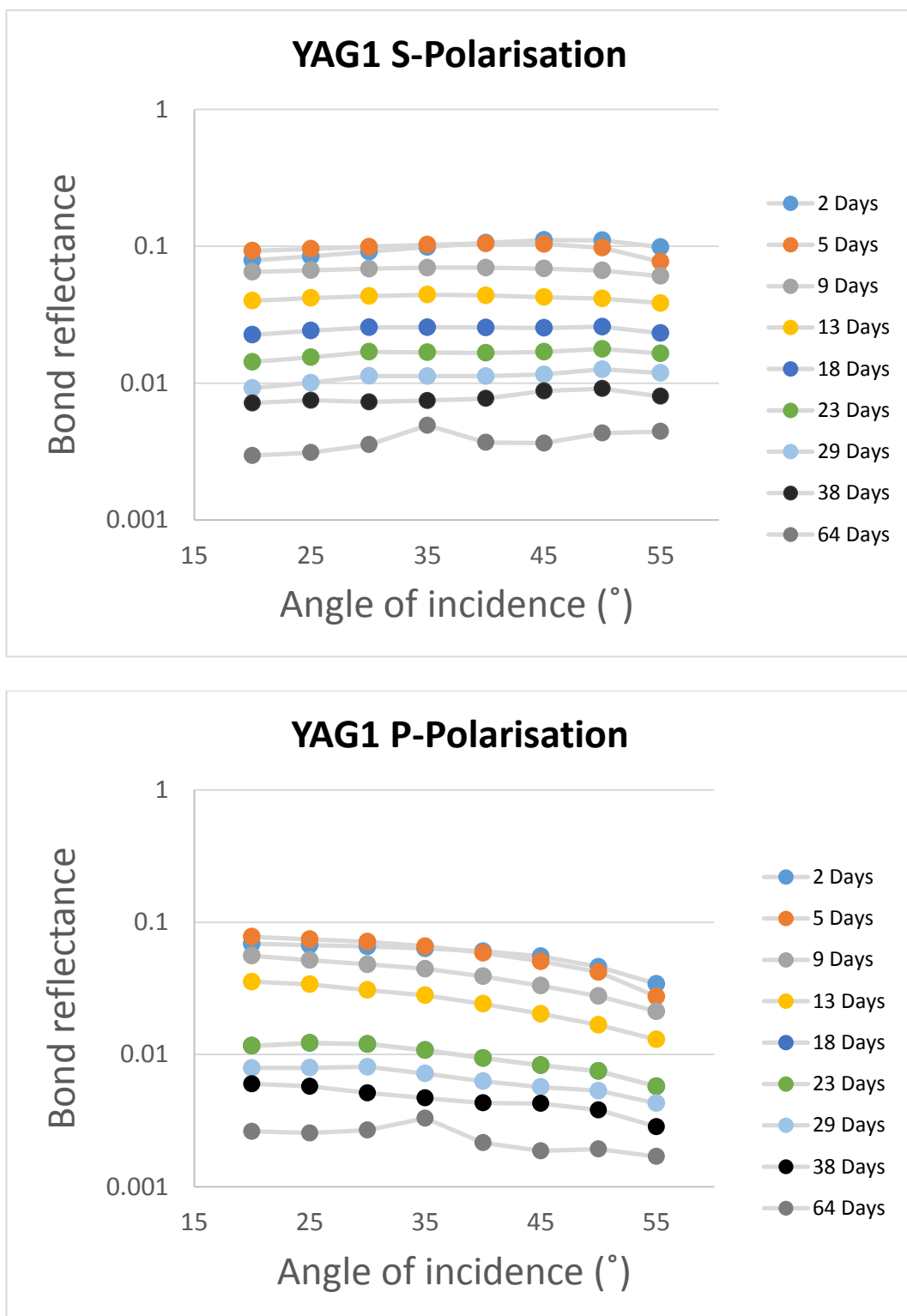


Figure 4-12: Angle-dependent bond reflectance for YAG1 and change with curing time in S-polarised (top) and P-polarised (bottom mode).

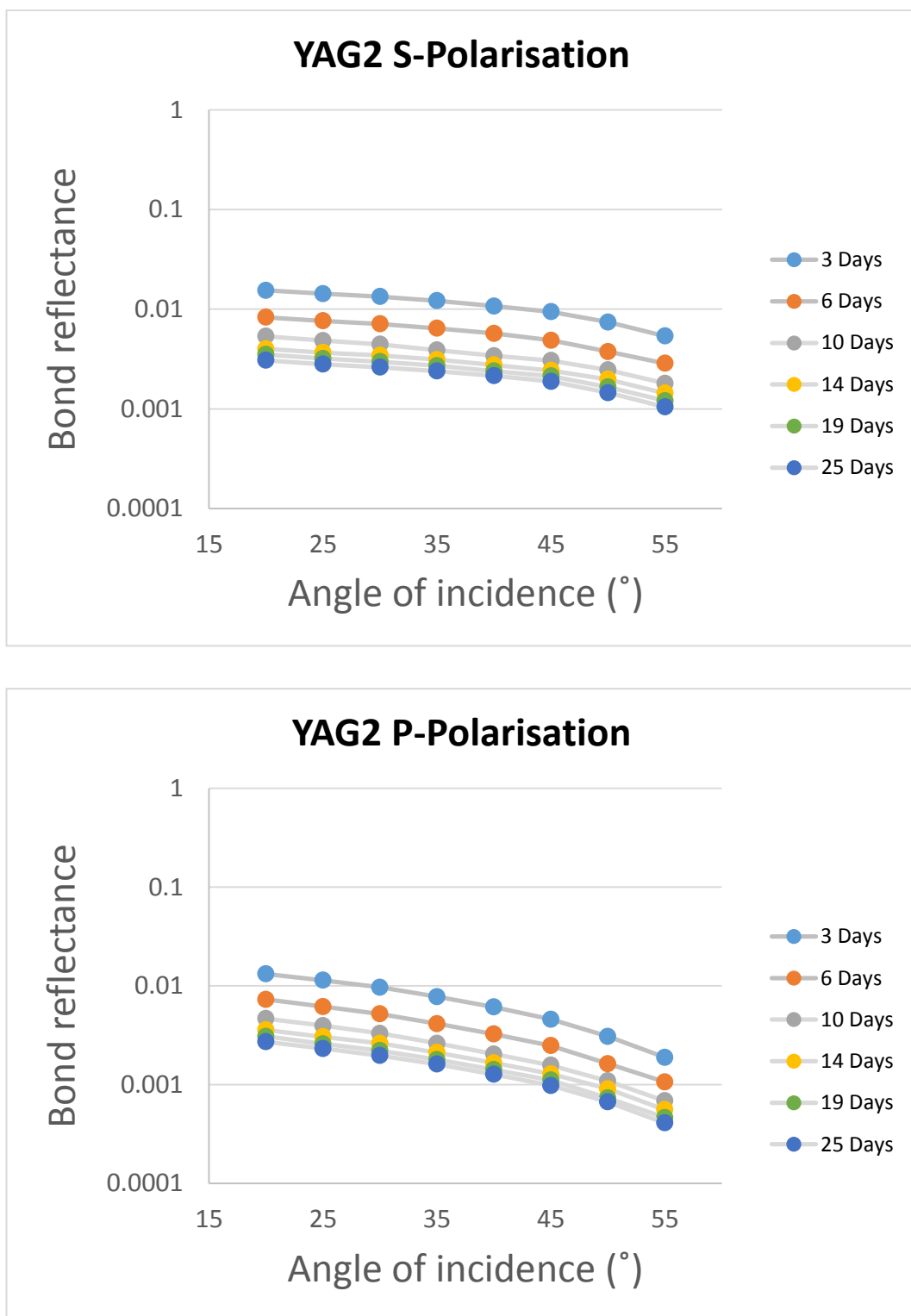


Figure 4-13: Angle-dependent bond reflectance for YAG2 and change with curing time in S-polarised (top) and P-polarised (bottom mode).

Looking at the results, the first observation is that the values are of the order of 0.1 % and therefore the background can be neglected as stated in section 4.2.2.3 . There is a similar trend between the variations of the reflectance with time for the two samples. The shape of the curves does not change much past the first week of curing and the reflectance moves towards lower values. There is however a noticeable difference in the values reached for each sample during the curing. Taking the value at 20° as representative for a measurement, the reflectance for YAG1 goes from 9.3 % to 0.3 % (S-polarisation) and 5.5 % to 0.2 % (P-Polarisation) in the span of 64 days whereas for YAG2 it decreases from 1.5 % to 0.3 % (S-Polarisation) and 1.3 % to 0.3 % (P-Polarisation) over 25 days of curing. The angle-dependence of the reflectance also looks different between the two samples which likely come from differences in the bond layer parameters.

#### 4.2.3.2 Bond parameters

As was shown in section 2.3.3, these reflectance measurements allowed the estimation of the thickness and refractive index of the bond layer. The Matlab script used was the same although the upper boundary of refractive index was increased to 1.9 to encompass the refractive index of YAG (1.815). The fits obtained were of overall good quality which strengthened the confidence in the setup and model. Examples of “good” and “bad” fits are displayed in Figure 4-14.

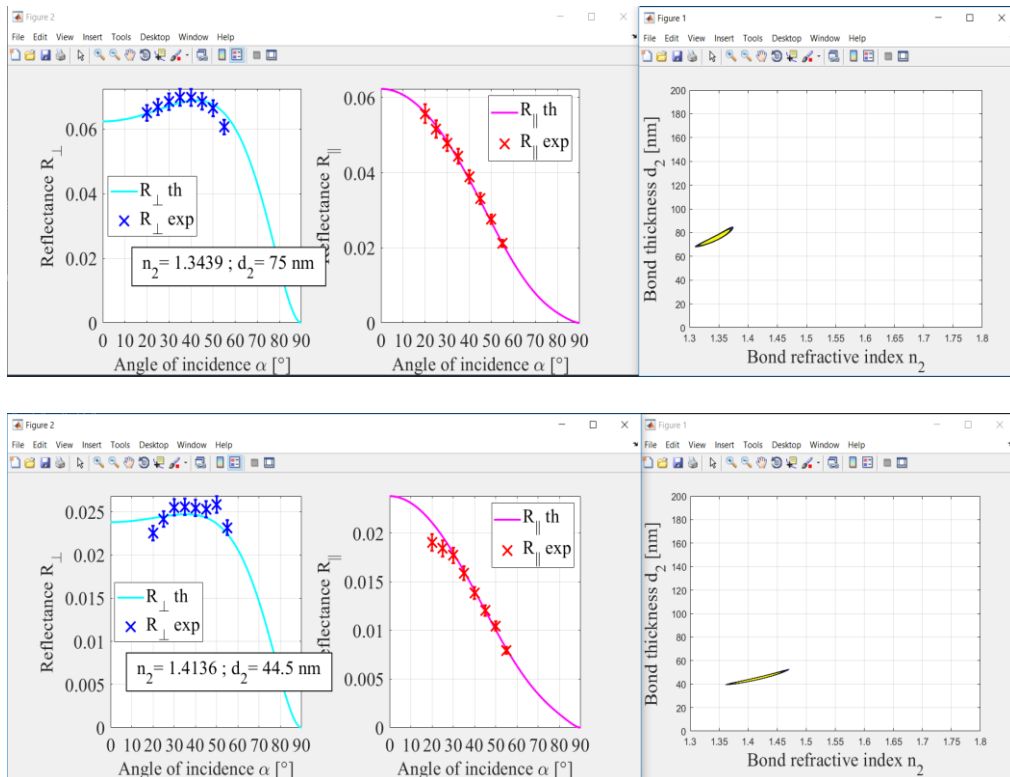


Figure 4-14: Examples of output of the Matlab script applied to the data for YAG1. Top: The best fit is very good for the point at 9 days. Bottom: The best fit is worse for the point at 18 days.

In particular it appeared that the quality of the fits was getting worse with time for YAG1 and the ones obtained after 23 days seemed looser (some points are not within error of the theoretical curve). The hypothesis is that upon curing, the bonds could develop some inclusions that displayed as high or low reflective spots. Due to refraction, the beam scanned a segment of about 4.5 mm on the bond interface. Therefore if it landed on one of those spots the smoothness of the curve got altered and the fit was not perfect. This happened noticeably for YAG1 at 64 days, 35° incidence where the point for both polarisations is not in line with the trend of the curve (Figure 4-12). The model worked best when the bond was homogeneous over the scanned segment which was the case for YAG2 for which the fits were good over all the measurements.

As an assessment of the homogeneity of the bond, after the trial was completed, the samples were rotated three times by 90° each time in order to measure different areas. Therefore the results available are the monitoring of parameters with time at one position for each sample and the parameters at four different locations for each sample at a given time (end of the trial). The results are displayed in Figure 4-15-16.

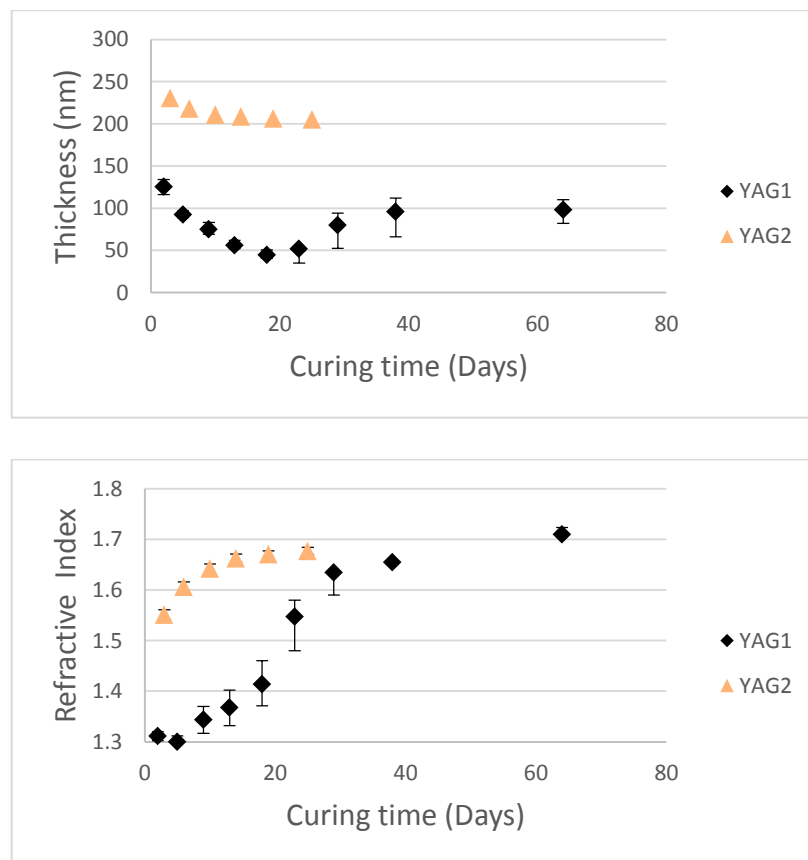


Figure 4-15: Variation of the thickness (top) and refractive index (bottom) with curing time for two YAG samples bonded with a sodium silicate solution.

The immediate observation is that the data from the two different samples do not match each other. Looking at the thickness first, it decreases with time for both samples in the first 25 days, from  $125^{+9}_{-9}$  nm to  $45^{+6}_{-4}$  nm for YAG1 and from  $230^{+1}_{-1}$  nm to  $205^{+1}_{-1}$  nm for YAG2. The gap between the two samples is not within error and it is clear that they progress on two different levels. This is sensible as the thickness is likely depending on the surface finish of the sample which can vary locally. At 25 days it looks like the bond layer thickness increases back for YAG1 and reaches  $98^{+12}_{-16}$  nm after 64 days. Although the trial was discontinued for YAG2, the thickness appears to slowly converge towards about 200 nm and there is no sign of a similar spring back.

When looking at the refractive index, YAG2 shows again a clear trend with an increase from  $1.551^{+0.009}_{-0.009}$  to  $1.676^{+0.007}_{-0.007}$  over 25 days and the slope decreasing towards a steady state regime. The trend for YAG1 is a bit more puzzling as the curve displays a point of inflection at 20 days and only from there starts to follow a similar behaviour with the refractive index rising from  $1.41^{+0.04}_{-0.04}$  to  $1.71^{+0.013}_{-0.005}$  in the next 45 days. The reason why this delay happens is not clear but measuring an initial refractive index between 1.3-1.4 is sensible as the refractive index of the initial solution is within this interval. The hypothesis is that the difference is due to the fact that YAG2 was left one more day curing before being picked up for the trial. The weight of the top flat when the part is laid down would have helped confining the bond layer and catalysed the reaction that led to the bond grasping whereas by picking the sample too early and leaving it in vertical position (thus with no help from gravity) the initiation of the reaction was delayed for YAG1. The final value reached for the refractive index in the case of YAG1 is higher than for YAG2 but still in a similar range. It seems sensible that the refractive index would be more homogeneous across the samples than the thickness which is likely sensitive to the topography of the surface.

This observation is confirmed by the results on the homogeneity trial displayed in Figure 4-16. It can be seen indeed that the measured thickness varies significantly across the bond interface but the refractive index seem to depend less on the sample and position. For YAG1 in particular the standard deviation in thickness is over 66 % of the average value. The results are more consistent for YAG2 as the deviation is down to 27 % and even lower than 10 % for three of the four data points. For both samples, the deviation on the refractive index is less than 3 % of the average value.

Given the spread of the values taken within a single sample, it is less surprising to witness differences across different samples. However in spite of this, the average values obtained are  $(n; d) = (1.66; 295 \text{ nm})$  for YAG1 and  $(n; d) = (1.69; 272 \text{ nm})$  for YAG2 which is a positive result on the consistency of the measurement. The few outlier points could be accounted for by local inclusions in the bond layer and bonding should be made to avoid them as they can be detrimental to the performance of the component.

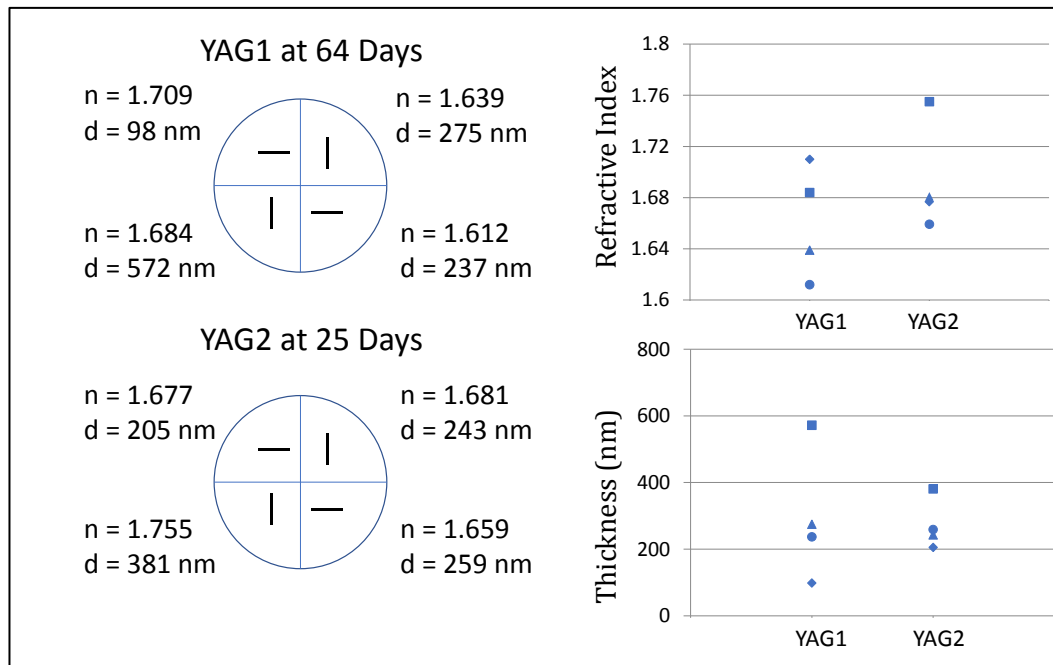


Figure 4-16: Variation of the bond parameters across four different positions on the two samples. The black segments illustrate the intervals scanned in the course of a measurement as a result of refraction.

#### 4.2.4 Discussion

From the results presented above, the value of 0.3 % can be considered representative for the reflectance of the interface of silicate-bonded YAG in a steady state (at 20° and regardless of the polarisation). Therefore the requirement for the reflectance of transmissive surfaces and interfaces in photonics (usually an upper limit at 0.1 %) is not quite met but surprisingly close. In the earlier work on phosphate glass (refractive index  $\approx 1.56$ ), the obtained values at advanced stage of curing were comprised between 0.01 % and 0.1 % and in her work on sapphire (refractive index  $\approx 1.77$ ) Mangano reported values at already 3 % [155]. With a refractive index even larger, YAG (refractive index  $\approx 1.82$ ) would have been expected to produce bonds of higher reflectivity making the process out of consideration for photonics applications. Instead the values obtained suggest that, as was the case for phosphate glass, the initial refractive index mismatch between the bond and the bulk material is actually mitigated through chemical reactions.

The estimation of the bond parameters seems to confirm this hypothesis with the parameters  $(n; d) = (1.69; 272 \text{ nm})$  taken as representative of this trial, keeping in mind the spread of data that lies behind. The first thing that is interesting to notice is that the estimated refractive index of the bond is well above the one of fused silica but at the same time below the one of YAG. This was already seen in the case of phosphate glass and the hypothesis is that the surface of the material gets etched and some elements from the bulk

mix with the silicate to form the bond network. However this contradicts the behaviour that was expected prior to the trial. In particular, the assumption was made that as alumina-based crystals, YAG and sapphire would behave similarly to a large extent with regards to bond properties. Mangano studied the bond parameters in silicate bonding of sapphire using reflectance measurements similar to the ones presented above. She reported that the refractive index of the bond increased from 1.3 with a similar trend as the one for YAG2 in this work, but actually capped at about 1.44 after 105 days and deduced that the bond was purely formed of silicate with no contribution from the bulk material. This seems to be in agreement with the literature and to invalidate an analogy in behaviours between silicon and aluminium oxides.

The results on the thickness are also overall higher than expected although it has been observed that the values taken spread over a large range. In section 3.2.2.3, the estimated thickness for the bonds between phosphate glass parts was of the order of magnitude of 100 nm and it was discussed how well it matched the results from other works. In her work on sapphire, Mangano found thicknesses in this range as well, at about 80 nm after 105 days. An immediate hypothesis to explain this discrepancy would be that the YAG samples were off-the-shelf commercial samples that were not prepared to the usual flatness requirement (60 nm peak to peak) for silicate bonding. The specified flatness was actually 80 nm which could have led to an increased surface mismatch between the parts and an increased bond thickness. Mangano however showed that there is little correlation between the surface mismatch and the thickness estimated through reflectance measurements. It seems therefore that the explanation could lie not within physical parameters but within the chemistry.

From these results, there seems to be sufficient evidence that YAG and sapphire should not be expected to behave in the same way with regard to bonding. Due to the discrepancy between the expectations from the literature and the results, it was decided to investigate further the chemistry of silicate bonding of YAG to try and remove the uncertainty on the mechanisms. This is the purpose of the section below.

### 4.3 Etching

In this section, a chemical analysis of the bonding solution is carried out to highlight whether etching of the bulk material occurs in the course of YAG bonding. The opportunity is taken to test phosphate glass as well for which every source seems to suggest that exchanges between the surface of the material and the bonding solution occur to ultimately form a bond.

#### 4.3.1 Method

The apparatus used to carry out the analysis was an Energy Dispersive X-Ray Fluorescence (EDXRF) spectrometer. Using filter papers to absorb the solution, it is possible to analyse liquid samples in the same way as solid ones. More details can be found in Appendix A.

Four test tubes were prepared. They were filled with 2 ml of sodium silicate solution each and a bulky sample of material was put inside each, making sure the whole sample was immersed. The samples were the 20 mm long rods used for the strength tests trials and therefore the active surface was about  $4.5 \text{ cm}^2$  (square-base rods) and  $4.15 \text{ cm}^2$  (circle-base rods). The whole area was treated as if the sample was about to be bonded (Cerox cleaning) so that the surface was reactive when put in the solution. One sample of fused silica, phosphate glass and YAG were used. The last tube was used as a witness.

The tubes were stored at room temperature for 5 days and then in a water-bath at  $70^\circ\text{C}$  for 6 more days in an attempt to speed up the reaction. The tubes were manually stirred on a regular basis. A first measurement was taken at 3 days, a second one after 4 hours at elevated temperature (on the fourth day) and a third one at 9 days. For each measurement a sample was prepared by picking 0.1 ml of solution and dropping it approximately homogeneously in a circle of 3 cm diameter as per recommendation. The paper was then dried in ambient atmosphere before being tested.

The analysis parameters were set to look for the main elements present in the bulk material. In the case of phosphate glass these were phosphate, aluminium and barium. In the case of YAG these were yttrium and aluminium. Sodium and silicon were added to the analysis as they are present in the sodium silicate solution or in the silica-based materials. The results are given in g/l thanks to the input of solution amount and effective surface.

#### 4.3.2 Results

The results are presented in Figure 4-17. It can first be observed that for each sample the initial sodium to silicon ratio remains constant across the measurements at about 7-10 to 20-25 g/l which match rather well the 11 to 27 ratio specified for the commercial solution. Even though the absolute values are higher for YAG the ratios are approximately maintained and therefore the hypothesis is that these higher values come from an experimental factor and not an actual chemical reaction.

It is hard to draw any conclusion on etching of fused silica from the amount of silicon as the solution is already rich in the element. What is interesting is that there are no hints of aluminium or yttrium in the solution containing the YAG sample even after several days of immersion at higher temperature. This suggests that no significant etching happens which

agrees with the literature but contradicts the hypothesis formulated in section 4.2.4. In comparison, the solution containing the phosphate glass sample has a behaviour that indicates etching of the bulk material. After three days of immersion, aluminium, phosphorus and barium are leached into the solution to an amount of 0.6 g/l, 2.1 g/l and 0.6 g/l, respectively. The ratio between phosphorus and the two other elements is about 3.5 compared to the ~6 of the bulk material which would suggest preferential etching of the non-phosphorus species. After a few hours of heating to prepare for the second measurement, the solution showed a singular behaviour compared to the others and turned into a gel as can be seen in Figure 4-18. The values presented in Figure 4-17 are misleading as the sample is not liquid and the filter paper method is not reliable anymore. The values are above 30 g/l for sodium (38 g/l) and silicon (96 g/l) but to focus on the leached elements the graph scale is not expanded. This time the ratio of phosphorus to aluminium and barium is about 1.3 and 5.5, respectively. It would appear that the elevated temperature favour etching of aluminium compared to barium. However all quantitative values are to be taken with care given the nature of the sample and the inadequate method of measurement. This is also the reason why there was no attempt at a third measurement on the sample.

#### 4.3.3 Discussion

With these additional results on YAG etching, it is possible to narrow further down the hypotheses on the mechanisms of silicate bonding of YAG. The reflectance measurements have shown that there is a layer of modified chemistry with a thickness of about 275 nm and refractive index about 1.67. The pure sodium silicate solution has a refractive index between 1.33 and 1.45 depending on its water content and therefore such a layer can only happen if the solution mixes with elements from the bulk. Indeed, Mangano showed that the refractive index of the layer would cap at 1.45 when there is no reaction as is the case for sapphire. Since the etching experiments showed that mixing did not happen by leaching elements from the surface into the solution, the remaining hypothesis is that the solution actually penetrates the bulk material through diffusion and creates that altered boundary layer.

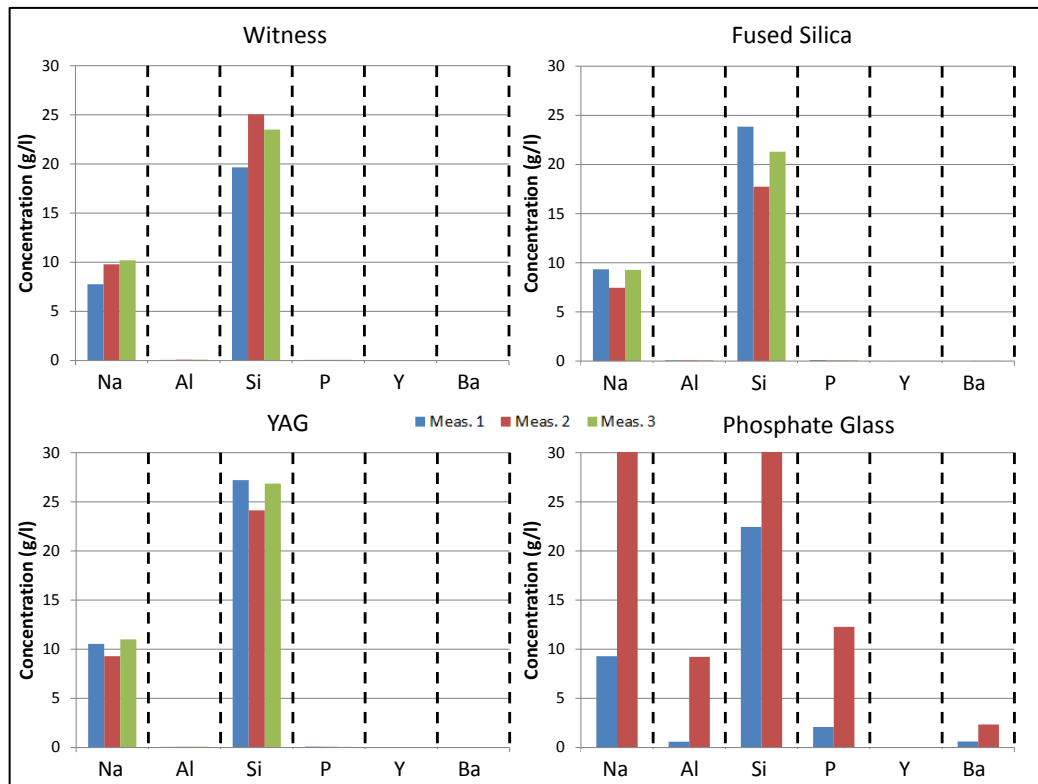


Figure 4-17: Chemical analysis of the solution after immersing bulky samples of various materials. The first measurement is taken after 3 days, the second measurement is taken after 4 days + 4 hours at 70°C and the third measurement is taken after 3 days + 6 days at 70°C.

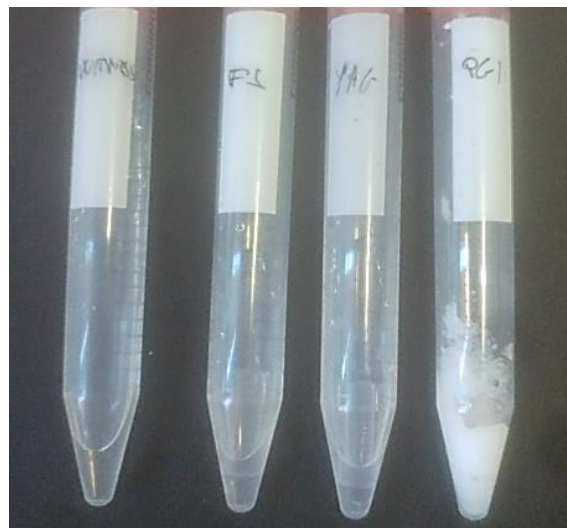


Figure 4-18: Test tubes taken out of the water-bath before the second measurement. From left to right: Witness, fused silica, YAG, phosphate glass. It is obvious that the tube containing phosphate glass was home for a chemical reaction turning the solution into a gel.

Diffusion of water into the network during the dehydration step was mentioned in section 2.2.3 but it was not thought as a refractive index modifier for the layer in contact with the solution. However if silica or even sodium is able to penetrate the material too, then this layer becomes a mixed silica/sodium-yttria-alumina layer with a refractive index between fused silica (1.45) and YAG (1.82) without any etching happening. This way, an agreement can be found between the bond parameter results and the etching experiment. It is quite hard to find support for the hypothesis in the literature given the specificity of the experiment. Diffusion coefficients of water, sodium and silica in YAG do not seem to be readily available. However, a recent study on the chemico-mechanical polishing of YAG has shown the superior performance of a slurry composed of silica in a sodium hydroxide solution to produce good surface finish compared to diamond or alumina based ones [156]. Although the mechanisms of chemico-mechanical polishing cannot really be put in parallel with the ones of static diffusion, the similarity in the chemical species involved could suggest particular interactions between molecular silica, sodium hydroxide and YAG that would support the hypothesis made above.

#### 4.4 Summary and conclusion

The objective of this chapter was to investigate the suitability of silicate bonding of YAG for photonics applications as it was done for phosphate glass in the two previous chapters. The material was selected as a representative of non-silica based crystalline materials for which the data were quite rare beyond some studies on sapphire.

The strength tests trial, although not extended through time, showed that the bonds displayed significant strength ( $24.3 \pm 2.2$  MPa) of the same order of magnitude as for the materials discussed in the previous chapter and therefore that effective bonding did occur. Incidentally, it was highlighted how the test setup was sensitive to the geometry of the sample and that care should be taken when comparing values across various trials. The hypothesis is that the distribution of the volume around the neutral axis as well as the presence of edges can lead to early failure of the sample.

With such strength, the bonded components can be handled and resist common shocks and vibration which is a minimum requirement. The next assessment should be to put bonded samples through manufacturing steps and see if they survive as this would increase the range of applications and the yield in production.

The focus was then put on the optical reflectivity of the bond as measured in the previous chapters. One more time the set-up was modified in order to increase its performances and guarantee usable measurements. The beam profile obtained ended up being satisfactory and following control measurements, the reflectivity measurements could be carried out without

---

any of the issues met with using the previous iterations of the setup. For this trial, it was decided to put the priority on the repeatability within two samples rather than exploring changes in the bonding parameters. The reflectance was monitored over two months to get an insight on the kinetics of the curing. A representative value of 0.3 % for the reflectance was obtained for both samples in the assumed steady state although the difference in the shapes of the curves already suggested differences in the parameters that lay beneath. This value is interesting as it is much closer to the requirement of 0.1 % than what was expected from the literature when starting the trial.

The study on the bond parameters seemed to confirm the interesting feature that chemical reaction occurred between YAG and the bonding solution leading to a bond layer with a refractive index of about 1.67 and a thickness of about 275 nm. From there, the assumption that sapphire and YAG belonged to the same class of non-silica based crystals had to be reviewed and YAG would be considered to have its own behaviour in the course of the bonding process.

To investigate this behaviour further, and mainly to check whether it would be similar to phosphate glass, chemical analysis of the bonding solution put into contact with pieces of bulk material was carried out. It actually appeared that YAG and phosphate glass displayed two really distinct behaviours. In fact, after only a few days elements from the bulk of phosphate glass started appearing in the solution signifying spontaneous etching of the surface whereas the solution in which YAG was immersed remained unaltered. Furthermore, when heating in an attempt to speed up the reaction, the solution surrounding the phosphate glass sample turned into a gel while YAG still showed no sign of reaction. From this trial two conclusions could be drawn. First the hypotheses on the chemical mechanisms leading to phosphate glass bonding that were put forward in the previous chapters seem to be confirmed. Then it seems that those mechanisms are not the same as the ones responsible for the bond properties witnessed in the case of YAG.

The final hypothesis that could be formed is that contrary to sapphire that does not form a mixed layer with the fused silica bond or phosphate glass that does form a mixed layer through etching of the surface, YAG forms a mixed layer through diffusion of the solution species in the bulk. This hypothesis seemed to be the only one leading to an agreement between the trials and actually could be supported by information found in the literature.

Regardless of the mechanisms involved, these results are very interesting for the prospect of silicate bonding in photonics applications. The reason advocated to avoid using it has been the fear of putting a silicate layer in components where the refractive index mismatch would lead to unacceptable reflectivity. However it was shown that YAG, a very common material for photonics and with a refractive index significantly higher than the materials that were

---

bonded before allowed a surprising low reflectivity to be reached compared to the expectations. This opens the way to dealing with materials on a case by case basis rather than disregarding the process based on considerations of similar materials and could bring silicate bonding on par with direct bonding techniques with respect to a range of applications.

---

## 5 Implementation of the bonding process in production

---

The previous chapters have focused on characterisation of properties of bonds to show that they are suitable by design for photonics applications. In this chapter, the focus is transferred to the implementation of the bonding process in production, i.e. how to go from a process designed for small volumes made in a laboratory to potentially a consistent, larger volume activity of a company. The compatibility of the process with the ones already in place in a factory that produces optical assemblies is also of interest. The particular aspects addressed in the trials are the reduction of the curing time in order to reduce lead time, the control of settling time of the bond to make the process easier for the operator and the improvement of the cleaning process to increase the yield.

### 5.1 Curing time reduction

In section 2.2.3, it was explained how the diffusion of water out of the bond affected its strength in the course of the curing step. The diffusion coefficient can be expressed by an Arrhenius' law [157].

$$D = D_0 \cdot e^{-\frac{E}{RT}} \quad (5.1)$$

Where  $D$  is the diffusion coefficient at the temperature  $T$ ,  $D_0$  the diffusion coefficient at  $T = \infty$ ,  $E$  the energy of activation of the mechanism and  $R$  the gas constant. According to equation 5.1, diffusion can be sped up by increasing the temperature of the system and consequently, the transitory regime of the curing kinetics could be reduced by doing so. This is the approach taken in this section.

In chapter 2, results on the curing time of bonds of phosphate glass parts estimated through strength tests were presented but did not help highlight the kinetic as the strength did not change in a noticeable way with time. The results discussed in the third chapter with the curing time tested through reflectivity measurements were more informative as a clear change of properties with time was highlighted. However the most important property to assess a fully cured bond remains its strength as it is the deciding factor in handling or manufacturing the component further. Therefore it was decided to use strength tests to investigate the curing time. The setup used was the one presented in section 2.2.1.3.

### 5.1.1 Trials

Crystal quartz was selected for curing trials at elevated temperatures as preliminary work had been carried out on the material by Beveridge and samples were readily available [136]. Moreover, products derived from bonded quartz had already been designed<sup>21</sup> and therefore it was of immediate interest to study the potential curing time improvement. Quartz is also anisotropic which makes it convenient to get samples with different surface coefficients of thermal expansion out of a single block of material. It allowed testing the robustness of the bond to thermal induced stresses occurring at the interface in the course of thermal treatment as introduced in chapter 1.

The samples used in this trial were crystal quartz rods with dimension 20 x 5 x 5 mm (40 mm x 5 mm x 5 mm once bonded), the bonding surface being a 5 mm x 5 mm face. The optical axes for each sample are aligned with the bonding surface sides and these were crossed at 90° for each pair of bonded samples to purposely involve thermal induced stresses as displayed in Figure 5-1.

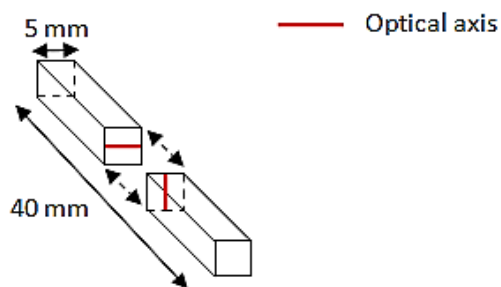


*Figure 5-1: Sketch of the bonded sample featuring the crossed optical axes*

The samples were manufactured at Gooch and Housego and put through the 7-stage factory cleaning process<sup>22</sup>. Afterwards surfaces were cleaned thoroughly with a wipe soaked in methanol before bonding. The solution used to make the bond was a sodium silicate solution diluted to a ratio of 1 to 6 in volume in distilled water and the amount of solution used was 0.8 µl/cm<sup>2</sup>. All bonds were made on the same day and broken after the desired curing time.

As the curing time at room temperature for quartz to reach full strength reported by Beveridge was about 4 weeks [136], a timescale capped by 28 days was proposed with a minimum size set of 5 samples broken each week. The large standard deviation in the results of the first sets prompted the increase of the size of the following ones. Samples were left for 48 hours at room temperature (RT) for the bond to allow primary bonding without inducing

<sup>21</sup> Internal communication

<sup>22</sup> Details of the process are given in Appendix B.

thermal effects. Samples were then put in the oven and heated at about 1 °C/min to the desired temperature. The ceiling temperature was kept moderately elevated and below the boiling temperature of water in order to make sure that no gas formed in the bond. Consequently, the two temperatures selected were 40°C and 80°C. An overview of the actual sets in this trial is shown in Table 5.1.

*Table 5.1: Final experimental parameters for each set. The number in brackets is the number of imperfectly bonded samples within the set. RT stands for room temperature.*

Set	Set size	Thermal treatment
1	6 (2)	2 days RT + 2 days 40°C
2	6 (2)	2 days RT + 7 days 40°C
3	8 (1)	2 days RT + 14 days 40°C
4	7 (2)	2 days RT + 21 days 40°C
5	5 (2)	2 days RT + 7 days 80°C
6	10 (3)	2 days RT + 14 days 80°C

At the end of the thermal treatment, twelve samples showed features at the interface which suggested incomplete bonds. Due to the small size of the sets, it was decided not to discard any sample before the measurements but to keep track of outlying results that could be linked to such features.

### 5.1.2 Results

Results of the breaking test are displayed in Figure 5-2. It can be seen that the samples that showed defects are not necessarily the weakest and therefore it is relevant to keep all of them in the statistics. The only exception is the weakest bond at about 2 MPa which is an outlier in its series and shows a strength that is typical of samples that have not formed a good chemical bond. The sample had been marked as bad following inspection but other similarly marked samples yielded significant strength so the correlation is not obvious.

Looking at the 40 °C curing temperature series, there does not seem to be a significant difference between the 2-day and 7-day sets with both having similar average and standard deviation at about  $13 \pm 7$  MPa. These very scattered values, with some bonds reaching 20 MPa while others remain below 10 MPa could be accounted for by the inhomogeneity of the bond at such early stage of curing. The sets at 14 and 21 days show a reduced scattering of the values and an increased average strength at about  $17 \pm 3$  MPa and  $16 \pm 3$  MPa, respectively. The fact that the strength seems to stop increasing after 14 days suggests that the bond reached a steady state after that time. The decrease in strength is not significant

and could be due to the statistical nature of the trial. However it is possible that this is a real effect which would align with the results from literature presented in section 2.2.3.

Looking at the series cured at 80 °C, the samples reach a strength of  $11 \pm 3$  MPa after 7 days and increases slightly to  $14 \pm 4$  MPa after 14 days. The standard deviation of the set at 7 days is half that of the one that cured at 40 °C for the same amount of time which could suggest that the bond is in a more advanced state of homogeneity. Comparing the strength reached by the two sets at the same curing time, it appears that the samples cured at 80 °C fail on average at lower stress than the samples cured at 40 °C though again there are within error of each other. Due to having limited amount of samples, it was not possible to investigate whether the samples from the series cured at 80 °C had reached a steady state or if the strength would have varied with more time. It seems however that the values are in a similar range as the ones from the 40 °C series after 14 or 21 days so it is believable that the bond has reached its full strength after 14 days.

Overall, both elevated temperatures seem to effectively decrease the curing time from four to two weeks. There is no evidence that higher thermal stresses weaken the sample as the values are in a similar range for 40°C and 80°C at the same curing time. Therefore, both temperatures can be used and since there is no clear improvement at 80°C, curing at 40°C will be recommended for crystal quartz bonds.

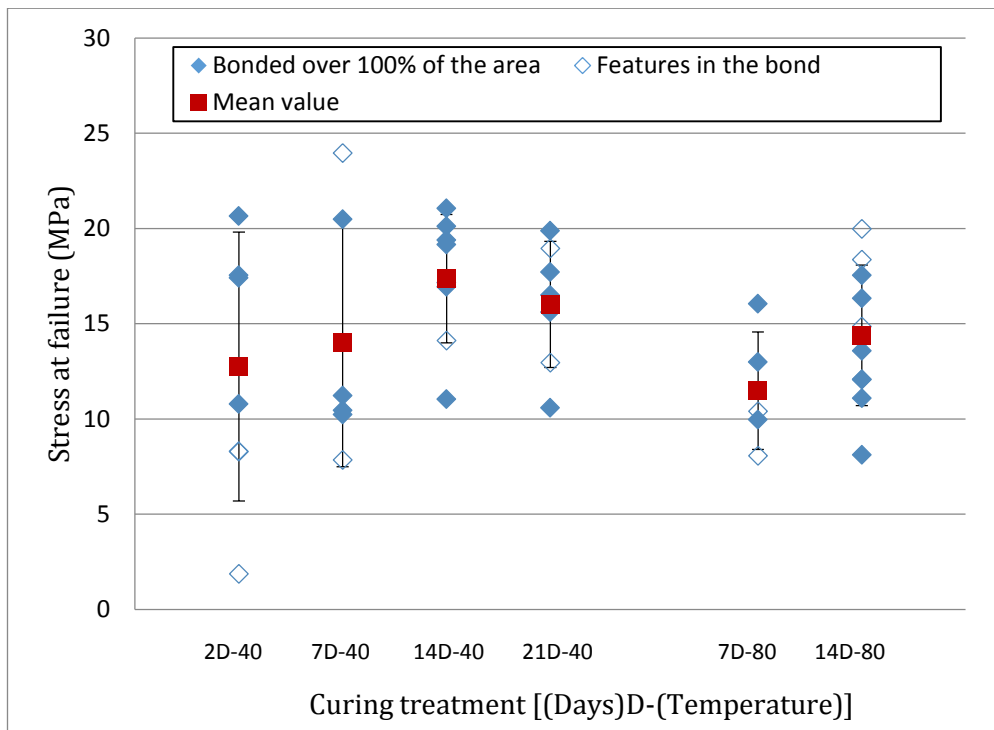


*Figure 5-2: Stress at failure of the bond depending on the curing time and curing temperature of the set. The hollow points correspond to the samples that were assessed as imperfectly bonded. The error bars illustrate the standard deviation in each set.*

## 5.2 Settling time

The settling time of a bond is the time available to slide the parts with respect to each other after contact before the bond grasps and cannot be reversibly moved in ambient conditions anymore. It is not a critical parameter to control from a process duration point of view as it ranges from a few seconds to a few minutes and therefore is negligible with regards to the curing time. However, having some control over it makes bonding easier for the operator. A very short settling time as is the case for optical contact requires pre-alignment of the parts and leaves a low margin of error, potentially decreasing the yield of adequate components and forcing reworks. A long settling time requires maintaining the parts alignment and makes the component sensitive to external events that can occur before the component holds itself. Therefore, an intermediate time between 30 and 200 seconds is often desired.

Reid [100] carried out a thorough investigation of the settling time of bonds between fused silica parts. He investigated the influence of temperature and initial concentration of hydroxide on the settling time of the bond and used the data to derive both the constant rate and activation energy of the reaction. The purpose of the trial was not to repeat his experiment but rather to study how it transferred to the other materials of interest in this project, namely phosphate glass and YAG. By changing the type of solutions and the nature of the material, the hope was also getting further insight into the chemical reactions leading to the formation of the bond.

### 5.2.1 Setup and modus operandi

The setup that was used is displayed in Figure 5-3 and described below.

The bottom part is held still thanks to a tailored crib. The loudspeaker membrane oscillates following the signal from the generator. A stiff paper band is clamped to the membrane and stuck to the top surface of the top part using double sided tape. The stiffness of the paper band ensures that the top part oscillates following the generator signal. A red diode module (633 nm) and an assembly of two adjoining photodiodes are placed on either side of the sample. A paper flag is stuck on the paper band above the sample, partially shielding the photodiodes from the light. When the paper band oscillates, the shadowed area on each diode varies and therefore the photodiodes record a periodic signal over time. The signal used is the difference between the signals from the two photodiodes.

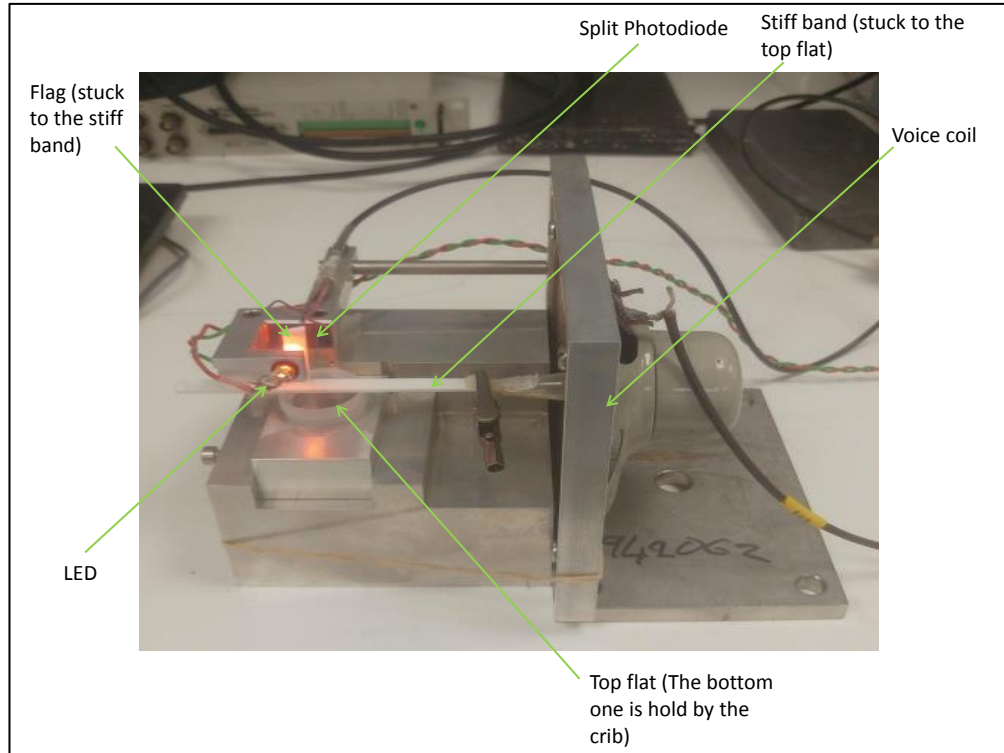


Figure 5-3: Captioned photograph of the setup for settling time measurements.

A drop of solution is placed on the top surface of the bottom part and the contact is made. The oscillating signal is then started and the photodiodes signal recorded. The measurement is stopped when the flag stops moving due to the bond settling or after ten minutes, whichever happens first. It is believed that when the bond has not grasped within the first ten minutes, the bonding failed and will not occur. A typical profile of the amplitude recorded versus time is displayed in Figure 5-4. The settling time is taken equal to the time at which the amplitude stabilizes after its more or less sudden decrease.

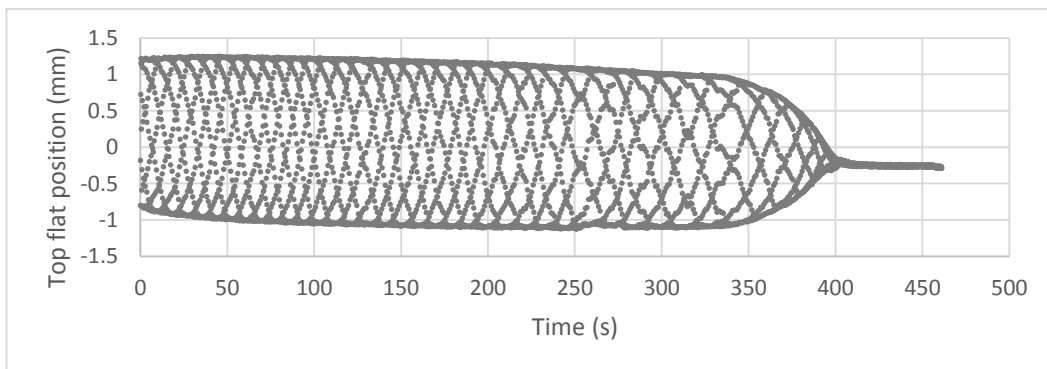


Figure 5-4: Typical pattern of a settling time measurement. In the early stage of the measurement, the top flat moves freely following the movement imposed by the loudspeaker membrane. When the bond starts grasping, the amplitude of the movement decreases until reaching a minimal value when the flat remains still.

### 5.2.2 Preliminary Study

There was a preliminary study at the University of Glasgow on the influence of various parameters on the obtained settling time with a similar layout for the setup<sup>23</sup>. The samples used were a fused silica bloc on a fused silica flat with a bonding surface of 5 mm x 10 mm. The results are summarised below:

- The settling time increases when the concentration of the hydroxide solution increases.

This is consistent with the hypothesis that the bond settles once a threshold pH, lower than the initial one, is reached. The pH decreases towards this value as the hydroxide ions present in the solution are consumed by the etched silicate. Increasing the initial concentration of hydroxide increases the difference between the initial value and the threshold to reach, delaying the settling of the bond.

- Changing the volume has no significant effect on the settling time.

This can be understood as the etching is a surface mechanism and increasing the volume of solution does not increase the area of reaction or the surface concentration of ions available.

- The settling time increases with an increasing amplitude or frequency of the sinusoidal movement imposed to the top flat.

This can be explained by the fact that moving away from a mechanical equilibrium with increasing speed (frequency) or displacement (amplitude) delays the formation of the bond by constantly pulling on the nascent bonds forming and likely breaking some of them before they can strengthen.

These results are taken as granted when carrying the trial described in the next section.

### 5.2.3 Trial

In the present work, the trial focused on the three materials used throughout the project, i.e. fused silica as a reference and phosphate glass and YAG as new materials. The samples for the various materials were of different sizes due to them not being designed especially for this trial. As a volume per area unit was used it was not believed that it would influence the results on the settling time. The solutions used were potassium hydroxide (KOH) and sodium hydroxide (NaOH) prepared to have a pH of 12 which was assessed using a Toledo pH-meter. A sodium silicate solution (noted NaSi later) diluted to 1: 6 in volume was also employed.

---

<sup>23</sup> Private communication G. Stewart.

The measurement was repeated eight times for each material and solution in order to investigate its robustness. However due to the limited amount of samples, it was necessary to use the same ones several times for this to be possible. They were rinsed abundantly with deionised water and wiped with methanol between each trial. Therefore it is believed that it did not affect the data and in fact, no correlation could be derived between the settling time and the number of times the sample was used. A few trials had to be discarded due to unsuitable behaviour of the setup following misalignment of the parts. The actual number of data points for each set is highlighted in Figure 5-5 (value in brackets).

A volume per area unit equal to  $2 \mu\text{l}/\text{cm}^2$  was used in each case. This is a larger volume than the one usually used in bonding trials (see e.g. [104][105][106]). Due to the layout of the setup, dispensing the solution on the bottom part was not easy. Using a larger volume made sure that a sufficient amount of solution was laid to prevent premature bonding by optical contacting of the parts. From the results presented in section 5.2.2, the volume of solution has no impact on the settling time and therefore this was not expected to affect the results.

The input signal to the loudspeaker was a sinusoidal signal with an amplitude of 4 V peak to peak, which converted into a movement amplitude of about 2.5 mm, and a frequency of 1 Hz. Stewart highlighted the influence of the amplitude and frequency of the signal on the settling time. The values taken here were rather based on the behaviour of the whole setup, to avoid unnecessary vibrations. As long as they remained constant through the whole trial they would be suitable to derive relevant conclusions. Given that all parameters that affect the settling time were different, it was not very relevant to try and put the values obtained in these trials in parallel with the ones from the study discussed in section 5.2.2. However it is likely that the trends observed are transferrable and knowing how the choice of parameters could have affected the trial is valuable information if further research was needed.

#### 5.2.4 Results and discussion

The results from the trial are presented in Figure 5-5. It can be seen that although the points are quite scattered in a common interval, between 200 and 550 seconds, some trends can be highlighted.

In the case of fused silica, the settling time with the three different solutions can be ranked quite easily. Potassium hydroxide, sodium hydroxide and sodium silicate yield an average settling time of  $397 \pm 84$  s,  $315 \pm 38$  s and  $235 \pm 28$  s, respectively. Therefore it is clear that the settling time is longer with hydroxide solutions than with sodium silicate solution. It also seems that the settling time using KOH is longer than for NaOH even if this is debatable as it can be seen that the difference is caused by the two outliers with high settling time for KOH. Yet studies report that NaOH is the most powerful hydroxide to etch silicate glass [158] and

as it is understood that the settling of the bond is driven by the etching of a sufficient amount of silicate from the bulk, this observation could actually be a real effect rather than a statistical one. The same reason is invoked to explain the difference between the average settling time of sodium hydroxide and sodium silicate bonded samples. In fact, if the settling of the bond requires a certain threshold of silicate in the solution to be reached, then increasing the initial concentration of silicate in the solution should decrease the settling time as it reduces the amount of etching necessary to reach that threshold, which is observed here.

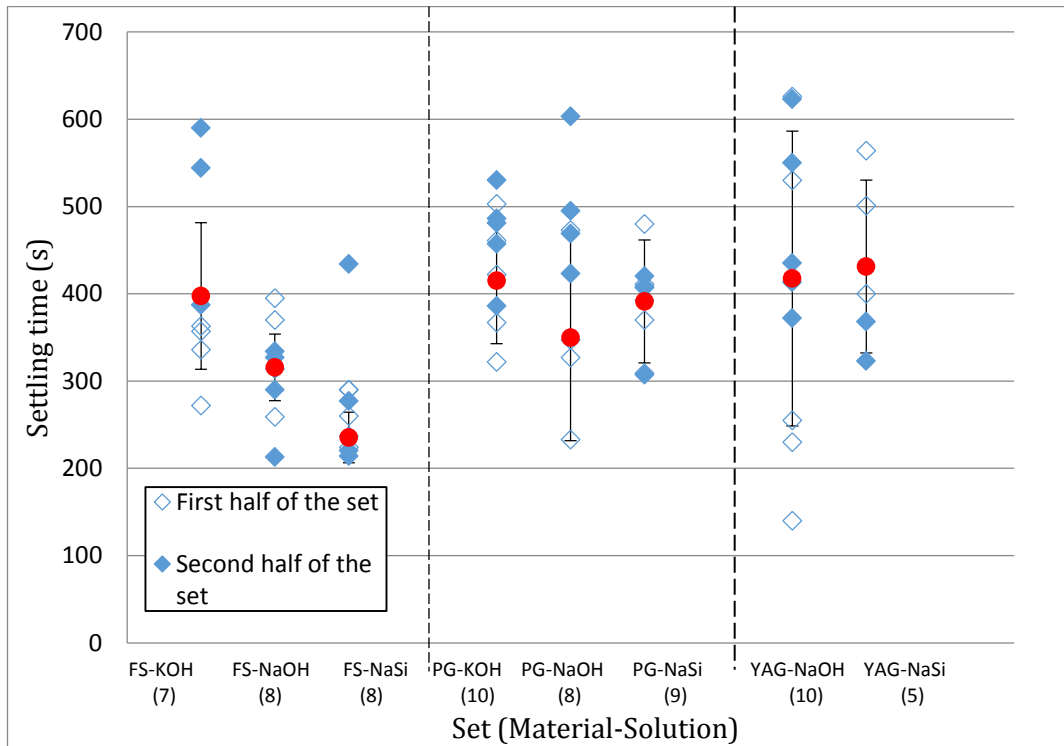


Figure 5-5: Settling time for all combinations of materials/solutions measured at RT. Since the samples had to be used several time, a distinction is made between the first half of measurements and the second one in order to highlight a possible impact of the repetition on the results. The error bars are derived from the standard deviation within each set. The numbers in brackets show the size of each set.

The results for phosphate glass are less clear as the intervals for the points largely overlap. The values obtained for KOH, NaOH and sodium silicate are  $415 \pm 72$  s,  $350 \pm 118$  s and  $402 \pm 70$  s, respectively. Based on the average values for each set and with due caution owing to the large standard deviations, some hypotheses can be formulated with regards to the chemistry of the process. The first one is that, as was the case for silica glass, NaOH is more powerful than KOH to etch phosphate glass, resulting in a reduced settling time in the case of the former. The second hypothesis, that would explain why the settling time with sodium silicate is longer than the one with sodium hydroxide, is that the bonding of phosphate glass would be driven by etching of phosphate out of the bulk. However, the presence of silicate in

the solution might inhibit the etching by saturating the solution contrary to the pure hydroxide solution. These hypotheses are speculative as the difference in average settling time could well be due to the uncertainty of the measurements.

Finally the results for YAG do not show meaningful variations as values for sodium hydroxide and sodium silicate are similar, at  $417 \pm 168$  s and  $431 \pm 98$  s, respectively but with very large standard deviation. Potassium hydroxide could not be tested in this case due to having only few samples available. Following the observations made in chapter 4, it is understood that the mechanisms that lead to bonding of YAG are different from the two other materials and this could be the source of larger standard deviation. However the results are too spread out to draw any reliable conclusion.

In the end, by varying the material and the nature of the solution, the trial allowed strengthening some hypotheses that were made regarding the mechanisms that take place in the course of bonding. Going back to the purpose of making the process easier for the operator, showing that the settling time stands between 200 and 500 seconds overall is satisfactory as it align well with the previous studies on the issue and makes sure that the time for alignment is convenient for the operator. It must be noted that due to the method of the measurement, the actual settling time of the bond is likely to be lower than these values. In fact imposing a periodic movement to the parts constantly stretches the bond and likely delays the settling. This is consistent with the observations made when making bonds without modulating the component position, where the settling time is more of the order of 90-180 seconds. Considering this effect, it can be expected that bonds that form in 500 seconds when a movement is imposed will form much quicker and fall down to the 100-200 seconds interval which is comfortable for production as explained at the beginning of the section. From there, the results from Stewart and Reid on the modifications of certain parameters (concentration, temperature, pH, etc.) to tune this settling time could be useful if deemed necessary.

### 5.3 Cleaning

The last aspect of the trials for implementation in a production environment was an investigation of cleaning tests as this had been identified as a key step to achieve successful bonds. Besides, Gooch and Housego was looking to improve their cleaning process in order to increase its yield. Therefore the benefits from the trials were multi-fold.

#### 5.3.1 Cleaning assessment method

Although the best way to assess the efficiency of a production cleaning process is to look at the yield of suitable parts, a more generic method of assessment had to be selected for

cleaning trials. There are numerous ways of doing so as described in e.g. [159]. In the frame of silicate bonding, the assessment of suitability of a surface is its hydrophilicity. In fact, a successful bond requires the aqueous solution to spread homogeneously across the surface which cannot happen if the surface is hydrophobic. Oxide-based glasses are naturally hydrophilic due to the hydroxyl radicals ( $\text{OH}$ ) that form at the surface [99]. Therefore a glass surface that does not show hydrophilic properties is a surface that has aged (and adsorbed species from the environment) or has been soiled. The case of oxide crystals is a bit more complicated as wetting properties of the surface can depend on the crystal structure as well as the surface state [161]. However no data could be found to suggest that it is the case for the materials studied in this work and therefore the hypothesis will be made that there is equivalence between hydrophilicity and cleanliness of the surface. Consequently, the Drop Shape Analysis (DSA) method was elected to assess the efficiency of the various cleaning processes. DSA uses a light source, a camera and a shape analysis algorithm to measure the contact angle between a liquid drop and a solid surface. When the liquid used is water, a hydrophilic surface leads to a well spread film whereas a hydrophobic surface leads to beading of the water drops as Figure 5-6 illustrates.

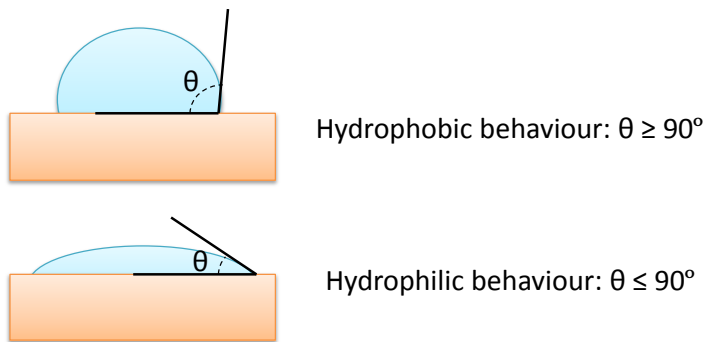
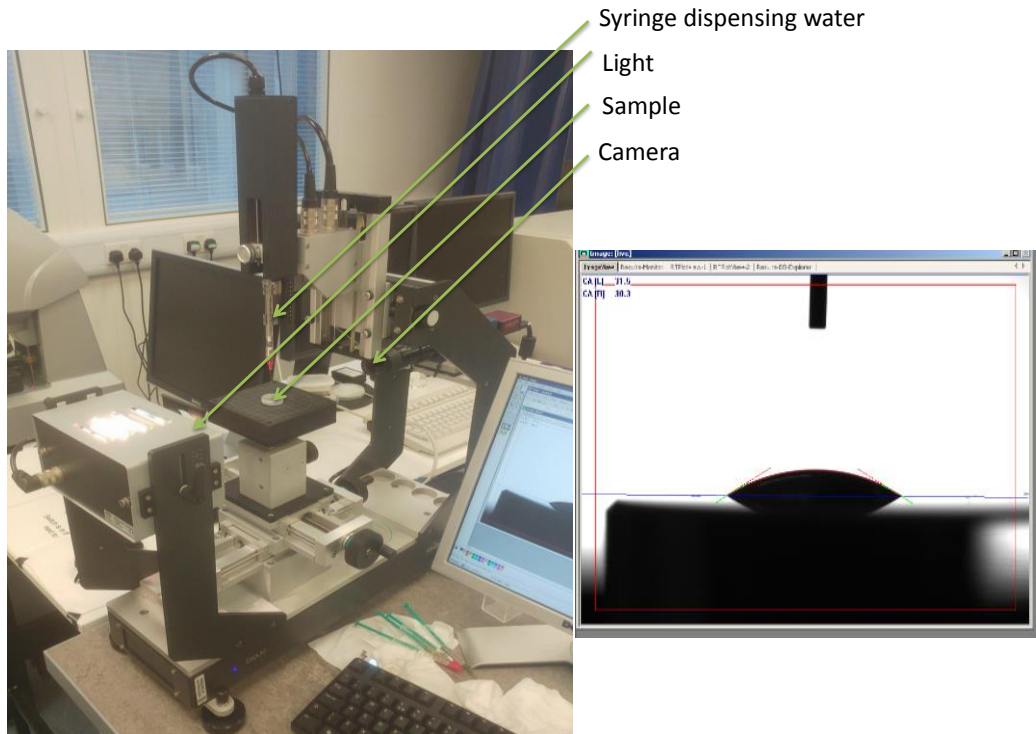


Figure 5-6: Sketch of contact angle on different surface states

A commercial device (DSA14 and DSA30 from Krüss GmbH at Gooch and Housego and at the University of Glasgow, respectively) was used to conduct the measurement. The sample is placed on a stage which stands between the lamp and the camera with the top surface being kept horizontal. A drop of distilled water is laid on the surface with a syringe. The lamp is turned on and the camera displays the image recorded. After a few seconds (enough time for the transitional spreading of the drop to end but before evaporation begins) the image is automatically analysed and the contact angle between the drop and the surface is recorded. A picture of the setup as well as a screenshot featuring the image analysis are displayed in Figure 5-7.

The accuracy of the measurement can be susceptible to effects such as reflection from the drop on the surface, tilt of the sample, etc. For this reason, the angle is measured 10 times for

each drop and, for each sample, between 3 and 7 drops (depending on the surface available) are used leading to a significant number of measurements allowing statistical treatment. The resolution of the measurement becomes insufficient below  $15^\circ$  as the drop does not stand out of from the surface enough anymore. However, high accuracy is not needed when this range of angles is reached as it already translates to a very hydrophilic surface, suitable for bonding.



*Figure 5-7: Left: DSA setup Right: Screenshot taken in the course of a measurement. The contrast between the drop and the background allows a good estimation of the contact angle.*

### 5.3.2 Cleaning processes

The regular cleaning process for bonding at the University of Glasgow is referred to as Cerium Oxide (Cerox) cleaning and consists in the following steps:

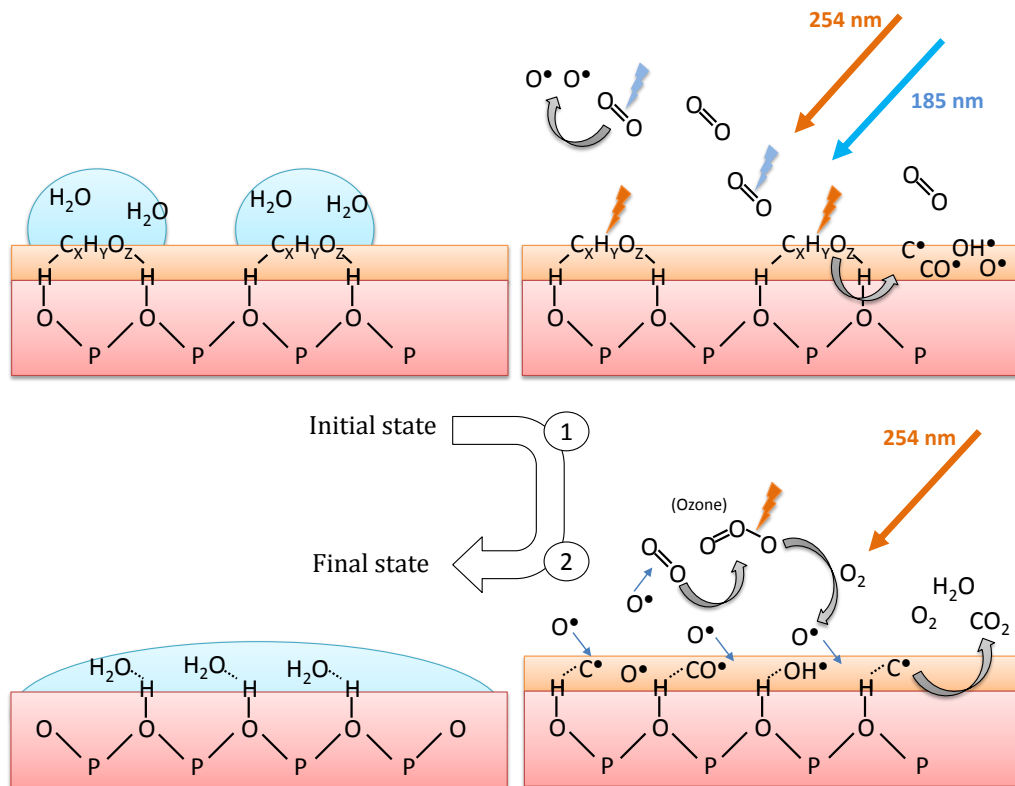
- Look at the surfaces to be bonded, use acetone to remove any stain.
- Scrub the bonding surface with a clean cloth damped in deionised (DI) water and with cerium oxide for a few tens of seconds, then rinse abundantly with DI water.
- Scrub the part with a clean cloth damped in DI water and with bicarbonate of soda for a few tens of seconds, then rinse abundantly with DI water. Look for remainder of cerium oxide, particularly on the edges and repeat as many times as needed to get rid of them.

- Rinse abundantly under DI water. Surface should look very hydrophilic (running water should form a thin sheet on the surface).
- Dry using a clean cloth damped with spectroscopic grade methanol (99.9% pure). Check surface for particles or any sign of contamination using a high brightness gooseneck lamp. Repeat until no contamination can be seen. If it can't be removed, start the cleaning procedure again.
- Wipe a single time using a clean cloth damped with high purity methanol just before bonding.

The process is less a cleaning than a surface activation process as the principle is to remove a few atomic layers to free some hydroxyl (OH) radicals on the surface and make it hydrophilic. It has been assessed as the most successful process at producing suitable surface state for Hydroxide Catalysed Bonding and is particularly effective for cancelling aging effects of the surface of older parts [160]. However the process has several drawbacks that make it unsuitable for production.

First, as a result of the scrubbing, the surface figure can get damaged. It has not been an issue for structural assemblies but could come into play for optical parts. Also, it is a quite cumbersome process and its duration is directly proportional to the number of parts as they have to be cleaned one by one. Therefore, although it is suitable for one-offs, any moderate to large sized set takes a long time to prepare which is the opposite of what production tries to achieve. It is also a dirty process as it uses powder compounds including cerium oxide that does not dissolve in water and therefore is tedious to clean. This means the process is not suitable for a clean room environment, where the bonding should take place, and increases the risk of cross contamination to other optics or tools. This requires several considerations to be taken into account for the implementation of a designated area for the cleaning/bonding process. Finally the process is not suitable for thin, very small, or more generally fragile samples due to the handling and mechanical action required. Samples could still be mounted on a back plate if needed but this makes the process even more complicated.

All these considerations suggested testing alternative cleaning processes that would be easier to implement. The process brought forward as a potential replacement was the UV/Ozone method which uses UV light to generate metastable ozone that then reacts with organic compounds [162]. For this process, the sample surface must be in an already rather clean and fresh state so that surface contaminants are not in the form of particles but rather chemical deposits. Generally speaking samples taken out of the factory that followed the 7-stage ultrasonic cleaning process (see Appendix B) will be suitable to endure the treatment. A cautious wipe with acetone can be made to prepare the surface.



*Initial state (top left): Water is beading on the surface due to organic contaminants inhibiting the hydroxyl ( $\text{OH}^\bullet$ ) radicals*

*Step 1 (top right): Contaminated surfaces are put under UV light in ambient atmosphere. The 185 nm wavelength breaks dioxygen molecules present in the air into very reactive  $\text{O}^\bullet$  radicals while the 254 nm wavelength breaks the organic compounds present on the surfaces into more reactive species that remain bound to the surface.*

*Step 2 (bottom right): After a few minutes, the 185 nm light is shut off while the 254 nm remains on. The 254 nm light breaks the bonds of the ozone molecule formed by the reaction of  $\text{O}^\bullet$  radicals and dioxygen, freeing more radicals to react with the remaining contaminants and destroying the toxic ozone ( $\text{O}_3$ ) gas. The various products of reaction react to form volatile  $\text{CO}_2$ ,  $\text{O}_2$  and  $\text{H}_2\text{O}$  that desorb in the atmosphere.*

*Final state (bottom left): The hydroxyl radicals are freed from the contaminant layer and can form hydrogen bonds with water molecules, greatly increasing the hydrophilicity of the surface and hence the spreading of the water drop.*

*Figure 5-8: Step by step illustration of UV/Ozone treatment, from the initial hydrophobic state (top left) to the final hydrophilic state (bottom left).*

UV/Ozone treatment is most effective at removing organic compounds that have been adsorbed onto the surface and that inhibit the reactivity of hydroxyl radicals. A combination of 185 nm and 254 nm wavelengths are used to remove these contaminants. The

mechanisms involved are described in Figure 5-8 with phosphate glass taken as the bulk material for illustration.

It can be seen that the process circumvents the various obstacles met with the implementation of the Cerox cleaning. In fact, UV/Ozone is clean, does not require extensive manipulation of the samples and increases yield for medium to large size batches of samples because a large number of samples can be cleaned in a UV/Ozone enclosure at the same time. It is also convenient for small parts or hard to reach ones. However, the process comes with its own drawbacks. First it is a finishing process and not a self-sufficient one. The samples have to come in an already good surface state as the process will not remove particles that are non-organic or too large. As said before, this should not be an issue as samples that come from the factory endure the 7-stage ultrasonic cleaning which should leave them free of such particles. The second and more problematic obstacle is the hazard occurring from the process. The lights used are in the UV-C and UV-A parts of the spectrum which are dangerous for organic tissue. Therefore they need to be shielded and the safest option is to use an interlocked closed box. Ozone is also a highly poisonous substance which means that the box has to be sealed during the whole process and the ozone levels monitored outside and inside the box to indicate when it can be opened safely. The University of Glasgow built a setup that fits both these safety requirements. Yet, for implementation in a production environment, it is more likely that a commercially available solution will be sought as it will be the most convenient way to tackle safety issues. Last but not least, the process excludes its own category of samples, this time based on the material they are made of. Most of assemblies containing organic parts (e.g. plastic compound) will have to be assessed for suitability as these can get damaged in the process. The use of UV light can cause light induced damage (as introduced earlier in this work) in inorganic material too which can result in the appearance of colour centres or tarnishing in the material. Circumventing this issue would require shielding the UV light inside the box while still allowing the ozone to circulate. It is feasible but will require tailored solutions rather than off-the-shelf commercial apparatus which can be expensive.

In the end, UV/Ozone cleaning seems to be more suitable for implementation in the current production process. It would fit well as a finishing process in the current production line and its major issue, its potential hazards, can be avoided by investing in tailored commercial solutions. However, to validate it as a solution, it had to be proven that the performances of the cleaning matched those of the previously chosen Cerox cleaning. This was the focus of the following trials.

### 5.3.3 Trials

#### 5.3.3.1 *Materials for silicate bonding*

The first part of the trials focused on the materials used in the bonding trials, i.e. phosphate glass, YAG and sapphire (which although not introduced in this work was of interest for other projects). It is not clear how much the efficiency of a cleaning process depends on the material and therefore it was decided to directly make the tests on the relevant ones. The trials were made at the University of Glasgow using their in-house built UV/Ozone cleaning device, a picture of which is displayed in Figure 5-9. The bulbs used generate the UV light and the ensuing generation and decay of ozone had been quantified. As a result, it takes 11 min to reach a ceiling concentration (about 225 ppm) of ozone and 15 min for it to decay down to safe level under the action of UV light. These were the durations used in the following trial.

The size and number of samples varied between the materials as they were based on the bonding trials. For each material, the set was measured in its initial state which could be either straight out of the factory or left in the atmosphere for some time (weeks to months). Then the set was split in two equally sized sets. One was cleaned using the Cerox cleaning process and the other using UV/Ozone. The purpose was to observe the relative change in hydrophilic properties rather than an absolute measurement of the cleanliness as the latter can depend on factors independent from the cleaning (surface roughness, crystalline structure, etc.). For each sample in each set, between 5 and 7 drops were used depending on the surface size available. This allowed averaging over the surface of the sample and be less sensitive to local effects. In the end, the measurement was taken on at least 10 drops for each material and each cleaning process. The results from the contact angle measurements are displayed in Figure 5-10.

The test could be made twice on phosphate glass thanks to having several batches of samples. For sapphire however, the very low number of samples forced the use of both surfaces of each sample. The Cerox cleaning was done on one face and the UV/Ozone on the other which is why the initial state for the two “sets” had to be measured twice. It can be seen that there was no significant difference from the values of the blue bars within each of the three sapphire sets.

The relative reduction of contact angle expressed by the ratio  $\frac{\theta_{final}}{\theta_{initial}}$  is displayed in

Figure 5-11.

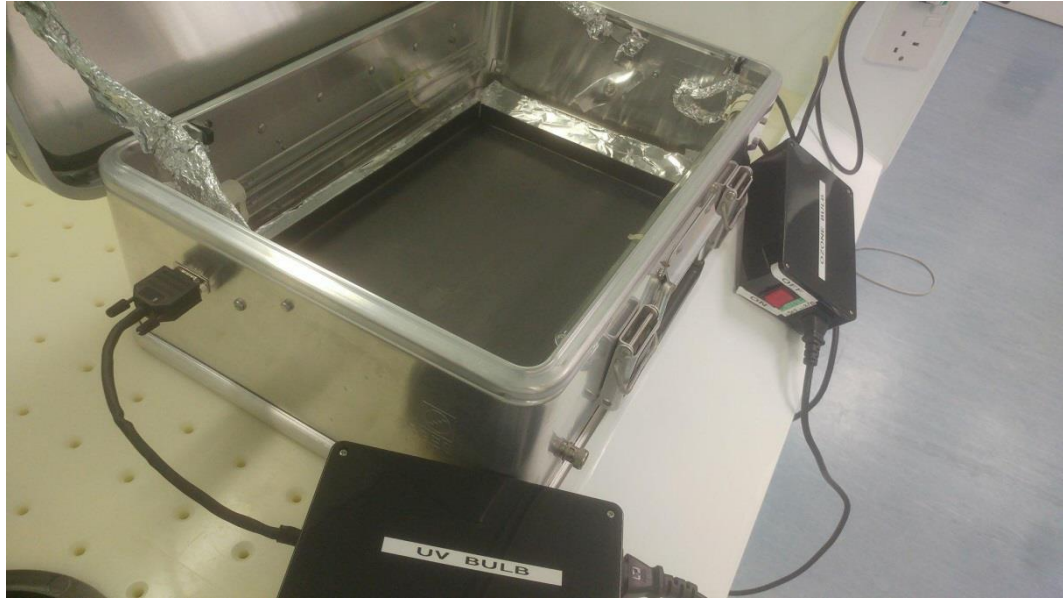


Figure 5-9: Photograph of the custom UV/Ozone box available at the University of Glasgow. Two low pressure mercury lamps are available to produce the UV radiation. One of the bulbs produces both 185 and 254 nm radiation whereas the former is blocked for the second bulb, only leaving the 254 nm through and allowing the destruction of ozone.

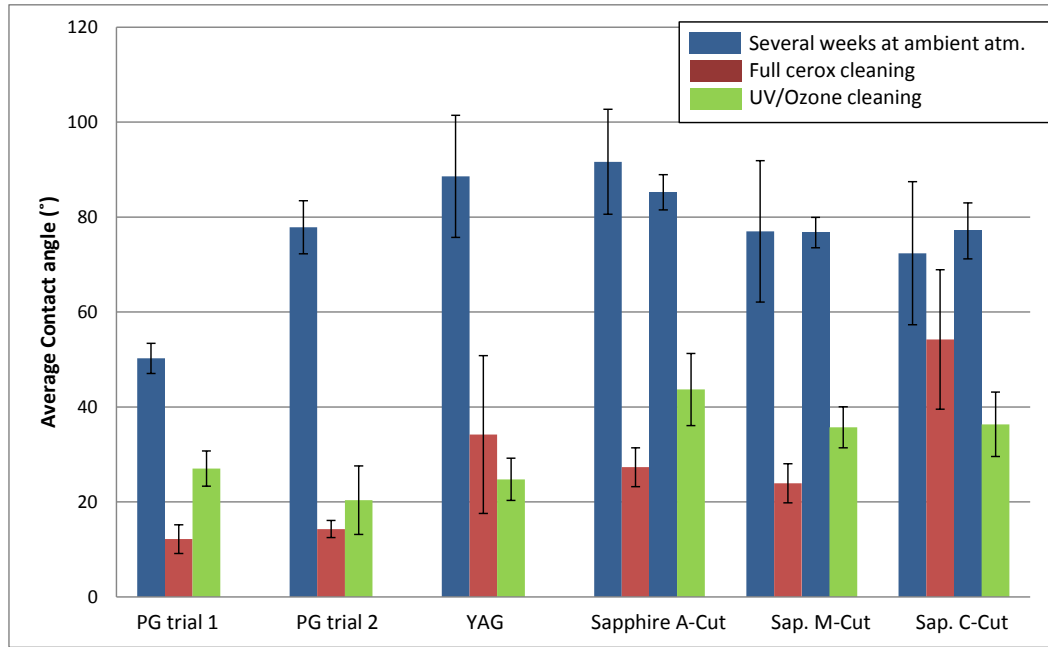


Figure 5-10: Averaged contact angle of the water drop on surfaces of various materials at various stages of cleaning. The error bars represent the standard deviation within each set.

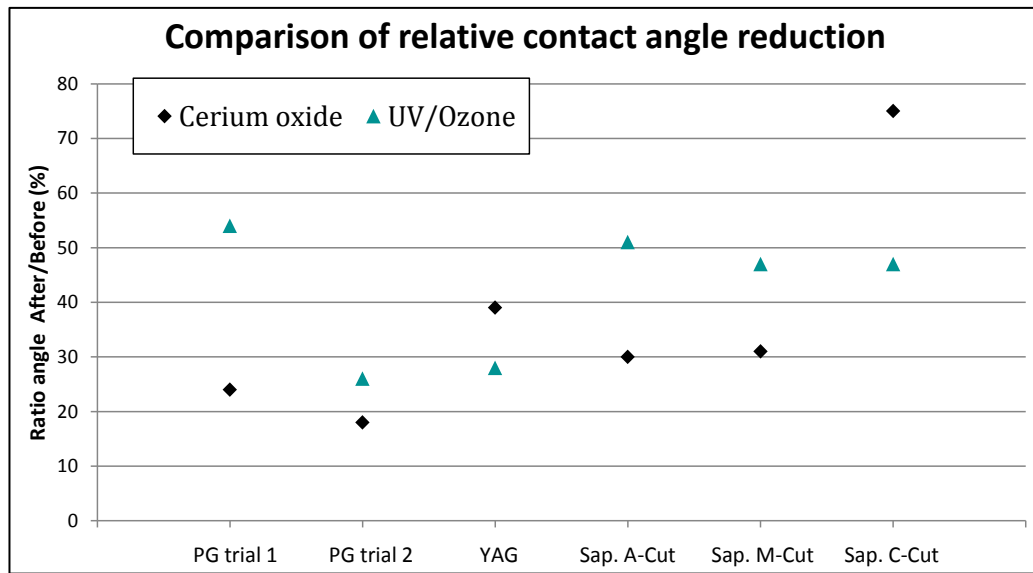


Figure 5-11: Relative change in contact angle depending on the material and the cleaning process.

The first observation from these results is the efficiency of both processes to increase the hydrophilicity of the surfaces. The contact angle between the drop of water and the surface is reduced by at least 50% in most of the cases for both processes. The exceptions are for PG1 with UV/Ozone and for the sapphire C-cut cleaned with cerium oxide. In the case of the former, the initial state already shows a relatively low contact angle and therefore the final angle is still satisfying at about 25°. In the case of the second, an explanation was sought in the crystalline structure of the material but no data were found to explain the result and it might just have come from an effect of the low set size.

In agreement with the previous knowledge, the cerium oxide process remains a more efficient process in most cases, with the possibility to consistently reach superhydrophilicity (contact angle < 10°) in the case of phosphate glass. The crystal samples do not go that low in contact angle likely due to their lattice structure which makes the removal of atomic layers more difficult. However they still show a large improvement of contact angle and reach the range of 25°-35° which has been observed to be suitable for bonding.

UV/Ozone cleaning, although less efficient than cerium oxide, still shows promising results. The contact angle reached for phosphate glass and YAG is about 25° with a reduction to about 30% of the initial value. In the case of sapphire, the values of 35°-45° obtained might however be borderline for successful bonding. Further trials on sapphire with larger set sizes could be of interest to see if this gap is consistently obtained or if the hydrophilicity can be increased further.

### 5.3.3.2 Case Study: Lithium Niobate transducers

Given the advantages of the UV/Ozone technique over the cerium oxide as they were detailed in section 5.3.2 and the fact that it also yielded surfaces of good hydrophilicity, it seemed relevant to try and implement the process in the production line. To that end, it was decided to use the process on samples used by the company.

The second part of the cleaning trials focused on Lithium Niobate ( $\text{LiNbO}_3$ ) which is a crystalline piezoelectric used as transducer in acousto-optic devices. It constitutes a significant part of Gooch and Housego's activity and therefore there was a drive to improve the yield on good parts, which involved the cleaning step. Moreover, transducers enter the category of thin parts for which scrubbing with cerium oxide is not practicable due to the risk of breaking which makes UV/Ozone cleaning all the more appealing.

In the course of the current manufacturing process, transducers are put into contact with wax that must be entirely removed before they can go to further steps. The current cleaning process involved soaking the sample in a hexane solvent to dissolve the wax before removing the hexane with acetone. The organic deposit from the hexane and acetone then need to be entirely removed. For the trials, samples have been taken after this cleaning process to be tested.

The set size was about 40 samples divided equally into three sets. The first step consisted in measuring the contact angle for all the samples. Five measurements were taken on each sample to probe several locations on the surface. Therefore the number of measurements for each set was about 60 which allowed a good statistical study. The second step was to measure each set after they were given a wipe with acetone to make sure they started in similar condition. This will constitute the reference to assess the efficiency of the various cleaning methods. In the third step, the three sets endured different cleaning processes and were measured again.

- The first set was given a wipe with spectroscopic grade methanol.
- The second set was exposed to UV-light at 254 nm for about 40 min. The 185 nm was not used here to test the efficiency of ozone-free cleaning. This is interesting as it allows getting rid of the poisonous agent in the process.
- The third set was exposed to ozone for about 25 min while the UV light was primarily shielded inside the box. This is to test the efficiency of cleaning with ozone alone which could pave the way to clean UV-sensitive materials.

The results are displayed in Figure 5-12. Looking at the figure, it must be pointed out that there seem to be a difference in the initial contact angle between the different sets (bar heights for each acetone set). Its origin is not known as the samples were picked randomly

from the raw set and prepared on the same day with the same chemical. As the uncertainties between the set overlap somewhat slightly it will be taken as a random effect as this does not affect the interpretation of the results

In fact, from the data presented, there are noticeable gaps between the samples cleaned with acetone and the ones that endured any of the three further steps as the contact angle goes from  $60^\circ$  to  $30^\circ$  using methanol, from  $50^\circ$  to  $10^\circ$  using UV and from  $45^\circ$  to below  $10^\circ$  using ozone (the values are rounded as the DSA does not allow accurate measurement and the focus is on the trend rather than the value). Therefore methanol already brings some improvement as a follow-up step to the acetone wipe while UV and ozone both allow reaching superhydrophilic surfaces. It is expected that methanol would render a more hydrophilic surface than acetone as it is hydrophilic itself as well as more volatile and therefore leaves less residue on the surface. This is the reason why, despite its toxicity, it is used as a preferred solvent in the cleaning process as it is done at the University of Glasgow. The fact that either UV or ozone can work independently is a good sign for implementation in production as it allows removal of the drawbacks of one or the other factor.

In a first step it was decided to attempt UV cleaning at Gooch and Housego to make further trials and discard the ozone part as the safeguards for the latter could not be implemented easily. A commercial UV box (PhoneSoap 2.0)<sup>24</sup> was bought for in-house cleaning trials. It is an interlocked box providing 254 nm light with the bulbs less than 1 cm away from the surface.

For the trial, 12 transducers were picked from the factory. They were tested for cleanliness four successive times, with a cleaning step between each. The first measurement was taken with the samples as received. The second measurement was taken after wiping the samples with acetone. The third measurement was taken after 20 min exposure to UV light using the UV-box. The last measurement was taken after 10 additional minutes of exposure due to observations on the results obtained in the third step (see below). For each sample in each measurement, the drop was laid at three different locations to assess the homogeneity of the surface state.

The results are displayed in Figure 5-13.

---

<sup>24</sup> <https://www.phonesoap.eu/products/uv-sanitizers-chargers/phonesoap-white>

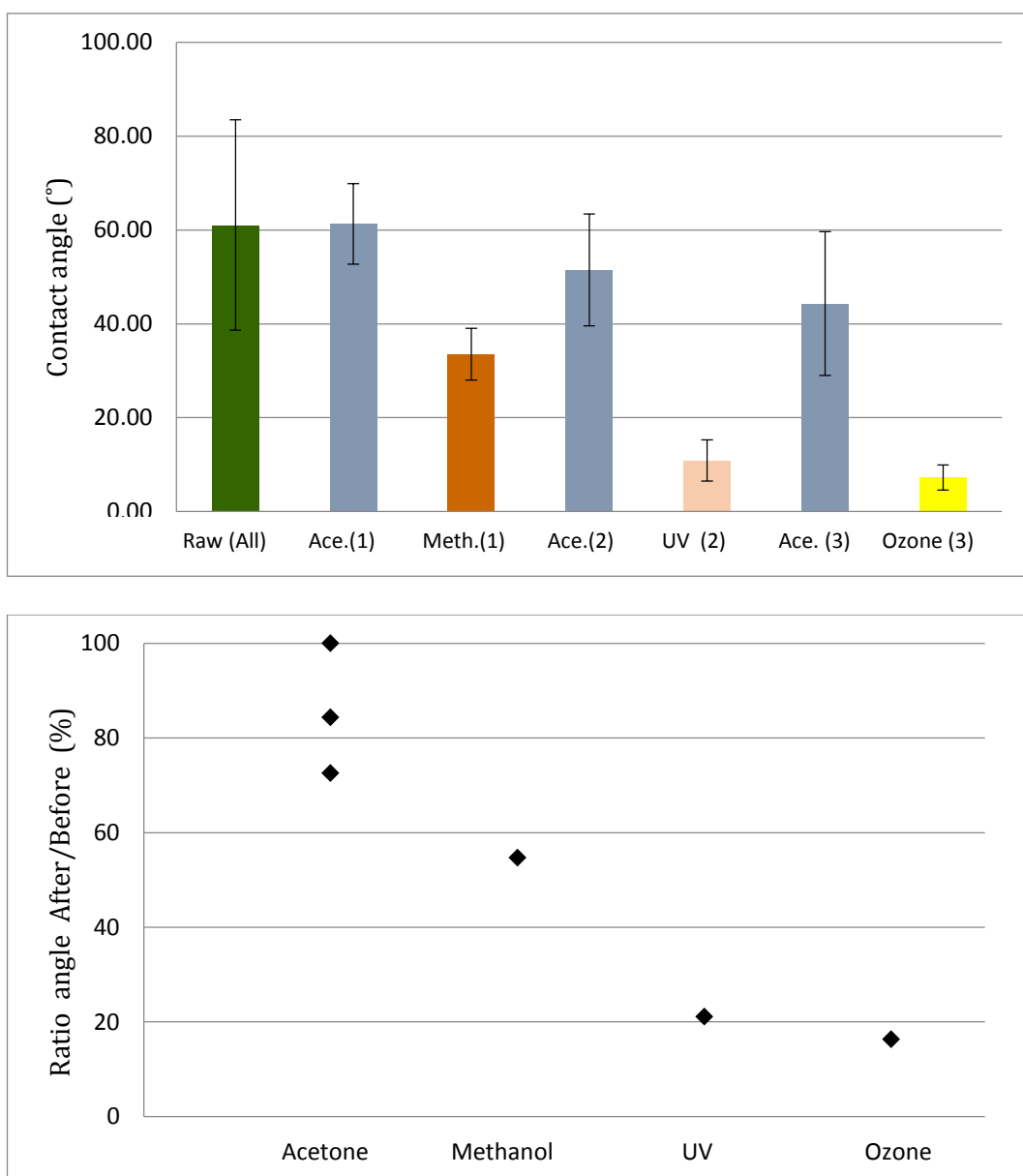
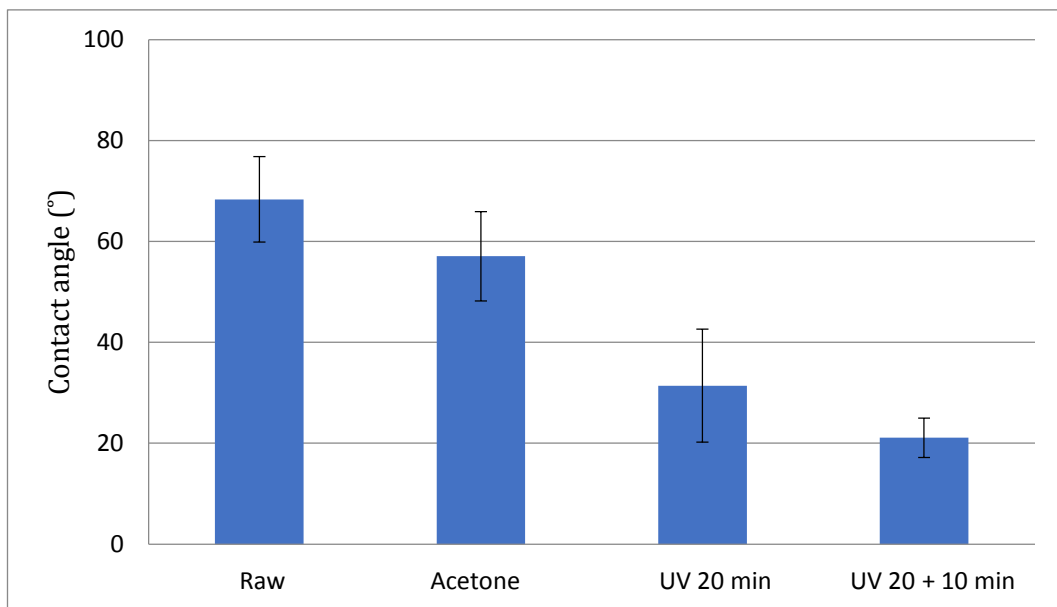


Figure 5-12: Top: Contact angle measurement on Lithium Niobate transducers at various stages of cleaning. The number in brackets denotes the set number. The error bars represent the standard deviation of the set. Ace: Acetone, Meth: Methanol. Bottom: Relative contact angle reduction. The value for the acetone sets are taken with respect to the raw samples and the values for the other methods are taken with respect to the respective acetone set (see top).



*Figure 5-13: Average contact angle of water on Lithium Niobate transducer in the course of the cleaning trial. Each cleaning step is carried out on the set resulting from the previous one. The black bars represent the standard deviation within each set*

The progress made between the successive steps appears clearly. From the raw samples, an acetone wipe allows reaching a contact angle of about  $55^\circ$  which compares well with the value of  $60^\circ$  already obtained in the previous trial. Then, UV exposure increases the hydrophilicity of the surface further and the contact angle measured is about  $30^\circ$ . It is not as low as the  $10^\circ$  reached in the previous trial and it can also be seen that the uncertainty has increased compared to the earlier stages. It was observed that the samples at the centre of the box, straight under the bulbs, were more hydrophilic (contact angle about  $15^\circ$ ) than the ones at the edge of the box (contact angle about  $40^\circ$ ). This suggests that having the bulbs too close to the surface will degrade the homogeneity of the lighting in the box, which seems to have a direct influence on the results obtained. For the last trial, the samples previously at the edge were brought to the centre while the ones already showing a good level of cleanliness were taken out. It can be seen that with 10 additional minutes at the centre of the box, the samples could reach the range of high cleanliness. There is still a gap with the  $10^\circ$  obtained in the previous trial which could be accounted for the difference in exposure time, power or setup layout. However the principle is proven to be working.

In the end, the trials showed that using a cheap commercial device, it was possible to reproduce the observations on the cleaning trials made at the University with a more thought-out setup. This is very promising for an implementation in production as it would be both safe and practicable to provide a UV-box for each operator bench to carry out the finishing cleaning step before the samples go further in their processes. However it is not known yet whether these results obtained on the test bench will convert in an increase in the

yield of the follow-up assembly steps. Due to the high level of activity in the factory, it was not possible to bring the process to the production line to make such tests but it clearly has potential and may be used in production at a later time.

The other trial of interest that could not be done within the timeframe of the project is the determination of the minimal exposure time required to obtain a yield higher than a certain percentage. It is noticeable, both from theory and experiments, that the exposure time influences the final surface energy. The trade-off between process time and yield is the main data required for an optimised production. However such a trial would have relied on the one advocated above to be done to link the process to the yield.

#### 5.4 Conclusion

This chapter has focused on highlighting some aspects of how silicate bonding, which is a process designed on a laboratory bench test, could be adapted for larger volumes of production and what the issues to address are. Although the process could not be brought all the way to the production line, these trials will still be a stepping stone for such an implementation to be done once they are complemented.

In the first part, it was shown using bonded quartz that increasing the curing temperature could help reaching the ceiling strength of the bond more quickly compared to room temperature. From a duration of four weeks at room temperature as reported by Beveridge, the curing step was brought down to two weeks when carried out at 40 °C which represents a significant saving of time in a production frame. From these initial trials, raising the temperature to 80 °C did not seem to bring any improvement time-wise. Further studies at 80 °C could be conducted but at the moment curing at 40 °C is recommended for quartz bonding until additional trials are done to find the optimal temperature that minimises the curing time while maintaining suitable bond properties.

The second part addressed the question of the settling time of the bond, with the purpose of making the process convenient for the operator. The trials did not focus on optimising this settling time but rather on getting an insight in the chemical mechanisms leading to bonding of new materials, i.e. phosphate glass and YAG. If the mechanisms were identified to be similar to the ones known for fused silica, then it was likely that the results gathered by Reid in previous studies on the matter could be applied to these materials. From a production point of view the settling time already falls in the desired range (400 s with movement which is expected to fall down to around 150 s with the parts remaining still) which is a positive result. The data gathered suggest that the behaviours are in fact different and hypotheses could be formulated on why this is the case. In agreement with the previous knowledge, it was shown that in the case of fused silica, reaching a threshold in silicate concentration in

the solution through etching of the surface was the determining factor for the bond to settle. Therefore solutions that etch more (sodium hydroxide) or contain an initial amount of silicate (sodium silicate) allow quicker settling than e.g. potassium hydroxide. However in the case of phosphate glass, having silicate in the initial solution does not seem to accelerate the settling time compared to a solution that only etches phosphate out of the bulk (sodium hydroxide). Hence, the hypothesis is made that the mechanisms are different but the fact that the standard error on the results is large could mean that this difference must be treated with caution. The trials should be redone on a larger scale and if it is proved that the hypothesis stands, the works from Reid and Stewart could be repeated to obtain conclusions tailored to phosphate glass. An experimental plan has been proposed at Gooch and Housego in the case that the tunability of the settling time becomes of interest later on,

Finally, the last part partially deviated from the process of bonding to focus on the more general issue of the cleaning processes within Gooch and Housego. It was identified that the current dirty cleaning process consisting of scrubbing the parts with a solid compound could be replaced by a clean UV/Ozone process with little loss of performance and high upside with regards to the ease of implementation. From the UV/Ozone process, a UV-only treatment was attempted and proved to be efficient enough to be worth bringing in-house. The next step in the trials, which was to bring the alternative cleaning step into the manufacturing process of Lithium Niobate transducers to see the change in yield, could not be done without interrupting the production. Due to the level of activity in the company, there was no opportunity to do so. That is the reason why, even if the process was deemed mature on the research test bench, it was currently put on hold before it can make the transition to production. The guidance for complementary trials was passed on so that they can be done at a later date.

---

## 6 General conclusion and outlooks

---

The purpose of this work was to investigate the potential of Hydroxide Catalysed Bonding (HCB) or Silicate Bonding (SB) for applications in the photonics industry. Selecting two common materials used as solid-state laser gain media, phosphate glass as an amorphous material and YAG as a crystalline material, trials on properties that had been only sparsely studied were carried out.

The first requirement was for the bond to show some non-negligible strength to allow handling and manufacturing processes to be carried out. This was successful by a large margin in the case of SB samples but only moderately so with HCB samples as the strengths obtained were low in the case of phosphate glass and the sample debonded under test in the case of physically small YAG samples. Since manufacturing was successful with larger samples, it is thought that edge effects could be occurring for samples with small bonded surfaces and could prevent manufacturability down to low sized-components. For this reason, SB samples which have shown significantly higher strengths look more promising from a mechanical point of view.

The second property of interest was the reflectivity of the bond. Although interest for both reflective and transmissive interfaces was described, this work strongly focused on working towards transmissive ones. The quoted tolerance for the reflectance of a surface or interface in a transmissive photonic component was at 0.1 % and therefore the objective was to see how good the bond performed with respect to that value. HCB phosphate glass met the requirement with a comfortable margin whereas both SB phosphate glass and SB YAG ended being above this value. However, it was shown that diluting the solution more could bring the reflectivity down and therefore that the requirement might be reachable with further work. It is possible that samples prepared in such a way would lose in strength and therefore the optimal solution might be found in a middle-ground between the two types of samples studied. Finding this compromise for the concentration of the solution, depending on the application, could be an avenue for further work.

The third property that was considered was the Light-Induced Damage Threshold of the newly produced interface. In this case, the quality of the bond is unequivocally linked to a high threshold and values around 1 GW/cm<sup>2</sup> were mentioned as a target. Most of the bonds tested seemed to meet the requirement with a good margin and therefore the trials were not significantly extended. It is not certain which parameters can affect the threshold and more trials should be carried out when specific applications for which there is concern make their appearance.

Aside from those properties that were tested with some possible applications in mind (such as composite laser rods), this project also presented numerous results to facilitate further work on the technique and provide information on what would be needed for its use in a production line. The reflectivity measurement setup was upgraded several times progressively increasing the quality of the measurements and the model and layout are now optimised for sample characterisation and derivation of bond thickness and refractive index in a non-destructive way.

The cleaning trials carried out have allowed the validation of an alternative process, UV/Ozone cleaning, to replace with little loss of performance the current scrubbing process where the latter would not be suitable or would be too time-intensive. There is still a whole area to explore with these results as it was not possible to take the process to the production line and prove an increase in the yield of suitable parts but the tests that were carried out on the bench are very promising.

Finally, all these trials further increased the expertise of the group on a bonding technique which keeps attracting interest across a number of fields. Study of the bonding mechanisms for YAG and phosphate glass through settling time and etching measurements, with the support of the reflectance trials, allowed hypotheses on the processes that occurred specifically for each of those materials to be made. Particularly, YAG seems to display a singular behaviour as it looks like the bulk does not get etched but instead that the bonding material diffuses into the surface, creating a layer that mitigates index mismatches. This is encouraging for the prospect to work with a larger range of materials, in particular some that would not be expected to produce a bond of good quality based on prejudice regarding the chemistry.

An axis of work that was introduced but not dealt with in the thesis is the one of the thermal-induced stresses that develop in the bond when the sample experiences heating or cooling from the temperature at which it was prepared. These stresses can lead to the failure of the component and therefore must be anticipated. Experimental trials would require numerous samples to obtain statistical results and therefore preliminary work should be carried out on analytical models and using Finite Elements Analysis. The Institute of Gravitational Research has already used FEA of bonds for various projects and it is expected that further progress in this direction will be made soon.

---

## Appendix A: Material characterisation

---

A various range of materials have been used throughout the project. Some of them were selected for applications purposes while other to test generic properties of the bonds. This section provides some details on the materials used.

### A.1 Material composition

Since datasheets were not always available for the material used, chemical analysis was carried out on samples to determine their chemical composition. This was particularly relevant for glass as the composition is not as set as for crystals and can significantly vary from a batch to the other.

#### A.1.1 Method

To study the chemical composition of the materials, a sample of each set was used for Energy Dispersive X-Ray Fluorescence (EDXRF) analysis using a Shimadzu EDX-8100 spectrometer. EDXRF uses X-Rays to excite electrons from the atoms of the first few outer layers of the material. Upon relaxation, these electrons release a photon with energy characteristic of the element through fluorescence. By analysing the fluorescence spectrum emitted it is possible to estimate qualitatively (and with calibration even quantitatively) the composition of the material.

#### A.1.2 Phosphate Glass

Phosphate glass has been the core material of investigation in this project. G&H manufactures and sells phosphate glass products and therefore the material was selected with specific applications in mind. The material used was sourced from Glass Technology Services Ltd (Sheffield, UK). It was developed and tailored for G&H needs and the formulation of the melt evolved between different sets of experiments but no datasheet could be obtained. The results of the chemical analysis are displayed in Table A.1-2. Since the material is made by melting oxides together, the results are expressed as weight percentage of oxides rather than chemical elements. These are derived by the software used.

## APPENDIX A: MATERIAL CHARACTERISATION

---

*Table A.1: Phosphate glass composition 1 (PGC1)*

Oxide	Approximate Weight percentage
P2O5	65
BaO	10
Al2O3	10
K2O	7
Various	< 5 each

*Table A.2: Phosphate glass composition 2 (PGC2)*

Oxide	Approximate Weight percentage
P2O5	55
Yb2O3	20
BaO	20
Various	<5 each

From the weight percentage and the molar masses of the oxides, it is possible to derive the molar composition of the glass through equation A.1.

$$n_i = \frac{m_i}{M_i * \sum_i \frac{m_i}{M_i}} \quad (\text{A.1})$$

With  $n_i$ ,  $m_i$ ,  $M_i$  the molar percentage, weight percentage and molar mass of the oxide, respectively. From equation and discarding the negligible contributions, the molar compositions of the glass are summarized in Table A.3.

*Table A.3: Equivalent molar composition of PGC1 and PGC2 (in percents).*

	P2O5	BaO	Al2O3	K2O	Yb2O3
PGC1	65	10	10	10	x
PGC2	60	20	x	7	10

It can be seen from these measurements that PGC2 is doped with a rare-earth ion (Ytterbium) whereas PGC1 is undoped. From the difference between the two compositions it is expected that some variation of the properties of the glass will be witnessed. The main concern is the potential for difference in refractive index which may skew the results if not accounted for. As no data sheet was available from the supplier, the refractive index had to be measured in house.

### A.1.3 YAG

YAG has been the second main material of interest in this study. It is also applications oriented but tackles the issue from the perspective of crystalline materials. As a crystal, the composition is more standardized than for glasses and it was not expected that large variations in the composition would be witnessed across the providers. The material used for the strength test comes from off-cuts from The Roditi International Corporation Ltd. They were not documented and were therefore tested for composition. The material used for the reflectivity tests were provided by Newlight Photonics and the datasheet specified pure undoped YAG.

The results from the EDXRF on the samples from Roditi are displayed in Table A.4.

*Table A.4: Composition of YAG samples provided by Roditi.*

Oxide	Weight percentage	Molar percentage
Y <sub>2</sub> O <sub>3</sub>	83	70.9
Al <sub>2</sub> O <sub>3</sub>	15	28.4
Various	<1 each	<0.5 each

### A.1.4 Silica glass

The fused silica used was the Corning 7980 fused silica. It was not tested for composition.

## A.2 Refractive index measurement

The reflectivity measurements carried out in this work required the refractive index of the substrate to be known with good precision. Given the various origins of the materials and sometimes the absence of datasheet, it was decided that in-house measurement of the refractive index would be necessary. The method selected to do so was the measurement of the beam deviation by a material slab of refractive index  $n$  and thickness  $d$  as illustrated in Figure A.1 and described below.

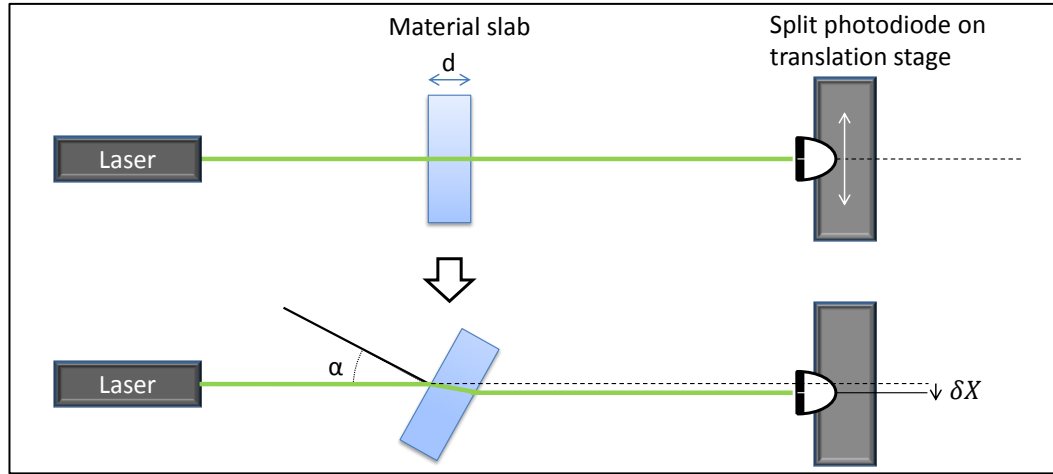


Figure A.1: Principle of refractive index measurement for bulky materials.

In the initial configuration, the beam hits the slab at normal incidence and is sent to a split photodiode set on a translation stage. The photodiode is centred on the beam when the power on each of its halves is the same which is assessed by measuring a difference of signal equal to zero on an oscilloscope. The slab is then rotated by increments of  $5^\circ$  or  $10^\circ$  (the thickness of the slab can limit the resolution) up to grazing incidence.

When the slab is rotated by an angle  $\alpha$ , the beam position on the photodiode is shifted by  $\delta X$ . Through geometrical considerations, the relation between  $\alpha$  and  $\delta X$  is given by equation A.2.

$$\delta X = d * \sin(\alpha) \left( 1 - \frac{\sqrt{1 - \sin^2(\alpha)}}{\sqrt{n^2 - \sin^2(\alpha)}} \right) \quad (\text{A.2})$$

For each angle, the photodiode is translated and positioned so that it is centred on the beam. The deviation is then measured with a precision of  $1 \mu\text{m}$ . By plotting the beam deviation versus the angle of incidence and using Matlab to fit a curve given by equation A.2, the refractive index can be obtained as displayed in Figure A.2.

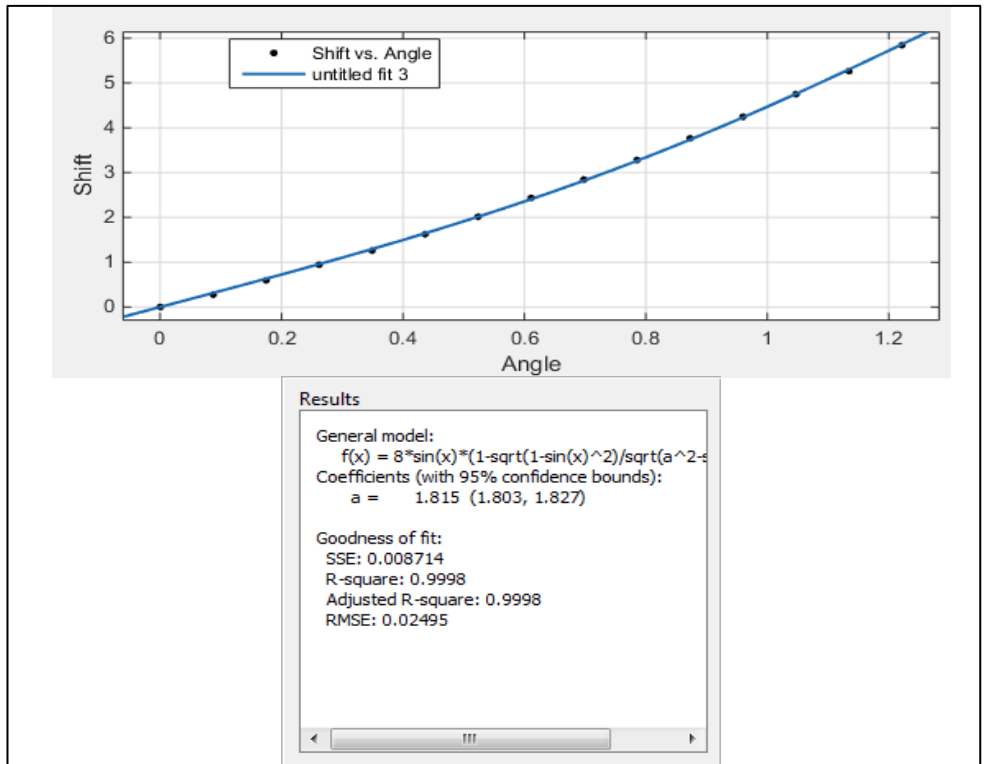


Figure A.2: Samples output from the Matlab curve fitting tool in refractive index measurements trial (YAG samples). The coefficient  $a$  is the value estimated for the refractive index. A R-square value close to 1 denotes a good match between the model and the data.

As can be seen in figure, the model fits well the experimental data with a R-square value equal to 0.9998. This proved that the proposed setup was suitable to make the measurement. The resulting values obtained for the refractive indices of relevance are summarized in Table A.5.

Table A.5: Results from the refractive index measurements.

Material and wavelength	Refractive index
PGC1 @ 532 nm	Not measurable due to striations in the substrate
PGC2 @ 532 nm	$1.564 \pm 0.007$
YAG @ 532 nm	$1.815 \pm 0.012$

These values of refractive indices are the ones that were used in the reflectivity measurements. As the refractive index of PGC1 could not be measured, its value was taken equal to the one of PGC2 in a first approximation. Since the trials on optical properties of PGC1 samples have been mostly qualitative this was not expected to have a large impact on the conclusions.

---

## **Appendix B: G&H 7-stage cleaning process**

---

This section describes the 7-stage cleaning process used in the production line at Gooch and Housego. The process is a fully automated and embedded bloc that takes sample batches through seven individual baths to thoroughly remove dust and residues from the surface. The apparatus is the Optimal UCS 120 from Optimal Technologies Ltd.

The containers are filled as follow:

- Bath 1: An alkaline containing fluid removes most of the contamination.
- Bath 2: Town main waters for rinsing.
- Bath 3: Neutral or slightly acidic detergent to complete cleaning and neutralisation of the surfaces
- Bath 4: Town main waters for rinsing.
- Bath 5: Deionised water (from a close looped purification system using activated carbon and mixed bed resin) to rinse from the contaminants contained in town main waters.
- Bath 6: Same as Bath 5. The holder is slowly pulled out so that water is removed by capillary forces.
- Bath 7: Infrared-heating element and air blade to remove the remaining water.

Every step can be assisted by agitation, heating up to 80<sup>0</sup>C and/or ultrasonics if the samples are suitable for those. The total duration from stage 1 to stage 7 is about 35 min. All samples from the factory go through the process before being shipped or used for assemblies, provided they can bear the treatment.

---

## Appendix C: Analysis of reflectance data: Bayesian analysis

---

Bayesian analysis was employed to make use of the reflectance data in the frame of the model described in 1.4.1. The method allows the inference of a set of parameters by calculating, for each set, the gap between the theoretical model and the experimental data before giving the most likely solution based on the minimum value found for this gap.

In the frame of this work, Bayes' theorem can be written

$$p(n_2, d_2 | D, M, I) = \frac{p(n_2, d_2 | M, I)}{p(D | M, I)} * p(D | M, n_2, d_2, I)$$

Where  $n_2$ ,  $d_2$  are the parameters to be found (respectively the refractive index and thickness of the bond), D denotes the experimental data, M denotes the model used, I denotes the prior information and the symbol “|” reads as “given”.

$p(n_2, d_2 | D, M, I)$  is the posterior Probability Density Function (PDF) of  $[n_2, d_2]$ . It is the probability of  $[n_2, d_2]$  being the desired parameters given the data, the model and the prior information. Obtaining this function is the purpose of the analysis.

$p(n_2, d_2 | M, I)$  is the prior probability density function of  $[n_2, d_2]$ . It is the suggested PDF without any experimental data. It can be considered constant as without data, any combination of  $n_2$  and  $d_2$  within the domain considered has the same probability.

$p(D | M, I)$  is the normalisation factor  $\left( \iint_{\Delta n_2 \Delta d_2} p(n_2, d_2 | D, M, I) dn_2 d d_2 = 1 \right)$  and is constant.

$p(D | M, n_2, d_2, I)$  is the likelihood of  $[n_2, d_2]$ . It represents the probability of obtaining the experimental data given a value of  $n_2$  and  $d_2$  and the theoretical model.

If it is assumed that the probability function for the likelihood follows a Gaussian distribution, then the posterior PDF can be written as

$$p(n_2, d_2 | D, M, I) = C * \exp \left( -\frac{1}{2} [(\chi_S^2 + \chi_P^2) - (\chi_S^2 + \chi_P^2)_{min}] \right)$$

With C a normalisation constant and

$$\chi_i^2 = \sum_{\alpha} \frac{(R_{\alpha,i}^{th} - R_{\alpha,i}^{exp})^2}{(\sigma_{\alpha,i}^{exp})^2}$$

Represents the sum of the residuals obtained at each angle  $\alpha$  within a measurement at the polarisation  $i$  (S or P). These are defined by the difference between the experimental data

$(R_{\alpha,i}^{exp})$  and the theoretical value associated with the values  $[n_2, d_2]$  ( $R_{\alpha,i}^{th}$ ), weighted by the error on the measurement ( $\sigma_{\alpha,i}^{exp}$ ).

$(\chi_S^2 + \chi_P^2)_{min}$  is the minimum value obtained for this sum when scanning the domain  $\Delta n_2 \Delta d_2$  which means that when  $(\chi_S^2 + \chi_P^2) = (\chi_S^2 + \chi_P^2)_{min}$ , the value of the PDF is maximum.

The algorithm performed by the Matlab script is therefore the following one.

- Take as input all the parameters (samples geometry, wavelength, range of analysis...)
- Take as input the experimental data. They are given as a matrix containing
  - o The angles at which the reflectance values were measured (usually seven or eight values).
  - o The error on the angle.
  - o The reflectance measured in S-polarised mode at each angle.
  - o The experimental error in S-polarised mode at each angle.
  - o The reflectance measured in P-polarised mode at each angle.
  - o The experimental error in P-polarised mode at each angle.
- For each pair of value  $[n_2, d_2]$  in the domain defined, calculate the theoretical reflectance value at angle  $\alpha$  given by the model. Then calculate the difference between the data point and the experimental data and weight with the experimental error. Sum the residuals over each value of angle and compare it with the current minimum residual. If it is lower set it at new minimum residual.
- When the loop is done, associate to each pair a probability based on the difference between the residual and the minimum residual found.
- Normalise the curve for the sum of probabilities over the domain to be 1.
- Return the pair  $[n_2, d_2]$  associated with minimum residuals.

As a visual aide, the script returns plots of the experimental curves superimposed with the theoretical curves associated with the most likely pair of parameters as well as a map of probability across the domain  $\Delta n_2 \Delta d_2$ . The latter is made by plotting the contour of the domains containing 68.3%, 95.5% and 99.7% of the probability density function volume.

The script used is presented on the next pages (from [105])

```

clear all
clc
close all

addpath(genpath('contourfcmap')); % https://uk.mathworks.
com/matlabcentral/fileexchange/29638-contourfcmap--filled-contour-
plot-with-precise colormap?s_tid=srchtitle
addpath(genpath('ploterr')); % http://www.mathworks.
com/matlabcentral/fileexchange/22216-ploterr
addpath(genpath('pcolorbar'));

%%%%%%%%%%%%%% %% parameters
%%%%%%%%%%%%%% %% n0 = 1; % refractive index of air
%%%%%%%%%%%%%% %% n1 = 1.564; % refractive index of material (green light)

lambda = 532; % wavelength of green laser light in nm

n2min = 1.3;
n2step = 0.0001;
n2max = 1.6;

d2min = 110;
d2step = 0.5;
d2max = 130;

n2for=((n2max-n2min)/n2step)+1;
d2for=((d2max-d2min)/d2step)+1;
n2d2for=round(n2for*d2for);

%%%%%%%%%%%%%% %% R_input.dat
%%%%%%%%%%%%%% %% A = importdata('R_inputRS.txt');

alpha_d=A(:,1); % alpha in degree
alpha_r=A(:,1).*(pi/180); % alpha in radians
alphaerr_d=A(:,2); % sigma(alpha) in degree
Rsmag=A(:,3); % Rs
Rserr=A(:,4); % sigma(Rs)
Rpmag=A(:,5); % Rp
Rperr=A(:,6); % sigma(Rp)
m=length(alpha_r);

% Rpmag=NaN(m,1);
% Rperr=NaN(m,1);
% Rsmag=NaN(m,1);
% Rserr=NaN(m,1);

```

```

%%%%% R_output.dat
%%%%%
%%%%%
j=1;
beta=zeros(m,1);
gamma=zeros(m,1);
delta2=zeros(m,1);
rs01=zeros(m,1);
rs12=zeros(m,1);
rp01=zeros(m,1);
rp12=zeros(m,1);
Rsmagth=zeros(m,1);
Rpmagth=zeros(m,1);
vect1=zeros(n2d2for, 4);

for n2=n2min:n2step:n2max
    for d2=d2min:d2step:d2max
        %% theoretical Rs and Rp %%
        for ind=1:m
            beta(ind)=asin((n0/n1)*(sin(alpha_r(ind))));
            gamma(ind)=asin((n0/n2)*(sin(alpha_r(ind))));
            delta2(ind)=(2*pi/lambda)*n2*d2*cos(gamma(ind));
            rs01(ind)=[(cos(alpha_r(ind)))-(sqrt(((n1/n0)^2)-
            ((sin(alpha_r(ind))^2)))/[(cos(alpha_r(ind)))+(sqrt(((n1/n0)^2)-
            ((sin(alpha_r(ind))^2)))];
            rs12(ind)=[(cos(beta(ind)))-(sqrt(((n2/n1)^2)-
            ((sin(beta(ind))^2)))]/ [(cos(beta(ind)))+(sqrt(((n2/n1)^2)-
            ((sin(beta(ind))^2)))];
            rp01(ind)=[(((n1/n0)^2)*cos(alpha_r(ind))-
            (sqrt(((n1/n0)^2)-((sin(alpha_r
            (ind))^2))))]/[((n1/n0)^2)*cos(alpha_r(ind))+(sqrt(((n1/n0)^2)-
            ((sin(alpha_r(ind))^2)))];
            rp12(ind)=[(((n2/n1)^2)*cos(beta(ind))-
            (sqrt(((n2/n1)^2)-((sin(beta
            (ind))^2))))]/[((n2/n1)^2)*cos(beta(ind))+(sqrt(((n2/n1)^2)-
            ((sin(beta(ind))^2)))];
            Rsmagth(ind)=[2*((1-
            ((rs01(ind))^2))^2)*((rs12(ind))^2)*(1-cos(2*(delta2(ind))))]/[1-
            (2*((rs12(ind))^2)*(cos(2*(delta2(ind)))))+((rs12(ind))^4)];
            Rpmagth(ind)=[2*((1-
            ((rp01(ind))^2))^2)*((rp12(ind))^2)*(1-cos(2*(delta2(ind))))]/[1-
            (2*((rp12(ind))^2)*(cos(2*(delta2(ind)))))+((rp12(ind))^4)];

        end
        %% X2 %%
        chi2mins=2000;
        chitots=0;
        for ind=1:m
            chi2s=(abs((Rsmag(ind)-
            Rsmagth(ind))^2)/((Rserr(ind))^2);

```

```

        chitots=chitots+chi2s;
    end
    if chitots < chi2mins
        chi2mins=chitots;
    end
    chi2minp=2000;
    chitotp=0;
    for ind=1:m
        chi2p=(abs((Rpmag(ind)-
Rpmagth(ind)))^2)/((Rperr(ind))^2);
        chitotp=chitotp+chi2p;
    end
    if chitotp < chi2minp
        chi2minp=chitotp;
    end
    %% output file %%
    vect1(j,:)=[n2 , d2 , chi2mins , chi2minp];
    j=j+1;
end
save('R_output.mat','vect1')

%%%%%%%%%%%%%
%% PDFz
%%%%%%%%%%%%%
addition=vect1(:,3)+vect1(:,4);
minimum=min(addition);
addminusmin=addition-minimum;
PDF=exp(-addminusmin/2);

PDFvolume=n2step*d2step*PDF;
sumPDFvolume=sum(PDFvolume);

PDFz=PDF/sumPDFvolume; % probability density
function (PDF)

PDFzCheck=n2step*d2step*PDFz; sumPDFzCheck=sum(PDFzCheck);
% the probability must be 1

vect2=[vect1(:,1), vect1(:,2), PDFz]; % [n2;d2;PDFz]

%%%%%%%%%%%%%
%% confidence levels
%%%%%%%%%%%%%
n2=n2min:n2step:n2max;
d2=d2min:d2step:d2max;
n_col=length(n2);
d_row=length(d2);

```

```

X = reshape(vect2(:,1),d_row,n_col);
Y = reshape(vect2(:,2),d_row,n_col);
Z = reshape(vect2(:,3),d_row,n_col);

sortPDFz = sort(PDFz,'descend');
lengthPDF=length(sortPDFz);
totPDFz=zeros(lengthPDF,1);
totPDFz(1) = n2step*d2step*sortPDFz(1);
for x = 2:lengthPDF
    totPDFz(x) = totPDFz(x-1) + n2step*d2step*sortPDFz(x);
end

% contour containing 68.27% of probability content
for xx3 = 1:lengthPDF
if totPDFz(xx3) >= 0.6827
    value3 = sortPDFz(xx3);
    break
else
end
end

% contour containing 95.45% of probability content
for xx2 = 1:lengthPDF
if totPDFz(xx2) >= 0.9545
    value2 = sortPDFz(xx2);
    break
else
end
end

% contour containing 99.73% of probability content
for xx1 = 1:lengthPDF
    if totPDFz(xx1) >= 0.9973
        value1 = sortPDFz(xx1);
        break
    else
    end
end

value4= max(sortPDFz);
cont=[value1 value2 value3 value4];

figure
map=[0 0 1 ; 0 1 0 ; 1 0 0];
tick=[0.15 ; 0.50 ; 0.85];
labels = {'99.73%', '95.45%', '68.27%', ''};
hh=contourf(X,Y,Z,tick);
%
set(hh.cbar,'YTick',tick,'YTickLabel',labels,'fontsize',20,'FontName','Times');
% set(gca,'fontsize',20,'FontName','Times');
xlabel('Bond refractive index  
n_2','fontsize',20,'FontName','Times')
ylabel('Bond thickness d_2 [nm]','fontsize',20,'FontName','Times')
grid on
savefig('d2_vs_n2.fig')

```

```

%%%%% Rs and Rp (th and exp) vs alpha
%%%%% n2 and d2 associated to the highest value of probability %%%
Zmax=max(max(Z)); % find the highest value of
probability
[row,column]=find(Z==Zmax);
n2_mostprob=X(row,column); % n2 associated to the highest value
of probability
d2_mostprob=Y(row,column); % d2 associated to the highest value
of probability

%%%% theoretical Rs and Rp with n2_mostprob and d2_mostprob %%%

alpha_d090=0:1:90;
alpha_r090=alpha_d090.*(pi/180);
m090=length(alpha_r090);
beta_r090=zeros(m090,1);
gamma_mostprob=zeros(m090,1);
delta2_mostprob=zeros(m090,1);
rs01_mostprob=zeros(m090,1);
rs12_mostprob=zeros(m090,1);
rp01_mostprob=zeros(m090,1);
rp12_mostprob=zeros(m090,1);
Rsmagth_mostprob=zeros(m090,1);
Rpmagth_mostprob=zeros(m090,1);
for ind=1:m090
    beta_r090(ind)=asin((n0/n1)*(sin(alpha_r090(ind))));
    gamma_mostprob(ind)=asin((n0/n2_mostprob)*(sin(alpha_r090(ind))));
    delta2_mostprob(ind)=(2*pi/lambda)*n2_mostprob*d2_mostprob*cos(gamma_mostprob(ind));
    rs01_mostprob(ind)=[(cos(alpha_r090(ind)))-(sqrt(((n1/n0)^2)-((sin(alpha_r090(ind)))^2))]/[(cos(alpha_r090(ind)))+(sqrt(((n1/n0)^2)-((sin(alpha_r090(ind)))^2))];
    rs12_mostprob(ind)=[(cos(beta_r090(ind)))-(sqrt(((n2_mostprob/n1)^2)-((sin(beta_r090(ind)))^2))]/[(cos(beta_r090(ind)))+(sqrt(((n2_mostprob/n1)^2)-((sin(beta_r090(ind)))^2))];
    rp01_mostprob(ind)=[(((n1/n0)^2)*cos(alpha_r090(ind))-(sqrt(((n1/n0)^2)-((sin(alpha_r090(ind)))^2))]/[((n1/n0)^2)*cos(alpha_r090(ind))+(sqrt(((n1/n0)^2)-((sin(alpha_r090(ind)))^2))];
    rp12_mostprob(ind)=[(((n2_mostprob/n1)^2)*cos(beta_r090(ind))-(sqrt(((n2_mostprob/n1)^2)-((sin(beta_r090(ind)))^2))]-
```

```

((sin(beta_r090(ind)))^2))]/[((n2_mostprob/n1)^2)*cos(beta_r090(ind)))+(sqrt (((n2_mostprob/n1)^2)-((sin(beta_r090(ind)))^2))];

Rsmagth_mostprob(ind)=[2*((1-
((rs01_mostprob(ind))^2))^2)*((rs12_mostprob(ind))^2)*(1-
cos(2*(delta2_mostprob(ind))))]/[1-
(2*((rs12_mostprob(ind))^2)*(cos(2*(delta2_mostprob(ind)))))+((rs12_mostprob(ind))^4)];

Rpmagth_mostprob(ind)=[2*((1-
((rp01_mostprob(ind))^2))^2)*((rp12_mostprob(ind))^2)*(1-
cos(2*(delta2_mostprob(ind))))]/[1-
(2*((rp12_mostprob(ind))^2)*(cos(2*(delta2_mostprob(ind)))))+((rp12_mostprob(ind))^4)];

end

%% plots %%
figure

% plot of theoretical and experimental Rs vs alpha
subplot(1,2,1)
aa= plot(alpha_d090,Rsmagth_mostprob,'c','LineWidth',2);
% theoretical Rs
hold on
bb= ploterr(alpha_d,Rsmag,alphaerr_d,Rserr,'x');
% experimental Rs plus error
set(bb(1),'MarkerEdgeColor',[0,0,1],'LineWidth',2,'markersize',15);
;
set(bb(2),'Color',[0,0,1],'LineWidth',2);
set(bb(3),'Color',[0,0,1],'LineWidth',2);
set(gca,'fontsize',20,'FontName','Times');
set(gca,'XLim',[0 90]);
set(gca,'XTick',(0:10:90));
set(gca,'YLim',[0 inf]);
xlabel('Angle of incidence \alpha
[^o]', 'fontSize',20,'FontName','Times');
ylabel('Reflectance R_{\perp}', 'fontSize',20,'FontName','Times');
legendone= legend([aa(1) bb(1)],'R_{\perp} th','R_{\perp}
exp','Location','best');
set(legendone,'FontSize',20);
grid on

% plot of theoretical and experimental Rp vs alpha
subplot(1,2,2)
dd= plot(alpha_d090,Rpmagth_mostprob,'m','LineWidth',2);
% theoretical Rp
hold on
ee= ploterr(alpha_d,Rpmag,alphaerr_d,Rperr,'x');
% experimental Rp plus error
set(ee(1),'MarkerEdgeColor',[1,0,0],'LineWidth',2,'markersize',15);
;
set(ee(2),'Color',[1,0,0],'LineWidth',2);
set(ee(3),'Color',[1,0,0],'LineWidth',2);
set(gca,'fontSize',20,'FontName','Times');
set(gca,'XLim',[0 90]);
set(gca,'XTick',(0:10:90));
set(gca,'YLim',[0 inf]);

```

```
xlabel('Angle of incidence \alpha
[°]', 'fontsize', 20, 'FontName', 'Times');
ylabel('Reflectance R_{||}', 'fontsize', 20, 'FontName', 'Times');
legendtwo= legend([dd(1) ee(1)], 'R_{||} th', 'R_{||}
exp', 'Location', 'best');
set(legendtwo, 'FontSize', 20);
grid on
str = ['n_2= ', num2str(n2_mostprob), ' ; d_2=
', num2str(d2_mostprob), ' nm'];
annotation('textbox', 'LineWidth', 1, 'BackgroundColor', 'white', 'Stri
ng', str, 'fontsize',
20, 'FontName', 'Times', 'FitBoxToText', 'on', 'HorizontalAlignment', 'c
enter', 'VerticalAlignment', 'middle');
savefig('R_vs_alpha.fig')
```

---

## Bibliography

---

- [1] N. Il'ichev, *Handbook of solid state lasers*, Woodhead publishing, 2014.
- [2] W.M. Steen, *Basic Laser Optics*, Springer, 2003.
- [3] O. Svelto, *Principles of Lasers*, Springer, 2010.
- [4] <https://www.rp-photonics.com/encyclopedia.html>, Wiley-VCH (2008), link valid on 07/02/2019.
- [5] C.K. Rhodes (Ed), *Excimer Lasers*, 1984.
- [6] P. Urquhart, Review of rare earth doped fibre lasers and amplifiers, IEE Proceedings J (Optoelectronics), 135 (6) pp. 385-407, 1988.
- [7] Course University of Maryland  
<https://ece.umd.edu/~davis/chapter13.pdf> valid on 07/02/2019.
- [8] W.F. Krupke, Ytterbium solid-state lasers – The first decade, IEEE Journal on selected topics in quantum electronics, 6 (6) pp. 1287-1295, 2000.
- [9] T.Y. Fan, Heat Generation in Nd:YAG and Yb:YAG, IEEE Journal of quantum electronics, 29 (6) pp. 1457-1459, 1993.
- [10] X. Peng, Power scaling of diode-pumped Nd:YVO<sub>4</sub> lasers, IEEE Journal of quantum electronics, 38(9) pp. 1291-, 2002.
- [11] [https://www.rp-photonics.com/quantum\\_defect.html](https://www.rp-photonics.com/quantum_defect.html), Wiley-VCH (2008), link valid on 07/02/2019.
- [12] R. Lavi, Heat reduction by direct pumping of Nd:YAG at 885 nm, OSA publishing, 68 pp. 441-443, 2002.
- [13] B. Canny, D. Curie, Non-radiative relaxation of solids: different pathways to the ground state. In: B. Di Bartolo (Ed) *Advances in Nonradiative processes in solids*. NATO ASI Series (Series B: Physics), vol. 249, Springer, 1991.
- [14] Y. Sato, T.Taira, Laser operation with near quantum-defect slope efficiency in Nd: YVO<sub>4</sub> under direct pumping into the emitting level, Applied Physics Letters, 82, 2003.
- [15] D.C. Brown, *High-Peak-Power Nd:Glass Laser systems*, pp. 5-6, Springer, 1981.
- [16] C.E. Weeb, J.D.C. Jones (Eds), *Handbook of laser technology and applications: laser design and laser systems*, vol 2 pp-764, Taylor & Francis Ltd, 2004.
- [17] M.E. Innocenzi & al., Thermal modeling of continuous-wave end-pumped solid-state lasers, Applied Physics Letters, 56, 1990.
- [18] B.R. Karstetter, R.O. Voss, Chemical strengthening of glass-ceramics in the system Li<sub>2</sub>O-Al<sub>2</sub>O<sub>3</sub>-SiO<sub>2</sub>, Journal of the American Ceramic Society, 1967.
- [19] J. Marion, Appropriate use of the strength parameter in solid state slab laser design, Journal of Applied Physics, 62, 1987.

## BIBLIOGRAPHY

---

- [20] W.D. Kingery, Factors affecting thermal stress resistance of ceramic materials, Journal of the American Ceramic Society, 38(1), 1955.
- [21] MIT Open course by M.J Hancock  
<https://ocw.mit.edu/courses/mathematics/18-303-linear-partial-differential-equations-fall-2006/lecture-notes/heateqni.pdf> valid on 07/02/2019.
- [22] A. Montmerle Bonnefois, Etude théorique et expérimentale d'un laser à solide de forte puissance moyenne, déclenché à haute cadence et possédant une bonne qualité de faisceau. Ph.D. Thesis, pp. 38-42, 2006.
- [23] J.M. Eggleston & al., The slab geometry laser –Part 1: Theory, IEEE Journal of Quantum Electronics, QE-20(3), pp. 289-300, 1984.
- [24] C.A. Carter, J.M. Harris, Comparison of models describing the thermal lens effect, Applied Optics, 23(3) pp. 476-481, 1984.
- [25] X. Peng & al., Study of the mechanical properties of Nd:YVO<sub>4</sub> crystal by use of laser interferometry and finite-element analysis, Applied Optics, 40(9), pp. 1396-1403, 2001.
- [26] W.A. Clarkson & al., Simple method for reducing the depolarization loss resulting from thermally induced birefringence in solid-state lasers, Optics Letters, 24(12) pp. 820-822, 1999.
- [27] W.C. Scott and M. de Wit, Birefringence compensation and TEM<sub>00</sub> mode enhancement in a Nd:YAG laser, Applied Physics Letters, 18(3), 1971.
- [28] J.G. Bai & al., Mitigation of thermal lensing effect as a brightness limitation of high-power broad area diode lasers, Proceedings of SPIE - The International Society of Optical Engineering, 2011.
- [29] W.R. Rapoport, C.P. Khattak, Titanium sapphire laser characteristics, Applied Optics, 27(13) pp. 2677-2684, 1988.
- [30] R. Moncorgé, Laser materials based on transition metal ions, Optical Materials, 63 pp. 105-117, 2017.
- [31] [https://www.rp-photonics.com/rare\\_earth\\_doped\\_gain\\_media.html](https://www.rp-photonics.com/rare_earth_doped_gain_media.html), Wiley-VCH (2008), link valid on 07/02/2019.
- [32] K. Petermann, Oxide laser crystals dopes with rare earth and transition metal ions in B. Denker and E. Schklovsky (Eds) *Handbook of solid-state lasers: Materials, System and Applications*, pp. 3-28, Woodhead Publishing, 2013.
- [33] B. Denker & al, Erbium (Er) glass lasers in B. Denker and E. Schklovsky (Eds) *Handbook of solid-state lasers: Materials, System and Applications*, pp. 341-358, Woodhead Publishing, 2013.
- [34] R. Ell & al. Generation of 5-fs pulses and octave-spanning spectra directly from a Ti:sapphire laser, Optics Letters, 26(6) pp. 373-375, 2001.
- [35] A.A. Kaminskii, Laser crystals and ceramics: recent advances, Laser & photonics review, 1(2), 2007.

- [36] J.H. Campbell & al, High-power solid-state lasers: a laser glass perspective, International Journal of Applied Glass Science, 2(1), 2011.
- [37] V.B. Kravchenko, Y.L. Kopylov, Oxide laser ceramics in B. Denker and E. Schklovsky (Eds) *Handbook of solid-state lasers: Materials, System and Applications*, pp. 54-81, Woodhead Publishing, 2013.
- [38] A.C. Erlandson & al, Comparison of Nd:phosphate glass, Yb:YAG and Yb:S-FAP laser beamlines for laser inertial fusion energy (LIFE), Optical Materials Express, 1(7) pp. 1341-1352, 2011.
- [39] J. Yang, Theory of thermal conductivity in *Thermal conductivity: Theory, properties and applications* by T.M Tritt (Ed), Springer, 2004.
- [40] T.Y. Fan, R.L. Byer, Diode Laser-Pumped Solid-state lasers, IEEE Journal of Quantum Electronics, 24 (6), 1988.
- [41] T.H. Maiman, Stimulated optical radiation in ruby, Nature, 187(4736), pp. 493-494, 1960.
- [42] R.L. Byer, Diode Laser-Pumped Solid-state lasers, Science, 239 (4841) pp. 742-747, 1988.
- [43] V.I. Arbuzov, Neodymium, erbium and Ytterbium laser glasses in B. Denker and E. Schklovsky (Eds) *Handbook of solid-state lasers: Materials, System and Applications*, pp. 110-138, Woodhead Publishing, 2013.
- [44] Course University of Maryland  
<https://ece.umd.edu/~davis/C8.pdf> valid on 07/02/2019.
- [45] O.K. Deutschbein & al., les verres phosphates, nouveaux matériaux lasers, Revue de physique appliquée, 2(1) pp. 29-37, 1967.
- [46] E.T.Y Lee, E.R.M Taylor, Thermo-optic coefficients of potassium alumino-metaphosphate glasses, Journal of Physics and Chemistry of Solids, 65(6) pp. 1187-1192, 2004.
- [47] M. Karabulut & al., Mechanical and structural properties of phosphate glasses, Journal of Non-Crystalline Solids, 288(1-3) pp. 8-17, 2001.
- [48] Y. Sato, T. Taira, Numerical model for thermal parameters in optical materials, Proc. SPIE 9893, Laser Sources and applications III, 98930F, 2016.
- [49] A Agnesi, F. Pirzio, Neodymium-doped yttrium aluminium garnet (Nd:YAG) and neodymium-doped yttrium orthovanadate (Nd:YVO<sub>4</sub>) in B. Denker and E. Schklovsky (Eds) *Handbook of solid-state lasers: Materials, System and Applications*, pp. 256-282, Woodhead Publishing, 2013.
- [50] [https://www.rp-photonics.com/vanadate\\_lasers.html](https://www.rp-photonics.com/vanadate_lasers.html) , Wiley-VCH (2008), link valid on 07/02/2019.
- [51] J. Vetrovec & al., Side-pumped solid-state disk laser for high-average power, US Patent 7200161, 2004.
- [52] A. Giesen, J. Speiser, Fifteen years of work on thin-disk lasers: results and scaling laws, IEEE Journal of selected topics in quantum electronics, 13(3), 2007.

- [53] P. Klopp & al., Highly efficient mode-locked Yb:Sc<sub>2</sub>O<sub>3</sub> laser, Optics Letters, 29(4) p. 391, 2004.
- [54] L. Schlie & al., Thin disk laser operations with unique thermal management, US Patent 8213471, 2012.
- [55] Y. Cha & al., Development and characterisation of a 400-W slab-type Nd:YAG gain module, Journal of the Optical Society of Korea, 16(1) pp. 53-56, 2012.
- [56] F. Liu & al., Interface and material engineering for zigzag slab lasers, Scientific reports 7, 16699, 2017.
- [57] V. Ashoori & al., Heat generation and removal in solid state lasers, Intech open science, 2012.
- [58] D.C. Brown & al., Heat-fraction-limited CW Yb:YAG cryogenic solid-state laser with 100% photon slope efficiency, Optics Express 16573, 18(16), 2010.
- [59] H.G. Stenhouse & al., Direct bonding Nd:YAG to sapphire wafers, OSA Publishing Laser congress 2017 (ASSL, LAC), 2017.
- [60] A. Kausas, Structured laser gain-medium by new bonding for power micro-laser, SPIE LASE, 2017.
- [61] M. Tsunekane & al., Efficient 946-nm laser operation of a composite Nd:YAG rod with undoped ends, Applied Optics, 37(24) pp. 5713-5719, 1998.
- [62] Y.T. Chang & al., Comparison of thermal lensing effects between single-end and double-end diffusion-bonded Nd:YVO<sub>4</sub> crystals for <sup>4</sup>F<sub>3/2</sub> → <sup>4</sup>I<sub>11/2</sub> and <sup>4</sup>F<sub>3/2</sub> → <sup>4</sup>I<sub>13/2</sub> transitions, Optics Express, 16(25) pp. 21155-21160, 2008.
- [63] N. Pavel & al., High average power diode end-pumped composite Nd:YAG laser passively Q-switched by Cr<sup>4+</sup>:YAG saturable absorber, Japanese Journal of Applied Physics, 40(1-3A), 2001.
- [64] J. Haisma, G.A.C.M Spierings, Contact bonding, including direct-bonding in a historical and recent context of materials science and technology, physics and chemistry: Historical view in a broader scope and comparative outlook, Materials Science and Engineering, R-37 pp. 1-60, 2002.
- [65] H.J. Butt, M. Kappl (Eds), Van der Waals Forces in *Surface and interfacial forces*, Wiley-VCH, 2010.
- [66] W.P. Maszara & al., Bonding of silicon wafers for silicon-on-insulator, Journal of Applied Physics, 64 pp. 4943-, 1988.
- [67] M. Shimbo & al., Silicon-to-silicon direct bonding method, Journal of Applied Physics, 60 pp. 2987-, 1986.
- [68] V. Greco & al., Optical contact and van der Waals interactions: the role of the surface topography in determining the bonding strength of thick glass plates, Journal of Optics A: Pure and Applied Optics, 3 pp. 85-88, 2001.
- [69] R.B. Holt & al., Research on optical contact bonding, American Periodicals from the Center for Research Librairies, 66-649, 1966.

- [70] Lord Rayleigh, A study of glass surfaces in optical contact, Proceedings of the Royal Society, A156 pp. 326-, 1936.
- [71] C.J. Killow & al., Construction of rugged, ultrastable optical assemblies with optical component alignment at the few microradian level, Applied Optics, 52(2) pp. 171-181, 2013.
- [72] A. Berthold & al., Glass-to-glass anodic bonding with standard IC technology thin films as intermediate layers, Sensors and Actuators, 82 pp. 224-228, 2000.
- [73] H. Moriceau & al., Low temperature direct bonding: an attractive technique for heterostructures build-up, Microelectronics Reliability, 52(2) pp. 331-341, 2012.
- [74] QY Tong, Low temperature wafer direct bonding, Journal of Microelectromechanical systems, 3(1) pp. 29-35, 1994.
- [75] O.M Akselsen, Diffusion bonding of ceramics, Journal of Materials Science, 27(3) pp. 569-579, 1992.
- [76] K. Fujioka & al., Ion diffusion at the bonding interface of undoped YAG/Yb:YAG composite ceramics, Optical Materials, 46(C) pp. 542-547, 2015.
- [77] J.G. Daly, An evaluation of New UV-cured adhesives and effects of post-cure UV exposure, Proceedings of SPIE 4771, 2002.
- [78] <https://www.norlandprod.com/adhesiveindex2.html>, Wiley-VCH (2008), link valid on 07/02/2019.
- [79] D.A. Dillard (Ed), *Advances in structural adhesive bonding*, pp. 4-10, Woodhead Publishing, 2010.
- [80] Notes from SPIE course: Fastening optical elements with adhesives by J.G. Daly, followed in October 2017 at Photonics West.  
<https://spie.org/PW/course/fastening-optical-elements-with-adhesives>
- [81] Z. Zhang & al., Active alignment of optical fibers to planar waveguides using a thermal-curing adhesive, Journal of Lightwave Technology, 23(2) pp. 567-572, 2005.
- [82] B. Goss, Bonding glass and other substrates with UV curing adhesives, International Journal of Adhesion and Adhesives, 22(5) pp. 405-408, 2002.
- [83] S. Prabhu & al., A survey of technical literature on adhesive applications for optics, Proceedings of SPIE 6665, 2007.
- [84] [http://www.epotek.com/site/files/brochures/pdfs/adhesive\\_application\\_guide.pdf](http://www.epotek.com/site/files/brochures/pdfs/adhesive_application_guide.pdf) valid on 07/02/2019.
- [85] <https://www.masterbond.com/properties/epoxies-low-coefficient-thermal-expansion> valid on 07/02/2019.
- [86] P.R. Yoder, *Opto-mechanical systems design* 2<sup>nd</sup> Ed., M. Dekker Inc., 1993.
- [87] F.E. Hovis & al., Mechanisms of contamination induced optical damage in lasers, Proceedings of SPIE 2428, pp. 72-83, 1995.

## BIBLIOGRAPHY

---

- [88] K. Watanabe & al., Development of fiber bundle type fan-out for multicore fiber, 17<sup>th</sup> Opto-Electronics and Communications Conference, 2012.
- [89] [https://www.dymax.com/images/pdf/literature/sg008\\_industrial\\_adhesives\\_sealer\\_guide.pdf](https://www.dymax.com/images/pdf/literature/sg008_industrial_adhesives_sealer_guide.pdf) valid on 07/02/2019.
- [90] A.E. Hatheway, Analysis of adhesive bonds in optics, Proceedings of SPIE 1998, 1993.
- [91] D. Peter & al., Influence of adhesive bond line thickness on joint strength, International Journal of Adhesion and Adhesives, 29(7) pp. 724-736, 2009-10.
- [92] R. Knetchel, Glass frit bonding: an universal technology for wafer level encapsulation and packaging, Journal Microsystem Technologies, 12(1-2) pp. 63-68, 2005.
- [93] M. Ebert, J. Bagdahn, Determination of residual stress in glass frit bonded MEMS by finite element analysis, Conference Paper, 2004.
- [94] B. Wang & al., Considerations for MEMS packaging, Proceedings of HDP'04, 2004.
- [95] DH. Gwo, Two unique aspects of gravity probe-B star-tracking space telescope: (1) focal-plane roof-edge diffraction and (2) fused-quartz bonding for 2.5-Kelvin applications, Proceedings of SPIE 3356, 1998.
- [96] A.A. van Veggel, C.J. Killow, Hydroxide catalysis bonding for astronomical instruments, Advanced Optical Technologies, 3(3) pp. 293-307, 2014.
- [97] M. Armano & al., Beyond the required LISA free fall performance: new LISA pathfinder results down to 20MHz, Physical Review Letters, 120(6), 2018.
- [98] LIGO Scientific and Virgo Collaborations (B.P. Abbott & al.), Observation of gravitational waves from a binary black hole, Physical Review Letters 116(6), 2016.
- [99] R.K Iler (Ed.), The chemistry of silica: solubility, Polymerization, colloid and surface properties and biochemistry of silica, John Wiley & Sons New York, pp. 116-, 172-, 281-, 1979.
- [100] S. Reid, Influence of temperature and hydroxide concentration on the settling time of hydroxyl-catalysis bonds, Physics Letters A, 363(5-6) pp. 341-345, 2007.
- [101] K.A. Haughian, Aspects of materials research for advanced and future generations of gravitational wave detectors, Ph.D. Thesis, pp. 164-165, 2012. <https://core.ac.uk/download/pdf/9656164.pdf>
- [102] M.H. Phelps, Hydroxide catalysis and indium bonding research for the design of ground-based gravitational wave detectors, Ph.D. Thesis, pp. 55-81, 2018. <http://theses.gla.ac.uk/30604/>
- [103] A. Preston & al., Hydroxide-bonding strength measurements for space-based optical missions, International Journal of Applied Ceramics Technologies, 5(4) pp. 365-372, 2008.
- [104] R. Douglas & al., Cryogenic and room temperature strength of sapphire jointed by hydroxide-catalysis bonding, Classical and Quantum Gravity, 31(4), 2014.

## BIBLIOGRAPHY

---

- [105] V. Mangano, Studies of some properties of hydroxide-catalysis bonds, Ph.D. Thesis, 2018. <http://theses.gla.ac.uk/30938/>
- [106] S. Sinha & al., Investigation of the suitability of silicate bonding for facet termination in active fiber devices, Optics Express, 15(20) pp. 13003-13022, 2007.
- [107] C.B. Dane, Design and operation of a 150 W near diffraction-limited laser amplifier with SBS wavefront correction, IEEE Journal of Quantum Electronics, 31(1) pp. 148-163, 1995.
- [108] J.H. Campbell & al., Development of composite polymer-glass edge cladding for NOVA laser disks, Damage in Laser Materials NIST special publication 752, 1986.
- [109] M. Strzelecki, STICKING together, White Paper Schott Glass Technologies, 2003.
- [110] S. Conzone & al., Low temperature joining of phosphate glass, US patent 6652972B1, 2003.
- [111] P.B.C. Bunker & al., Phosphate glass dissolution in aqueous solution, Journal of Non-crystalline solids, 64 pp. 291-316, 1984.
- [112] J.E. Sundeen, Advances in bonded YAG composite laser gain media, Proceedings of SPIE 6216, 62160N, 2006.
- [113] M. De Vido & al, Characterisation of adhesive-free bonded crystalline Yb:YAG for high energy laser applications, Optical Materials Express, 7(2) pp. 425-432, 2017.
- [114] O. Lyngnes & al., Laser gain media to heat sink integration for improved thermal management, White Paper from Advanced Thin Films, 2010.
- [115] K.R. Williams, Etch rates for micromachining processing – Part II, Journal of Microelectromechanical Systems, 12(6) pp. 761-778, 2003.
- [116] T.S. Rutherford, An edge-pumped Yb-YAG slab laser and phased array resonator, Ph.D. Thesis, pp. 98-101, 2001. <https://books.google.co.uk/>
- [117] O.S. Heavens, *Optical properties of thin solid films*, Dover Publications, pp.50-, 1991.
- [118] A. Taylor, Aspects of optical metrology system for space-borne gravitational wave detectors, Ph.D. Thesis, pp. 16-44, 2014. <http://theses.gla.ac.uk/5741/>
- [119] A.A. Manenkov, Fundamental mechanisms of laser induced damage in optical materials: today's state of understanding and problems, Optical Engineering, 53(1), 2014.
- [120] ISO standards 21254-1-2,-3 and -4
- [121] W.T. Chen, C.W. Nelson, Thermal stress in bonded joints, IBM journal of Research and Development, 23(2), 1979.
- [122] CH. Hsueh, Thermal stresses in elastic multilayer systems, Thin Solid Films, 418 pp. 182-188, 2002.
- [123] E. Suhir, Analysis of interfacial thermal stresses in a trimaterial assembly, Journal of Applied Physics, 89(3685), 2001.

- [124] J. Wang, S. Zeng, Thermal stresses analysis in adhesive/solder bonded biomaterial assemblies, *Journal of Applied Physics*, 104(113508), 2008.
- [125] L. Cunningham & al., Re-evaluation of the mechanical loss factor of hydroxide-catalysis bonds and its significance for the next generation of gravitational wave detectors, *Physics Letters A*, 374(39) pp. 3993-3998, 2010.
- [126] M. Masso Reid, Properties of bonded silicon for future generations of gravitational wave observatories, Ph.D. Thesis, pp. 196-, 2019.  
To be published on <http://theses.gla.ac.uk/>
- [127] E.J. Elliffe & al., Hydroxide-catalysis bonding for stable optical systems for space, *Classical and Quantum Gravity*, 22 pp. 257-267, 2005.
- [128] I.C. Engin, Theories on rock cutting, grinding and polishing mechanisms in *Tribology in Engineering* by H. Pihtili (Ed), 2013.
- [129] HS. Kim, T. L. Schmitz, Shear strength evaluation of hydroxide catalysis bonds for glass-glass and glass-aluminium assemblies, *Precision Engineering*, 37(1) pp. 23-32, 2013.
- [130] B. Hammant, The use of 4-point loading tests to determine mechanical properties, *Composites*, 2(4) pp. 246-249, 1971.
- [131] N.L. Beveridge & al., Low-temperature strength tests and SEM imaging of hydroxide catalysis bonds in silicon, *Classical and Quantum Gravity*, 28(8) pp. 85014, 2012.
- [132] T. Accadia & al., Status of the Virgo project, *Classical and Quantum Gravity*, 28(11), 2011.
- [133] S.M. Aston & al., Update on quadruple suspension design for Advanced LIGO, *Classical and Quantum Gravity*, 29(23), 2012.
- [134] B. Willke & al., The GEO 600 gravitational wave detector, *Classical and Quantum Gravity*, 19(7), 2002.
- [135] K.A. Haughian, Aspects of materials research for advanced and future generations of gravitational wave detectors, Ph.D. Thesis, pp. 81-, 2012.  
<https://core.ac.uk/download/pdf/9656164.pdf>
- [136] N.L. Beveridge & al., KTP on Adhesive Free Bonding, Internal document Gooch and Housego and University of Glasgow, 2013.
- [137] M.H. Phelps, Hydroxide catalysis and indium bonding research for the design of ground-based gravitational wave detectors, Ph.D. Thesis, pp. 48-49, 2018.  
<http://theses.gla.ac.uk/30604/>
- [138] B.C. Bunker, Molecular mechanisms for corrosion of silica and silicate glasses, *Journal of Non-Crystalline Solids*, 179 pp. 300-308, 1994.
- [139] R.H. Doremus (Ed), *Diffusion of reactive molecules in solids and melts*, John Wiley and Sons, pp. 74-, 2002.
- [140] S.N. Crichton & al., Subcritical crack growth in a phosphate laser glass, *Journal of the American Ceramic Society*, 82(11) pp. 3097-30104, 1999.

- [141] C.B. Thorsness & al., Dehydroxylation of phosphate laser glass, Proceedings of SPIE 4102, Inorganic Optical Materials II, 2000.
- [142] Project presentation University of Missouri:  
[mse.mst.edu/media/academic/glassres/documents/tischendorf%20update.ppt](http://mse.mst.edu/media/academic/glassres/documents/tischendorf%20update.ppt)
- [143] R.H. Doremus, Diffusion in alumina, Journal of Applied Physics 100, 101301, 2006.
- [144] M.Rusdi, Y. Moroi, Study on water evaporation through 1-alkanol monolayers by the thermogravimetry method, Journal of Colloid and Interface Science, 272(2) pp. 472-479, 2004.
- [145] V. Mangano, Studies of some properties of hydroxide-catalysis bonds, Ph.D. Thesis, pp. 82-83, 2018. <http://theses.gla.ac.uk/30938/>
- [146] L. Chen, An efficient erbium doped phosphate laser glass for high average power pumping, Journal of Alloys and Compounds, 482(1-2) pp. 261-263, 2009.
- [147] A.A. Rasid, Characterisation of erbium doped phosphate glass, AIP Conference Proceedings 1217, 380, 2010.
- [148] L. Cunningham & al., Re-evaluation of the mechanical loss factor of hydroxide-catalysis bonds and its significance for the next generation of gravitational wave detectors, Physics Letters A, 374(39) pp. 3993-3998, 2010.
- [149] W. Plass & al., High-resolution knife-edge laser beam profiling, Optics Communications, 134(1-6) pp. 21-24, 1997.
- [150] J. Alda, Laser and Gaussian beam propagation and transformation, in *Encyclopedia of optical engineering*, Marcel Dekker Inc., 2003.
- [151] H. Kogelnik & T. Li, Laser Beams and Resonators, 5(10) pp. 1550-1567, 1966.
- [152] S.A. Self, Focusing of spherical Gaussian beams, Applied Optics, 22(5), 1983.
- [153] Course University of Oxford  
<http://www.materials.ox.ac.uk/teaching/ug/ugtdp.html> valid on 07/02/2019
- [154] Course University of California San Diego  
[http://cem01.ucsd.edu/~vitaliy/courses/ece182/18206\\_files/SpatialFiltering.pdf](http://cem01.ucsd.edu/~vitaliy/courses/ece182/18206_files/SpatialFiltering.pdf) valid on 07/02/2019
- [155] V. Mangano, Studies of some properties of hydroxide-catalysis bonds, Ph.D. Thesis, pp. 176-, 2018. <http://theses.gla.ac.uk/30938/>
- [156] J. McKay, Chemical Mechanical polishing and direct bonding of YAG and Y<sub>2</sub>O<sub>3</sub>, Ph.D. Thesis, pp. 29-47, 2016. <https://escholarship.org/uc/item/7zd130dt>
- [157] C. Wert, C. Zener, Interstitial atomic diffusion coefficients, Physical Review, 76(1169), 1949.
- [158] V. Molchanov, N. Prikhid'ko, Corrosion of silicate glasses by alkaline solutions, Bulletin of the Academy of Sciences of the USSR, Division of chemical science, 6(10) pp. 1179-1184, 1957.

## BIBLIOGRAPHY

---

- [159] R. Kohli, K Mittal (Eds), Methods for monitoring and measuring cleanliness of surfaces, in *Developments in Surface Contamination and Cleaning*, pp. 107-178, Elsevier Inc, 2012.
- [160] LIGO Document E050228-v2, Silicate bonding procedure (Hydroxide-catalysis bonding), 2010.
- [161] Kaplan, Wayne D. et al. "A Review of Wetting versus Adsorption, Complexions, and Related Phenomena: The Rosetta Stone of Wetting." *Journal of Materials Science* 48.17 (2013): 5681–5717.
- [162] J.R. Vig, UV/Ozone cleaning of surfaces, *Journal of Vacuum Science & Technology A*, 3(3), 1985.

